Microscopic radiative strength functions and fission barriers for r-process nucleosynthesis

Vom Fachbereich Physik
der Technischen Universität Darmstadt

zur Erlangung des Grades
eines Doktors der Naturwissenschaften
(Dr. rer. nat.)

genehmigte Dissertation von
Dipl.-Phys. Hans Peter Loens
aus Darmstadt

Referent: Prof. Dr. K. Langanke
Korreferent: Prof. Dr. J. Enders

Tag der Einreichung: 1.2.2011
Tag der Prüfung: 24.2.2011

Darmstadt 2011
D17

Contents

Abstract

Nuclear astrophysics aims to answer the fundamental question of the origins of the elements in the universe, and relatedly to address the role of nuclear reactions as engines of stellar evolution, dynamics, and explosion. Nuclear astrophysics is thus a true interdisciplinary field combining astrophysics with nuclear physics.

In this thesis we focus on the r-process, which is considered to form about half of the elements with nucleon numbers A>70. In order to perform simulations of the r-process, different astrophysical and nuclear physics input is needed. One of the crucial inputs on the nuclear physics side are cross sections for radiative neutron capture and induced fission reactions. Most of the r-process isotopes are very neutron-rich and could not yet be produced experimentally. Therefore we have to employ theoretical predictions for the cross sections. These cross sections are generally calculated with the Hauser-Feshbach model.

To employ the statistical model to the determination of radiative capture reactions, one needs radiative strength functions. Generally E1 and M1 transitions dominate in r-process reactions. The strength functions are needed on a global scale and one has used a Lorentzian parametrisation for the strength functions motivated by the success of describing the electric giant dipole resonance by such a form. This turned out to be successful for nuclei close to stability. However, it has been observed that neutron-rich nuclei show enhanced E1 strength at energies far below the giant resonance, which is not correctly described by the Lorentzian ansatz. We will study the influence of such low-lying strength on cross sections relevant for r-process nucleosynthesis. Moreover, the Hauser-Feshbach model needs the strength functions also for excited states. Here one usually makes the bold approximation that the strength for all excited states is the same as for the ground state. This assumption goes with the name of Brink's hypothesis. It was originally formulated for giant collective resonances and has been verified experimentally for these collective modes. It is an open question if it is also valid for the aforementioned additional strength.

In this thesis we utilise two microscopic nuclear structure models to obtain the strength functions for selected nuclei. For the electric dipole strength function we adopt the relativistic-quasi-time-blocking approximation (RQTBA) and for the magnetic dipole strength the nuclear shell model. We calculated radiative neutron capture cross sections with the Hauser-Feshbach model using the results of the RQTBA model for chains of tin and nickel isotopes. The results show that additional low-energy strength from a pygmy resonance can affect the radiative neutron capture cross section. However, the impact of such low-lying E1 strength on (n,γ) cross sections turns up to be very sensitive to the interplay of the neutron separation energy and the nuclear level density. Generally, the RQTBA strength functions predict smaller radiative neutron capture cross sections than those obtained from a Lorentzian parametrisation.

In a second approach, we calculated magnetic dipole strength functions from the interacting shell model for iron nuclei. The shell model allows us to obtain the strength functions also for excited states, thus enabling us to discuss Brink's hypothesis for the M1 strength function. This hypothesis is theoretically confirmed by our results for the large collective spin-flip resonance. However, the hypothesis fails for the low-energy strength, in particular the scissors mode. We find noticeable differences to cross section calculations where often used parametrisations of the M1 strength are employed, indicating that an improved description of M1 strength functions is needed.

The r-process can also reach the region of the nuclear chart, where fission becomes important. Hence, the various fission processes must be included in r-process simulations. To describe such processes, fission barriers are essential. We calculated fission barriers for even-even nuclei within the Skyrme-Hartree-

Fock-BCS model. A particular focus is put on the sensitivity of these quantities to the used Skyrme functional and the role of reflection asymmetric shapes in nuclei. The results show a strong dependence on the used Skyrme functional regarding the barrier heights. Hence we expect noticeable differences in the rates of the various fission processes, if calculated with the different fission barriers. This will in turn affect r-process network simulations as fission can interrupt the r-process flow and move matter from the actinide or super-heavy regions to intermediate mass regions. Therefore also the formation of long-lived super-heavy elements in the r-process is very sensitive to the interaction used to calculate the fission barriers.

Zusammenfassung

Die Nukleare Astrophysik hat zum Ziel die fundamentale Frage nach dem Ursprung der Elemente in unserem Universum zu klären und dabei auch die Rolle von Kernreaktionen in der Entwicklung von Sternen und in Sternexplosionen zu verdeutlichen. Aufgrund der engen Verknüpfung von Astrophysik und Kernphysik in der Nuklearen Astrophysik kann diese als ein interdisziplinäres Feld angesehen werden.

In dieser Doktorarbeit beschäftigen wir uns mit dem r-Prozess, von dem man annimmt, dass er etwa die Hälfte aller Elemente mit Massenzahl $A>70$ erzeugt. Es sind verschiedenste astrophysikalische und kernphysikalische Größen nötig um diesen Prozess erfolgreich simulieren zu können. Zwei aus kernphysikalischer Sicht sehr wichtige Größen sind dabei Wirkungsquerschnitte für Neutroneneinfang und induzierte Spaltprozesse. Die meisten der im r-Prozess relevanten Isotope sind sehr neutronenreich und konnten bisher experimentell noch nicht hergestellt werden. Aus diesem Grund muss man auf theoretische Vorhersagen zurückgreifen um besagte Wirkungsquerschnitte zu beschreiben. Die Standardmethode zur Berechnung von Wirkungsquerschnitten für den r-Prozess ist der Hauser-Feshbach-Formalismus.

Dieses statistische Modell benötigt Stärkefunktionen zur Beschreibung der Photonenübergänge in den Wirkungsquerschnitten. Im Allgemeinen geht man dabei davon aus, dass E1 und M1 Überänge dominieren. Die Stärkefunktionen müssen in großer Anzahl für jeden relevanten Kern berechenbar sein, weswegen man dabei in der Regel auf die Beschreibung dieser Funktionen durch Lorentzfunktionen, die an die Dipol-Riesenresonanz angepasst sind, zurückgreift. Diese Beschreibung erweist sich als sehr erfolgreich bei stabilen Kernen. Allerdings wurde in neutronenreichen Kernen zusätzliche Stärke in Photonenübergängen weit unterhalb der Riesenresonanz gemessen, die nicht durch eine Lorentzfunktionen beschrieben werden kann. In dieser Arbeit werden wir den Einfluss solcher niederenergetischer Stärke auf die Strahlungsüberänge in Neutronen-Einfangsreaktionen, die im r-Prozess eine Rolle spielen, untersuchen. Das Hauser-Feshbach Modell beschreibt auch Strahlungsüberänge zwischen angeregten Zuständen, so dass die Stärkefunktion für dieser Überänge auch für angeregte Zustände bekannt sein muss. Hierbei nutzt man meist die gewagte Hypothese, dass die Stärkefunktionen für die Photonenübergänge aller angeregten Zustände durch die Stärkefunktion des Grundzustandes approximiert werden kann. Diese Approximation nennt man Brinks Hypothese. Ihre ursprüngliche Formulierung betraf ausschließlich kollektive Riesenresonanzen und ihre Gültigkeit bezüglich dieser Resonanzen wurde experimentell bestätigt. Es ist jedoch eine offene Frage, ob diese Hypothese auch auf die vorhergehend diskutierte niederenergetische Stärke anwendbar ist.

In dieser Arbeit nutzen wir zwei mikroskopische Kernstrukturmodelle, um die Stärke-Funktion für bestimmte Kerne zu berechnen. Für die Beschreibung der elektrischen Dipolübergänge verwenden wir die “relativistic-time-blocking-approximation” (RQTBA) und für die Beschreibung der magnetischen Dipolübergänge verwenden wir das Schalenmodell. Mit Hilfe des Hauser-Feshbach-Modells haben wir Wirkungsquerschnitte für Neutroneneinfänge mit Hilfe des RQTBA Modells für verschiedene Zinn und Nickel Isotope berechnet. Unsere Resultate zeigen, dass besagte niederenergetische Stärke einen Einfluss auf den Wirkungsquerschnitt hat, der jedoch empfindlich von dem Zusammenspiel zwischen der Neutronenschwelle und der Zustandsdichte abhängt. Die Verwendung des RQTBA-Modells ergibt im Allgemeinen geringere Wirkungsquerschnitte im Vergleich zu den Wirkungsquerschnitten, die mit Hilfe der Lorentzfunktion berechnet wurden.

In einem zweiten Ansatz haben wir die magnetische Dipol Stärke-Funktion von Eisen-Isotopen mit Hilfe des Schalenmodells berechnet. Das Schalenmodell ermöglicht es uns, die Stärke-Funktionen von angeregten Zustände zu beschreiben, so dass wir Brinks Hypothese bezüglich der M1 Übergänge untersuchen können. Unsere Resultate bestätigen die Gültigkeit dieser Hypothese in Bezug auf die

kollektive spin-flip Riesenresonanz. Jedoch versagt die Hypothese bezüglich der niederenergetischen Stärke, insbesondere bezüglich der "scissors mode". Unsere Resultate zeigen deutliche Unterschiede zu Berechnungen in denen weit verbreitete Parametrisierung der M1 Stärke verwendet wurden. Daraus folgern wir, dass eine verbesserte Beschreibung der M1 Übergänge notwendig ist.

Der r-Prozess kann auch die Region auf der Nuklidkarte erreichen, in der Spaltung auftreten kann. Aus diesem Grund müssen verschiedenste Spaltungsprozesse in r-Prozess Simulationen berücksichtigt werden. Die Spaltbarriere bildet hierbei eine fundamentale Größe bei der Beschreibung von Spaltprozessen. Wir haben diese Spaltbarrieren für gerade-gerade Kerne im Rahmen des Skyrme-Hartree-Fock-BCS Modells berechnet. Dabei wurde ein besonderes Augenmerk auf den Einfluss des verwendeten Skyrme Funktionals auf die Barriere und auf reflektionsasymmetrische Kernformen gelegt. Die Resultate zeigen eine starke Abhängigkeit der Spaltbarrieren von dem verwendeten Skyrme Funktional. Deshalb erwarten wir deutliche Unterschiede zwischen den Raten der verschiedenen Spaltprozesse, wenn unterschiedliche Skyrme Funktionale verwendet werden. Dies kann wiederum die r-Prozess Simulationen betreffen, denn Spaltprozesse können den Fluss des r-Prozesses unterbrechen und synthetisierte Materie aus dem Bereich der Aktiniden oder der superschweren Elemente in niedrigere Massenbereiche befördern. Aus diesem Grund hängt die Formation von langlebigen superschweren Elementen im r-Prozess stark von der in der theoretischen Beschreibung der Spaltbarrieren verwendeten Wechselwirkung ab.

Part I

Theory

1

Nuclear Astrophysics

The field of nuclear astrophysics is an interdisciplinary field within physics, combining astrophysics and nuclear physics. One of its many fascinating aspects is the combination of the physics of objects with very large dimensions (astrophysics) and the physics of the smallest scales (nuclear physics and particle physics). The goal of nuclear astrophysics is the description of the nuclear processes occurring in the universe and the effect these processes have on its evolution.

In the 1930s a series of papers, e.g. by Bethe [Bet39], laid the foundations of nuclear astrophysics. Later, in the 1950s the famous paper by Burbidge, Burbidge, Fowler, and Hoyle [BBFH57] reviewed the nucleosynthesis processes in the universe. A historical overview on the development of nuclear astrophysics up to 1957 (the release year of [BBFH57]) can be found in [Tri10]. A general introduction on nucleosynthesis can be found in [WIP$^+$97, AT99, KTW98, Boy08].

The term *nucleosynthesis* compasses the nuclear physics of all processes that create the elements in our universe and the influence of the astrophysical conditions on the properties of these processes. In principle a variety of different processes exist or are assumed to exist, however we can classify the most important processes qualitatively in three groups:

1. Big Bang nucleosynthesis: The first nucleosynthesis process is believed to have taken place in the first minutes after the Big Bang in which neutrons and protons were formed and from these primarily hydrogen and helium were created as well as some lithium. The hydrogen and helium formed in the Big Bang became the fuel of the first stars.

2. Stellar nucleosynthesis: In stars, hydrogen is burned to heavier elements via the so-called pp-chain (which creates helium) and the CNO cycle. The CNO cycle occurs in massive stars and depending on the mass the star may successively go through periods of helium, carbon, neon, oxygen, and silicon burning in its core. The burned material can be later ejected into the stellar surrounding by solar wind or supernovae.

3. Explosive nucleosynthesis: These processes are taking place under extreme conditions like supernovae explosions or neutron star mergers, involving reaction flows on very fast time-scales.

In this thesis we will particularly discuss improvements on the nuclear structure input for the determination of the reaction cross sections needed for r-process nucleosynthesis, i.e. radiative neutron capture reactions.

The heavy elements in the universe are made by neutron capture processes and at least two different scenarios are required to explain the observed abundances in the universe. The first has to be a process occurring at small neutron densities. Therefore the time-scales of neutron captures are slow compared to the time-scales of β-decays. This process is called the s-process and it follows closely the valley of stability. This causes abundance peaks for stable nuclei with magic neutron numbers and explains the relatively large observed abundances of A=88, 138, 208 nuclei. The second process is needed due to three reasons: first, because there exist several stable isotopes which cannot be synthesised in the s-process, since these nuclei are shielded from the s-process flow by β-decays. Second, the long-lived actinides ^{232}Th, ^{235}U, and ^{238}U have been observed on earth and in stellar atmospheres. These three isotopes cannot be formed in the s-process as α-decay terminates the s-process around ^{207}Bi. Third, the observed abundances show broad peaks at A=130 and A=195, which cannot be explained by the s-process.

All these nuclei are formed by a process that needs high neutron densities (about 10^{20} neutrons per cm^3) and temperatures (about 10^9 K) [CTT91], thus exhibiting rapid neutron captures and their reverse reactions. Therefore, the time-scales for these reactions are much smaller than the time-scales for the β-decays. This process is called the r-process [CTT91, WWM$^+$94, TWJ94, AGT07, Boy08, SCG08] and it is believed that about half of the elements heavier than $A \approx 60$ are made in this process. The extreme conditions enable the r-process to run through very neutron-rich nuclei with neutron separation energies $S_n = 2 - 3$ MeV. The r-process path follows an isotopic chain until a so-called $(n,\gamma) \leftrightarrows (\gamma,n)$-equilibrium is reached and the r-process does not proceed until a β-decay occurs. These β-decays shift the nuclei towards stability until (n,γ)-reactions take over again, running again along the (now larger in Z) isotopic chain until the $(n,\gamma) \leftrightarrows (\gamma,n)$-equilibrium is reached again. However, a different scenario occurs at the magic neutron shell closures. For these nuclei, the (n,γ) reaction rate drops and they usually have longer β-decay half-lives than their neighbours. Thus matter piles up in these nuclei and “waits” until a β-decay occurs. These nuclei are called *waiting point* nuclei. This accumulation of matter at neutron-rich nuclei with magic neutron shell-closures gives the two broad peaks at A=130 and A=195 in the observed abundances, because after the r-process has stopped, these nuclei decay back to stability forming the nuclei in these regions.

It is still an open question in which environments one could encounter the conditions an r-process needs. Only explosive scenarios that produce or release huge amounts of neutrons on very short time-scales can account for such conditions. Two possible settings are regarded as the best candidates for an r-process site: (i) type II supernovae with high-entropy ejecta and (ii) neutron star mergers [QW07] (Hence, the r-process is an example of explosive nucleosynthesis as defined above). One could also think of other “merger” scenarios of two massive objects, e.g. a neutron-star black hole merger, but these are not encountered frequently enough (compared to the two mentioned possibilities) to play an important role.

While the r-process is ongoing, i.e. while neutron capture reactions persist, elements with larger proton numbers are synthesised. This continues until the r-process hit regions in which fission may occur, i.e. when nuclei are produced at energies beyond their fission barrier. Fission moves matter from the current mass region to lower mass regions. Additionally, fission is usually accompanied by the emission of free neutrons. This can lead to the so-called *fission cycling*, i.e. heavy synthesised nuclei fission and thus feed lighter nuclei and the free neutrons add to the total neutron flux. In this way a circuit can establish, leading to the terminology of fission cycling.

With time, more and more neutrons are bound in nuclei and the neutron flux declines. This reduces the time-scales of the (n,γ) reactions and β-decays become important. This is generally called the *freeze out*. After the freeze out, the synthesised neutron-rich isotopes decay back to stability. For heavy nuclei, this decay chain is usually interrupted by β-delayed fission or α-decay. In principle, fission may affect the r-process in the following reactions:

- **Neutron-induced fission:** Neutron induced fission is generally the dominating type of fission-reaction as long as there are enough neutrons. It can become a strong competitor to (n,γ)-reactions and has the capability to interrupt the r-process path and lead to fission cycling [MPMZ$^+$07, PKP$^+$05].
- **β-delayed fission:** A nucleus decays via β-decay to an excited state in the daughter nucleus which then may fission. This becomes important after the freeze-out when no free neutrons are available and the synthesised isotopes decay back to stability [CTT91, PT03, MPMZ$^+$07].

- **Spontaneous fission:** As *spontaneous* fission we understand the fission of a nucleus in its ground state, i.e. a non-induced fission. This becomes important after the freeze-out.
- **γ- and ν-induced fission:** These types of fission can become important depending on the astrophysical conditions. In general, they are less likely than the other fission-decays mentioned above, though [Qia02, KLF04, MPMZ$^+$07].

These considerations show that fission is an important process that needs to be taken into account for r-process simulations that reach the nuclear region in which fission can occur. In particular, fission affects the predicted abundances of the aforementioned thorium and uranium isotopes. These isotopes are synthesised either directly from β-decays after the freeze-out or indirectly by α-decays of heavier isotopes. Fission may now affect the flow of matter into the regions which decay to the isotopes which in turn decay by α-decay to thorium and uranium. At the same time it can also affect the synthesis of the elements that decay by β-decay to thorium and uranium. Both isotopes are two standard cosmo chronometers (because of their long half-life), i.e. it is possible to date back to the formation of the star. This is similar to the method of ^{14}C dating in archaeology.

The r-process runs through isotopes with extreme neutron excess, therefore many of the relevant isotopes have not yet been synthesised in experimental facilities and experimental data on these isotopes is very scarce. Thus, we need to establish theoretical models to predict the needed quantities for an r-process simulation. Moreover, these quantities are needed globally for the many nuclei involved in the reaction network. The most important input to r-process simulations are the nuclear masses as they mainly determine the path of the r-process [CTT91]. Several different mass models are on the market, the most commonly used ones for astrophysics are the Finite-Range-Droplet-Model (FRDM) [MNMS95], the Extended Thomas-Fermi with Strutinski integral (ETFSI) [APDT95], or the various Hartree-Fock-Bogoliubov mass models (see [GCP09] and references therein). The half-lives affect the relative abundances of the r-process and most of them are also experimentally not known. The third important quantity are the neutron capture cross sections. Again, the general problem is that these are not known experimentally and we have to fall back on theoretical predictions. The default theoretical approach towards (n,γ) cross sections for r-process nucleosynthesis is the Hauser-Feshbach model. A lot of different nuclear structure input from experiment and/or theory enter the determination of the reaction rates.

A crucial input to the (n,γ) reaction rates are radiative strength functions that describe the probability of γ-decays. These are usually described by a Lorentzian representation as this was found successful for the description of the giant dipole resonance in stable nuclei. In the last years, a lot of effort has been put into the experimental observation and theoretical prediction of low-lying collective strength. The two most prominent examples are (i) the pygmy mode, that is believed to result from a neutron-skin that oscillates against a proton-neutron core (see section 5.2.2), and (ii) the so-called *scissors* mode for which it is believed that deformed proton and neutron cores oscillate against each other in a mode similar to a scissor (see section 5.2.4). We will study the effect of both collective modes in the determination of (n,γ) rates for r-process simulations, because E1 and M1 transitions are usually treated in macroscopic models (for more details see section 5.3). With the capabilities of two nuclear structure models, i.e. the relativistic-quasi-time-blocking-approximation (see [LRT08, LRTL09, LRT10] and references therein) and the shell model (see [CMPN$^+$05] and references therein), we are enabled to calculate these transitions on a microscopic level and to obtain possible low-energy collective modes. In addition, these results can be put into the Hauser-Feshbach model (see section 2.2.1) allowing us to study the effect of these low-lying collective modes on the (n,γ) rates needed for r-process simulations and to prognosticate how relevant these and other connected issues can become.

In Hauser-Feshbach model calculations we need the radiative strength function also for excited states. These are usually obtained by using Brink's hypothesis. This hypothesis states that the strength function is independent of the initial state and we may approximate the strength function of any excited by the strength function of the ground state. This is a very simplifying assumption. We will see that this hypothesis can be considered to be valid for giant collective resonances, but it fails for low energies, in particular for the low-lying M1 strength.

In the discussion above we put a specific emphasis on fission within the r-process network. Fission is usually described as a tunnelling process through one or more potential barriers. In order to get hold of the fission probability, several quantities are needed, in particular the height(s) and the width(s) of the barrier(s). These quantities are usually described with macroscopic methods.[1] Again, with the increase in computer power and new methods being developed, we started out for a survey of microscopic fission barriers on the basis of the Skyrme-Hartree-Fock-BCS model (see [BHR03, SR07, EKR11]). On the basis of our results, which were obtained in collaboration with the nuclear structure theory group of the University of Erlangen, we will qualitatively discuss the possible influence of the used Skyrme functional on the r-process in the actinide and super-heavy region. We will also identify certain features in the evolution of the fission barriers with proton and neutron number that might affect the r-process.

---

[1] We have to be more specific here: purely macroscopic models, e.g. liquid drop models, usually fail in describing the fission barriers adequately, i.e. microscopic-macroscopic models are needed in which a macroscopic part is calculated and on top of that microscopic corrections are introduced, e.g. the Strutinski method. A prominent example is the Finite-Range-Droplet-Mass model (FRDM) [MNMS95].

2

Nuclear Reactions & Nuclear Decays

The physics of nuclear reactions is a very diversified field. As a reaction, we may define the interaction between two or more particles via one or more of the four standard forces in nuclear physics. This usually leads to an exchange of momentum and energy between the particles. In this context, a decay is also considered a reaction.

In this thesis we will regard only a small number of possible reactions albeit they are the relevant ones for r-process nucleosynthesis. We will therefore focus on radiative neutron capture reactions (see chapter 5) and on the phenomena of fission chapter 6. These reactions are all mediated by the strong nuclear force and the electromagnetic force. We will not regard reactions governed by the weak force in this thesis.

2.1 Basics of Nuclear Reactions

The main classification of nuclear reactions is usually done according to the reaction time-scales: On the one hand, there are processes which occur *fast* - fast means that the reaction time is comparable to the fly-by time if both reaction partners would not interact. These processes are scattering processes in which only a few nucleons are involved, i.e. only the nucleons on the surface of the nucleus interact with the projectile. On the other hand are the processes which occur on much slower time scales. In these reactions a large number or even all nucleons are involved in the reaction. These reactions are called compound nucleus reactions. The basic idea is that both reaction partners fuse and form a highly excited compound nucleus. These rather slow reactions (relative to the fly-by-time) are considered in this thesis and will be discussed in more detail in section 2.2.1.

2.1.1 Conservation Laws

Conservation laws define the conservation of a particular property or quantum number, however - for the sake of completeness - we should mention that some of these conservation laws are fulfilled only approximately (see below) and some do not apply for certain interactions. These quantum numbers are conserved because they are related to certain transformations, e.g. the angular momentum is related to rotational transformations, and the Hamiltonian of our system is symmetric under these transformations. For example, if the Hamiltonian is symmetric under the parity transformation, i.e. $[\hat{H},\hat{\Pi}] = 0$ with $\hat{\Pi}$ being the parity operator, then the assigned quantum number parity is conserved [GM96, chap. 2].

The most important conservation laws regarding nuclear reactions mediated by fundamental forces we consider here are (see for example [FL96, Ber07]):

1. Conservation of energy and kinetic momentum
2. Conservation of total angular momentum
3. Conservation of Baryonic number: below the meson production threshold (≈ 140MeV) no process (mediated by the strong force!) can transform a neutron into a proton and vice versa
4. Conservation of charge
5. Conservation of isospin (fulfilled only approximately)
6. Conservation of parity

The conservation of isospin is only approximate since the nuclear interaction is not completely isospin-independent. This is indicated by the difference in mass between neutrons and protons, neglecting the effect of the electromagnetic force.

2.1.2 Notation and Definitions

In this thesis we will mainly focus ourselves on reactions involving two particles. A common notation for such a reaction is

$$A + a \longrightarrow B + b, \tag{2.1}$$

with the projectile a, the target A, the ejectile b and the residual or daughter B.[1] A more compact notation is given by

$$A(a,b)B. \tag{2.2}$$

In our case the particles a and b are either protons, neutrons, α-particles or γ-rays.

2.1.2.1 The Q-value

The Q-value determines the energetical possibility of a reaction. For the definition we have to differentiate between nuclear and atomic masses, the latter ones also include the masses and binding energies of the electrons. In this thesis we will always refer to nuclear masses unless stated otherwise - the definition of the nuclear mass can be found in appendix A. We can define the so-called *Q-value*, which is the difference between the initial mass and the final mass[2] by,

$$Q = m_a + m_A - (m_b + m_B). \tag{2.3}$$

From this definition an important consequence arises: if the Q-value is negative, e.g. the final mass is larger, the reaction is energetically not allowed.

A simple example for the Q-value - and its relation to the energetical possibility of a reaction - is the neutron separation energy S_n (see section A.3; $Q = -S_n$): if it is negative (and the Q-value positive), the nucleus can emit neutrons until it reaches a positive neutron separation energy. If the neutron separation energy is positive (and the Q-value negative), then the emission of a neutron is not possible as long as the nucleus is not excited above the separation energy.

2.2 The Compound Nucleus

The picture of the *compound nucleus* is based upon Bohr's independence hypothesis (original article [Boh36]; for more recent and extensive articles or books see [FPW54, MW79, Fes92, CTT91, FL96, RTK97, Ber07, MRW10]). The basic assumption of this hypothesis is that the formation and the decay

---

[1] Here the upper-case characters depict nuclei, while lower-case characters depict the much lighter projectiles or ejectiles.

[2] We use the convention $c^2 = 1$ through out this thesis.

of the compound nucleus are independent of each other. This implies that an excited nucleus is formed and hence a large number of states can be excited in the interplay between the target nucleus and the projectile. Bohr's hypothesis has been experimentally verified by S. N. Ghoshal in 1950 [Gho50].

2.2.1 Hauser-Feshbach Model

In light nuclei, we see individual resonances in cross section measurements. These are related to particular states in the nucleus. A very prominent example is the so-called *Hoyle* state in ^{12}C which is very important for the triple-α reaction (see e.g. [CFN$^+$07, CFN$^+$10] and references therein). This state corresponds to a resonance in this reaction.

The compound nucleus picture and one of its theoretical formulations, the Hauser-Feshbach model, are in complete contrast to the single resonance model. The large number of nucleons (= many degrees of freedom) and in particular the high excitation energies give rise to many accessible states. The idea of Hauser and Feshbach [FPW54, Fes92, FL96] was to use statistical averages over the resonances instead of treating the resonances separately. Therefore, the applicability of the Hauser-Feshbach model is strongly coupled to the formation of a compound nucleus and the existence of many overlapping resonances at the compound excitation energy.

In order to represent a compound nucleus reaction we may redefine our notation for reactions of eq. (2.1) in the following way,

$$A + a \longrightarrow \text{highly excited compound nucleus} \longrightarrow B + b, \tag{2.4}$$

but we will keep the short-handed notation of eq. (2.2). It is important to note that the term "highly excited" in eq. (2.4) is relative: one can either achieve this "high excitation" by capturing on a relatively stable nucleus or if the projectile's kinetic energy is large enough.

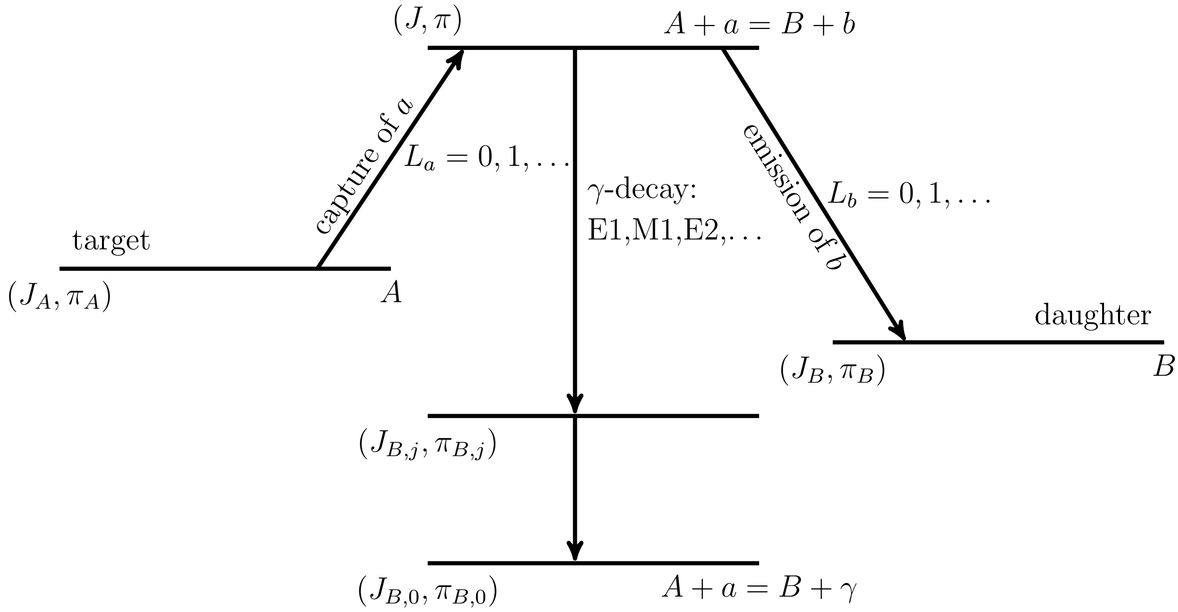

Figure 2.1: Scheme of a Hauser-Feshbach reaction; for the notation see also eq. (2.1). The additional indices for γ-decay emphasise the possibility of cascades which could also occur in other decay channels as secondary decays. $L_{a,b}$ stands for the relative angular momentum which has to be coupled with the intrinsic spin of the corresponding particle $s_{a,b}$ and the spin of the target-state J_A, i.e. see eq. (2.6). The parity conservation is obtained like in eq. (2.7).

Figure 2.1 shows the principle schematics of a compound nucleus reaction. Here we capture the projectile a with a relative kinetic energy E_a (usually in the centre-of-mass system) and an intrinsic spin s_a on the target A which is in a quantum state (E_A,J_A,π_A). The relative angular momentum is given by l. An intermediate compound state is formed with the quantum numbers (E,J,π) which are restricted by the conservation laws (see also section 2.1.1); E stands for the excitation energy of the compound nucleus (relative to its ground state) and J,π for the corresponding spin and parity quantum numbers. By applying the conservation laws discussed before, we obtain the following equations:

$$E = E_A + E_a - Q_a \tag{2.5}$$
$$|J_A - l - s_a| \leq J \leq J_A + l + s_a \tag{2.6}$$
$$\pi = (-1)^l \cdot \pi_A \cdot \pi_a, \tag{2.7}$$

with Q_a being the Q-value for the reaction. In this thesis we only consider particles with $\pi_a = +1$. The same conservation laws apply for the decay of the compound nucleus. Regarding the emission or absorption of electromagnetic radiation, eqs. (2.5) to (2.7) can be rewritten with X depicting the type of electromagnetic transition and L depicting the multipolarity (see chapter 5):

$$|J_A - \mathrm{L}| \leq J \leq J_A + \mathrm{L} \tag{2.8}$$
$$\pi = (-1)^L \cdot \pi_A \quad \text{for X = electric} \tag{2.9}$$
$$\pi = (-1)^{L-1} \cdot \pi_A \quad \text{for X = magnetic.} \tag{2.10}$$

It is important to note that eqs. (2.5) and (2.10) are given for the projectile and the target. We may safely exchange A by B and a by b to obtain the selection rules for the decay.

2.2.1.1 The Model

As Bohr's hypothesis is the basis for the Hauser-Feshbach model, we need to translate this first into a mathematical prescription: the cross section has to factorise into a part describing the formation, i.e. the formation cross section σ_F, and a part describing the decay probability G. At this place it is convenient to use the concept of reaction *channels*. A reaction channel is specified by the particles as well as the quantum numbers involved, e.g. the γ-channel describes all possible γ-decays that might occur for a fixed compound state.

If α is the entrance channel and β the exit channel we obtain [FL96],

$$\sigma^J_{\alpha\to\beta} = \sigma^J_F(\alpha) \cdot G^J(\beta), \tag{2.11}$$

with J being the compound spin and $\sigma^J_F = \sum_{\beta'} \sigma^J_{\alpha\to\beta'}$ being the sum over all possible exit channels (here denoted as β'). Consequently, the sum over all decay probabilities has to be unity,

$$\sum_{\beta'} G^J(\beta') = 1. \tag{2.12}$$

From basic quantum mechanics we know that time-reversal symmetry gives us the so-called *principle of detailed balance* [FL96]. This principle is often used in (reaction) physics and in case of the Hauser-Feshbach model it can be written as,

$$k^2_\alpha \cdot \sigma^J_{\alpha\to\beta} = k^2_\beta \cdot \sigma^J_{\beta\to\alpha}, \tag{2.13}$$

with k_ι being the wave number of channel ι. Additionally, we have absorbed the spin factors that account for the degeneracy of the spins into σ. We can now combine eq. (2.11) and eq. (2.13) and find the following relation,

$$\frac{k^2_\alpha \cdot \sigma^J_F}{G^J(\alpha)} = \frac{k^2_\beta \cdot \sigma^J_F}{G^J(\beta)}, \tag{2.14}$$

in which both sides depend on a particular channel which can be chosen arbitrarily. Hence, both sides of eq. (2.14) must be equal to a channel independent quantity which we call I,

$$G^J(b) = \frac{k_b^2 \sigma_F^J(b)}{I}, \tag{2.15}$$

and by making use of eq. (2.12) and eq. (2.11) we obtain the Hauser-Feshbach formula,

$$\sigma_{a\to b}^J = k_a^2 \cdot \frac{\sigma_F^J(a) \cdot \sigma_F^J(b)}{\sum_{b'} k_{b'}^2 \sigma_F^J(b')}. \tag{2.16}$$

From elementary quantum mechanics, we know that the cross section for the scattering of a particle on a potential can be written as [Fes92, FL96],

$$\sigma = \frac{\pi}{k^2} \sum_{l=0}^{\infty} (2l+1) T_l, \tag{2.17}$$

with the T_l being the so-called *transmission coefficients.* These coefficients give the probability of the penetration of the potential barrier. Here we already see that the transmission coefficients are dimensionless because the dimensions of the cross section [(length)^2] result from the $1/k^2$ factor. By inserting eq. (2.17) into eq. (2.16), we find the structure of the Hauser-Feshbach formula re-written with transmission coefficients, i.e.

$$\sigma \propto \frac{T_a T_b}{\sum_{b'} T_{b'}}. \tag{2.18}$$

A full derivation of the Hauser-Feshbach formula is not within the scope of this thesis. Therefore, the interested reader is referred to the literature [HWFZ76, CTT91, Fes92, FL96, RTK97, RT00, RT01, Ber07, Loe07] and we only quote the needed results. Another important relation we will need later is the relation between the transmission coefficient T and the decay width $\mathit{\Gamma}$, i.e.

$$T = \frac{2\pi}{D} \mathit{\Gamma} = 2\pi \cdot \rho \cdot \mathit{\Gamma}. \tag{2.19}$$

Here we used the level density ρ, which is the inverse of the level spacing D.

Following the literature cited above, the Hauser-Feshbach cross section $\sigma_{\mathrm{HF}}(E)$ for the reaction $A(a,b)B$ is given by,

$$\sigma_{\mathrm{HF}}(k_a) = \frac{\pi}{k_a^2} \sum_{J,\pi} (2J+1) \frac{1+\delta_{Aa}}{(2J_A+1)(2J_a+1)} W(a,b,J,\pi) \frac{T_a(E,J,\pi) T_b(E,J,\pi)}{T_{tot}(E,J,\pi)}) \tag{2.20}$$

with k being the wave number of the incoming particle a, (E,J,π) being the compound state properties of the target nucleus, $W(a,b,J,\pi)$ being the width fluctuation corrections that account for the fact that Bohr's hypothesis is not always completely fulfilled, and $T_{\mathrm{channel}}(E,J,\pi)$ the transmission coefficient of the respective channel. T_{tot} is the sum over all transmission coefficients. The factor $(1 + \delta_{Aa})$ takes into account that for identical projectiles and targets, i.e. $A = a$, the cross section doubles.

Alternatively we may re-write eq. (2.20) to distinguish between specific states in the involved nuclei and to describe the reaction in the centre-of-mass system. Hence, the Hauser-Feshbach cross section for the reaction $A^\mu(a,b)B^\nu$ - with ν and μ depicting certain states - is given by,

$$\sigma_{ab}^{\mu\nu}(E_{Aa}) = \frac{\pi\hbar^2/(2m_{Aa}E_{Aa})}{(2J_A^\mu+1)(2J_a+1)}(1+\delta_{Aa})\sum_{J,\pi}(2J+1)W(a,b,J,\pi)\frac{T_a^\mu(E,J,\pi;E_A^\mu,J_A^\mu,\pi_A^\mu)T_b^\nu(E,J,\pi;E_B^\nu,J_B^\nu,\pi_B^\nu)}{T_{\text{tot}}(E,J,\pi)}, \tag{2.21}$$

with E_{Aa} being the kinetic energy of particle a in the centre-of-mass system and m_{Aa} being the reduced mass. In this thesis we will always work in the centre-of-mass system and hence we abbreviate E_{Aa} by E_a in the following. Note that we have assumed here that the particles and ejectiles a and b cannot be excited. This is a valid approximation for neutrons, protons, and α-particles regarding the temperatures of the astrophysical plasmas we will consider. Table 2.1 gives an overview about the different quantities occurring in eq. (2.21).

observable	explanation
(E,J,π)	compound state properties, i.e. excitation energy, spin, and parity
$(E_k^\beta, J_k^\beta, \pi_k^\beta)$	the state labelled β in the nucleus k with the corresponding quantum numbers for excitation energy, spin, and parity
$T_l^\beta(E,J,\pi;E_k^\beta,J_k^\beta,\pi_k^\beta)$	transmission coefficient giving the probability for a transition from the compound state (E,J,π) to the state β in the nucleus k by the emission of the particle l

Table 2.1: Table summarising various quantities in the Hauser-Feshbach formula eq. (2.21).

Equation (2.21) describes the transition from the state μ in the target via the compound state depicted by (E,J,π) to the state ν in the residual nucleus, but for general cross sections we need consider all energetically available states and we account for this by summing over these states, i.e. evaluating $\sum_\nu \sigma^{\mu\nu}$. Therefore, we have to switch over to a description of the transmission coefficient that accounts for this fact:

$$T_b(E,J,\pi) = \sum_{\nu=0}^{\omega} T_o^\nu(E,J,\pi;E_B^\nu,J_B^\nu,\pi_B^\nu) + \int_{E_B^\omega}^{E-S_B} \sum_{J_B,\pi_B} T_b(E,J,\pi;E_B^\nu,J_B^\nu,\pi_B^\nu)\rho(E_B,J_B,\pi_B)dE_B, \tag{2.22}$$

with ω being the highest experimentally known state in the final nucleus up to which the level scheme is considered complete. For excitation energies above ω a level density prescription is employed.

The last step is the calculation of the single transmission coefficients T_j^μ for particles, i.e.

$$T_a^\mu(E,J,\pi;E_A^\mu,J_A^\mu,\pi_A^\mu) = \sum_{l=|J-s|}^{J+s} \sum_{s=|J_A^\mu-J_a|}^{J_A^\mu+J_a} T_{a_{ls}}(E_{Aa}^\mu) \tag{2.23}$$

Regarding particle channels, this is done by obtaining the nuclear penetrabilities $T_{j_{ls}}(E_{ij}^\mu)$ from solving the Schroedinger equation of the scattering process on the potential given by the optical model. For the γ-channel we have to use radiative strength functions f_{XL} (see section 5.3) which depend on the energy of the photon E_γ (see section 5.3 for more details), i.e.

$$T^{\mu}_{a=\gamma}(E,J,\pi;E^{\mu}_{A},J^{\mu}_{A},\pi^{\mu}_{A}) = T_\gamma(E_\gamma;\mathrm{XL}) = 2\pi f_{\mathrm{XL}}(E_\gamma)E_\gamma^{2L+1}, \tag{2.24}$$

with $E_\gamma = E - E^{\mu}_{A}$. The type and multipolarity XL define which $(J \rightarrow J^{\mu}_{A}, \pi \rightarrow \pi^{\mu}_{A})$-combinations are allowed (see eqs. (2.8) and (2.10) and section 5.1.4.). In order to obtain the complete γ-transmission coefficient giving the complete probability for γ-transitions in nucleus A, we have to apply eq. (2.22) with the modification that $T^{\nu}_{b} = \sum_{\mathrm{XL}} T^{(}E_\gamma;\mathrm{XL})$, i.e. we sum over all types and multipolarities we consider.

The Hauser-Feshbach is by definition conserving all quantum numbers such as spin and parity. However, the optical models applied are usually neither spin-dependent nor parity-dependent. They only give the nuclear penetrabilities depending on the kinetic energy of the particle and the relative angular momentum.

Therefore these dependencies have to be included in a different way for the compound nucleus. The problem of sensitivity to parity and spin in the target and the daughter nuclei is usually mapped onto the level density prescription (see chapter 3). We can also introduce a parity-dependence in to the compound nucleus by introducing parity-dependent weighting factors β [LLMP$^+$08],

$$T(E,J,\pi) \longrightarrow \widetilde{T}(E,J,\pi) = \beta(E,\pi;J)\cdot T(E,J,\pi), \tag{2.25}$$

with

$$\beta(E,\pi;J) = 2\cdot\frac{\rho(E,J,\pi)}{\sum_\pi \rho(E,J,\pi)}. \tag{2.26}$$

This enables us to take into account a possible non-equipartition of parity at the compound excitation energy E. However, the optimal solution would be optical models that are sensitive to parity and spin. Despite some locally applicable[1] parity-dependent optical models [WFL83], no globally applicable optical models that are sensitive to parity or spin exist.

2.2.1.2 The Input to the Hauser-Feshbach Model

A very extensive overview over the input and important steps of a Hauser-Feshbach calculation is given in fig. 2.2, in which the blue nodes specify nuclear structure input and the red nodes input or methods from reaction theory. This figure shows the complex and extensive input structure into a Hauser-Feshbach calculation and can be easily extended to include other channels. In principle, we have to collect experimental data - if available - or utilise theoretical nuclear structure models to obtain the input quantities (blue). In fig. 2.2 we have summarised this with the uppermost black box. In reality, we are currently not able to consistently compute all these quantities from a single theoretical model, hence we have to fall back on several different nuclear models. The nuclear deformation we have not marked as an input as it does not directly affect the calculations. It is embedded in the other input quantities as it affects only these, e.g. the radiative strength function by a splitting of the giant dipole resonance (see section 5.3.2.3). The giant resonance parameters are an optional input as we can either obtain the radiative strength function directly from a nuclear structure model or by using parametrisations of giant resonances. The resulting cross section and reaction rates can be renormalised to experimental data if the latter is available.

In fig. 2.2 we have intentionally omitted the possible relations between the different nuclear inputs and - analogous to the deformation - absorbed this into the determination within the nuclear structure model. We do not intend to give a full account on all the relevant quantities as this would be beyond the scope of this thesis. Instead we will shortly cover the quantities we will deal with in this thesis.

Nuclear deformation plays a very generic role as it affects in principle all quantities, although its overall effect on the cross section is usually small. Its main influence would enter in the nuclear mass if

---

[1] With "locally applicable" we mean that these models are confined to only one or few nuclei.

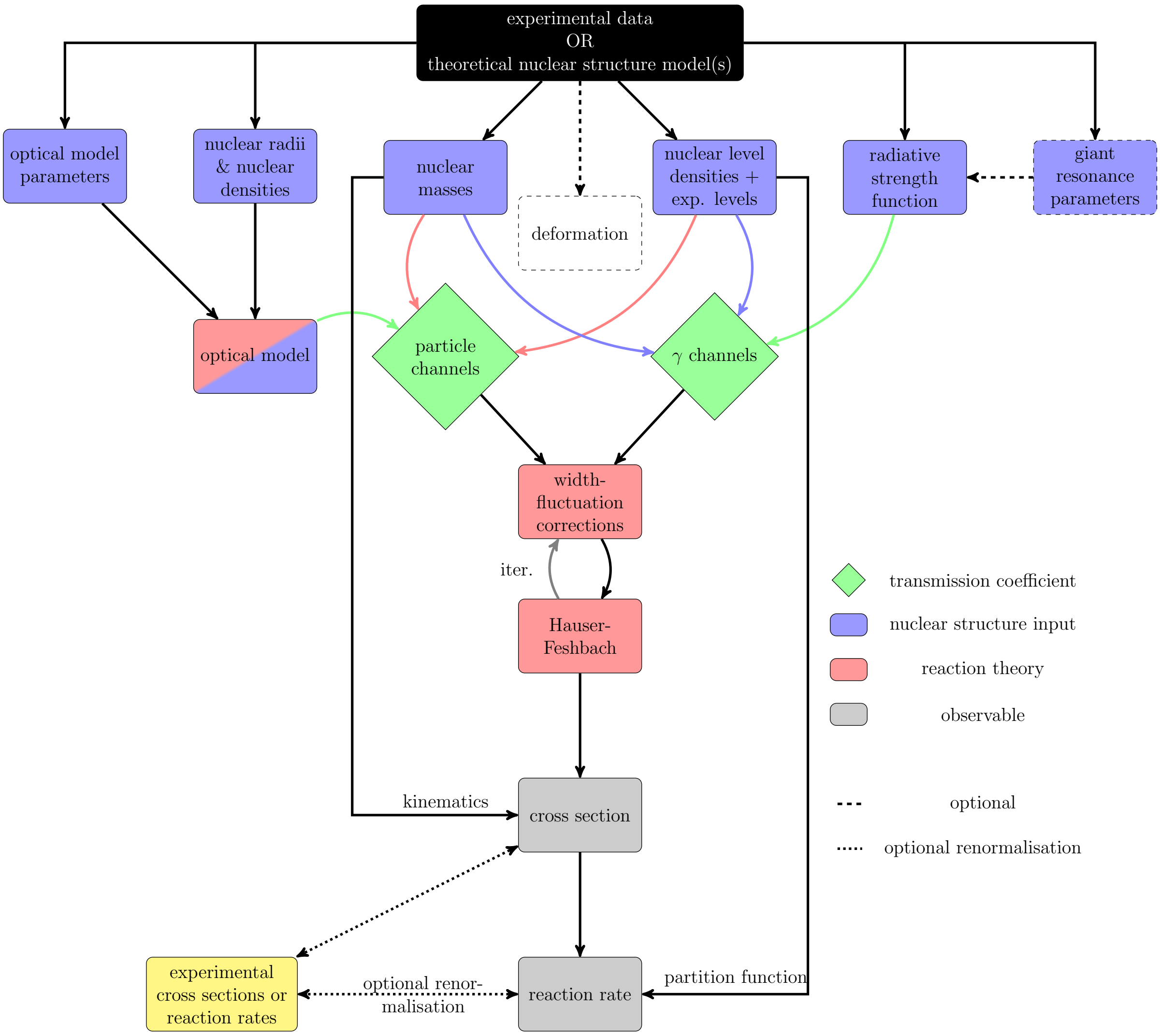

Figure 2.2: Diagram showing the complex structure of a Hauser-Feshbach calculation. The blue nodes are nuclear structure input, the red nodes are nuclear reaction theory methods and input. The green nodes denote intermediate steps; the green nodes are transferred to observables (grey nodes) by the red methods. See the text for further details.

the nucleus is deformed, but this influence is already incorporated in the mass itself. In chapter chapter 8 we will discuss nuclei which all show a well-deformed shape due to a large gain in binding resulting from deformed shapes. As the nuclear masses define our kinematics and thresholds, deformation can play an important role here. The nuclear masses are a key quantity in reaction calculations. They define thresholds and Q-values. In this thesis we will discuss (n,γ) reactions for which the neutron-separation energy S_n is the key quantity. This energy defines us our minimum excitation energy of the compound nucleus.

The nuclear level density is well known to have a large influence on Hauser-Feshbach predictions [RTK97]. We need it to estimate the number of states at energies for which experimental levels are not given or not completely known. We also use it to predict the distribution of states with specific spin and parity because the raw transmission coefficients we obtain are not sensitive to these quantities. The nuclear level density usually rises exponentially, thus becoming an important property in the Hauser-Feshbach model. At the same time, we use experimental level data derived from [IAEb]. This allows us a more realistic description of the low-energy regime for nuclei in or near the valley of stability; we do not have to use a level density for these energies.

The radiative strength function gives us the probability of a γ-transitions for a certain γ-energy E_γ and for a certain type and multipolarity (see section 5.3). Slightly similar, the optical model gives us transition probabilities for particle channels. Both quantities can be analytically modelled with parameters.

Finally, the width fluctuations try to account for the fact that Bohr's hypothesis is usually not completely fulfilled, especially if a certain reaction channel is dominating the cross section. These corrections can become very complicated, so that we will therefore stick to a very simple description outlined in [THW74].

2.2.1.3 Applicability of the Statistical Model

As it was stated in section 2.2.1.1, the basic assumption of the Hauser-Feshbach model is the existence of a reasonably large number of overlapping resonances, i.e. that $\langle \mathit{\Gamma} \rangle / D \gg 1$ with D being the level spacing. As the level spacing is the inverse of the level density, we can rewrite the aforementioned condition as $\langle \mathit{\Gamma} \rangle \cdot \rho \gg 1$.

Generally, in order to be able to apply the Hauser-Feshbach model we need a sufficiently large number of levels within the compound nucleus in a certain energy interval. The states in this interval can act as "doorway" states to the formation of the compound nucleus. In case of neutron capture, this energy range is around the compound excitation energy given by the sum of the neutron's kinetic energy and the neutron separation energy in the compound, i.e.

$$E_{\mathrm{ex.,cmp.}} = E_{\mathrm{kin}} + S_n. \tag{2.27}$$

In case of charged particle reactions, this becomes different due to the Coulomb barrier. The Coulomb barrier strongly suppresses the cross section for low energies. With increasing projectile energy, the transmission probability rises by orders of magnitude. Thus the relevant energy window for charged particles is usually larger than for neutrons. In order to determine the applicability of the statistical model for astrophysical charged particle reactions one has to make use of the Gamow peak concept (see [RTK97] for more details and references).

The mean kinetic energy of the particle is given by the temperature of the astrophysical plasma, i.e. for higher temperatures we also have larger mean kinetic energies. Rauscher et al. [RTK97] performed a large scale examination for all nuclei relevant for the nucleosynthesis of elements heavier than iron and identified the minimum temperature needed, so that the statistical Hauser-Feshbach model can be applied. In general, the application of the Hauser-Feshbach model for magic nuclei can become problematic because these nuclei usually exhibit particularly small level densities due to the shell-gap. The same applies to light nuclei which also have rather small level densities.

2.3 Thermonuclear Reaction Rates

Thermonuclear reaction rates are a key ingredient to nucleosynthesis simulations [HWFZ76, CTT91, RTK97, RT00]. They are obtained by folding the nuclear cross sections with an energy or velocity distribution accounting for the finite temperature environment. As we have to account for the finite temperature, we also have to carefully distinguish the states in all nuclei. We do not have to care for a possible excitation of the projectiles or ejectiles as we have restricted ourselves to protons, neutrons, α-particles, and photons. The latter cannot be excited, since neutrons and protons would need extremely high temperatures to be excited to a $\mathit{\Delta}$-resonance for example, and α-particles have their first excited state at 20.21MeV. In order to excite these particles, we would need much higher temperatures than the ones at which the r-process generally takes place (around 10^9 Kelvin).

By definition, the number of reactions r per cm^{3}s per pair of nuclei (A,a) within an astrophysical plasma with the related number densities n_A and n_a is given by [FCZ67, FCZ75, CTT91],

$$r = \frac{n_A n_a}{1 + \delta_{Aa}} \langle \sigma v \rangle . \tag{2.28}$$

Within here we have used the so-called reaction rate, which is obtained by folding the cross section with a Maxwell-Boltzmann velocity distribution for the particles,[1] i.e.

$$\langle \sigma_{ab}^{\mu} v \rangle = \sqrt{\frac{8}{m\pi}} (kT)^{-3/2} \int\limits_{0}^{\infty} E_a \cdot \sigma_{ab}^{\mu} e^{-E_a/kT} dE_a. \tag{2.29}$$

where the symbol $\langle \ldots \rangle$ denotes averaging over the velocity distribution of the reacting particles and m is the reduced mass. Here we have used $\sigma_{ab}^{\mu} = \sum_{\nu} \sigma_{ab}^{\mu\nu}$.

2.3.1 Stellar Reaction Rate

Equation (2.29) gives a general description of a thermonuclear reaction rate. In our case, we have to specifically account for the possible excitation of the target. Therefore, we define the so-called *Maxwellian averaged* cross section,

$$\sigma_{ab}^{*} = \frac{\sum_{\mu} (2J_A^{\mu} + 1) e^{-E_A^{\mu}/kT} \sum_{\nu} \sigma_{ab}^{\mu\nu}}{\sum_{\mu} (2J_A^{\mu} + 1) e^{-E_A^{\mu}/kT}}, \tag{2.30}$$

with the '*' representing the excitation of the target. The reaction rate within a plasma obeys $\langle \sigma v \rangle^{*} = \langle \sigma^{*} v \rangle$, i.e. we can exchange the sum in eq. (2.30) with the integral in eq. (2.29). Thus we get (with E_a being the relative kinetic energy of the particle in the centre-of-mass system) from combining these two equations,

$$\langle \sigma^{*} v \rangle = \left(\frac{8}{\pi m} \right)^{1/2} \frac{1}{(kT)^{3/2} G(T)} \cdot \int\limits_{0}^{\infty} \sum_{\mu} \frac{2J_A^{\mu} + 1}{2J_A^{0} + 1} \sigma_{ab}^{\mu} E_a e^{-(E_a + E_A^{\mu})/kT} dE_a \tag{2.31}$$

where $G(T)$ is the *partition function* of the target, defined by,

$$G(T) = \frac{\sum_{\mu}^{\omega} (2J_A^{\mu} + 1) e^{-E_A^{\mu}/kT} + \int_{E_A^{\omega}}^{\epsilon_A^{\max}} \sum_{J^{\mu},\pi^{\mu}} (2J^{\mu} + 1) e^{-E_A^{\mu}/kT} \rho(\epsilon_A^{\mu}, J^{\mu}, \pi^{\mu}) \; dE_A^{\mu}}{(2J_A^{0} + 1)}. \tag{2.32}$$

The evaluation of the partition function is divided into two different energy regimes: an energy regime for which experimental states are known and an energy regime where a level density has to be used. The border between both regimes is given by the highest experimentally known state used within the calculation depicted by ω.

---

[1] We may safely assume for the temperatures we discuss that we may treat neutrons, protons, and α-particles classically.

3

Nuclear Level Densities

The nuclear level density is an important and fundamental quantity in nuclear physics. While nuclear levels display a discrete spectrum at low energies, the mean spacing between these levels reduces with increasing energy. Above a certain energy - usually only a few MeV - the distances between the levels become so small that it is often experimentally not possible to differentiate single levels. At this point we have to move from an individual description of every level towards a global and continuous description of the number of levels per unit energy interval.

A good summary of the state of affairs until 1972 is given in the paper on nuclear level densities by J.R. Huizenga and L.G. Moretto [HM72][1], as well as [Eri59, Eri60]. For the more recent advances in this field the reader is referred to the references given in this thesis (see [BBC$^+$06, chap. 6] for an application-oriented overview). For a more global overview about recent methods on calculating nuclear level densities besides the Fermi gas approaches, the reader is referred to the citations at the end of section 3.2.2; especially for an overview on more recent practical applications the reader should refer to [KHG08].

The nuclear level density is an important and crucial ingredient in the prediction of cross sections and nuclear reaction rates needed in various applications (see also section 2.2.1.2 and fig. 2.2), including astrophysical nucleosynthesis [CTT91], which are calculated within the framework of the statistical model or Hauser-Feshbach model. The general uncertainties in the predictions obtained the Hauser-Feshbach model are usually dominated by the uncertainties in the nuclear level density and the nuclear mass model [HWFZ76, CTT91, RTK97].

3.1 General Definitions

The nuclear level density of a nucleus with A nucleons and an excitation energy E is defined as,

$$\rho_{\text{nucl}}(E) = \frac{N(E+\mathit{\Delta} E) - N(E)}{\mathit{\Delta} E} \xrightarrow{\mathit{\Delta} E \to 0} \frac{dN}{dE}. \tag{3.1}$$

with $N(E)$ being the number of levels up to energy E.

In principle we may calculate N in the most obvious way by counting the number of levels in the needed energy interval, or in the words of quantum physics: we calculate all eigenvalues E_i and their

---

[1] Until the 1970s, the nuclear level density was mostly described in the Fermi gas model and its enhanced versions because of their analytical accessibility (see also section 3.2.1.1).

degeneracy of the nuclear Hamiltonian $\hat{H}_{\text{nucl.}}$,

$$\hat{H}_{\text{nucl}}\big|\Psi\big\rangle = E_{\text{nucl, i}}\big|\Psi\big\rangle, \tag{3.2}$$

and count how many of these fall into the interval $[E,E+dE]$. However, this is impossible and simplifications are needed.

3.2 Methods of Calculation

There are many different approaches trying to calculate the nuclear level density. Depending on the underlying nuclear model, they usually try to formulate the Hamiltonian and from that derive the level density. This can be done not only depending on the neutron number, proton number, and excitation energy, but also depending on spin and parity, i.e. predicting the nuclear level density for certain J^π values.

3.2.1 Independent Particle Model(s)

Most nuclear level density models are based upon the independent particle model (see chapter 4). The advantage is that in this model we may derive the level density simply from counting. The basis of the independent particle model is the assumption that the fermions may only occupy states with the specific properties (E,J^π); also often called single-particle states. If the nucleus is in its ground state, all those levels are filled up to the Fermi level. By exciting the nucleus we may excite the Fermions from filled states below the Fermi level to states above it. The remaining "holes" are called *hole-states* while the counterparts are called *particle-states*. Obviously, the more energy, the more states are available above the Fermi level, i.e. the number of ways to distribute the protons and neutrons among the available states is $N(E)$ (see eq. (3.1)).

3.2.1.1 The Fermi gas model

The Fermi gas model is a simple model for the atomic nucleus; most of the relevant formulae can be derived analytically and that is why it was the first level density model to be formulated. In principle, the Fermi gas model assumes that the nucleons form a Fermi gas within the nucleus. In that sense it is a independent particle model, however with an additional approximation: the single particle states are equipartitioned in energy.

In the introduction we assumed that the level density only depends on the nucleon number A and the excitation energy E to systematically show the approach. In reality, we need to incorporate the differences between the two nucleon types as well as other effects, especially pairing correlations. This was done in a pioneering paper by Bethe [Bet36] in which he derived the total level density for a two-component Fermi gas. We define the total level density as,

$$\rho(E) = \sum_{J,\pi} \rho(E,J,\pi). \tag{3.3}$$

However, the Fermi gas model can provide us only with $\rho(E)$, but for reaction rate determinations we need the level density separated into the different spins and parities, i.e. $\rho(E,J,\pi)$. This has to be introduced from outside the Fermi gas model and is done via multiplicative factors, i.e.

$$\rho(E,J,\pi) = \rho(E)\cdot F(E,J)\cdot \Pi(E,\pi). \tag{3.4}$$

One often speaks of spin- and/or parity-projected level densities in that context. The spin distribution is usually a Gaussian distribution employing an additional parameter σ, which is called the spin cut-off parameter. The parity distribution has often been assumed to be uniform, i.e. $\Pi(E,\pi) = 1/2$, which is a convenient approximation for most nuclei at moderate or higher excitation energies. However, recent developments in theoretical and experimental physics showed that this assumption is not valid for certain nuclei (see for example [KLM$^+$07, KÖL$^+$07] for experimental developments and [ABLN00, HG07, HKZ03, MRMPA03, MRMP$^+$07, NA97, NA98b, ÖLMPD07] for theoretical developments).

The definitions of the spin- and parity factors $F(E,J)$ and $\Pi(E,\pi)$ in eq. (3.4) can be found in the following literature [LLMP$^+$08, RTK97, CTT91]. Again it is important to emphasise that the factorisation in eq. (3.3) is an approximation we have to make. In reality, the nuclear shell-structure enforces correlations between the spin and the parity distribution.

This entanglement can only be treated in microscopic nuclear level densities. Examples for microscopic alternatives for the determination of the nuclear level density are the shell model Monte Carlo method [Lan98, NA97, ABLN00, ALN07, ÖLMPD07], which is capable of predicting the parity and spin distribution with a very good agreement to experiment, or Hartree-Fock-Bogoliubov level densities [HG06, HG07, GHK08].

Following [HWFZ76, RTK97] the total nuclear level density of the Fermi gas model is given by,

$$\rho(N,Z,E) = \frac{1}{\sqrt{2\pi\sigma^2}} \frac{\sqrt{\pi}}{12a^{1/4}U^{5/4}} e^{2\sqrt{aU}}, \tag{3.5}$$

with $U = E - \delta$, σ being the *spin cut-off* parameter, and a being the *level density parameter*. The spin cut-off parameter gives the width of the Gaussian distribution for the spin parameter $F(E,J)$ in eq. (3.4). The level density parameter is a measure of the increase of levels with energy (see [BBC$^+$06] and references therein for more details). As discussed above, the level density is a measure of the increase of levels per unit energy interval, i.e. it depends on the combinatorics of distributing the nucleons along the available particle-levels. However, we know that nucleons tend to form pairs as this is energetically favourable. In order to excite a paired nucleon, we have to break the pair first which costs energy. Therefore, we have to take the effect of pairing into account. This is done by the parameter δ which shifts the excitation energy thus giving an effective excitation energy U [GC65, HM72, RTK97]. This shift is different for even-even, odd-even, and odd-odd nuclei.

Apparently, slightly two different nomenclatures have evolved during the last decades regarding the back-shifted Fermi gas level density. In principle, the two definitions are very similar, however they fundamentally differ in the way the back-shift δ is determined. On the one hand, there are approaches which fix the back-shift and then do the fitting of the remaining parameters [HWFZ76, CTT91, RTK97]. On the other hand one could also include the back-shift into the fitting procedure [KHG08]. The latter way of obtaining the level density parameters has been used much less than the one in which the back-shift is fixed from outside. The reason is the divergence of the back-shifted Fermi gas level density at low energies, which we have to overcome either by switching to the constant temperature level density (see section 3.2.2) or by numerically bypassing the divergence [GF85, KHG08].

3.2.1.2 The back-shift

Historically, different parametrisations of the back-shift δ have evolved [HWFZ76, CTT91, RTK97, KHG08]. In the 70s and 80s a very general parametrisation depending on the square root of A was usually used, e.g.:

$$\delta(A) = \begin{cases} \frac{12}{\sqrt{A}} & \text{for even-even nuclei} \\ 0 & \text{for even-odd nuclei} \\ \frac{-12}{\sqrt{A}} & \text{for odd-odd nuclei.} \end{cases} \tag{3.6}$$

Alternatively, it is possible to derive the back-shift from masses as it has been done in [RTK97]. We will also use this approach for the back-shift in this thesis when discussing results obtained with a back-shifted Fermi gas level density:

$$\delta = \frac{1}{2}\left[\mathit{\Delta}_n(Z,N) + \mathit{\Delta}_p(Z,N)\right] \tag{3.7}$$

with

$$\begin{aligned}\mathit{\Delta}_n(Z,N) &= \frac{1}{2}\left[2E_{\text{bin}}(Z,N) - E_{\text{bin}}(Z,N-1) - E_{\text{bin}}(Z,N+1)\right]\\ \mathit{\Delta}_p(Z,N) &= \frac{1}{2}\left[2E_{\text{bin}}(Z,N) - E_{\text{bin}}(Z-1,N) - E_{\text{bin}}(Z+1,N)\right]\end{aligned} \tag{3.8}$$

and $E_{\text{bin}}(Z,N)$ being the binding energy of the nucleus with the corresponding proton and neutron numbers. This approach has the advantage that it reproduces the pairing gap much better than the simple approximation of eq. (3.6). However, at the same time this approach can become problematic near the drip line if nuclei beyond the mass model's drip line are not provided.

Nevertheless, when we are close to magic shell closures, calculating the back-shift from mass differences would also incorporate shell-effects into the back-shift. As shell-effects we understand here the influence the nuclear shell structure has on the mass and the level density. For example, it is energetically less favourable to excite nucleons in a closed shell compared to nucleons in an open shell. These shell-effects often - similar to pairing effects - result in a particular large energy gap between the ground state and the first excited state as well as particularly strong nuclear binding. With increasing energy these effects vanish, though, therefore we would like to damp the shell-effects in the level density parameter a with increasing energy. Consequently, it might be problematic to have the shell-effects additionally involved in the back-shift resulting from the mass differences. Moreover, a general problem is the fact that the back-shift is the same for any excitation energy, although we know that pairing effects (and shell effects) become weaker with increasing excitation energy. Therefore, an energy-dependent back-shift might bring an improvement regarding the predictive powers of the back-shifted Fermi gas level density.

3.2.1.3 Accounting for shell-effects

As *shell-effects* we may generally define any features in the level density or nuclear mass that result from peculiarities of the nuclear shells. In general, these are correlations that cannot be described in a classical macroscopic model, e.g. the liquid drop model. In this context, the shell-gap of a nucleus is a shell-effect. The shell-gap is an energy gap in the low-energy spectrum of a nucleus that occurs in magic nuclei, i.e. the energy gap to the first excited state is usually notably large.[1] The shell-effects often emerge as a correction to the binding energy, see [MNMS95] for example.

We have already mentioned before in section 3.2.1.2 that shell-effects vanish with increasing excitation energy, hence we will have to damp these effects. This issue was first tackled in [IST75] - for more references see [BBC$^+$06, chap. 6]. The idea is to modify the level density parameter a to make it energy-dependent and to damp out the shell-effects, i.e.

$$a(E,Z,N) = \tilde{a}(A)\left(1 + C(Z,N)\frac{f(E-\delta)}{E-\delta}\right), \tag{3.9}$$

with $\tilde{a}$ being the energy-independent level density parameter parametrised as in [HWFZ76, CTT91], i.e.

$$\tilde{a} = \alpha A + \beta A^{2/3}, \tag{3.10}$$

---

[1] A different definition of the shell-gap is the energy gap in the single-particle spectrum at closed shells. Both definitions are correlated but not the same. We will use both definitions in this thesis and the context should clarify which definition we mean. In the context of level densities, we mean the energy gap in the level spectrum, not the single-particle spectrum.

and $f(E)$ being a damping function,

$$f(E) = 1 - e^{-\gamma E}. \tag{3.11}$$

The quantity $C(Z,N)$ has to give a measure on the relevance or magnitude of shell-effects; it is therefore the shell correction energy in a liquid drop model. The parameters (α,β,γ) have to be obtained from fitting to experimental data.

3.2.2 Gilbert-Cameron Approach

The Fermi gas expression in eq. (3.5) diverges for low energies, i.e. $U \to 0$. Gilbert and Cameron proposed a way to circumvent this problem by combining the back-shifted Fermi gas level density with the so-called *constant temperature* level density [GC65], which we will shortly discuss in the following.

Experimentally, it has been observed that the number of levels $N(E)$ up to a certain energy E has an exponential form that can be parametrised as follows,

$$N(E) \propto e^{\frac{E-E_0}{T}}, \tag{3.12}$$

with E_0 and T being parameters that need to be fitted. The parameter T can be interpreted as a temperature, hence the name constant temperature formula. The parameter E_0 can be compared to the back-shift of the back-shifted Fermi gas formula (see eq. (3.5)) thus incorporating pairing effects and shell gaps.

The idea of the Gilbert-Cameron approach is to match the constant temperature level density and the back-shifted Fermi gas level density by finding a matching point at which both level densities and their first derivatives are equal. However, it is non-trivial to find this matching point, especially because this matching point does not necessarily exist.

3.2.3 Microscopic Methods

We already gave an account on possible microscopic methods to calculate the nuclear level density in the preceding section. In this section we would like to collect all relevant approaches following fully microscopic treatments. The advantages of these approaches are that for some of them we obtain the level densities spin- and parity projected and we do not need to match two different level density prescriptions. The possible alternatives are therefore microscopic level densities from Hartree-Fock-Bogoliubov approaches [DG01, HG06, HG07], level densities from shell model Monte Carlo calculations [Lan98, NA97, NA98a, ÖLMPD07], or binomial level densities based on moment-techniques of the nuclear Hamiltonian [Zuk01, HKZ03].

4

Nuclear Structure Models

The modelling of nuclear structure has a long tradition, starting in the beginning of the 20th century with the first models for the atomic nucleus since E. Rutherford discovered it [Rut11]. With the discovery of the neutron by Chadwick, the constituents of the nucleus were finally known and the first nuclear models were formulated.

The first models to be developed were motivated by classical physics, e.g. the liquid drop models in which the nucleus is described as a drop of finite size of a liquid consisting of neutrons and protons. Additional phenomenological contributions were introduced which already gave a hint of the incompleteness of the rather simple "drop" picture.

Historically, the Fermi gas model was the first to take quantum effects into account (e.g. the Pauli principle). In this model, the nucleons form a Fermi gas, i.e. it is assumed that they move almost freely inside the nucleus and are subject to the Pauli principle.

Both models are still in use today, the liquid-drop formalism has evolved to the so-called microscopic-macroscopic models in which microscopic corrections are applied to account for the insufficiencies of the macroscopic part. A prominent example is the FRDM mass model [MNMS95]. The Fermi gas model is often used in level density approaches, see chapter 3.

In this chapter, we will restrict ourselves to microscopic models. Microscopic models of the atomic nucleus have to employ a nucleon-nucleon interaction. However, the attempts to derive such an interaction from quantum chromo dynamics are still ongoing. Therefore, so-called *effective* interactions are employed of which many are specifically constructed to be used in certain contexts, e.g. the effective interactions in the shell model are restricted to a certain valence space.

4.1 The Nuclear Many-Body Problem

In general, any microscopic model of the nucleus has to incorporate a microscopic Hamiltonian $\hat{H}$. This Hamiltonian contains the aforementioned effective interaction. In this thesis we will only regard non-relativistic models and assume that only two-body interactions are relevant. Thus we can write down a general Hamiltonian in second quantisation [GM96, RS00, BG77],

$$\hat{H} = \sum_{ij} t_{ij} \hat{a}_i^+ \hat{a}_j + \frac{1}{4} \sum_{ijkl} \bar{v}_{ijkl} \hat{a}_i^+ \hat{a}_j^+ \hat{a}_l \hat{a}_k, \tag{4.1}$$

in which the indices - which run over all available states, i.e. $i = 1, \ldots, \infty$ - label the single-particle states in an arbitrary complete orthonormal basis. The $\bar{v}_{ijkl}$ are the antisymmetrised matrix elements of the two-body interaction. The idea is now to diagonalise the Hamiltonian in eq. (4.1), thus obtaining the eigenvalues and eigenfunctions. However, our Hilbert space is of infinite dimensionality. It is therefore not possible to perform this task in the complete Hilbert space. We have to do certain approximations to reduce the Hilbert space. In this thesis we will restrain to the following two options: either we restrict the number of particles and states or we approximate the eigenstates of the Hamiltonian by simpler wave functions. The first alternative is used in the shell model in which we divide our particle space into a core, a valence, and an external space, assuming that the relevant correlations we are interested in are feasible within the valence space. The second alternative is the so-called *Hartree-Fock* method in which the many-body state is approximated by a Slater determinant.

4.2 Skyrme-Hartree-Fock-BCS

In this chapter, we will discuss the basic properties of the Skyrme-Hartree-Fock-BCS model in a shortened scheme. At various steps we will refer the reader to the literature for more details. An introduction and summary of methods based upon the Hartree-Fock approach and its generalisation to include pairing interactions can be found in [RS00, GM96, Man75, Goo79]. For a broader overview on methods the reader should refer to [BHR03] and for a review specialised on the Skyrme functional see [SR07, EKR11].

The Hartree-Fock ansatz is a mean-field ansatz, i.e. instead of describing the interactions between all nucleons individually, we assume that every nucleon feels a mean-field created by the other particles. In principle this corresponds to the reduction of a complex many-body problem to a one-body problem. This is achieved by the assumption that the wave function of the system of A nucleons can be approximated by a Slater determinant. A Slater determinant Φ is a product wave function of one-body wave functions ϕ_α, the reader is referred to the literature for an extensive discussion on the properties of Slater determinants.

In the occupation number representation we may write a Slater determinant as,

$$\big|\, \Phi \,\big\rangle = \prod_{i=1}^{A} \hat{a}_i^{+} \big|\, \mathrm{vac} \,\big\rangle, \tag{4.2}$$

which is a subsequent application of creation operators $\hat{a}_i^{+}$ on the vacuum state $\big|\, \mathrm{vac} \,\big\rangle$. The indices of the creation operators correspond to the one-body wave functions of which the Slater determinant is constructed.

4.2.1 The Hartree-Fock Method

The Hartree-Fock method is an approximative method towards problems in many-body physics. As we stated before, the basic assumption is that the particles do not interact but are subject to a mean potential constructed from the other particles. In order to obtain the ground state of a system, i.e. the state with minimal energy, we make use of a variational principle (see e.g. [RS00] or books on general quantum mechanics). In practice we try to find the Slater determinant that gives the best approximation to the ground state, i.e. we use the variational principle with respect to the Slater determinant that minimises the energy of our system. We have to put an additional constraint to this variation in order to ensure that the state is normalised. This variation can be written as,

$$\delta \big\langle\, \Phi \,\big|\, \hat{H} - \lambda \,\big|\, \Phi \,\big\rangle = \delta E = 0. \tag{4.3}$$

Here $\hat{H}$ is the nuclear Hamiltonian and we have already introduced the Lagrange parameter λ which ensures the normalisation.

For practical reasons, one often changes to a density functional description. This is an alternative description of the Hartree-Fock problem and turns out to be more convenient than the description with creation operators, i.e. we postulate an energy functional as follows,

$$E[\{\phi_1, \phi_2, \dots, \phi_\alpha\}] = \langle \varPhi \,|\, \hat{H} \,|\, \varPhi \rangle - \sum_\beta \lambda_{\alpha\beta} \langle \phi_\alpha \,|\, \phi_\beta \rangle. \tag{4.4}$$

We already note here that this functional $\mathcal{E}$ depends on the one-body wave functions ϕ_α which construct our Slater determinant $\varPhi$; the second part of eq. (4.4) assures the normalisation. We may always do an unitary transformation and therefore have the possibility to set $\lambda_{\alpha\beta} = \delta_{\alpha\beta}\epsilon_\alpha$. In this formulation eq. (4.3) is equivalent to minimising eq. (4.4) with respect to the single-particle wave functions. Thus we get,

$$\frac{\delta E}{\delta \phi^*_\beta} = \left(\hat{h} - \epsilon_\beta\right) \phi_\beta = 0. \tag{4.5}$$

These equations define the one-body Hamiltonian $\hat{h}$ and its solution determines the single-particle wave functions ϕ_α and the single-particle energies ϵ_α.

The pairing correlations play an important role in nuclear physics and cannot be neglected for the ground state properties of most nuclei, with doubly magic nuclei being the exception. These correlations can be introduced by the so-called *BCS-method*, which originates from solid state physics [BCS57] but was soon applied to nuclear physics [BMP58, Bel58]. The idea of this method is the transformation of the particles of the system to so-called *quasi-particles* which create a many-particle-state of independent quasiparticles, i.e. we can describe the pairing correlations on the one-hand and retain the convenient approximation of independent (quasi-) particles. An extensive overview over the BCS approximation as well as the more general Bogoliubov transformations can be found in [GM96, RS00]. For our purposes, we only need the definition of the so-called BCS ground state, which is given by,

$$|\,\mathrm{BCS}\,\rangle = \prod_{\alpha>0} \left(u_\alpha + v_\alpha \cdot \hat{a}^+_\alpha \hat{a}^+_{\bar{\alpha}}\right) |\,\mathrm{vac}\,\rangle \tag{4.6}$$

with α being the index numbering the single-particle states, $\bar{\alpha}$ being the conjugate time-reversal state of α and $|\,\mathrm{vac}\,\rangle$ being the vacuum state. The product runs over half of the single-particle states. The u_α and v_α are variational parameters and can be interpreted that $|v_\alpha|^2$ and $|u_\alpha|^2$ represent the probability that a certain pair state (α,$\bar{\alpha}$) is occupied or is not, respectively [RS00].

4.2.2 Density Matrix Formalism

Instead of the description in the second quantisation with creation and annihilation operators, one may describe a many-body problem in the *density matrix* formalism. This approach has several practical advantages, see [Ben97] for more details. With the help of our creation and annihilation operators, we can define so-called mean-field operators, i.e.

$$\begin{aligned} \hat{\phi}^+ &= \sum_\alpha \phi^*_\alpha \hat{a}^+_\alpha \\ \hat{\phi} &= \sum_\alpha \phi_\alpha \hat{a}_\alpha. \end{aligned} \tag{4.7}$$

Here the ϕ_α are our single-particle wave functions.

The one-body density operator is then given by,

$$\hat{\rho} = \hat{\phi}^+ \hat{\phi}. \tag{4.8}$$

With the help of this operator, we may define the one-body density matrix, i.e.

$$\rho = \left\langle \Phi \,\middle|\, \hat{\phi}^{+}\hat{\phi} \,\middle|\, \Phi \right\rangle = \sum_{\alpha\beta} \rho_{\alpha\beta}\phi^{*}_{\beta}\phi_{\alpha}. \tag{4.9}$$

Here we have used the following relation, i.e.

$$\rho_{\alpha\beta} = \left\langle \Phi \,\middle|\, \hat{a}^{+}_{\beta}\hat{a}_{\alpha} \,\middle|\, \Phi \right\rangle. \tag{4.10}$$

In principle we would also need two-body densities but these can be written as antisymmetrised products of one-body densities in case of Slater determinants. The Hohenberg-Kohn theorem guarantees us the existence of an energy functional $E[\rho]$ if we use a local two-body interaction. In appendix C we have summarised the densities that will occur in this formalism when the so-called Skyrme functional is used.

4.2.3 Skyrme's Interaction

So far we have only discussed a method but not from where we take our interaction from. Since we intend to use a mean-field method based upon Slater determinants we cannot use a realistic nucleon-nucleon interaction such as AV18 or CD-Bonn. In contrary, we have to use a so-called *effective* interaction. In this thesis we will make use of the so-called Skyrme force [Sky59, SR07]. As we will make use of a energy density functional method in this thesis, we will use the terminology of a Skyrme functional from now on.

An alternative formulation of many-body quantum mechanics can be achieved by making use of the so-called *density matrices.* The goal is similar to the formulation with wave functions, i.e. the reduction of an A-body density matrix formalism to a one-body density matrix formalism. The Hohenberg-Kohn-Theorem [HK64] guarantees the existence of an energy functional $E[\rho]$, with ρ being a local density. This makes it possible to formulate everything in the scope of a density functional theory, as we have already mentioned before. The final goal is therefore to construct an effective energy density functional derived from an effective interaction, that approximates our many-body problem.

By defining $E[\rho] = \int \mathcal{E}[\rho]\ d\boldsymbol{r}$ we define such an energy functional as follows (see [BHR03, SR07] and references therein),

$$E = E_{\mathrm{kin}} + E_{\mathrm{Skyrme}} + E_{\mathrm{Coulomb}} + E_{\mathrm{pair}} - E_{\mathrm{corr}}, \tag{4.11}$$

that consists of a part for the kinetic energy E_{kin}, the mean-field represented by the Skyrme functional E_{Skyrme}, the functional representing the coulomb interaction E_{Coulomb}, the pairing functional E_{pair} and correction terms summarised in E_{corr}. The latter are arbitrarily defined as negative.

[Ben97, Klü08, Erl11, EKR11].

A definite Skyrme functional does not exist, because there exist a large number of different Skyrme-Functionals [BHR03, SR07]. In this work we use the following representation of the Skyrme functional $E_{\mathrm{Skyrme}} = \int \mathcal{E}_{\mathrm{Skyrme}}\ d^3r$ as follows,

$$\begin{aligned} E_{\mathrm{Skyrme}} = \int d^3r \Bigg(& \frac{b_0}{2}\rho^2 - \frac{b'_0}{2}\sum_q \rho_q^2 + b_1(\rho\tau - \boldsymbol{j}^2) - b'_1\sum_q(\rho_q\tau_q - \boldsymbol{j}_q^2) \\ & -\frac{b2}{2}\rho\Delta\rho + \frac{b'_2}{2}\sum_q \rho_q\Delta\rho_q + \frac{b3}{3}\rho^{\alpha+2} - \frac{b'_3}{3}\rho^{\alpha}\sum_q \rho_q^2 \Bigg) + E_{\mathrm{LS}} \end{aligned} \tag{4.12}$$

Here we have made use of an alternative notation of the Skyrme parameters. The relations to the original Skyrme parameters can be found in appendix B. The definitions of the densities $(\rho, \tau, \boldsymbol{J})$ can be found in appendix C. The densities without an index are considered to be the sum over the neutron and the proton contribution, i.e. for any density $\mathit{\Gamma}_q$

$$\mathit{\Gamma} = \mathit{\Gamma}_p + \mathit{\Gamma}_n, \tag{4.13}$$

this also holds for vectorial densities. Moreover, we would like to point out here, that we only regard even-even nuclei, therefore we assume time-reversal symmetry and thus time-odd terms vanish and are not considered in eq. (4.12). An overview on the Skyrme functional including time-odd terms can be found in [Erl11, PERN10, SR07, EKR11].

For the spin-orbit functional in eq. (4.12) different formulations exist. We use the following form [SR07],

$$E_{\mathrm{LS}} = \int d^3r \left\{ -b_4 \left(\rho \boldsymbol{\nabla} \cdot \boldsymbol{J} + \boldsymbol{s} \cdot (\boldsymbol{\nabla} \times \boldsymbol{j}) \right) - b_4' \sum_q \left[\rho_q \boldsymbol{\nabla} \cdot \boldsymbol{J}_q + \boldsymbol{s}_q \cdot (\boldsymbol{\nabla} \times \boldsymbol{j}_q) \right] \right\}. \tag{4.14}$$

This is not the complete form given in [SR07], but the missing terms vanish for the Skyrme functionals we utilise in this thesis. For the spin-orbit functional of eq. (4.14) we have not omitted the time-odd terms.

The coulomb functional E_{Coulomb} is treated in the Slater approximation. In this approximation, the finite size of the nucleons is neglected. If one includes this effect, the intrinsic charge distribution would change and the mathematical treatment would become much more complicated.

The definitions of the kinetic and the pairing part for later use. The kinetic part is given by

$$E_{\mathrm{kin}} = \sum_q \frac{\hbar^2}{2m_q} \int \tau_q(\boldsymbol{r})\, d^3r, \tag{4.15}$$

with q running over neutrons and protons. τ_q is the kinetic energy density of the respective nucleon type and m_q the mass. The term $\hbar/2m_q$ is usually Skyrme force specific. Many Skyrme forces set $m_p = m_n$ because the relative error is small and can be absorbed into the error of the Skyrme parameters. However, for nuclei with large differences in the proton and the neutron number (exotic and super-heavy nuclei), this assumption might become doubtful.

The pairing part is according to [SR07],

$$E_{\mathrm{pair}} = \frac{1}{4} \sum_q \int V_{\mathrm{pair},q}\, \chi_q^2\, d^3\boldsymbol{r}, \tag{4.16}$$

with $\chi_q(\boldsymbol{r})$ being the pairing density [Ben97] and $V_{\mathrm{pair},q}$ the pairing potential of the nucleon type q. The pairing potential is usually defined in two possible ways, either as DI-pairing (also called “volume” pairing), i.e.

$$V_{\mathrm{pair},q}^{\mathrm{DI}} = V_{0,q} \tag{4.17}$$

or as a DDDI-pairing (also called “surface” pairing),

$$V_{\mathrm{pair},q}^{\mathrm{DDDI}} = V_{0,q} \cdot \left(1 - \frac{\rho}{\rho_0} \right). \tag{4.18}$$

Here ρ_0 is usually defined to have values around $\rho_0 \approx 0.16\ \mathrm{fm}^{-3}$, i.e. the equilibrium density of nuclear matter. Many older Skyrme functionals, such as SLy6 functional (see chapter 8) have been fitted regarding DI pairing but it is possible to obtain the parameters $V_{0,q}$ (which are not part of the Skyrme functional) also for DDDI pairing.

In numerical calculations it is very inefficient (if even possible) to regard all single-particle states for the pairing as this would lead to divergencies in the pairing functional. It is therefore needed to restrict the phase-space of pairing by a weighting function f_α. This weight shows up in all densities and currents where the BCS amplitudes v_α and u_α occur. The simplest ansatz is to use a Θ-function for a given cut-off energy ϵ_{cut}, i.e.

$$f_\alpha(\epsilon_\alpha) = \Theta(\epsilon_{\text{cut}} - \epsilon_\alpha). \tag{4.19}$$

This is known to work well for large pairing spaces [DFT84]. It is however preferable to have a smooth cut-off. This can be achieved by a Fermi-function, i.e.

$$f_\alpha(\epsilon_{\text{cut}}) = \frac{1}{1 + e^{(\epsilon_\alpha - (\epsilon_F + \epsilon_{\text{cut}}))/\Delta\epsilon}}, \tag{4.20}$$

with ϵ_F being the Fermi energy. Typically one sets $\epsilon_{\text{cut}} = 5$ MeV and $\Delta\epsilon = \epsilon_{\text{cut}}/10$ MeV (see [BRRM00] and references therein).

For fission barriers, the correction term E_{corr} becomes important. Generally, we may divide this correction term into three parts, i.e.

$$E_{\text{corr}} = E_{\text{c.m.}} + E_{\text{rot}} + E_{\text{vib}}, \tag{4.21}$$

in which $E_{\text{c.m.}}$ is a centre-of-mass correction and the other term represent rotational and vibrational corrections. For the centre-of-mass term different methods of calculation exist, varying strongly in complexity and quality. Skyrme parameter sets are usually confined to one of these methods, see [Ben97] for more details. The other contributions from vibrational and rotational modes are extensively discussed in [Klü08, EKR11].

4.2.4 The One-Body Hamiltonian

As we have stated before, we obtain our one-body Schrödinger equation

$$\hat{h}_q \phi_\alpha = \epsilon_\alpha \phi_\alpha \tag{4.22}$$

with the single-particle energies ϵ_α from the variation of the energy functional with regard to the one-body wave functions. This variation we may rewrite as a variation with regard to the densities by using the chain-rule, i.e.

$$\hat{h}_q \phi_\alpha = \frac{\delta E}{\delta \phi_\alpha^*} = \int d^3 r' \frac{\delta E}{\delta \boldsymbol{\Gamma}} \frac{\delta \boldsymbol{\Gamma}}{\delta \phi_\alpha^*}, \tag{4.23}$$

with Γ being a vector of the relevant densities defined in appendix C. After a lengthy calculation we obtain the following form of the one-body Hamiltonian [Ben97],

$$\begin{aligned} \hat{h}_q = & \underbrace{\frac{\delta E}{\delta \rho_q}}_{U_q} - \boldsymbol{\nabla} \cdot \left[\underbrace{\frac{\delta E}{\delta \tau_q}}_{B_q} \boldsymbol{\nabla} \right] - i \left[\underbrace{\frac{\delta E}{\delta \boldsymbol{J}} - \boldsymbol{\nabla} \frac{\delta E}{\delta \boldsymbol{\nabla} \boldsymbol{J}_q}}_{\boldsymbol{W}_q} \right] \cdot \boldsymbol{\nabla} \times \hat{\boldsymbol{\sigma}} \\ & + \underbrace{\frac{\delta E}{\delta \boldsymbol{s}_q}}_{\boldsymbol{S}_q} \cdot \hat{\boldsymbol{\sigma}} - \boldsymbol{\nabla} \cdot \left[\hat{\boldsymbol{\sigma}} \cdot \underbrace{\frac{\delta E}{\delta \boldsymbol{\tau}_q}}_{\boldsymbol{C}_q} \right] \cdot \boldsymbol{\nabla} - \frac{i}{2} \left[\boldsymbol{\nabla} \cdot \underbrace{\frac{\delta E}{\delta \boldsymbol{j}_q}}_{\boldsymbol{A}_q} + \underbrace{\frac{\delta E}{\delta \boldsymbol{j}_q}}_{\boldsymbol{A}_q} \cdot \boldsymbol{\nabla} \right]. \end{aligned} \tag{4.24}$$

Here we introduced the scalar and vector potentials $\boldsymbol{A}_q$, B_q, $\boldsymbol{C}_q$, $\boldsymbol{S}_q$, U_q, and $\boldsymbol{W}_q$. For the explicit discussion of these quantities we refer the reader again to the literature [Ben97, Klü08]. Note that we have not omitted the time-odd terms here; in a time-even system the potentials $\boldsymbol{A}$, $\boldsymbol{C}$, and $\boldsymbol{S}$ vanish. Additionally to the variation with respect to the single-particle wave functions we also have to vary with respect to the BCS amplitudes u_α.

In our calculations we solve the system of equations, i.e. eq. (4.22), with the help of the gradient method [Ben97, RS00]. The solution provides us with the single particle wave functions, energies and BCS amplitudes that can be used to determine the various densities and thus the value of the functional at the solution "point" that determines our ground state energy.

A very fundamental problem of the BCS approximation is that the BCS states are not eigenstates of the particle number operator $\hat{N}$. Moreover, the introduction of the pairing leads to a possible phase-transition. In order to avoid these phase-transitions we apply the method of *stabilised pairing* [EKR08]. We do not perform a projection on the particle number, though.

The collective corrections we treat as described in [Klü08, EKR11].

4.2.5 The Effective Mass

In principle the method of using effective masses originates from classical mechanics, where one rewrites the equations of motions in a way that they decompose in a kinetic term and a potential term. To do that one usually has to introduce a mass-like quantity that appears in the kinetic term. The method of using reduced masses in classical mechanics for a two-body system is a prominent example. In quantum mechanics, the effective masses and their definition depend on the used method. In non-relativistic theories one usually differentiates between a *isoscalar* effective mass and a *isovector* effective mass (see [JM89, GSBP03] and references therein). In relativistic mean-field models, these effective masses a slightly different: here one differentiates between the *Dirac* mass and the *Landau* mass [JM89, Typ05].

In the Skyrme-Hartree-Fock model the derivative with respect to the kinetic energy density τ (see eq. (4.15) and eq. (4.24)) is given by,

$$B_q = \frac{\delta E}{\delta \tau_q} = \frac{\hbar^2}{2m_q} + b_1\rho - b_1'\rho_q, \tag{4.25}$$

with $\rho = \rho_p + \rho_n$ being the sum for the particle density of protons and neutrons. The effective mass m_q^* is now defined as [Ben97],

$$B_q = \frac{\hbar^2}{2m_q^*} \quad \text{with} \quad m_q^* = \frac{m}{1 + \frac{2m}{\hbar^2}\left(b_1\rho - b_1'\rho_q\right)}. \tag{4.26}$$

Generally speaking, the effective mass is a measure of the velocity-/momentum-dependent terms in the used interaction. One usually gives the effective mass in its relation to the bare nucleon mass m^*/m. One can decompose the effective mass into two parts [GSBP03],

$$\frac{\hbar^2}{2m_q^*} = \frac{2\rho_q}{\rho}\frac{\hbar^2}{2m_s^*} + \left(1 - \frac{2\rho_q}{\rho}\right)\frac{\hbar}{2m_v^*} \tag{4.27}$$

with m_s^* being the *isoscalar* effective mass and m_v^* the *isovector* effective mass. The isoscalar mass we will later need in chapter 8 because this quantity strongly affects the shell-structure predicted by a certain Skyrme functional.

In section 5.3.2.1 we will discuss a sum rule for electric dipole transitions and we will see that the calculated deviation from this sum rule is due to velocity-dependent terms in the nuclear interaction. Therefore, the effective mass is a measure of the deviation of this sum rule. In particular, this could be a way to experimentally constrain the effective mass as it is possible to measure the exhaustion of the sum rule. In practice this is often done vice versa: a certain exhaustion factor κ is assumed (usually 0.2-0.3) -

thus fixing a certain range for m_v^* - and used as input to the fitting procedure to determine the Skyrme parameters.

4.2.6 Constrained Hartree-Fock

Up to know we have only discussed a method that is only capable of calculating the ground state of a nucleus. For the microscopic description of fission we need to fix the deformation from outside, though. By doing this, we are able to scan through the deformation landscape and thus obtain the potential energy surface. A possible method to achieve this, is the so-called *constrained Hartree-Fock* method (see [BGG89] for an overview). The idea is to force a certain deformation via Lagrange multipliers and modify the Hatree-Fock Hamiltonian,

$$\hat{H}_{\mathrm{cHF}} = \left(\hat{H}_{HF} - \lambda \hat{Q}_{20}\right). \tag{4.28}$$

We have restricted ourselves to the quadrupole deformation ($\hat{Q}_{20}$ is similar to the quadrupole operator) as this is the most important deformation regarding fission. The Lagrange parameter λ is chosen so that the desired quadrupole deformation α_{20} is achieved. With eq. (4.28) we have for every λ a specific eigenvalue problem belonging to a certain quadrupole deformation α_{20},

$$\hat{H}_{\mathrm{cHF}} \big| \Psi^{\alpha_{20}} \big\rangle = E \big| \Psi^{\alpha_{20}} \big\rangle. \tag{4.29}$$

The operator $\hat{Q}_{20}$ is chosen as

$$\hat{Q}_{20} = r^2 Y_{20} \kappa_{\mathrm{cut}}(\boldsymbol{r}), \tag{4.30}$$

with $\kappa_{\mathrm{cut}}(\boldsymbol{r})$ being a damping function. This function is needed in the calculation to confine the action of the operator to the nucleus as it can lead to numerical artefacts especially at the edges of the numerical box [RMRG95]. It is possible to extend this method to even higher multipole moments. However, in this thesis we will consider only quadrupole deformations. The octupole and hexadecupole deformation we will discuss in chapter 8 are obtained by testing for these deformations in the vicinity of the current quadrupole deformation. For example, a possible octupole deformation is obtained by artificially forcing a octupole deformation and then allowing the system to find its energetical minimum. By using the wave function from the previous quadrupole deformation we are thus able to construct a path of quadrupole deformations with varying octupole and hexadecupole deformations. This method is computationally much easier to handle and much faster than constraining the octupole and hexadecupole deformation and scan these for the minimum energy. However, we cannot be sure to find the true fission path through the potential energy surface, as this method can lead to jumps in the predicted path.

4.3 Nuclear Shell Model

In 1949 Maria Goeppert-Mayer [May49] and Haxel, Jensen, and Suess [HJS49] explained the phenomenon of magic shell closures by introducing a spin-orbit term into a harmonic oscillator mean-field, i.e.

$$U(r) = \frac{1}{2} m\omega^2 r^2 + D \cdot \boldsymbol{l}^2 - C \cdot \boldsymbol{l} \cdot \boldsymbol{s}, \tag{4.31}$$

in which the first term represents an isotropic harmonic oscillator, the second term is an orbit-orbit term and the last term is the spin-orbit coupling needed to reproduce the phenomenon of magic numbers[1]. With every term, the single-particle levels become less degenerate, e.g. they split. With the potential

---

[1] It has been shown that in relativistic approaches this coupling comes out naturally and does not have to be inserted specifically.

of eq. (4.31) it was possible to explain the above mentioned magic numbers as well as to predict basic properties of nuclei.

The general method to obtain a mean-field in a system of interacting nucleons is the Hartree-Fock approximation, which was discussed before. In this method, the eigenstates of the many-body Hamiltonian are Slater determinants. There are now two properties of the general nucleon-nucleon interaction that render the Hartree-Fock approximation inefficient: (i) the strong short-range repulsion and (ii) the tensor force. Therefore we cannot use the Hartree-Fock approximation in conjunction with a realistic nucleon-nucleon interaction. However, the success of the independent particle Hamiltonian suggested that it was possible to regularise the free nucleon-nucleon interaction in the nuclear medium. We will come to that issue in section 4.3.1.1.

From now on, we employ the following assumptions for the nuclear shell model: the protons and neutrons in the nucleus interact via two-body forces and the dynamics are described by a non-relativistic Schrödinger equation. There might be additional meson and quark-gluon degrees of freedom, which we do not regard here. For further details the reader should regard the large list of books covering the mathematics and physics of the shell model [BG77, Hey94]; for a short introduction covering the applications of shell model see [Gra04, Ots09, PN01]. A very extensive and recent review on the modern nuclear shell model for advanced readers can be found in [CMPN$^+$05] and a review specialised on neutron-rich nuclei is given by [Bro01].

We can apply Wick's theorem, with a defined core as the reference state, to the general nuclear Schrödinger equation. By following the literature we obtain [BG77, Hey94],

$$\hat{H} = E_0 + \sum_i \epsilon_i : \hat{a}_i^+ \hat{a}_i : + \frac{1}{4} \sum_{ijkl} \overline{v}_{ijkl} : \hat{a}_i^+ \hat{a}_j^+ \hat{a}_l \hat{a}_k : . \tag{4.32}$$

Here : ... : symbolises the normal ordering of the operators [BG77, Hey94, RS00]. The ϵ_i are the single-particle energies obtained from a mean-field. The last term of eq. (4.32) is a two-body term and is called the *residual* interaction. This residual part now contains all correlations that go "beyond" the mean-field. It is the treatment of this term that differentiate Hartree-Fock based methods from the shell model.

4.3.1 The Large Scale Shell Model

In this thesis we will employ the so-called *large scale shell model*, which we will call from now on simply "shell model". The ingredients needed for this model are basically three. First, we need to define a space that acts like a basis for our calculations. This space is called the *valence space*. Second, we need an effective interaction that has been specifically developed for the chosen valence space. With this interaction we try to describe the nucleon-nucleon correlations inside our valence space. Third, we finally need a numerical method that allows us to efficiently diagonalise the Hamiltonian matrix and to solve the many-body Schrödinger equation. To sum it up, a shell model calculation consists of diagonalising the Hamiltonian matrix in the basis of all Slater determinants that can be constructed by the distribution of all particles in the valence space.

In the following we will make use of the method of second quantisation and other quantum-mechanical tools. The reader is referred to the literature regarding these issues, for example [BG77, RS00, Hey94, BM69].

4.3.1.1 The Spaces

As the nucleus is a system of A particles that interact with each other within a finite volume, the exact solution of the Schrödinger equation describing the dynamics has to be obtained in an infinite space that is composed of the shells generated by the nucleonic potential. This is really an impossible task! Therefore, besides the mean-field approximation, we also trim the Hilbert space we are dealing with. We approximate the solution in the infinite Hilbert space by solving the problem in a finite space, the *valence space*, and by using a so-called *effective interaction*. Due to the imposed restrictions to the Hilbert space we have to renormalise the interaction in such a way that

$$\left\langle \Psi \,\middle|\, \hat{H} \,\middle|\, \Psi \right\rangle = \left\langle \Psi_{\text{eff.}} \,\middle|\, \hat{H}_{\text{eff.}} \,\middle|\, \Psi_{\text{eff.}} \right\rangle \tag{4.33}$$

is fulfilled, wherein $\hat{H}_{\text{eff.}}$ and $\Psi_{\text{eff.}}$ are the Hamiltonian and wave functions in the restricted Hilbert space, i.e. the valence space. We may generalise eq. (4.33) also for other operators because it is the obvious postulation that the expectation value of an operator should be the same in the infinite Hilbert space and the valence space.

We trim the Hilbert space in such a way that low-energy shells, which can usually be neglected as long as the excitation of the nucleus is not too high, are removed. Consequently we end up with three different 'spaces': (1) the inert core, (2) the valence space, and (3) the external space. The inert core contains all orbits that are forced to be filled and it has to be below the Fermi energy. The valence space is the part of the Hilbert space in which we allow nucleon excitations. The particles in that space we call *valence particles*. The distribution of the valence particles is governed by the interaction. The external space consists of the orbits we exclude, i.e. to which we do not allow excitations. These orbits are always empty! Figure 4.1 shows schematically the relevant spaces as well as in which space the nucleons may be excited.

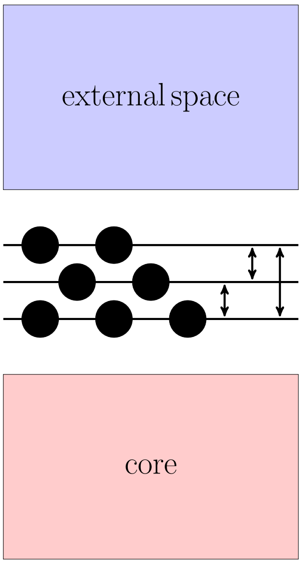

Figure 4.1: Schematic picture of the nuclear shell model: the red coloured core is fixed and its nucleons are not allowed to be excited. The external space is the space that is left empty, i.e. no excitations may occur into or in this space. The arrows indicate the active space, i.e. the shells between which correlations are allowed.

We have to choose the valence space according to which nuclei and quantities we want to study and it is a non-trivial task to determine the optimum valence space. In this thesis we will only work with two valence spaces, the first being the pure pf-shell for nuclei with $20 \leq \mathrm{Z} \leq 32$ and $20 \leq \mathrm{N} \leq 32(40)$[1] with the inert core being a ^{40}Ca core. The second valence space we will be dealing with is based upon a ^{48}Ca core, i.e. the neutron $f_{7/2}$-orbital is full and the $g_{9/2}$ orbital is available for neutron excitations. The latter valence space allows us to calculate neutron-rich nuclei in the pf-shell.

As stated above, we have to choose the valence space also according to the quantities we intend to study. If we want to study spin-flip excitations like in M1 or Gamow-Teller transitions, we have to make sure that the relevant spin-orbit partners between which the spin-flip occurs are within our model space. A further example are collective isovector E1 transitions, because for these we would have to include at least two harmonic oscillator shells.

---

[1] In principle beyond N=32 one has to take the $g_{9/2}$-orbital into account; in this thesis we will keep this valence space even up to N=40.

4.3.2 The Basis

A fundamental problem in all applied quantum-mechanics is the choice of the basis in which the problem can be solved in the easiest way. This also applies for shell model calculations. Basically there exist two formulations of the basis: on the one hand the so-called *m-scheme* and on the other the *coupled scheme*.

Since we will only discuss results obtained from the shell model code ANTOINE [Cau], that is programmed in the m-scheme, we will discuss this basis and refer to [BG77, CMPN$^+$05] for the coupled scheme, which finds application in the shell model code NATHAN.

4.3.2.1 The m-Scheme

The m-scheme basis is built from all Slater determinants constructed from all possible configurations that the chosen valence space allows. This makes it easy to calculate the many-body matrix elements since they are equal to the decoupled two-body matrix elements up to a phase [CMPN$^+$05]. It is therefore not necessary to calculate coefficients of fractional parentage or Wigner-9J-coefficients [BG77, Hey94]. The physical states are obtained by simply diagonalising the Hamiltonian matrix $\left\langle \varPhi_\alpha \,\middle|\, \hat{H}_{\text{eff.}} \,\middle|\, \varPhi_\beta \right\rangle$, with the $\varPhi$ being the mentioned Slater determinants.

In this approach, the only good quantum numbers are the projections J_z and T_z of the angular momentum and the isospin. Therefore, all possible (J,T) are within this basis and the dimensions of the matrices become maximal[1] which means the dimensionality d becomes

$$d \propto \begin{pmatrix} D_n \\ n \end{pmatrix} \cdot \begin{pmatrix} D_p \\ p \end{pmatrix} \tag{4.34}$$

with n being the number of neutrons in the valence space, p being the number of protons in the valence space, and $D_{n,p}$ being the degeneracies of the neutron and proton spaces. Although the dimensionality is large, the Hamiltonian matrix is sparse and we can make use of methods exploiting the sparseness of matrices.

4.3.3 The Lanczos Method

Since we have to obtain the eigenvalues of the Hamiltonian we have to diagonalise matrices of very high dimensionality when operating in the m-scheme (see eq. (4.34)), and thus we not only have the problem of much needed CPU time but also a storage problem.

Then we need to use iterative methods that allow for a fast convergence of the lowest eigenvectors of the hamiltonian matrix. in the applications of this thesis we use the Lanczos method as explained in [PN01].

4.3.3.1 Lanczos Strength Functions

We have to shortly discuss the terminology in this chapter before we start sketching the way we may obtain a strength function from the Lanczos method. In this chapter the term “strength function” is defined a little bit different to the general definition we will use later in this thesis. Here strength function is - in conformance with the late following definition - a function describing the distribution of transitions strength depending on energy. However, the strength function presented here gives a discrete spectrum, while in chapter 7 a strength function will always be a continuous function.

As already mentioned, a very convenient side-effect of the Lanczos method is the possibility to calculate spectroscopic properties of the nucleus, especially strength functions. The idea [WWK80] is very simple: Let us assume that we have obtained the ground state $\left|\,\mathrm{gs}\,\right\rangle$ of given nucleus from the conventional Lanczos method. Furthermore, let $\varOmega^{\mathrm{L}}$ denote an operator, with multipolarity L, that we are interested

---

[1] *Maximal* in this context really means that the dimensionality is as large as it can get in the corresponding valence space.

in. By letting this operator act on an initial state $\big|\,\text{ini}\,\big\rangle$ we obtain the sum rule state $\Omega^{\text{L}}\big|\,\text{ini}\,\big\rangle$. The norm of this state is the sum rule or the total strength of the operator Ω^{L} in the initial state, i.e.

$$N = \sqrt{\big\langle\,\text{ini}\,\big|\,(\Omega^{\text{L}})^{+}\Omega^{\text{L}}\,\big|\,\text{ini}\,\big\rangle}. \tag{4.35}$$

If the operator Ω^{L} does not commute with the Hamiltonian, i.e. $\left[\hat{H},\Omega^{\text{L}}\right]\neq 0$, then the sum rule state is not necessarily an eigenstate. However, it is always possible to describe the sum rule state in the basis of the eigenstates of the Hamiltonian, i.e.

$$\Omega^{\text{L}}\big|\,\text{ini}\,\big\rangle = \sum_j S(E_j)\big|\,E_j\,\big\rangle, \tag{4.36}$$

with the $S(E_j)$ being the coefficients for the basis transformation. These coefficients fulfil the following property,

$$\big\langle\,\text{ini}\,\big|\,(\Omega^{\text{L}})^{+}\Omega^{\text{L}}\,\big|\,\text{ini}\,\big\rangle = \sum_j S^2(E_j). \tag{4.37}$$

The quantity $S(E_j)$ is given by

$$S(E_j) = \big\langle\,E_j\,\big|\,\Omega^{\text{L}}\,\big|\,\text{ini}\,\big\rangle. \tag{4.38}$$

We should consider here, that the sum rule state as defined above is not normalised, however the square of normalisation constant N^2 is given by $N^2=\sum_j S^2(E_j)$. Hence, the normalised sum rule state $\big|\,\Lambda\,\big\rangle$ can be written as,

$$\big|\,\Lambda\,\big\rangle = \frac{1}{N}\sum_j S(E_j)\big|\,E_j\,\big\rangle. \tag{4.39}$$

We now obtain the strength function by using the sum rule state as the pivot for the Lanczos procedure. The Lanczos methods diagonalises the Hamiltonian matrix thus obtaining a matrix M that diagonalises the Hamiltonian. This matrix M gives us the transformation between the eigenstates of the Hamiltonian matrix, i.e. the $\big|\,E_j\,\big\rangle$, and the Lanczos vectors which we get from the procedure. Since we chose the sum rule state as the pivot, i.e. defined it as the first Lanczos vector, we can easily obtain the $S(E_j$ from the matrix M.

Nevertheless, we must keep in mind that the Lanczos method is an approximative procedure. Therefore we have to consider the strength function obtained from the Lanczos method as an approximation to the “real” strength function. To get an estimation on the quality we may start from statistics, i.e. we recapitulate that every distribution can be characterised by its moments. In case of the gauss distribution, the two moments are the centroid and the standard deviation. Therefore, if we assume a Gaussian profile around an eigenvalue E_j of the Hamiltonian, we may write [PN01],

$$g(E_j) = \frac{1}{\sqrt{2\pi\sigma^2}}\cdot e^{-(E-E_0)^2/2\sigma^2}. \tag{4.40}$$

These two moments we may write as,

$$
\begin{aligned}
E_0 &= \langle \Lambda \,|\, \hat{H} \,|\, \Lambda \rangle = \frac{1}{N^2} \sum_j E_j \; S^2(E_j). \\
\sigma^2 &= \langle \Lambda \,|\, (\hat{H} - E_0)^2 \,|\, \Lambda \rangle = \frac{1}{N^2} \sum_j (E_j - E_0)^2 \; S^2(E_j).
\end{aligned}
\tag{4.41}
$$

After n iterations in the Lanczos method we have n eigenvalues of the Hamiltonian matrix and consequently $2n$ moments of the Gaussian distributions. In fig. 4.2 we have plotted the M1 strength function of ^{56}Fe in the upper panel for n=50 Lanczos iterations and n=1000 Lanczos iterations. If we convolute the discrete spectra with Gaussians, then we obtain the functions in the lower panels. These show that the strength function deduced from 50 Lanczos iterations and the strength functions deduced from 1000 Lanczos iterations are very similar and that the contained information is almost identical. Thus, it is not necessary to perform a large number of iterations to receive a realistic description of our problem. This fact strongly reduces the needed calculation time.

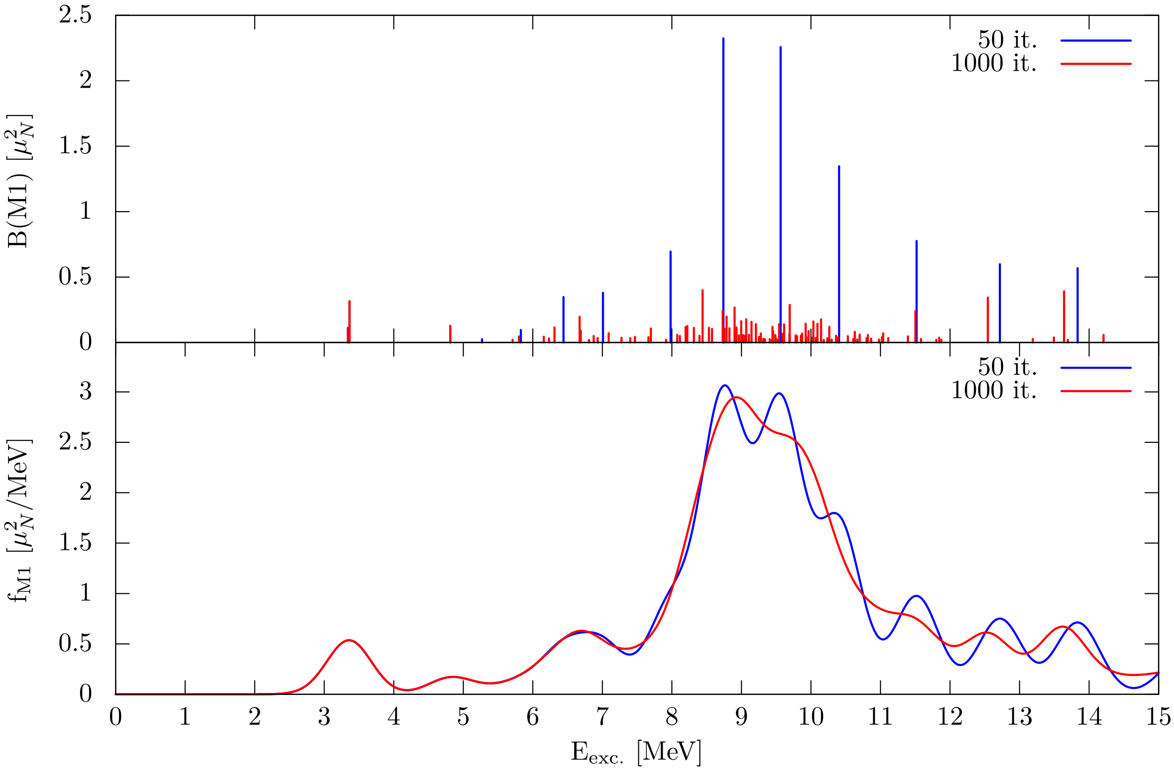

Figure 4.2: Upper panel: B(M1) strength distribution on the ground state of ^{56}Fe calculated with n=50 Lanczos iterations and n=1000 Lanczos iterations. Lower panel: convolution with Gaussians of the discrete B(M1) strength distributions shown in the upper panel.

5

γ-ray Transitions in Nuclei

The excited nucleus usually releases energy by the emission of particles or γ-rays, with the latter being the only existing mode of disexcitation that does not change the composition of the nucleus, i.e. it conserves the number of protons and neutrons. These *electromagnetic* transitions in nuclei are mediated solely by the electromagnetic force and often also occur as secondary decays after previous decays. Electromagnetic decays or transitions, respectively, can also be related to collective phenomena in nuclei, in particular giant resonances or rotational modes.

Generally, electromagnetic transitions in nuclei can be characterised by their type (electric or magnetic) and the angular momentum L they carry. It is possible to derive operators for a given type X and a given multipolarity L. The probability of a electromagnetic transition between two states in a nucleus for a given type and multipolarity can be derived by calculating the overlap of the corresponding operator between both states. In this chapter we will shortly introduce the relevant operators and then discuss the general treatment of electromagnetic transitions in the *strength function formalism* used in many reaction calculations.

5.1 Electromagnetic Transitions

In this thesis we will abbreviate the type of radiation (magnetic or electric) by X and the multipolarity by L.

5.1.1 The Electromagnetic Field

The electromagnetic field consists of of an electric component $\boldsymbol{E}$ and a magnetic component $\boldsymbol{B}$. The energy density of the electromagnetic field is proportional to $\boldsymbol{E}^2 + \boldsymbol{B}^2$ [Jac98]. The corresponding electromagnetic interaction is mediated by the relativistic four-vector potential $(\phi,\boldsymbol{A})$, with ϕ being the scalar potential and $\boldsymbol{A}$ being the vector potential.

The electromagnetic field is mathematically described by the Maxwell equations. These equations, their meanings as well as their derivation, can be found in any introductory textbook about the classical theory of electrodynamics (see for example [Jac98]). For our purpose, we only need two equations defining the relations between the potentials and the electromagnetic field, i.e.

$$\boldsymbol{E} = -\boldsymbol{\nabla}\phi - \frac{1}{c}\frac{\partial \boldsymbol{A}}{\partial t} \tag{5.1}$$

$$\boldsymbol{B} = \boldsymbol{\nabla} \times \boldsymbol{A}. \tag{5.2}$$

As indicated above, the energy of the electromagnetic field is given by

$$E = \frac{1}{8\pi}\int (\boldsymbol{E}(\boldsymbol{r},t)^2 + \boldsymbol{B}(\boldsymbol{r},t)^2) d^3r. \tag{5.3}$$

5.1.2 Electromagnetic Multipole Operators

The interaction of a nucleus with an electromagnetic field described by the relations of eq. (5.2) and eq. (5.3), can be formulated by the Hamiltonian[1]

$$\hat{H} = \hat{H}_{\text{nucl}} + \hat{H}_{\text{field}} + \hat{H}_{\text{inter}}. \tag{5.4}$$

For our case we assume that we "know" the nuclear Hamiltonian $\hat{H}_{\text{nucl}}$ and we also assume that we know its eigenfunctions. The Hamiltonian for the electromagnetic field $\hat{H}_{\text{field}}$ can be easily derived from eq. (5.3). Whereas the structure of the interaction Hamiltonian $\hat{H}_{\text{int}}$ is much more complicated and we refer to the many textbooks on nuclear physics covering that topic, such as [BW52, BG77, LC81, GM96, RS00, Ber07, Hey94]. The interaction Hamiltonian $\hat{H}_{\text{int}}$ can be written in terms of a scalar charge density ρ and a vector current density $\boldsymbol{j}$, the latter consisting of an *orbital* part stemming from the movement of the protons and a *spin* part originating from the spin distribution of the nucleus.

The derivation of the multipole operators is a lengthy and cumbersome task. We will only recapitulate some important results. The basic idea is to rewrite $\hat{H}_{\text{int}}$ in terms of multipole operators, i.e.

$$\hat{H}_{\text{int}} = \sum_{\text{L}m} a_{\text{L}m}\hat{Q}_{\text{L}m} + b_{\text{L}m}\hat{M}_{\text{L}m}. \tag{5.5}$$

The $a_{\text{L}m}$ and $b_{\text{L}m}$ are expansion parameters [RS00]. The operators in eq. (5.5) are defined as follows,

$$\hat{Q}_{\text{L}m} = \sum_{i=1}^{A} e(i) r_i^{\text{L}} Y_{\text{L}m}(\Omega_i) \tag{5.6}$$

$$\hat{M}_{\text{L}m} = \mu_N \sum_{i=1}^{A} \left\{ g_s^i \hat{s}_i + \frac{2}{\text{L}+1} g_l^i \hat{l}_i \right\} \cdot \left(\hat{\nabla} r^{\text{L}} Y_{\text{L}m}(\Omega)\right)_{r=r_i}. \tag{5.7}$$

Here $\hat{Q}$ stands for electric transitions and $\hat{M}$ for magnetic ones, $e(i)$ is the charge of the ith nucleon, $\hat{l}_i$ and $\hat{s}_i$ are the orbital and spin angular momenta of the ith nucleon. The *g-factors* or *gyromagnetic factors* are $g_s = 5.586$ for free protons, $g_s = -3.826$ for free neutrons, $g_l = 1$ for protons, and $g_l = 0$ for neutrons. Here we made also use of the very often used abbreviation

$$\mu_N = \frac{e\hbar}{2mc}, \tag{5.8}$$

usually called the *nuclear magneton.* The notation for the operators eq. (5.7) has been chosen in that

---

[1] It is important to note that the electromagnetic field does not only interact with the nucleons but also with the mesons that are continuously being emitted and absorbed. This leads to additional terms in the currents. The inclusion of this effect is comparatively small and we will neglect this here; for a discussion see for example [LC81].

way, since the expectation values of these operators are the electric or magnetic multipole moment of a specific state.

As a last note we should mention that the magnetic sub-states depicted by μ are degenerate and we can later sum over these as we do not care about polarisation effects.

5.1.3 Transition Probabilities

Regarding the electromagnetic transitions in nuclei, the most important point is that the nucleus and the electromagnetic field interact weakly, thus enabling us to use time-dependent perturbation theory, i.e. using *Fermi's golden rule* (see for example [CTDL99a, CTDL99b]),

$$\mathcal{T}_{fi} = \frac{2\pi}{\hbar} \left| \langle f \,|\, \hat{H}_{\text{int}} \,|\, i \rangle \right|^2 \; g(E_f), \tag{5.9}$$

with $\mathcal{T}$ being the transition probability and $g(E_f)$ being the state density at E_f. By evaluating eq. (5.9) with the help of eqs. (5.5) and (5.7) and introducing the so-called *long wavelength approximation*[1] we finally obtain after a longer calculation following [RS00],

$$\mathcal{T}_{fi}(\mathrm{XL}) = \frac{1}{2L+1} \sum_{m_i, m_f, m} \mathcal{T}_{fi}(\mathrm{XL}, m), \tag{5.10}$$

where we sum over the sub states depicted by m. The operators in eq. (5.7) are spherical tensor operators (see e.g. [RS00, Suh07]) to which we may apply the Wigner-Eckart theorem [Eck30, Wig31] (see also [CTDL99b, Suh07, GM96, RW10]).

This theorem allows us to decompose the matrix elements of a spherical tensor operator into a product of two factors: one factor (which is usually called the *reduced matrix element*) is independent of the angular momentum orientation, i.e. independent of m; the second factor is a Clebsch-Gordan coefficient in case of rotational symmetry. The advantage of this theorem is that it allows a fast calculation of many matrix elements.

The transition probability is now obtained by carrying out the sum,[2]

$$\mathcal{T}_{fi}(\mathrm{XL}) = \frac{8\pi(\mathrm{L}+1)}{\hbar \mathrm{L}((2\mathrm{L}+1)!!)^2} \left(\frac{E_\gamma}{\hbar c}\right)^{2\mathrm{L}+1} \left| \langle f \,|\, \hat{\mathcal{O}}_{\mathrm{XL}} \,|\, i \rangle \right|^2, \tag{5.11}$$

in which $\hat{\mathcal{O}}_{\mathrm{XL}}$ stands for the corresponding operator depicted by XL. By using the Wigner-Eckart theorem and the orthogonality relations of the coupling coefficients (following [RS00]), we obtain for the transition probability,

$$\mathcal{T}_{fi}(\mathrm{XL}) = \frac{8\pi(\mathrm{L}+1)}{\hbar \mathrm{L}((2\mathrm{L}+1)!!)^2} \left(\frac{E_\gamma}{\hbar c}\right)^{2\mathrm{L}+1} \; B(\mathrm{XL}, J_i \to J_f). \tag{5.12}$$

Here we have introduced the so-called *reduced transitions probabilities* $B(\mathrm{XL})$ which are given by,

$$B(E\mathrm{L}, J_i \to J_f) = \frac{1}{2J_i+1} \left| \langle f \,||\, \hat{Q}_{\mathrm{L}} \,||\, i \rangle \right|^2 \tag{5.13}$$

$$B(M\mathrm{L}, J_i \to J_f) = \frac{1}{2J_i+1} \left| \langle f \,||\, \hat{M}_{\mathrm{L}} \,||\, i \rangle \right|^2. \tag{5.14}$$

---

[1] The assumption is that the photon wavelength is large compared to the nuclear radius. Therefore, this assumption is valid for $E_\gamma \lesssim 10$ MeV.

[2] This is not as trivial as it looks and involves a lengthy calculation. See the literature for more details.

The matrix elements in eq. (5.14) are also called *reduced* matrix elements, because they do not contain any angular momentum information.

An important relation between the reduced transition probabilities can be derived from the principle of detailed balance (see also section 2.2.1.1). This principle connects the reduced transition probabilities by

$$(2J_i+1)B(\mathrm{XL}, i \to f) = (2J_f+1)B(\mathrm{XL}, f \to i). \tag{5.15}$$

Consequently, the probability for the absorption of a photon with energy E_γ on a state i with a certain type and multipolarity XL leading to the state f is proportional to the probability of the emission of a photon from state f with energy E_γ with type and multipolarity XL leading to state i. The proportionality factor is given by the $(2J+1)$ factors which take into account the degeneracy of the states. The principle of detailed balance is the mathematical consequence of the time-reversal symmetry in nuclear reactions, i.e. the a reaction may also occur in its backwards direction and the probabilities have to be connected.

5.1.4 Selection Rules

From the preceding section, we know that the matrix elements $\langle\, J_f m_f \,|\, \hat{\mathcal{O}}_{\mathrm{XL},m} \,|\, J_i m_i \,\rangle$ can be written (using the Wigner-Eckart theorem) as

$$\langle\, J_f m_f \,|\, \hat{\mathcal{O}}_{\mathrm{XL},m} \,|\, J_i m_i \,\rangle = \frac{\langle J_i m_i \mathrm{L} m | J_f m_f \rangle}{\sqrt{2J_f+1}} \langle\, J_f \,||\, \hat{\mathcal{O}}_{\mathrm{XL}} \,||\, J_i \,\rangle. \tag{5.16}$$

The structure of the Clebsch-Gordan coefficients $\langle J_i m_i \mathrm{L} m | J_f m_f \rangle$ gives us the general selection rules from the coupling of spins, i.e.

$$\begin{aligned} |J_i - J_f| \le \mathrm{L} \le J_i + J_f \\ m_f - m_i = m. \end{aligned} \tag{5.17}$$

The only exception to eq. (5.17) is the forbidden transition 0 → 0 because the photon has an internal angular momentum of 1.

In order to derive the selection rules for parity, we introduce the multipole moments of a state $|\,\Psi\,\rangle$ by

$$Q_\mathrm{L} = \langle\, \Psi \,|\, \hat{Q}_\mathrm{L} \,|\, \Psi \,\rangle \tag{5.18}$$
$$M_\mathrm{L} = \langle\, \Psi \,|\, \hat{M}_\mathrm{L} \,|\, \Psi \,\rangle. \tag{5.19}$$

Q_L is the electric multipole moment and M_L the magnetic moment. Therefore we skip the type symbol X for the next steps.

We know that the strong and the electromagnetic interactions conserve parity (see also 2), therefore we may choose $|\,\Psi\,\rangle$ to be an eigenstate of the parity operator $\hat{\Pi}$.

From eq. (5.7) we see that the electromagnetic operators have the following structure (due to readability we leave out the operator hat "^" here)

$$Q_\mathrm{L} \propto r^\mathrm{L} Y_\mathrm{L} \tag{5.20}$$
$$M_\mathrm{L}^l \propto \boldsymbol{l} \cdot \boldsymbol{\nabla}(r^\mathrm{L} Y_\mathrm{L}) \tag{5.21}$$
$$M_\mathrm{L}^s \propto \boldsymbol{s} \cdot \boldsymbol{\nabla}(r^\mathrm{L} Y_\mathrm{L}). \tag{5.22}$$

Here we divided the magnetic operator $\hat{M}_\mathrm{L}$ into two parts: the orbital part l and the spin part s. In order to examine how these operators change or conserve the parity, we simply need to have a look at the behaviour of the single components of the operators, e.g. the effect of the parity operator on the different parts.

The spherical harmonic Y_{L} has the parity $(-1)^{\mathrm{L}}$ while r^{L} has the parity $+1$. Hence the operator for the electric L-pole operator has the parity $(-1)^{\mathrm{L}}$. For the magnetic L-pole operator the situation is different: the vectors $\boldsymbol{l}$ and $\boldsymbol{s}$ are so-called axial vectors or pseudo-vectors[1], and therefore their parity is $+1$. The parity of the nabla operator $\boldsymbol{\nabla}$ is -1 and - as stated above - the parity of $r^{\mathrm{L}}Y_{\mathrm{L}\mu}$ is $(-1)^{\mathrm{L}}$. Consequently, the parity of the magnetic L-pole operator has a parity of $(-1)^{\mathrm{L}-1}$.

All in all, electric and magnetic transitions fulfil the same rules regarding the spin, but they differ regarding the parity, although the change in parity depends on the multipolarity. To sum it up, we finally have the following selection rules for electromagnetic transitions,

$$\begin{aligned} &|J_i - J_f| \leq \mathrm{L} \leq J_i + J_f \\ &\qquad \pi_i = (-1)^L \cdot \pi_f \quad \text{for electric transitions} \\ &\qquad \pi_i = (-1)^{L+1} \cdot \pi_f \quad \text{for magnetic transitions.} \end{aligned} \tag{5.23}$$

In table 5.1 we have summarised the change in parity for the most important transition types and multipolarities.

	L=1	L=2	L=3
magnetic	no	yes	no
electric	yes	no	yes

Table 5.1: Table showing the change in parity for magnetic and electric dipole, quadrupole, and octupole transitions.

From eq. (5.12) we see that the magnitude of the transition probability is sensitive to the photon energy E_γ and the reduced transition probability, which in turn depends on the type and multipolarity XL. In general, the reduced transition probabilities of electric transitions are larger than their magnetic counterpart for a fixed multipolarity L. Moreover, the larger the multipolarity, the smaller the transition probability. From this we may deduce a rough order of magnitude with E1 transitions being the dominant transitions, followed by M1 and E2 transitions which both can be of comparable magnitude [BG77, RS00]. M2 and E3 transitions are usually not considered any more in astrophysical reaction rate studies, unless states are involved that can only be connected via these transition types. It is important to note that these considerations are only true in the spirit of uniformly distributed parities and spins. In reality, shell-effects, especially at low energies, may favour certain spins and/or parities thus suppressing certain XL combinations.

5.2 Collective Phenomena

Collective phenomena in nuclei are excitations in which a large number of nucleons, or even all nucleons, participate. Generally these excitations occur at higher energies compared to the so-called single-particle excitations in which only one or a few nucleons are involved.

5.2.1 Giant Resonances

The giant resonances in nuclei are collective excitation modes involving all nucleons. The designation “giant” is due to the large magnitude of the resonance. As we have already implied with the section title, there exist several different giant resonances. Reviews about giant resonances can be found in [Sv81, Van87] or in the book of Bortignon *et al.* [BBB98] and Speth and Wambach [SW91].

---

[1] Pseudo-vectors are vectors that do not change their sign under a parity transformation. An example is the angular momentum vector $\boldsymbol{L} = \boldsymbol{r} \times \boldsymbol{p}$.

The first of this “group of resonances” to be discovered was the electric *Giant Dipole Resonance*: measurements revealed that the photoabsorption cross sections on various nuclei exhibited a very broad resonance structure at relatively high energies [SW91]; additionally it was found that the resonance energy, i.e. the maximum, scales with the mass number A. This was a first indication that these resonances are of collective nature.

It is possible to categorise the giant resonances according to the following specifications:

- multipolarity
- character, i.e. isovector or isoscalar

A schematic picture of collective resonances, their properties, and their qualitative collective origin can be found in fig. 5.1. It is important to emphasise that the collective modes shown in fig. 5.1 are all considered as “giant resonances”, i.e. they are large in amplitude/magnitude due to their collectivity, although several of the sketched resonances are not “giant” resonances in the original sense because the excitation probability for a particular mode is much smaller compared to other modes. In principle, the electric giant dipole resonance has the largest excitation probability, i.e. it dominates the photoabsorption cross section in the energy range where it is located. We will see later in section 5.2.2 that there can be other collective modes, which are “smaller” in the sense that their collective behaviour does not necessarily involve all nuclei and consequently these modes are observed (and predicted) at considerably smaller excitation energies.

The two columns on the left of fig. 5.1 represent electric resonances and the two columns on the right magnetic resonances. The strongest resonance is the isovector ($\varDelta T = 1$) electric ($\varDelta S = 0$) dipole (L=1) giant resonance. The *isovector* resonances are modes in which protons oscillate against the neutrons; vice versa in the *isoscalar* modes protons and neutrons oscillate in phase. For a given multipole mode, i.e. L fixed, the isovector modes are located at higher excitation energies as more energy (compared to the isoscalar mode) is needed to separate protons and neutrons [Van87]. The magnetic resonances with $\varDelta S = 1$ are called *spin-flip* resonances. In the isoscalar spin-flip resonance, the nucleons with spin up oscillate against the neutrons with spin down. The isovector spin-flip resonance is an oscillation of spin up neutrons against spin down protons and spin down neutrons against spin up protons. A very recent overview on the experimental and theoretical results on the magnetic dipole excitations can be found in [HvR10].

So far, we have only considered the modes in fig. 5.1 on a macroscopic collective level. On the microscopic level, these excitations can be viewed as complicated particle-hole excitations [Van87, BBB98].

5.2.2 Pygmy Dipole Resonance

The electric giant dipole resonance is usually dominating the photon-absorption cross section for energies up to 10-20 MeV (depending on the nucleus) since the energy-weighted Thomas-Reiche-Kuhn sum rule (see section 5.3.2.1) is usually exhausting the photoabsorption cross section by 80 to 90 % [GM96] (see also section 5.3.2.1).

However, in the past years additional low-lying E1 strength was found at energies notably below the giant dipole resonances, see for example [AKF^{+}05, EvE^{+}03, ELS^{+}10, KPA^{+}07, KPZ06, ÖEv^{+}07, WBC^{+}09], in particular in nuclei with notable neutron excess. The currently most favoured explanation is to describe this additional low-lying strength as a collective mode in which a skin of neutron oscillates against a core of protons and neutrons - a schematic picture of this motion can be seen in fig. 5.2. Such a collective mode has been named a *pygmy* resonance. However, it is not clear yet, if the experimentally observed additional strength is really resulting from such a collective excitation. Nevertheless, the fact that this additional E1 strength can be found at energies far below the giant dipole resonance might affect radiative capture cross section calculations for stellar nucleosynthesis [LLL^{+}09, Gor98]. We will address this issue in section 7.2.

The question of the origin of this low-lying strength is currently subject to the theoretical modelling, as it is experimentally not possible yet to observe the nature of this strength. General overviews about the theoretical description of pygmy dipole resonances within the random-phase approximation can be found in [KS09, AK09] (short overviews) and [PVKC07] (extensive overview). For an introduction to experimental possibilities see [KPZ06].

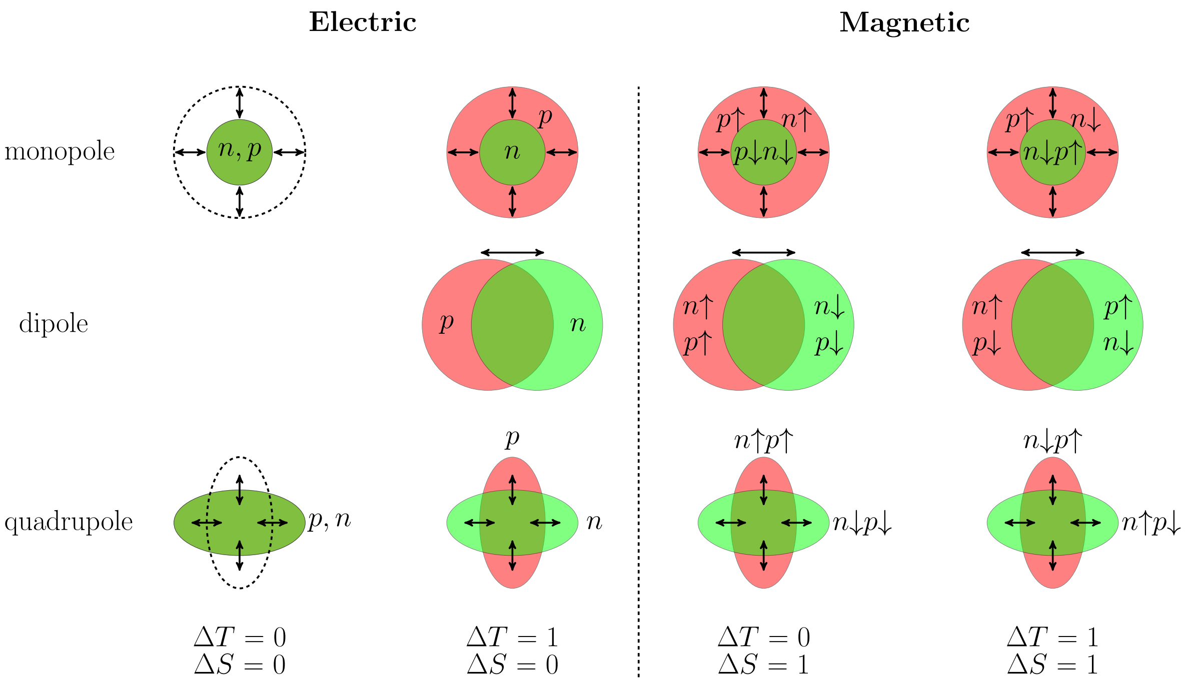

Figure 5.1: Schematic diagram showing the different giant resonances for L=0 (monopole), L=1 (dipole), and L=2 (quadrupole) modes as well as the dependency on isoscalar and isovector character; inspired by [Van87]. See section 5.2.1 for further explanations.

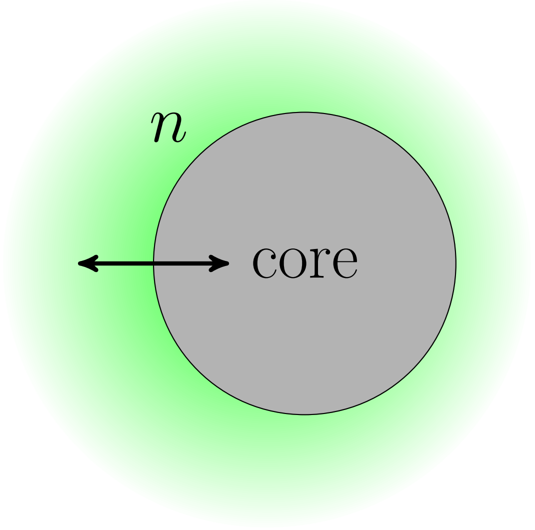

Figure 5.2: Schematic picture of the pygmy dipole resonance: the neutron "skin" of a nucleus with large neutron-excess oscillates against a core consisting of protons and neutrons.

A very prominent example for a nucleus that may possibly exhibit such a pygmy dipole resonance is ^{208}Pb. Several recent experiments show a pronounced strength at low energies in this nucleus [RHK$^+$02, EvE$^+$03, SMB$^+$10].

The phenomenon of a pygmy dipole resonance is not necessarily restricted to a neutron skin - a proton skin could evoke similar behaviour. A candidate for a proton pygmy resonance is ^{100}Sn according to [TL08].

5.2.3 Spin-Flip Resonance

The spin-flip resonance belongs to the magnetic transition types. The magnetic dipole operator can be written as (see also eq. (5.7)) [HvR10],

$$\hat{M}(\mathrm{M1}) = \sqrt{\frac{3}{4\pi}} \sum_i \left[g_s^i \hat{s}_i + g_l^i \hat{l}_i \right] \mu_N \tag{5.24}$$

with the orbital and spin g-factors for neutrons and protons. It is possible to split $\hat{M}(\mathrm{M1})$ into an isoscalar and an isovector term as follows (see also fig. 5.1),

$$\hat{M}(\mathrm{M1}) = \underbrace{\sqrt{\frac{3}{4\pi}} (g_J \hat{J} + g_S \hat{S}) \mu_N}_{\hat{M}(\mathrm{M1,isoscalar})} + \hat{M}(\mathrm{M1,isovector}). \tag{5.25}$$

The first part of the isoscalar part depends on the angular momentum operator $\hat{J}$ and does not induce any M1 transitions. The second part depends on $g_S = \frac{g_s^p + g_s^n - 1}{2}$ which becomes small due to the g-factors nearly cancelling each other. The isovector part of eq. (5.25) can be written as [HvR10],

$$\hat{M}(\mathrm{M1,isovector}) = \sqrt{\frac{4}{4\pi}} \left[\frac{1}{2} \left(\hat{L}_p - \hat{L}_n \right) + \frac{1}{2} (g_s^p - g_s^n) \left(\hat{S}_p - \hat{S}_n \right) \right] \mu_N . \tag{5.26}$$

The first part describes the relative angular momentum between protons and neutrons; this part is responsible for the so-called scissors mode, which we will discuss in section 5.2.4. The second part is the spin-flip part and it is the $\Delta T_z = 0$ part of the Gamow-Teller operator. This term is usually relatively large (compared to the other terms) because the g-factors sum up (see section 5.1.2).

It has been empirically found [FWR+90, Ric95] that the centroid of the spin-flip resonance is located at roughly $E_0 = 41 A^{-1/3}$, thus exhibiting a shell model like energy dependence.

The fact that the spin part of the isovector M1 component is related to the Gamow-Teller operator plays an important part in nuclear astrophysics because the neutrino-nucleus cross sections needed in supernova models are dominated by Gamow-Teller transitions [LMP03].

5.2.4 Scissors Mode

The *scissors* mode is considered to be - like the pygmy dipole resonance - a collective mode occurring at low energies but only in deformed nuclei. It has found first experimental verification as additional strength below the spin-flip resonance [FWR+90, HvR10, Ric95, Ric04]. The schematic picture of the scissors mode is that the neutrons and protons in a deformed nucleus oscillate against each other, similar to the movement of scissors (see fig. 5.3). Microscopically this mode can be related to the orbital part of the M1 operator in section 5.1.2 and eq. (5.24). The fact that a scissors mode might induce additional strength at low-energies can also become important for radiative capture reactions (see section 7.3).

It has been shown in [EvRR05] that the total strength of the scissors mode can be parametrised with a sum rule approach and that this strength depends on the deformation of the nucleus. For the spin-flip resonance, there are no model independent sum rule approaches existing, yet.

For exotic neutron-rich nuclei another possible type of “scissors mode” is proposed: in deformed neutron-rich nuclei, the neutron skin might oscillate around a deformed core. This is slightly similar to the pygmy resonance (see section 5.2.2). This mode would probably be located even below a possible scissors mode because less nucleons are involved in the collective movement. However, it is an open question if such a mode really exists.

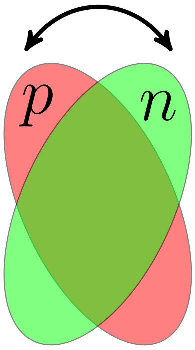

Figure 5.3: Schematic picture of the magnetic scissors mode: two deformed cores consisting of either protons or neutrons oscillate in a scissors-like motion against each other.

5.3 Radiative Strength Functions

As we have seen in the previous sections sections 5.1 and 5.2 about electromagnetic transitions in nuclei, these transitions can be classified according to their type and multipolarity. In chapter 2 we have already discussed average reduced widths giving decay probabilities and their relation to the transmission coefficient.

The radiative strength function formalism is a statistical description of the distribution of the average reduced radiative width. It is important to emphasise that this distribution depends on photon energy and is usually categorised according to the transition's type and multipolarity. The type and multipolarity we will abbreviate by the term "XL", with "X" depicting the type (magnetic or electric) and "L" depicting the multipolarity. An introduction regarding radiative strength functions can be found in [BEF+73]; for a more recent overview see [KB08]. An overview about different analytical approaches can be found in [KU90, PKK+08] and an excellent overview regarding the practical applications and methods of calculation can be found in [BBC+06, chap. 7].

5.3.1 Definition of Radiative Strength Functions

The photon strength function, radiative strength function, or gamma strength function f_{XL} is defined by the average value of partial radiation width $\overline{\varGamma}^{\gamma}_{ab}$ for the γ-decay from an initial level a with the quantum numbers (E_a,J_a,π_a) to a final level b with the quantum numbers (E_b,J_b,π_b). This can be written as,

$$\overline{\varGamma}^{\gamma}_{ab}(\mathrm{XL}) = \frac{f_{\mathrm{XL}}(E_\gamma)E_\gamma^{2L+1}}{\rho(E_a,J_a,\pi_a)} \tag{5.27}$$

with ρ being the level density. From reaction theory we know (see also section 2.2.1) that the relation between a decay-width $\varGamma$ and the transmission coefficient is given by $T = \frac{2\pi}{D}\varGamma$. Therefore the γ-transmission coefficient is given by,

$$T^{\gamma}_{ab}(\mathrm{XL}) = \frac{2\pi}{D(E_a,J_a,\pi_a)}\overline{\varGamma}^{\gamma}_{ab}(\mathrm{XL}) = 2\pi \cdot f_{\mathrm{XL}} \cdot E_\gamma^{2L+1}. \tag{5.28}$$

In reaction calculations we are usually not interested in the specific initial and final states a and b (this is a consequence of Brink's hypothesis, see section 5.3.1.2). Thus we rewrite eq. (5.28) as,

$$T^{\gamma}_{\mathrm{XL}}(E_\gamma) = 2\pi \cdot f_{\mathrm{XL}}(E_\gamma) \cdot E_\gamma^{2L+1}. \tag{5.29}$$

5.3.1.1 Absorption & Decay Strength Functions

Quantum-mechanically we have to differentiate between the capture of a photon and the emission of a photon as we change the spin of the nucleus. The reduced matrix elements have to fulfil the principle of detailed balance, i.e.

$$(2J_i + 1)B(\mathrm{XL},i \rightarrow f) = (2J_f + 1)B(\mathrm{XL},f \rightarrow i). \tag{5.30}$$

For the radiative strength function this would be much more complicated as the strength function is the statistical distribution of the reduced matrix elements with respect to the energy. Equation (5.30) is generally true and the states i and f can be arbitrarily chosen. Unfortunately, we usually do not have all needed reduced matrix elements $B(\mathrm{XL})$ available as we only have the reduced matrix elements for the absorption of a photon on the ground state (because we make use of Brink's hypothesis). Hence we will have to differentiate between strength functions describing the **absorption** and strength functions describing the **emission** of a photon:

- $\overrightarrow{f}$ for absorption
- $\overleftarrow{f}$ for emission

According to [BEF+73, BBC+06] these two strength functions can be written as

$$\overrightarrow{f}_{\mathrm{XL}} = \frac{E_\gamma^{-2L+1}}{(\pi\hbar c)^2} \frac{\langle\, \sigma_{\mathrm{XL}} \,\rangle}{2L+1} \tag{5.31}$$

$$\overleftarrow{f}_{\mathrm{XL}} = E_\gamma^{-(2L+1)} \frac{\langle\, \mathit{\Gamma}_{\mathrm{XL}} \,\rangle}{D}, \tag{5.32}$$

with $\langle\, \sigma_{\mathrm{XL}} \,\rangle$ being the average photoabsorption cross section and $\langle\, \mathit{\Gamma}_{\mathrm{XL}} \,\rangle$ the average decay width for the transition and multipolarity XL.

5.3.1.2 Brink's Hypothesis

The so-called *Brink's hypothesis* [Bri55, Axe62] is a often used assumption for the description of γ-transitions in nuclear reactions modelled with the Hauser-Feshbach formalism. The main assumption is that the radiative strength distribution does not change considerably with excitation energy, i.e. the absorption radiative strength function built on an excited state can be approximated by the absorption strength function built on the ground state. Regarding the definitions in the previous section, assuming the validity of Brink's hypothesis is equivalent to setting $\overrightarrow{f} = \overleftarrow{f}$.

Brink's hypothesis was initially derived for highly collective phenomena, in particular giant resonances. Its adoption to the complete energy range of γ-transitions in a reaction was introduced because methods that could globally describe the radiative transitions were not available. Experiments have shown that the hypothesis is fulfilled in good approximation for the giant dipole resonance region (see [ST07] and references therein).

In case of r-process nucleosynthesis, we generally operate in energy regions far below the giant resonance region. Brink's hypothesis is therefore questionable, especially for very low transition energies. Hence, many different models which modify the Lorentzian form factor by improving the low energy description have been developed so far [MSC81, KU90, PKK+08] - see [BBC+06] for an overview.

5.3.2 Electric Dipole Transitions

The electric dipole transitions, or E1 transitions, are usually dominating the γ-channel (see section 5.1.4). The most important mechanism is the electric giant dipole resonance. This resonance can be parametrised with a Lorentzian form factor. Therefore the standard approach on describing the E1 strength function is based upon a parametrisation of the resonance with one, two, or three Lorentzians[1] corresponding to the oscillation modes along a certain axis.

A problem within this approach is the low-energy tail, as the resonance is far above the relevant threshold in r-process reactions. Hence we have to rely on an extrapolation to low energies. It is obvious from experimental data that this is not a good approximation for low energies. Unfortunately, the γ-energy region up to 8 MeV is the relevant energy region in case of (n,γ)-reactions on stable nuclei and for r-process nuclei this region is only up to 3-5 MeV. Therefore a variety of different analytical approaches have been developed that try to solve this issue and to give more reliable results for low energies [KU90, PKB$^+$06, PKK$^+$08]. Nevertheless, none of these models can universally describe the E1 strength as pointed out in [KB08].

At the same time, these models also tackle the problem of the Brink hypothesis by introducing a temperature description of the final state and therefore distinguishing between the upward strength function and the downward strength function. However, none of these models can account for low-lying collective strength.

5.3.2.1 Thomas-Reiche-Kuhn Sum Rule

The Thomas-Reiche-Kuhn sum rule for E1 transitions is a nice example for the application of sum rules in nuclear physics. Sum rules for electromagnetic transitions in nuclei are classified to their order n which defines the power of the energy in the following basic definition[2] [Are79],

$$\varSigma^n_{\mathrm{XL}} = \int\limits_0^\infty E^n_\gamma \sigma_{\mathrm{XL}}(E_\gamma)\; dE_\gamma. \tag{5.34}$$

Note that this definition requires the integral in eq. (5.34) to exist. The observable $\varSigma^0_{\mathrm{E1}}$ is the so-called Thomas-Reiche-Kuhn sum rule. In the context of radiative strength functions one often speaks of the *energy-weighted* sum rule. This is not in conflict with the order $n = 0$ mentioned here, as $\sigma(E_\gamma) \propto E_\gamma \cdot f(E_\gamma)$. A derivation of the sum rule can be found for example in [GM96, Ber07]. In general, the Thomas-Reiche-Kuhn sum rule for the photoabsorption cross section gives,

$$\int \sigma_{\mathrm{E1}}\; dE_\gamma = \frac{2\pi^2 e^2 \hbar c}{mc^2}\frac{NZ}{A}. \tag{5.35}$$

If we assume a Lorentzian shape $L(x,\varGamma,E_0)$ for the cross section, i.e.

$$\sigma_{\mathrm{E1}} = \sigma_0 \frac{\varGamma^2 E^2_\gamma}{(E^2_0 - E^2_\gamma)^2 + \varGamma^2 E^2_\gamma} = E_\gamma \sigma_0 \cdot L(E_\gamma,\varGamma,E_0), \tag{5.36}$$

and make use of

$$\int x \cdot L(x)\; dx = \varGamma \cdot \frac{\pi}{2}, \tag{5.37}$$

---

[1] One Lorentzian for spherical nuclei, two for deformed axially symmetric nuclei, and three for triaxial nuclei.

[2] It is also possible to define the sum rule on the basis of reduced matrix elements B(XL) [VPRL01], i.e.

$$m = \sum_i B(\mathrm{XL}; i \to f) E^{i \to f}_\gamma \tag{5.33}$$

we obtain for the strength function by combining eq. (5.31) with eqs. (5.35) to (5.37),

$$\int \overrightarrow{f}_{\mathrm{E1}} E_\gamma \, dE_\gamma = \frac{9}{4\pi} \frac{(\hbar c)^2}{2mc^2} e^2 \frac{NZ}{A}. \tag{5.38}$$

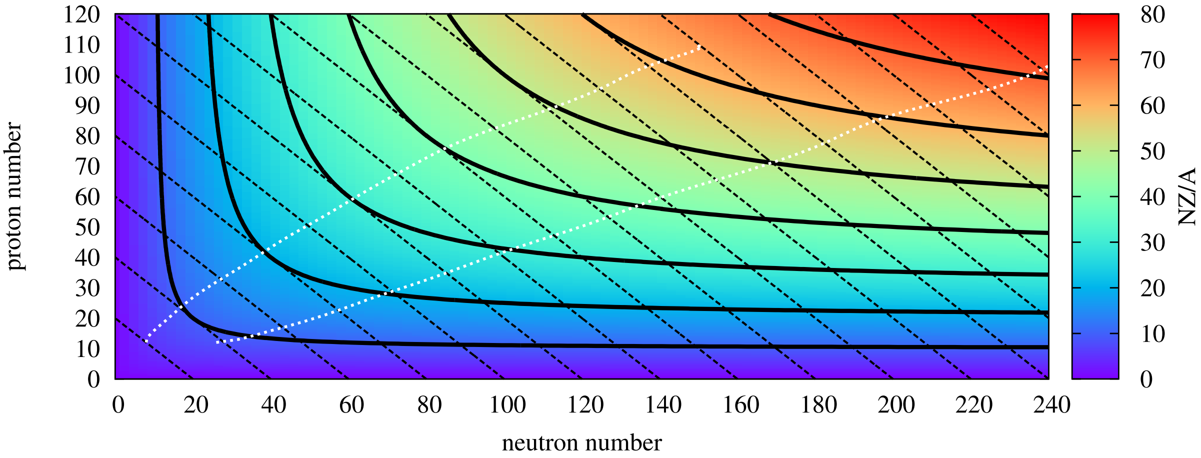

Figure 5.4: Overview plot of the function NZ/A in eq. (5.38). The thick lines correspond to values of NZ/A equal to 10,20, et cetera, the dashed lines correspond to values of constant A, i.e. 20,40,60, et cetera, and the white lines roughly define the drip lines given by the HFB14 mass model [GSP07].

In eq. (5.38) we see that the Thomas-Reiche-Kuhn sum rule, which gives an approximation to the integrated strength, only depends on the neutron and proton number of the nucleus. In fig. 5.4 we have plotted the function NZ/A and note that the E1 strength increases the heavier a nucleus becomes. Interestingly, we see the largest increase for nuclei with N $\approx$ Z. In that simple picture we would expect that N=Z nuclei would show the largest (n,γ)-rates for fixed A. However, for the even-even N=Z nuclei we have to take isospin selection rules into account [RT00, RT01, RW10], lowering the dipole strength considerably and thus negating the increased total strength.

Regarding the r-process, we can see that the total E1 strength increases with neutron number for a fixed proton number as expected. It is important to note, that this only affects the total strength. In the end we have to distribute the total strength with a Lorentzian depending on the width Γ and the centroid E_0 of the resonance. Due to the nature of the Lorentzian distribution, its low-energy tail - which is interesting for r-process - is much more affected by these parameters than by the total strength.

As we have already mentioned before in section 5.2.2, the Thomas-Reiche-Kuhn sum rule exhausts the photoabsorption cross section by about $\approx$80% disregarding other types of transitions at this point. This results from an approximation made in deriving the Thomas-Reiche-Kuhn sum rule in [GM96]: the approximation that the nuclear Hamiltonian does not contain non-local terms, i.e. velocity/momentum-dependent terms.If these effects are taken into account, the sum rule becomes larger. One usually accounts for this fact by multiplying the total strength by a factor 1.1 - 1.4 [LS89].

5.3.2.2 Lorentzian Strength Functions for E1 Transitions

In principle, the most simple way to obtain the E1 strength function would be within the single particle model for which the reduced matrix elements $B(E1)$ are constant and only depending on the number of nucleons [BW52, RS00, GM96] - the values are usually called *Weisskopf estimates* as they approximately give the relative magnitude between electric and magnetic transitions. However, it is important to note, that the Weisskopf estimates are too small for electric and too large for magnetic transitions [RS00].

A more realistic method than the single-particle approach is to parametrise the giant dipole resonance with a Lorentzian function. The normalisation has to come from the energy-weighted Thomas-Reiche-Kuhn sum rule. In principle, there exist slightly different "notations" which distinguish themselves only by constants, i.e. the relations between the strength function, the photoabsorption cross section and the transmission coefficient.

The usual and by far most common relation is the following,

$$f_{\mathrm{E1}} = \frac{1}{3\pi^2(\hbar c)^2} \cdot \frac{1}{E_\gamma}\sigma_{\mathrm{E1}} = \frac{4}{3\pi}\frac{e^2}{\hbar c}\frac{1}{mc^2}\frac{NZ}{A}\frac{\varGamma E_\gamma}{(E_0^2 - E_\gamma^2)^2 + (\varGamma E_\gamma)^2}. \tag{5.39}$$

For the last step we used the results of section 5.3.2.1 and together with

$$T_{\mathrm{E1}}(E_\gamma) = 2\pi \cdot f_{\mathrm{E1}} \cdot E_\gamma^3, \tag{5.40}$$

we obtain the γ-Transmission coefficient for the strength function of eq. (5.39) (see also [HWFZ76, CTT91, RTK97, RT00, LLL$^+$09]). We should note here, that in this approach the upward and the downward strength functions are exactly the same, i.e. $\overrightarrow{f} = \overleftarrow{f}$.

An alternative strength function that will be used later in this thesis is given by,

$$f'_{\mathrm{E1}} = \frac{9\hbar c}{16\pi^3} \cdot \frac{1}{E_\gamma}\sigma_{\mathrm{E1}}, \tag{5.41}$$

resulting in a slightly different relation between strength function and transmission coefficient:

$$T_{\mathrm{E1}}(E_\gamma) = \frac{32\pi^2}{27}\frac{E_\gamma^3}{(\hbar c)^3} f'_{\mathrm{E1}}. \tag{5.42}$$

If the strength function is modelled by a Lorentzian, we usually multiply the function by a factor of 1.1 - 1.4 to account for effects not considered by the Thomas-Reiche-Kuhn sum rule, as we have noted at the end of section 5.3.2.1.

5.3.2.3 Deformed Nuclei

In deformed nuclei a splitting of the resonance occurs depending on the type of deformation. In spherical symmetry, no definite axis of symmetry exists and we may arbitrarily chose a direction and thus have the same oscillation regarding all directions because of the symmetry. In axially symmetric deformed nuclei we can define the axis of symmetry and have therefore two modes of oscillation, i.e. one along the symmetry axis and one perpendicular, and would need two Lorentzians for the fit, i.e.

$$\sigma(E_\gamma)_{\mathrm{axial}} \propto \sum_{i=1}^{2} \frac{i}{3}\frac{\varGamma_i E_\gamma}{(E_{0,i}^2 - E_\gamma^2)^2 + (E_\gamma^2 \varGamma_i^2)}, \tag{5.43}$$

with $i = 1$ being the oscillation along the symmetry axis.

In the rare case of a triaxial nucleus we would have three modes, i.e. we would need three Lorentzians to conveniently describe the photo absorption cross section, i.e.

$$\sigma(E_\gamma)_{\mathrm{triaxial}} \propto \sum_{i=1}^{3} \frac{1}{3}\frac{\varGamma_i E_\gamma}{(E_{0,i}^2 - E_\gamma^2)^2 + (E_\gamma^2 \varGamma_i^2)}. \tag{5.44}$$

5.3.2.4 GDR Parameters

The parameters ($\varGamma$,E_0) of the giant dipole resonance (GDR) can be obtained in two different ways: for experimentally feasible nuclei they can be obtained from a fit to the photoabsorption cross section and for exotic nuclei we have to rely on theoretical predictions. The fit to experimental data can become problematic when the nucleus is deformed as the resulting splitting into two or even three resonances that overlap could be interpreted as one resonance with a very broad width $\varGamma$.

There exists a large number of models and approaches describing the GDR parameters. Most of these are essentially based upon a liquid drop picture of the nucleus. Historically, the first models were the Steinwedel-Jensen model, in which the nucleus is an ideal two-component fluid and the GDR is assumed to be an acoustic mode of density oscillations in which it is assumed that the fluids are compressible but the combined fluid is not, and the Goldhaber-Teller model in which incompressible neutron and proton spheres oscillate against each other. The Steinwedel-Jensen model scales the centroid energy E_0 with $A^{-1/3}$ while the Goldhaber-Teller scales it with $A^{-1/6}$. Phenomenologically, the centroid energies can be predicted reasonably well for spherical nuclei by a combination of the Goldhaber-Teller and Steinwedel-Jensen models (see for example [BBC$^+$06]). For deformed nuclei, the predictions become less good, however one can still obtain satisfying results by implying a certain deformation (see [BBC$^+$06]).

The situation changes for the width Γ as this quantity is less easy to parametrise. In principle there exist different ansatzes how to phenomenologically parametrise the width, for example by surface effects on the nuclear drop. We will postpone this discussion to chapter 7 where we will shortly stress the origins of the parameters used in this thesis.

5.3.3 Magnetic Dipole Transitions

The magnetic dipole transitions are usually much smaller in magnitude compared to the electric dipole transitions. However, they do not change the parity (E1 transitions do change the parity) and therefore, these transitions - together with parity conserving E2 transitions (see section 5.3.4) - may dominate for low E_γ.[1] For r-process nuclei, the maximum E_γ is slightly above the neutron separation energy, i.e. S_n =2-5 MeV[2], and M1 transitions could compete with E1 transitions. A very recent and extensive review on the physics of magnetic dipole excitations in nuclei is given by [HvR10].

In theoretical nuclear reaction models that need to be applicable over the whole nuclear chart, the M1 transitions are mostly described by their single-particle strength or a phenomenological Lorentzian representing the spin-flip resonance. The single-particle strength function is a broad approximation, giving a constant strength. For reaction rate calculations, one has used the following formula for the M1 transmission coefficient [HWFZ76][3],

$$T^{\mathrm{sp}}_{\mathrm{M1}}(E_\gamma) = 15\pi \left(\frac{e^2}{\hbar c}\right)\left(\frac{1}{m_p^2 c^4}\right)\kappa_M E_\gamma^3, \tag{5.45}$$

with m_p being the proton mass and $\kappa_M = 0.05$ being a correction factor. This correction factor tries to compensate the overestimation of the M1 strength in the single-particle model. The corresponding strength function we obtain from eq. (5.29) thus having,

$$f^{\mathrm{sp}}_{\mathrm{M1}}(E_\gamma) = \frac{15}{2}\left(\frac{e^2}{\hbar c}\right)\left(\frac{1}{m_p^2 c^4}\right)\kappa_M. \tag{5.46}$$

Here a problem with eq. (5.45) becomes obvious as this has the unit MeV when assuming κ_M dimensionless.

Alternatively, we may describe the M1 transitions with a Lorentzian that represents the spin-flip resonance. In section 5.2.3 we have already discussed that there is a phenomenological dependence of the centroid E_0 of the spin-flip resonance with A. By assuming a constant width Γ, we can describe the M1 strength function according to [BBC$^+$06] with,

$$E_0 = 41 \cdot A^{-1/3}\ \mathrm{MeV} \qquad \Gamma = 4\ \mathrm{MeV}. \tag{5.47}$$

---

[1] For low energies, both parities are not uniformly distributed. In magic and near magic nuclei, the energy of equipartition of both parities may even lie above the relevant particle threshold[LLMP$^+$08].

[2] The kinetic energy of the neutron can be neglected, as the temperature is usually not high enough. The relevant neutron energies for a plasma with T=10^9K (the typical r-process temperature) are in the region of 10-100 keV.

[3] The formula (17) in that paper is not fully correct as it contains hc instead of $\hbar c$. The numerical value is correctly calculated with $\hbar c$

The last missing parameter is the total strength. We obtain this quantity by parametrising the M1 strength at 7 MeV by [KU95, BBC⁺06],

$$f_{\mathrm{M1}}^{\mathrm{Lor}}(7\ \mathrm{MeV}) = 1.58 \cdot 10^{-}9 \cdot A^{0.47 \pm 0.21}\ \mathrm{MeV}^{-3}. \tag{5.48}$$

As we can see, this parametrisation has a large uncertainty. The fitted nuclei were nuclei with neutron separation energies between 6-7 MeV. Additionally, there is an uncertainty factor of 3 related to the strength. Despite all these uncertainties, the different energy dependence of $f_{\mathrm{M1}}^{\mathrm{Lor}}(E_\gamma)$ compared to $f_{\mathrm{M1}}^{\mathrm{sp}}(E_\gamma)$ can change the (n,γ) cross section notably. Especially at low energies, the single-particle approach might drastically overestimate the M1 strength. However, even with the Lorentzian approach to the M1 strength, we are not able to include low-energy M1 strength from a possible scissors mode or other origins.

In order to tackle this insufficiency, we may use the nuclear shell model (see section 4.3). This model gives us the reduced transitions probabilities $B(\mathrm{M1})$. These we fold with Gaussians to obtain a continuous function, which we call $\varPhi_{\mathrm{M1}}^{\mathrm{M1}}$ (see section 7.3.1). The advantages of the shell model are that we can calculate the strength function not only for the ground state but also for excited states and we can treat odd-nuclei equivalently. The major disadvantage is the restricted model space that does not allow us to calculate a large region of nuclei and, depending on the nucleus, gives only reasonable results up to several MeV. For higher energies, we would need a larger valence space, thus drastically increasing the dimensionality of the problem.

So far, we have only discussed the spin-flip resonance in this section. It is a general issue that the integrated (total) strength of the M1 resonance cannot be so easily calculated compared to the E1 case; for the latter we have seen that the energy-weighted Thomas-Reiche-Kuhn sum rule gives a very good approximation (see section 5.3.2.1). We can define sum rules for M1 transitions, however these are generally model dependent, thus making comparisons difficult [HvR10, LS89]. Interestingly, the situation is slightly better for the scissors mode, i.e. the orbital M1 strength. It was shown by Enders *et al.* [EvRR05] that it is possible to obtain a parameter free description of the orbital strength.

5.3.4 Quadrupole Transitions

Although we will not regard quadrupole transitions or transitions of higher multipolarity in this thesis, we will shortly discuss these, as there is a particular problem for the most common parametrisations used for nuclear reaction calculations. We will discuss this issue in section 5.3.4.1.

According to [BBC⁺06], the E2 strength function tries to parametrise the isoscalar giant resonance mode (a $0\hbar\omega$ mode). The isovector mode is located a much higher energies (it is a $2\hbar\omega$ mode) and therefore not relevant for most nuclear astrophysical reactions. The parameters are as follows,

$$E_0 = 65 \cdot A^{-1/3}\ \mathrm{MeV} \tag{5.49}$$

$$\varGamma = 6.11 - 0.021 \cdot A\ \mathrm{MeV} \tag{5.50}$$

$$\sigma_0 = 0.00014 \cdot Z^2 \cdot \frac{E_0}{A^{1/3}\varGamma}\ \mathrm{mb}. \tag{5.51}$$

Experimentally, the total E2 strength still gives rise to several questions [EKvP07] because the energy-weighted sum rule for E2 transitions is more exhausted in doubly magic nuclei compared to semi magic nuclei.

The M2 transitions can be either modelled in the single-particle picture (see for example [RS00]) or in the Lorentzian picture of section 5.3.3 by multiplying the M1 strength function with 0.0008 [BBC⁺06].

5.3.4.1 Problem of the Lorentzian Prescription for $L \geq 2$

From the experimental point of view, we can parametrise resonances like the Giant Dipole Resonance (E1) or the Giant Quadrupole Resonance (E2) with a Lorentzian. As already discussed, the analytic form of a Lorentzian form factor is the following:

$$L(E_\gamma) \propto \frac{E_\gamma^2\ \Gamma^2}{(E_\gamma^2 - E_0^2)^2 + E_\gamma^2\ \Gamma^2}. \tag{5.52}$$

Moreover, the general relation between the gamma-strength function f_{XL} and the corresponding cross section is given by

$$f_{\mathrm{XL}}(E_\gamma) = \frac{1}{2L+1}\ \frac{\sigma_{\mathrm{XL}}}{(\pi\hbar c)^2}\ E_\gamma^{-2L+1} \tag{5.53}$$

with E_γ being the gamma energy and the according transmission coefficient T_{XL} is given by

$$T_{\mathrm{XL}}(E_\gamma) = 2\pi\ f_{\mathrm{XL}}(E_\gamma)\ E_\gamma^{(2L+1)}. \tag{5.54}$$

If we now go small transition energies, i.e. $E \rightarrow 0$, the functional form of eq. (5.52) becomes proportional to E_γ^2. By combining this with the energy dependencies of the strength function and the transmission coefficient, we obtain,

$$T_{\mathrm{XL}} \xrightarrow{E_\gamma \rightarrow 0} T_{\mathrm{XL}} \propto E_\gamma^2 \cdot E_\gamma^{-2L+1} \cdot E_\gamma^{2L+1} = E_\gamma^4. \tag{5.55}$$

We see that for small E_γ the transmission coefficient has a dependency of E_γ^4 for every multipolarity. This shows the problem in describing the strength function with a Lorentzian independent of the involved multipolarity. If we go back one step to the strength function we can see that - again for $E_\gamma \rightarrow 0$ - the strength function diverges at $E_\gamma = 0$ for any multipolarity $L > 1$:

$$f_{\mathrm{XL}}(E_\gamma) \propto T_{\mathrm{XL}}(E_\gamma) E_\gamma^{-2L-1} \propto \frac{E_\gamma^4}{E_\gamma^{2L+1}} = 1/E_\gamma^{2L-3}. \tag{5.56}$$

Therefore, the approach to use the analytical form (or energy dependence) of a Lorentzian is questionable in the context of the strength function formalism for transitions with multipolarity $L \geq 2$.

6

Fission

The phenomenon of *fission* was discovered in 1939 by Hahn and Straßmann: they bombarded uranium with neutrons and observed barium as a product. By comparing the proton numbers of uranium (Z=92) and barium (Z=56), Hahn and Straßmann realised that the uranium nucleus must have been ruptured in two nuclei of lower mass and proton number. The process in which a nucleus separates into two fragments of considerably smaller masses is called fission.

The first model used to describe the nuclear fission process was based upon the liquid-drop model [BW39]. One assumes that the neutron excites oscillations in the nucleus (the drop). The amplitudes of these oscillations are so large that the drop disrupts into two parts of roughly similar size. We will later define two different modes of fission, the symmetric and the asymmetric fission (see section 6.3), the latter leading to products of rather different mass. The process of fission releases a lot of energy and usually several neutrons. These neutrons can be absorbed by other nuclei which then may undergo fission too. The resulting chain reaction can be controlled to produce energy as it is done in contemporary nuclear power plants.

The mode of fission found by Hahn and Straßmann is called an *neutron-induced* fission since a neutron[1] is captured to excite the nucleus, a compound nucleus is formed and the probability to fission is strongly increased because of the large excitation. Alternatively, it is also possible that a nucleus fissions without being excited. This is called *spontaneous* fission. Spontaneous fission becomes important as decay mode for heavy and especially super-heavy nuclei where it may compete with α-decay.

An overview about the nuclear fission process can be found in many textbooks, in particular those regarding basic nuclear physics such as [Ber07] as well as specific books dedicated to the topics, e.g. [VH73, W$^+$91], or review articles, e.g. [BL80, MPMZ$^+$07, SR07]. Two short and recent historical overviews are given by [Świ09] and [Möl10], the first giving an account of some interesting anecdotes, the latter focusing on the liquid-drop approach (see section 6.2) from the early 1950s and 1960s up to now. A survey on the practical issues in reaction calculations can be found in [BBC$^+$06, chap. 8].

---

[1] The are also other induced fission types, see chapter 1.

6.1 Static Description of Deformation

We may describe the surface of a nucleus in terms of spherical harmonics depending on the angles $\mathit{\Omega} = (\mathit{\Theta},\mathit{\Phi})$ (see e.g. [VH73, RS00, GM96]), i.e.

$$R(\mathit{\Omega}) = R_0 \left(1 + \sum_{\lambda=0}^{\infty} \sum_{\mu=-\lambda}^{\lambda} \alpha_{\lambda\mu} Y_{\lambda\mu}(\mathit{\Omega})\right). \tag{6.1}$$

Here R_0 is the nuclear radius for the spherical case. The coefficients $\alpha_{\lambda\mu}$ give the strength of a particular deformation with λ being the multipole parameter[1]. The multipole parameters λ define different forms of deformation the nucleus can have. We can easily see from eq. (6.1) that the dipole term (λ=1) describes only a shift of the complete nucleus in the coordinate system, hence we shall disregard it from now on. Moreover, we will also disregard the octupole term (λ=3) at this point.

The process of fission is largely described by the quadrupole, i.e. λ=2, deformation. Therefore, we restrict ourselves to quadrupole deformations at this point and we may rewrite eq. (6.1) as

$$R(\mathit{\Omega}) = R_0 \left(1 + \sum_{\mu=-2}^{2} \alpha_{2\mu} Y_{2\mu}(\mathit{\Omega})\right). \tag{6.2}$$

The nucleus can be described by an ellipsoid with the five coordinates (α_{2-2},α_{2-1}, ... ,α_{22}). We can now transform into the body-rigid or intrinsic system in which we may reduce the number of relevant coordinates to two, i.e. the coordinates α_{20} and $\alpha_{22} = \alpha_{2-2}$. It is important to note that the α coefficients change with this transformation, i.e.

$$\alpha_{2\nu} = \sum_{\nu=-2}^{2} \alpha_{2\mu} \mathcal{D}^{2}_{\mu\nu}{}^{*}, \tag{6.3}$$

with the $\mathcal{D}^2_{\mu\nu}$ being the corresponding Wigner D-functions [RS00]. Historically an alternative parametrisation of the nucleus has evolved from this fact, the so-called β-γ-parametrisation or Hill-Wheeler coordinates:

$$\alpha_{20} = \beta \cos\gamma \tag{6.4}$$

$$\alpha_{22} = \frac{1}{\sqrt{2}} \beta \sin\gamma. \tag{6.5}$$

The properties of the trigonometric functions sinus and cosine now define a deformation plane in which β is strictly positive and $\gamma \in [0°,60°]$[2] The parameter γ gives a measure of the triaxiality of the nucleus, i.e. deformations with $\gamma = 0°,60°$ correspond to an axial-symmetric nucleus. For $\gamma = 0°$ we have prolate shapes, for $\gamma = 60°$ we have oblate shapes. It is important to note that the β-γ-coordinates can describe quadrupole deformations only; for reflection asymmetric shapes we need odd $\lambda \geq 3$ values.

As we will only discuss axially symmetric shapes in this thesis, we consider only $\gamma = 0°$ and $\gamma = 60°$ - here we haven chosen the z-axis as the symmetry axis. In this case all $\alpha_{\lambda\mu}$ vanish for $\mu \neq 0$. The remaining $\alpha_{\lambda 0}$ are often defined as [RS00],

$$\alpha_{\lambda 0} = \beta_\lambda, \tag{6.6}$$

---

[1] In general, the coefficients are time-dependent $\alpha_{\lambda\mu} = \alpha_{\lambda\mu}(t)$ but since we do not regard time-dependent approaches in this thesis, we omit any possible dependencies on time.

[2] In principle γ can go up to 360°, however for 0°,120°, and 240° we obtain axial symmetric shapes with either the z-,y-, or x-axis as the symmetry axis. Therefore, we only need to regard the interval [0°,60°] [RS00].

hence the quadrupole deformation in axial symmetry is given by β_2. Table 6.1 summarises the important properties of these β_λ.

$\beta_2 < 0$	$\gamma = 60°$	oblate
$\beta_2 > 0$	$\gamma = 0°$	prolate

Table 6.1: Table showing the relations between prolate and oblate nuclear shapes in axial symmetry.

In practice, several different definitions of nuclear deformation exist. An overview can be found in [LVH70].

6.2 Fission in the Liquid Drop Model

As we have stated in the introduction of this chapter, it is possible to model the fission process in the liquid drop model. The basic idea is that the nucleus is a charged drop of an incompressible liquid[1]. In this model the binding energy is given by the famous semi-empirical Bethe-Weizsäcker formula. Over the decades a large amount of different liquid-drop models exhibiting various microscopic extensions have been developed.

In the liquid drop model we describe the binding energy of a nucleus with N neutrons and Z protons parametrised in different terms, a volume part a_V, a surface part a_S, a coulomb term a_C, a symmetry term a_Sym, and a pairing term a_P. The latter two are needed phenomenologically; they would not occur in a classical charged liquid drop. Hence we may write [RS00, Ber07, VH73, W$^+$91],

$$B(N,Z) = a_\mathrm{V} A + a_\mathrm{S} A^{2/3} + a_\mathrm{C}\frac{Z^2}{A^{1/3}} + a_\mathrm{Sym}\frac{(N-Z)^2}{A} - a_\mathrm{P}. \tag{6.7}$$

In order to discuss fission within the liquid drop model, we have to deal with deformation, i.e. non-spherical nuclei. The dominant term in eq. (6.7) is the volume term; it expresses the fact that the nuclear binding is approximately proportional to the number of nucleons. Since we assume volume conservation in order to reflect the saturative behaviour of the nuclear density (= incompressibility) the volume term is not affected by deformation. The surface term takes into account the reduction of nuclear binding for the nucleons on the surface of the nucleus. Hence this term is negative in relation to the volume term. The surface term is the smallest for a sphere; any distortion away from a sphere results in a larger contribution from the surface term. The Coulomb term describes the repulsion of the protons, hence if we deform the nucleus this term decreases due to the larger separation of nucleons compared to a sphere. The symmetry term - as introduced in eq. (6.7) - depends only on the nuclear volume and is therefore independent of deformation. The pairing term is neglected here, although pairing should change with deformation, however on much smaller scales than the other terms.

Let us consider only small, axially symmetric and reflection symmetric[2] deformations. Hence we may approximate the nuclear surface by,

$$R(\Omega) = R_0\left[1 + \alpha_2 P_2(\cos\Omega)\right]. \tag{6.8}$$

The corresponding surface and coulomb terms for such deformations are given by [BW39, VH73, W$^+$91]

$$E_\mathrm{def.,S} = E_\mathrm{S}\left(1 + \frac{2}{5}\alpha_2^2\right) \qquad E_\mathrm{def.,C} = E_\mathrm{C}\left(1 - \frac{1}{5}\alpha_2^2\right) \tag{6.9}$$

---

[1] The incompressibility is required to reflect the saturation of the nuclear force due to the strong repulsion at very short distances.

[2] In axial symmetry, we define *reflection symmetry* or *mirror symmetry* as the symmetry related to an axis perpendicular to the symmetry axis. In order to describe mirror asymmetric shapes we need the odd orders in eq. (6.1).

with $E_{\mathrm{spher.,S}}$ and $E_{\mathrm{spher.,C}}$ being the terms for the spherical case (see eq. (6.7)). The decrease in the coulomb term $\varDelta E_{\mathrm{C}} = -1/5\alpha_2^2 E_{\mathrm{spher.,C}}$ must be smaller than the increase in the surface energy $\varDelta E_{\mathrm{S}} = 2/5\alpha_2^2 E_{\mathrm{spher.,S}}$ in order to be stable against deformation. The drop will become unstable when the ratio of the changes becomes unity, i.e.

$$\frac{|\varDelta E_{\mathrm{C}}|}{\varDelta E_{\mathrm{S}}} \approx 1 \Longleftrightarrow E_{\mathrm{C}}/2E_{\mathrm{S}} = \chi \approx 1. \tag{6.10}$$

We may define the latter fraction of eq. (6.10) as the fissibility parameter χ (see also [BW39, VH73, W$^+$91]). For values of χ below unity, the nucleus will be stable against small deformations; for values larger than unity there is no potential barrier to inhibit a spontaneous division of the drop, i.e. the Liquid-Drop model predicts that these nuclei are unstable against spontaneous fission. We may now use the terms in eq. (6.7) to estimate the fission probability of a nucleus: the closer its fissibility to unity the higher the probability. If the fissibility is larger than unity the nucleus cannot exist in this liquid drop model as it would instantly separate. According to eq. (6.7), we can write the fissibility parameter as,

$$\chi = \frac{a_{\mathrm{C}}\dfrac{Z^2}{A^{1/3}}}{(2a_{\mathrm{S}}A^{2/3})} = \frac{a_{\mathrm{C}}}{2a_{\mathrm{S}}}\frac{Z^2}{A}. \tag{6.11}$$

A short handed formula is derived in [VH73] using fitted values for a_{C} and a_{S},

$$\chi = \frac{Z^2}{50.13 \cdot A}. \tag{6.12}$$

This corresponds to the fact that all nuclei with $\frac{Z^2}{A} \geq 50$ are unstable against spontaneous fission in the liquid drop model. Nuclei with $\frac{Z^2}{A} < 50$ or $\chi < 1$ have a local minimum at β, $\gamma = 0$ (see section 6.1) because the liquid drop model always predicts spherical ground states for all stable nuclei.

6.3 Symmetric and Asymmetric Fission

In the picture of section 6.2 we have assumed mirror (or reflection) symmetric shapes of the nucleus (see also footnote 2 on p. 55). As stated in the introduction of this chapter, we call a fission in which the two main products are of nearly equal mass a *symmetric* fission. Consequently, we may also have *asymmetric* fission, i.e. the two final nuclei have different masses.

The question if a nucleus fissions symmetrically or asymmetrically is defined by the fission path. The fission path is the path of lowest energy through the multidimensional deformation plane, which is spanned by the deformation parameters. Moreover, it is possible that there are several paths competing - certain nuclei are known to fission either symmetrically or asymmetrically with comparable probability.

The asymmetric fission can only be described by including odd and higher order terms in eq. (6.1); in particular the λ=3 term or octupole term. A general review on mirror asymmetric shapes in nuclei (also regarding fission) can be found in [AB93, BN96].

6.4 Barrier Transmission

The barrier is determined by the path of smallest energy towards infinite quadrupole deformation through the potential energy surface starting at the ground state deformation. Every point of this surface represents the binding energy of the nucleus for the given deformation. The path of smallest energy leading through this landscape is called the fission path. However, it is usually very difficult to find this path due to several reasons:

1. It is extremely time-consuming to calculate the energy surface in all dimensions as this is non-trivial

- especially when going to deformations up to the scission point[1] and beyond.

2. After having calculated the deformation landscape, one still has to solve the problem to find the correct fission path. The usual approach is to use gradient techniques, however these techniques may heavily depend on a sufficiently fine grid. As an alternative, nuclear physicists have copied a method from geophysics: the immersion or watershed techniques. These techniques are usually used to find and define watersheds in mountain areas. Similarly, one can adapt these algorithms to the energy landscape in the deformation space and henceforth obtain the fission path with a very good predictability.

Problem 1 of the above mentioned problems can be “simply” tackled by computer power, refined algorithms and improved physics. Problem 2 is principally solvable by the above mentioned immersion or watershed techniques.

Nevertheless, on a large scale examination - as we will perform in chapter 8 - we cannot solve the problems above by the given solutions as the calculations would be still too time-consuming. Therefore, we have to make approximations, such as assuming axial symmetry, which reduce the effort to calculate the fission path.

The first “quantum-mechanical” description of the fission process was given by Hill and Wheeler [HW53]. In their ansatz they assumed a single-barrier within the potential energy surface, i.e. they mapped the complicated many-body problem of fission to a one-body barrier penetration problem. In the following, the fission path is given by $V(\beta)$ with β being the deformation. Additionally, there is a mass parameter $\mu(\beta)$ which we will connect with the collective mass later. For a given energy E below the barrier, the penetrability is given by the WKB approximation (see for example [BL80, W$^+$91]),

$$P_f(E) = \exp\left[-2\int\limits_{\beta_1}^{\beta_2}\sqrt{\frac{2\mu(\beta)(V(\beta)-E)}{\hbar^2}}\,d\beta\right]. \tag{6.13}$$

Here $\beta_{1,2}$ are the two deformations for which $V(\beta_{1,2}) = E$. As we would like to have a consistent notation to [SEK$^+$09, Klü08], we rewrite eq. (6.13) with the inverse collective mass (now having units of MeV),

$$B_{20}(\beta) = \frac{\hbar^2}{2\mu(\beta)}, \tag{6.14}$$

thus having

$$P_f(E) = \exp\left[-2\int\limits_{\beta_1}^{\beta_2}\sqrt{\frac{V(\beta)-E}{B_{20}}}\,d\beta\right]. \tag{6.15}$$

The problem of the WKB approximation is that it breaks down for small barriers. Historically, the barrier has been modelled by an inverted parabola because for such an analytic form of $V(\beta)$, the integral in eq. (6.13) can be evaluated analytically, i.e.

$$P_f(E) = \frac{1}{1+\exp\left(\dfrac{2\pi(E_B-E)}{\hbar\omega_B}\right)}. \tag{6.16}$$

---

[1] The scission point is the point in the energy landscape at which the nucleus - when pictured similar to a liquid drop - would rupture into two parts.

Here E_B is the barrier maximum and ω_B the frequency of the inverted oscillator. The collective mass B_{20} has been assumed to be constant and absorbed into the frequency ω_B. Equation (6.16) is known as the *Hill-Wheeler* expression [HW53].

As we can see from eq. (6.15), the penetration probability does not only depend on the height and the width of the fission barrier (the width is given by the limits of the integral in eqs. (6.13) and (6.15)) but also the collective mass. Here arises a general problem of the description of fission, as the change of this quantity with deformation has usually been neglected, like in the approach with the inverted parabola which we discussed above. The latter approach is still the standard for the calculation of neutron-induced fission and β-delayed fission rates for r-process simulations [CTT91, MPMZ$^+$07, PKP$^+$05, PKR$^+$10] because of its simplicity and its applicability for energies above the fission barrier, i.e. $E \geq E_B$. However, it has been shown, that especially for spontaneous fission a convenient treatment of the collective mass is needed (see for example [SEK$^+$09]).

Finally, we should note that we have omitted several other aspects affecting the fission probability here. These aspects can be usually considered as secondary since they do not have such a large influence on the fission probability like the barrier height or the collective mass. Although maybe less important, we will shortly discuss these aspects as a closing remark:

- The energy in eq. (6.13) has to be thoroughly considered as this can include small excitations. The quantum mechanical ground state energy is not given by the global minimum of the potential energy surface, instead it is usually slightly higher in energy.
- The barrier structure can become very complicated, i.e. having multiple humps (barriers). Between two barriers, the so-called fission isomers exist and the fission probability is usually treated as two (or more) combined penetrations of the given barriers.
- Besides the quantum-mechanical correction of the ground state energy (see uppermost bullet), we would also have to consider what is called the ’repetition time’ [SEK$^+$09]. Classically, this is the frequency at which the nucleus impinges on the barrier, trying to tunnel through the latter. However, this is only relevant for spontaneous fission.

Part II

Results

7

Microscopic Radiative Strength Functions

Radiative strength functions are an important ingredient for Hauser-Feshbach calculations of (n,γ) reaction rates and one usually assumes that E1 and M1 transitions dominate. In recent years, a lot of effort has been made to improve the experimental observation and theoretical prediction of low-lying strength in E1 and M1 transitions. We will therefore examine the possible influence of such low-lying strength on (n,γ) reaction rates occurring at astrophysical conditions.

In this chapter, we will discuss different (microscopic) approaches towards E1 and M1 strength functions. We will start with an introduction defining and explaining the needed quantities and phenomena. This is followed by a section about microscopic E1 strength functions in (n,γ) reactions of selected tin and nickel isotopes. In the recent years, growing effort has been put into the experimental observation and theoretical description of the pygmy resonance. With the advent of the RQTBA model (discussed below), a huge improvement of the description of pygmy resonances was achieved. Therefore, we will specifically discuss the role of low-energy phenomena in E1 transitions, i.e. the pygmy dipole resonance and its influence on (n,γ) cross sections and reaction rates. A first study of the relevance of low-lying E1 strength has been performed in [Gor98]. For an introduction to the strength function formalism see section 5.3.

The second part of this chapter is devoted to microscopic M1 transitions obtained from shell model calculations and the applicability of the Brink hypothesis. For the M1 transitions a lot of experimental and theoretical effort has been put into measuring and predicting the Scissors mode, which we introduced in section 5.2.4. Hence, we intend to study the occurrence of this mode and the possible relevance for (n,γ) reaction rates in iron-group nuclei.

7.1 Introduction

The concepts and physics of radiative strength functions have been introduced in section 5.3, whereas the physics of electromagnetic transitions were covered in chapter 5. In this first section, we will shortly discuss certain general features and aspects of radiative strength functions regarding the physics of nuclear reactions.

But first of all, we need to clarify the nomenclature since there exist three different designations for these strength functions with regard to electromagnetic transitions, i.e. (i) *radiative strength functions*, (ii) *photon strength functions*, or (iii) γ-strength functions. All three labels represent the same quantity in the context of nuclear physics. The latter being more specific by emphasising that the considered radiation is gamma radiation.

It is worthwhile to recall an important property of (n,γ) reactions under astrophysical conditions before discussing the following issues: The r-process generally takes place at temperatures of $T_9 = 10^9$ Kelvin.

At these temperatures we may still treat the neutrons classically (see section 2.3) and the most important neutron energies lie between 1-100 keV. The neutron capture probability is usually large for these energies and shows an approximately constant behaviour in these regimes due to the dominance of s-wave capture. This has an important effect on the Hauser-Feshbach cross section, which is proportional to a factor $T_n T_\gamma / \sum_i T_i$. For neutron-rich nuclei we may assume that $\sum_i T_i = T_n + T_\gamma$ because all other channels like proton or α emission are negligibly small. If we additionally assume that $T_n \gg T_\gamma$, which is true for s-wave (and sometimes p-wave) capture, the sum in the denominator cancels with the neutron transmission coefficient in the nominator. Thus, the cross section depends on the γ-transmission coefficient, i.e. it is very sensitive to changes in T_γ. Therefore, radiative strength functions are important for the determination of (n,γ) reaction rates and any nuclear structure effects they are able to resolve may affect the cross section.

7.1.1 Quadrupole and Higher-Order Strength Functions

In this chapter we will focus on dipole strength functions as these are usually the dominating ones, as we have seen in section 5.3 - although the phase-space factor of eq. (5.29) goes with E^{2L+1}, i.e. E^3 for dipole (L=1) transitions and E^5 for quadrupole (L=2) transitions. Historically, the electric giant dipole resonance was the first giant resonance that was observed due to its magnitude. It turned out that this resonance can be parametrised with a Lorentzian function. Hence, it is the general approach to use a Lorentzian representation to describe an electromagnetic strength function, in particular for electric dipole transitions.

In fig. 7.1 we have plotted different radiative strength functions for E1, M1, E2, and M2 transitions and we notice the predominance in total magnitude of the E1 strength function. For the individual transmission coefficients we have a different energy dependence so the dipole transitions become weaker compared to the quadrupole transitions. Moreover, the strength functions used in fig. 7.1 are simple Lorentzians which do not resolve any structure effects, e.g. a scissors mode. The inclusion of these structures, which would occur at low energies, into the strength might shift the picture. This is a crucial drawback of the analytic strength functions, as these are not able to account for the structure effects at low energies.

7.1.2 Relevant Energy Ranges

In fig. 7.2 we show a schematic picture of the γ-decay in a compound nucleus. The maximum E_γ is given by the sum of the kinetic energy of the incoming particle (in the centre-of-mass system) and the separation energy of that particle in the compound nucleus. The decay is divided in two regions, i.e. the decay to experimentally known states and into the continuum region for which we have to apply a level density formalism. For r-process nuclei the experimental spectrum, and often even the ground state's spin and parity, are not known. Therefore, we will discuss in the following how the level density prescription and the energetical dependence of the single γ-transmission coefficient define an energy region which dominates the γ-decay.[1]

The γ-transitions in nuclei are subject to three different aspects determining their magnitude: the strength function, the energy-dependence of the transmission coefficient given by E_γ^{2L+1} (the phase-space; see eq. (5.45)), and the folding with the level density (see eq. (2.22) and the previous section). The strength function incorporates all the nuclear structure information regarding the transition strengths. If we neglect the strength function for the moment and only regard the level density and the phase-space factor, we obtain a competition between these two quantities, which we have visualised in fig. 7.3.

The energy dependence E_γ^{2L+1} clearly emphasises transitions of larger energies in fig. 7.3. The transition with the largest E_γ is always the transition to the ground state (for a fixed compound energy) and thus the E_γ^3 term favours this transition. On the other hand, the level density increases with excitation energy, i.e. there are many states at low E_γ to which the compound state can decay to. Thus, we have a competition of the phase-space factor and the level density as both favour different E_γ regions. The dominant transitions (despite the detailed information of the strength function) will therefore lie in between the two extremes, depending on the level density and the maximum E_γ available. This interplay

---

[1] Note that this accounts for a fixed compound energy only!

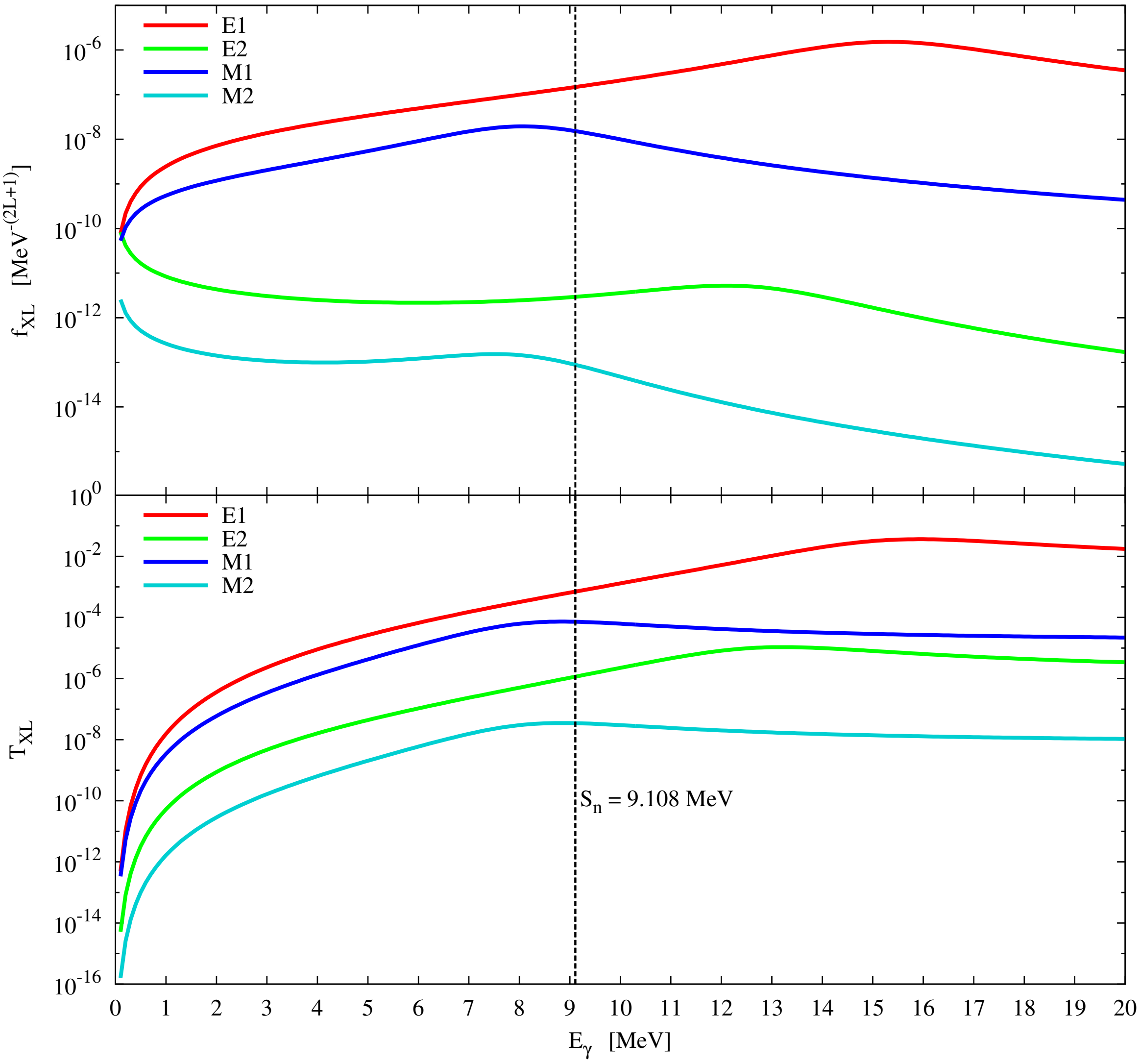

Figure 7.1: Upper panel: radiative strength functions f_{XL} of ^{120}Sn for different transition types (here we nicely see the problematic behaviour of E2 and M2 for $E_\gamma \to 0$; see section 5.3.4.1); lower panel: the corresponding transmission coefficients calculated from eq. (5.29); the vertical dashed line depicts the neutron separation energy.

is schematically shown in fig. 7.3. It was shown in [Rau08] that the most important energy range lies between 2 MeV and 4 MeV for most nuclei - in our example in fig. 7.3 we see that the maximum is shifted to 5 to 6 MeV because we have neglected the energy dependence of the Lorentzian that has been used in [Rau08].

The energy range of the dominant transitions can also change due to particular nuclear structure effects in the strength function that cannot be accounted for in the Lorentzian approach. Finally, we have implicitly assumed that the level density is of comparable magnitude for all spins and parities. This assumption is a good approximation at reasonable large excitation energies but strongly depends on the nucleus. Recent theoretical [ABLN00, ALN07, GHK08, HG06, LLMP$^+$08, MRMP$^+$07, NA97, ÖLMPD07] and experimental [KLM$^+$07, KÖL$^+$07] studies have shown that these assumptions are not convenient for certain nuclei at low energies.

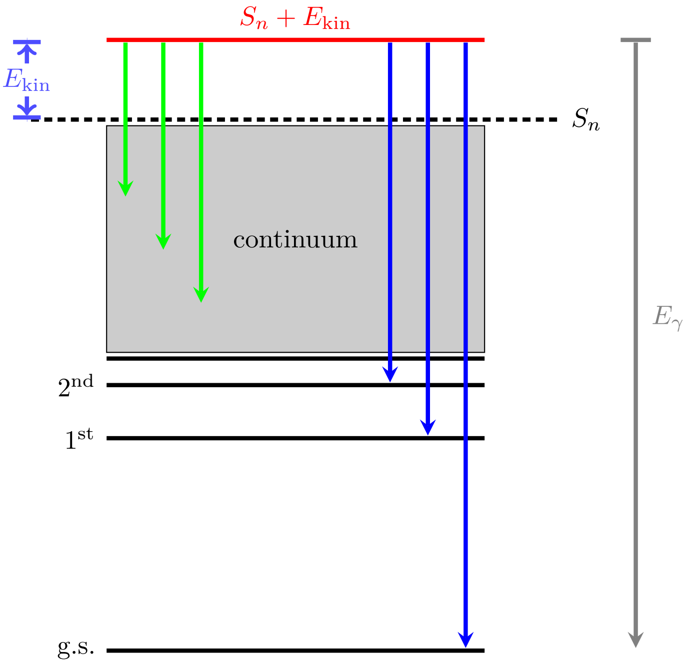

Figure 7.2: Schematic picture of the relevant γ-transitions taking place in a (n,γ) reaction. The compound excitation energy is given by the sum of the neutron separation energy and the kinetic energy of the neutron. This defines the maximum E_γ that may occur. There are two regions into which γ-decays can occur: (i) into the experimentally known discrete region (blue arrows) and (ii) into the continuum region (grey shaded area; green arrows). We define the continuum region as the region in which we have to use a level density prescription. We do not consider transitions to states above the neutron separation energy, as this could lead to $(n,n'\gamma)$.

Multipolarities of $L = 2$ or higher would not affect our qualitative discussion as these transitions are usually much smaller than the dipole $L = 1$ transitions (see section 7.1.1) as long as the compound excitation energy is considerably high. Nevertheless, at low excitation energies where individual levels can be distinguished, the higher multipolarities - in particular the E2 transitions - can become the dominant transition modes, e.g. for rotational modes. But as we are not able to regard these structures because for r-process nuclei the low energy spectra is not known, we do not include E2 (and M2) transitions in our calculations presented here.

7.1.2.1 The γ-Integrand

In the following, we will introduce a quantity what we will call the *γ-integrand* from here on. This is the sum of the integrands of eq. (2.22) over all compound spins and parities at a fixed compound excitation energy, i.e.

$$\gamma - \mathrm{integrand}(E_\gamma) = \sum_{J,\pi} T_\gamma(E_\gamma = E \to E^\nu)\rho(E^\nu), \tag{7.1}$$

with E begin the compound excitation energy, J the compound spin, π the compound parity, and E^ν the final state. From this quantity we can approximately deduce which energy regions in the γ-transitions are the most relevant ones. However, it is important to note that this works only for E_γ. We intentionally disregard spin and parity selection rules, which can strongly affect the transitions to experimental known states. However, this only occurs when the ground state spin of the target nucleus strongly differs from the spin of the regarded excited state in the compound. In such a case we would have to weight the γ-integrand with the probability of a neutron capture of the needed partial wave. Moreover, we plot

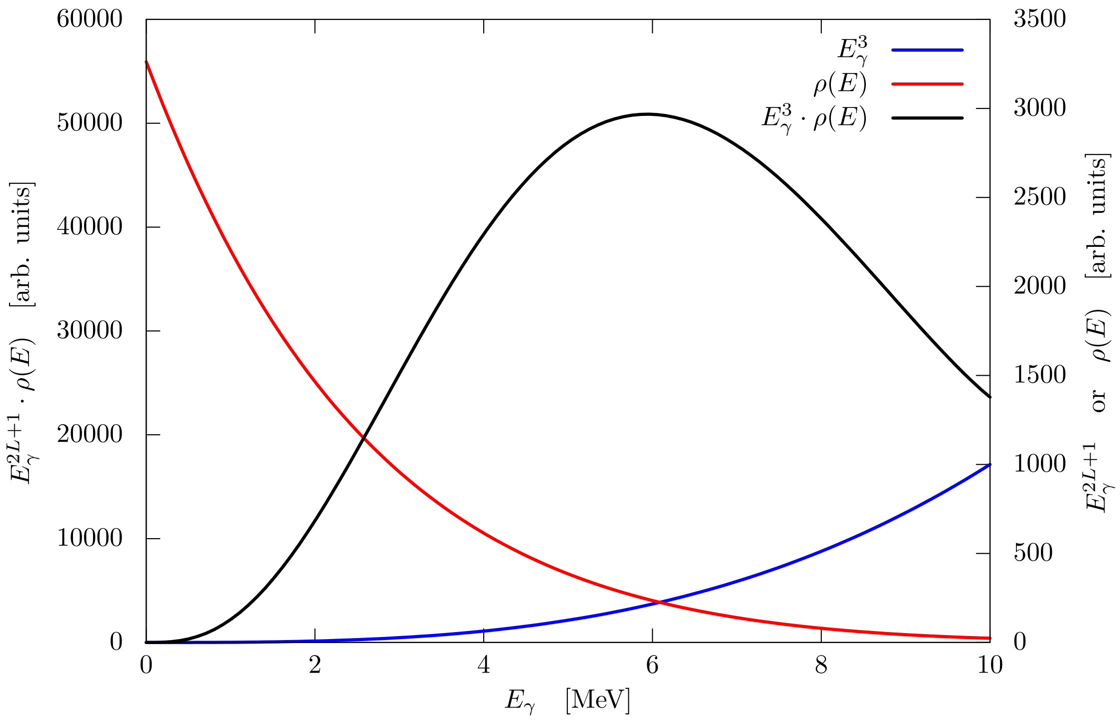

Figure 7.3: This figure shows schematically the discussed influences for $L = 1$ transitions (except the structure of the strength function). The red curve represents the E_γ^3 dependence, while the blue curve is a simple Fermi gas level density; note that for the level density the excitation energy is given by $E = 10\text{ MeV} - E_\gamma$ in case of this figure. The black curve is the product of the both functions. The right y-axis corresponds to the red and the blue curve, the left y-axis to the black curve. Note that the units of the y-axes are arbitrary.

the integrand for a fixed compound- or neutron-energy. The discrete points to the right are always the transition to the ground state and (if included) transitions to excited states.

7.1.2.2 The Reaction Rate

We have already discussed the definition of the reaction rate in section 2.3.1. As this is the key ingredient for r-process nucleosynthesis simulations, any changes due to different nuclear structure input may affect the simulation itself. However, it is crucial to remark that there are two possible changes that can occur: the reaction rate can change in magnitude and in its temperature dependence. A change in its magnitude is a shift by a multiplicative factor and can be easily accounted for. This is done for the reaction rates needed in the s-process for example. A data point at a certain energy is measured and the theoretically obtained reaction rate is adjusted to this data point. A change in the temperature dependence might have a stronger impact, possibly causing the r-process to run a slightly different path. Thus the predicted yields of certain isotopes could be different.

Additionally, we need to emphasise that the uncertainties in the (n,γ) cross section resulting from the radiative strength function can be considered small compared to the combined uncertainties stemming from the level density treatment, the nuclear mass model, and the assumptions of the Hauser-Feshbach model. It is therefore not useful to compare the predictions for different strength functions to experimental cross sections or rates, as there are other sources of uncertainty in our calculations that prevent us from acceptably assessing the quality of the strength function. As we are mainly interested in the general effect the different strength functions may have on the reaction rates, we only compare the predicted GDR parameters to experiment where data is available.

7.2 Microscopic E1 Strength Functions

The E1 strength functions we will discuss in this section are either obtained from the Lorentzian prescription (see section 5.3.2.2) or from a microscopic model. For both approaches we adopted several models. Moreover, this section will be thematically divided in two parts. First of all we will give a detailed discussion of the reactions considered and broach the astrophysical relevance of the particular reactions only slightly. The main discussion about the general astrophysical relevance can be found in the summary of this section.

7.2.1 Nomenclature and Definitions

We will elaborate the influence of six different radiative strength functions on Hauser-Feshbach calculations in this chapter whereof two are derived from one of the four approaches mentioned above. The models LD+SC [CTT91] (Liquid-Drop+Surface-Coupling) and RIPL-2 [BBC$^+$06] are based upon a Lorentzian parametrisation of the Giant Dipole resonance. The parameters are obtained from different approaches, though. The LD+SC parametrisation utilises a droplet mass model to obtain the centroid E_0 [MSK$^+$77] and a phenomenological approach for the width Γ [TA83, CTT91] in which the GDR width is described as a superposition of a macroscopic width (due to the viscosity of the "nuclear fluid") and a coupling to quadrupole surface vibrations. The RIPL-2 parametrisation obtains the centroid from a fit to the Goldhaber-Teller [GT48] and Steinwedel-Jensen [SJ50, SJJ50] approaches for spherical nuclei. These parameters are changed for deformed nuclei according to the deformation given by the finite-range droplet mass model (FRDM) [MNMS95]. The width is obtained from a phenomenological relation to the centroid energy [BBC$^+$06].

The two microscopic models employed by us are the HFB-model which is based upon a Hartree-Fock-Bogoliubov (HFB) calculation plus a quasiparticle random-phase approximation (QRPA) on top [GKS04]. In this model, the ground state and its properties are obtained within an HFB method. The QRPA method is capable of describing harmonic oscillations with small amplitudes around a spherical nucleus and can describe particle-hole correlations. The HFB results for odd-nuclei were obtained by using the filling approximation, in this approximation the odd nucleus is treated like an even nucleus regarding pairing. This approximation is very questionable for strength functions because we will see in section 7.3 that the ground state radiative strength functions of odd nuclei often show additional strength at low energies; for more details about the reasons for the use of this approximation see [GKS04].

In this thesis we define the RQTBA (relativistic quasi time-blocking approximation) model as the default model as it has been demonstrated that this model reproduces experimental cross sections very well for certain nuclei (see [LRT08, LLL$^+$09, LRTL09] and references therein). The RQTBA is an extension of a (relativistic) QRPA with the inclusion of particle-vibration coupling [BM75]. This approximation makes it feasible to study the effects of coupling single-nucleon degrees of freedom to collective vibrations. The particle-vibration coupling enhances the obtained single-particle structure compared to the (R)QRPA as it also incorporates 2p2h-excitations and phonon couplings. This leads to a considerable fragmentation of the giant dipole resonance and of a possible low-lying pygmy mode, i.e. it resolves more nuclear structure effects compared to "pure" QRPA. However, this model currently assumes spherical symmetry for the nucleus and has been applied to even-even nuclei only.

The specific differences between the **HFB+QRPA** model of [GKS04] and the RQTBA model are the aforementioned fragmentation and the underlying mean-field. The **HFB+QRPA** makes use of non-relativistic Skyrme forces while the RQTBA is based upon a relativistic mean-field approach.

The microscopic models give the upward or absorption strength function, based upon the ground state (see section 5.3.1). In order to use these strength functions for the description of the emission of photons, we assume Brink's hypothesis to be valid (see section 5.3.1.2). We will revisit this issue more closely in the summary in chapter 9.

In order to disentangle the differences between the microscopic approaches and the Lorentzian approaches, especially for the LD+SC approach as this has been employed in r-process reaction rate determinations [RTK97, RT00], we have performed a fit of a Lorentzian to the RQTBA results to obtain the centroid energy E_0. The width was chosen to be the same of the LD+SC approach (see [CTT91]). In this way we obtained the parameters for the RQTBA+MLO (RQTBA + modified Lorentzian) and RQTBA+SLO (RQTBA + standard Lorentzian) approaches. This has the advantage that potentially existent additional strength below the giant resonance does not contaminate the fit, i.e. the fitted width would not be predicted too large. Moreover, we therefore do not have to identify a possible pygmy resonance and subtract it for the fit, but keep it for the total strength.

The problem with the Lorentzian approximations is the low-energy tail as experiments have shown that the Lorentzian overestimates the strength at low energies. Therefore, methods were developed to account for this fact. In this thesis we make use of a very simple approach by making the width in the nominator of eq. (5.39) energy dependent [MSC81, CTT91],

$$\mathit{\Gamma}(E_\gamma) = \mathit{\Gamma} \cdot \sqrt{\frac{E_\gamma}{E_0}}. \tag{7.2}$$

We have applied this modification to all Lorentzian approaches except the RQTBA+SLO approach. For the RQTBA+MLO and the RQTBA+SLO approach we ensured that the integrated strength up to 25 MeV is the same as in the RQTBA approach. In this way we distributed any additional low-energy strength in the RQTBA approach over the whole range we regard. The difference between the both approaches is that the energy-dependent width from eq. (7.2), which is used in the RQTBA+MLO method, shifts the strength to energies beyond the centroid of the resonance compared to the RQTBA+SLO method, the latter predicting larger values at low energies (see figs. 7.4 to 7.24).

The difference between the six strength functions to be discussed are summarised for a better overview in table 7.1. Many of the aspects of this chapter have been addressed in [LLL+09].

As we apply different models for the electric dipole strength function, we need to consider that these models give different predictions for other observables, in particular the nuclear mass. The results in this chapter were either obtained by using experimental masses from [AWT03, WAT03] or invoking the FRDM [MNMS95] or the HFB14 [GSP07] mass models. When there is no mass model specified, the masses will be derived from experimental data. The liquid-drop model of Hilf *et al.* [MSK+77, vHT76] is used for the determination of the centroid in the LD+SC-approach. The corresponding neutron separation energies are close to the experimentally obtained values. For the nuclei $^{131-134}$Sn we did not take the values of [AWT03, WAT03], we used the values given in [DAB+08] which were obtained from Penning trap measurements at ISOLTRAP (Cern).

In the case of the relativistic mean field model, that forms the basis of the RQTBA model, the nuclear masses are usually predicted much less reliable compared to the mass models mentioned above. However, energy differences like the neutron separation energy are usually reproduced in much closer agreement with experiments.

An overview on the neutron separation energies can be seen in table 7.2. The important aspect we can conclude from this table is, that the predicted neutron separation energies do not notably deviate. The slightly larger difference in the neutron separation energy for ^{134}Sn is not a problem, as we use the experimental value anyway. However, the difference in ^{140}Sn between both models should be kept in

name	type	explanation
RQTBA	microscopic	relativistic quasi time-blocking approximation; see text
RQTBA+MLO	Lorentzian	E_0 from RQTBA; $\mathit{\Gamma}$ from [TA83] with energy dependence from [MSC81]; same strength as RQTBA up to 25 MeV
RQTBA+SLO	Lorentzian	E_0 from RQTBA; $\mathit{\Gamma}$ from [TA83]; same strength as RQTBA up to 25 MeV
LD+SC	Lorentzian	E_0 from [MSK+77] and $\mathit{\Gamma}$ from [TA83]
RIPL-2	Lorentzian	parameters from [BBC+06]
HFB	microscopic	HFB + QRPA from [GKS04]

Table 7.1: Overview on the strength functions used in chapter 7.

nucleus	exp. [MeV]	HFB14 [MeV]	RMF [MeV]
^{130}Sn	7.62	7.30	8.00
^{132}Sn	7.35	7.10	7.65
^{134}Sn	3.54	3.80	4.60
^{136}Sn	3.78	3.55	3.36
^{138}Sn	-	3.50	3.27
^{140}Sn	-	4.16	3.15

Table 7.2: This tables shows experimental and theoretical neutron separation energies S_n for different tin isotopes. The HFB14 model is a Hartree-Fock-Bogoliubov mass model [GSP07] and the RMF stands for the relativistic mean field underlying the RQTBA model (see [LRT08, LLL$^+$09, LRTL09] and references therein). It is important to note, that the neutron separation energy given by the RMF model is not the one obtained from differences of nuclear masses (see section A.3). The given value is the positive value of the Fermi energy.

mind for the discussion of the reaction ^{139}Sn(n,γ)^{140}Sn.

7.2.2 Tin Isotopes

The following results have been obtained from Hauser-Feshbach calculations using the mass model HFB14 [GCP09], the level densities of [GHK08], the treatment of parity-dependence in the compound of [LLMP$^+$08], and a Lorentzian function for the M1 transitions (see section 7.3 and [BBC$^+$06]). E2 and M2 transitions have not been regarded here. All calculations have been performed assuming spherical nuclear shapes - i.e. any predicted deformation from the mass model was set to zero. This is a valid approximation as tin nuclei are magic nuclei.

We present (n,γ)-reaction for selected tin isotopes from ^{100}Sn to ^{140}Sn. The $h_{11/2}$-intruder shell plays a peculiar role in tin isotopes, leading to isomeric states in odd tin isotopes and influencing the nucleosynthesis of the stable tin isotopes, as discussed in [NKT$^+$94]. An overview on the relevant nuclear physics for the r-process around ^{132}Sn is given by [KPA$^+$05]. Measurements of (n,γ)-reactions on certain tin isotopes at astrophysical energies can be found in [WVT$^+$96].

The neutron-deficient nuclei ^{100,106,110,114}Sn are included because for these nuclei the photo disintegration rate could be affected by the pygmy strength (see section 5.2.2). The (γ,n)-rate can be easily calculated from the (n,γ)-rate [RT00]. However, we will see that for the aforementioned nuclei the (n,γ)-rates do not differ much in their temperature dependence, rather in their absolute magnitude, but a general shift directly translates into the (γ,n)-rates thus showing no more specific peculiarities resulting from low-lying E1 strength.

Possible pygmy resonances in tin isotopes have been experimentally addressed in [AKF$^+$05, KPA$^+$07, KAB$^+$07, ÖEv$^+$07, ÖEL$^+$09]. Besides the previously discussed RQTBA approach, this issue has been addressed theoretically for tin isotopes for example in [PNVR05, TL08, INY09]. A recent overview on the theoretical approaches to pygmy resonances is given by [PVKC07]. An experimental study on radiative strength functions and level densities can be found in [TLA$^+$10].

7.2.2.1 ^{100}Sn

The doubly-magic nucleus ^{100}Sn is formed in the reaction ^{99}Sn(n,γ)^{100}Sn. The neutron separation energy is very large for this proton-rich N=Z nucleus, i.e. $S_n = 17.65$ MeV, therefore this reaction is obviously not in the r-process path. Moreover, it is questionable if ^{99}Sn exists. The dominant exit channel for neutron capture reactions on ^{99}Sn is proton emission. Although, the reaction ^{99}Sn(n,p)^{99}In has a much larger cross section than the reaction ^{99}Sn(n,γ)^{100}Sn, it is instructive to examine this reaction as some peculiar features can be discussed. Moreover, ^{100}Sn is a candidate for a possible proton pygmy resonance [TL08].

The large gap in the integrand (upper right panel) of fig. 7.4 between E_γ = 13-18 MeV results from the fact that ^{100}Sn shows the typical features of a doubly magic nucleus in the HFB level densities and the HFB mass model. In a doubly magic nucleus, the first excited state lies at a relatively high excitation energy because of the energy gap between the closed magical orbit and the next orbit. Therefore, we have no transitions into this region, i.e. there are no transitions with the corresponding E_γ. Interestingly, this energy range coincides with the giant dipole resonance of most of the strength functions shown in fig. 7.4. This reaction is therefore an example in which for radiative neutron capture reactions at astrophysical energies the giant dipole resonance does not contribute to the reaction cross section (provided that the level densities of [GHK08] are used).[1] If we increase the neutron energy, the integrand would start at higher energies and the gap would move out of the giant resonance region to higher E_γ. The isolated dot to the very right in the integrand is the transition to the ground state. Generally, a shell gap of roughly 5 MeV in the level density [GHK08] should be regarded with suspicion, even though ^{100}Sn might be doubly-magic. The problem is that the experimental verification on the doubly-magic features of this nucleus remains an open question.

The centroids of all strength functions - except for the HFB model - are very similar, i.e. the are located around 16.1 to 16.4 MeV (see table 7.3). The HFB model however, predicts a slightly shifted centroid and even additional considerable strength beyond 19 MeV- this strength we will see for neutron energies above 1-2 MeV. The width of the RIPL-2 approach is slightly larger compared to the other Lorentzian models (see table 7.3).

The second peak around 11 MeV in the RQTBA strength function in fig. 7.4 - which we might associate with a pygmy resonance - can be identified with the peak in the γ-integrand at this energy. For all strength functions - except for the RQTBA- we can deduce the order of magnitude for the cross section and the reaction rate by comparing the strength functions. We see that the RQTBA+SLO strength function is the largest, followed by the RIPL-2, the RQTBA+MLO, and the LD+SC strength functions, the latter two being so close in magnitude that we cannot differentiate them (this is also obvious from the parameters in table 7.3). The HFB strength function is considerably lower for all E_γ up to 1-2 MeV above the neutron threshold, while the RQTBA strength function is the smallest up to energies of 14 MeV. Above 14 MeV the RQTBA strength function is clearly the largest in magnitude. However, as we have already discussed above, the energy region between 14-18 MeV is blocked for γ-transitions and for neutron energies up to 3-4 MeV. Therefore, the cross section obtained with the RQTBA strength function is the smallest up to about 1 MeV. For larger neutron energies, the integrand will start to populate the resonance region in the RQTBA strength function (but also in the others) and the corresponding cross section increases. Nevertheless, the RQTBA cross section can only compete with the HFB cross section and not with the others, because the RQTBA strength function is by far the smallest up to 10-11 MeV.

The bump around 0.35 MeV in the cross section (lower left panel of fig. 7.4) corresponds to the 18 MeV[2] grid point in the level density [GHK08] from the parity treatment in the compound (see fig. 7.5). Between 17 MeV and 18 MeV the level density shows a damping of negative parity states in the compound nucleus. For lower energies (energies below 8-9 MeV; not shown in fig. 7.5), negative parity states are also strongly damped because this nucleus is considered doubly magic and protons and neutrons just fill the $g^{9/2}$ shell with positive parity. Therefore, the parity conserving M1 transitions are enhanced while at the same

model	E_0 [MeV]	Γ [MeV]
RQTBA+MLO/RQTBA+MLO	16.43	4.24
LD+SC	16.12	4.24
RIPL-2	16.28	5.36

Table 7.3: Theoretical Lorentzian parameters of the giant dipole resonance in ^{100}Sn.

---

[1] In case of the back-shifted Fermi gas model of [RTK97], the energy gap would be 3.4 MeV. Hence this level density would give rather similar results.

[2] The neutron separation energy of 17.65 MeV plus the 0.35 MeV gives 18 MeV.

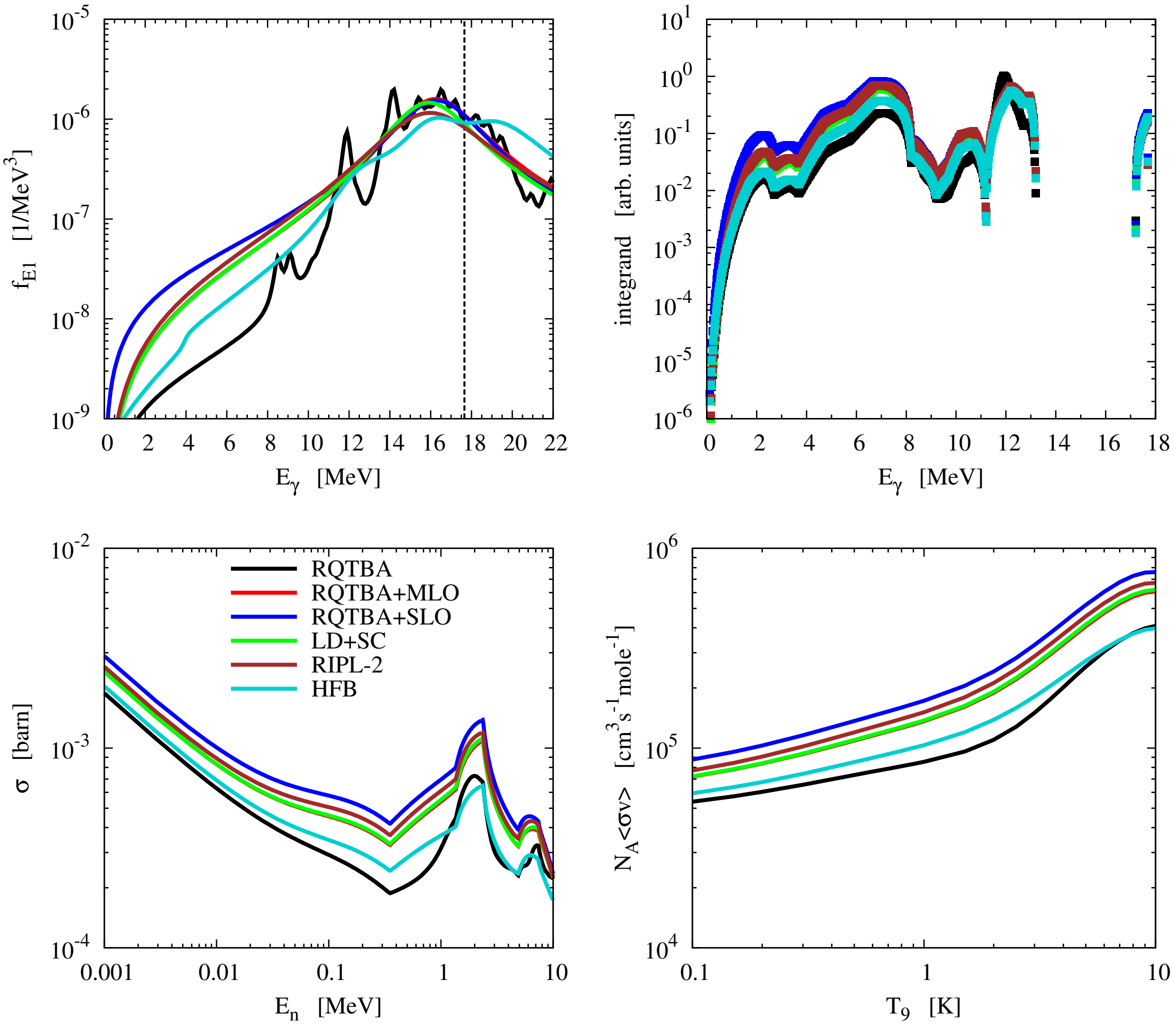

Figure 7.4: ^{99}Sn(n,γ)^{100}Sn - the upper left panel shows the different E1 strength functions and the vertical line marks the neutron separation energy. The upper right panel shows the γ-integrand as explained in section 7.1.2.1 evaluated for a kinetic neutron energy of $E_{\mathrm{kin}} = 40$keV. The lower-left panel shows the laboratory ^{99}Sn(n,γ)^{100}Sn cross section. The lower-right panel shows the stellar reaction rate. Note that the red line is beneath the green line due to the similar parameters (see table 7.3).

time the parity changing E1 transitions are damped. This gives a reduction of the (n,γ) cross section compared to the case in which all parities are equally distributed. However, at the 18 MeV grid point the damping of the negative parity states weakens, thus enhancing the E1 transitions relative to the results obtained with kinetic neutron energies which resulted in a compound energy below 18 MeV. Therefore, we see a rise in the cross section in fig. 7.4. The same holds for the kinks at 1.35 MeV and 2.35 MeV (corresponding to the 19 MeV and 20 MeV grid points) and the dip at 4.85 MeV (corresponding to the 22.5 MeV grid point). We see these “numerical” effects so strongly emphasised because the grid spacing at these energies is very large and since we have not reached the equipartition of both parities yet (see fig. 7.5). Moreover, the level density predicts an oscillatory behaviour between both parities with regard to their dominance. This behaviour is problematic, as there is no equipartition in energy even above 20 MeV, far above all relevant particle thresholds. This casts doubts upon the quality of the level density [GHK08] for this particular nucleus, or at least doubt on the quality of the parity distribution for this nucleus.

Figure 7.4 demonstrates the possible influence of the tail of the Lorentzian. The individual peaks we

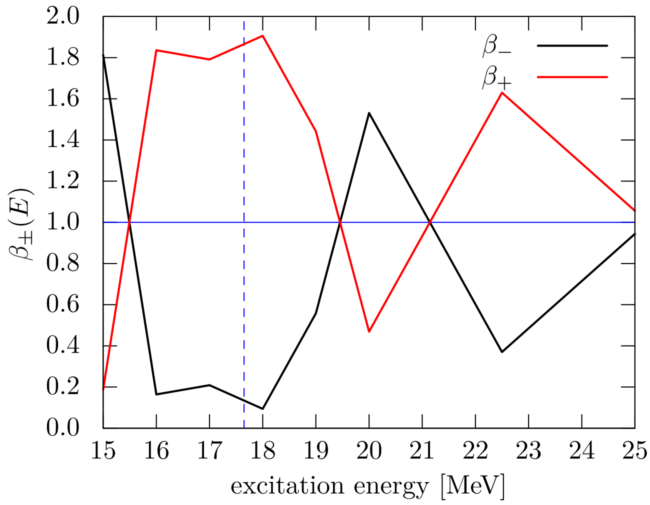

Figure 7.5: Plot of the $\beta_\pm(E)$-values (see eq. (2.26)) of ^{100}Sn derived from the level density of [GHK08] around the neutron threshold; the latter is indicated by the vertical dashed line.

see in the strength function are damped due to the large neutron separation energy (and the resulting large number of possible transitions). In fig. 7.6 we show exactly the same figure, but with the parity weighting switched off. The individual structure of the E1 strength function is clearly visible, but does not affect the reaction rate considerably nonetheless.

Finally, it is important to note that as ^{100}Sn is an even-even N=Z nucleus, we have to consider a damping in the isovector dipole transitions, i.e. the E1 transitions, due to isospin selection rules. This is accounted in the calculations of fig. 7.4 in a very crude manner by simply dividing $\mathit{\Gamma}_\gamma$ or T_γ by a factor of 1.5 (see [HWFZ76, CTT91] for more details; for an improved method see e.g. [RTGW00]).

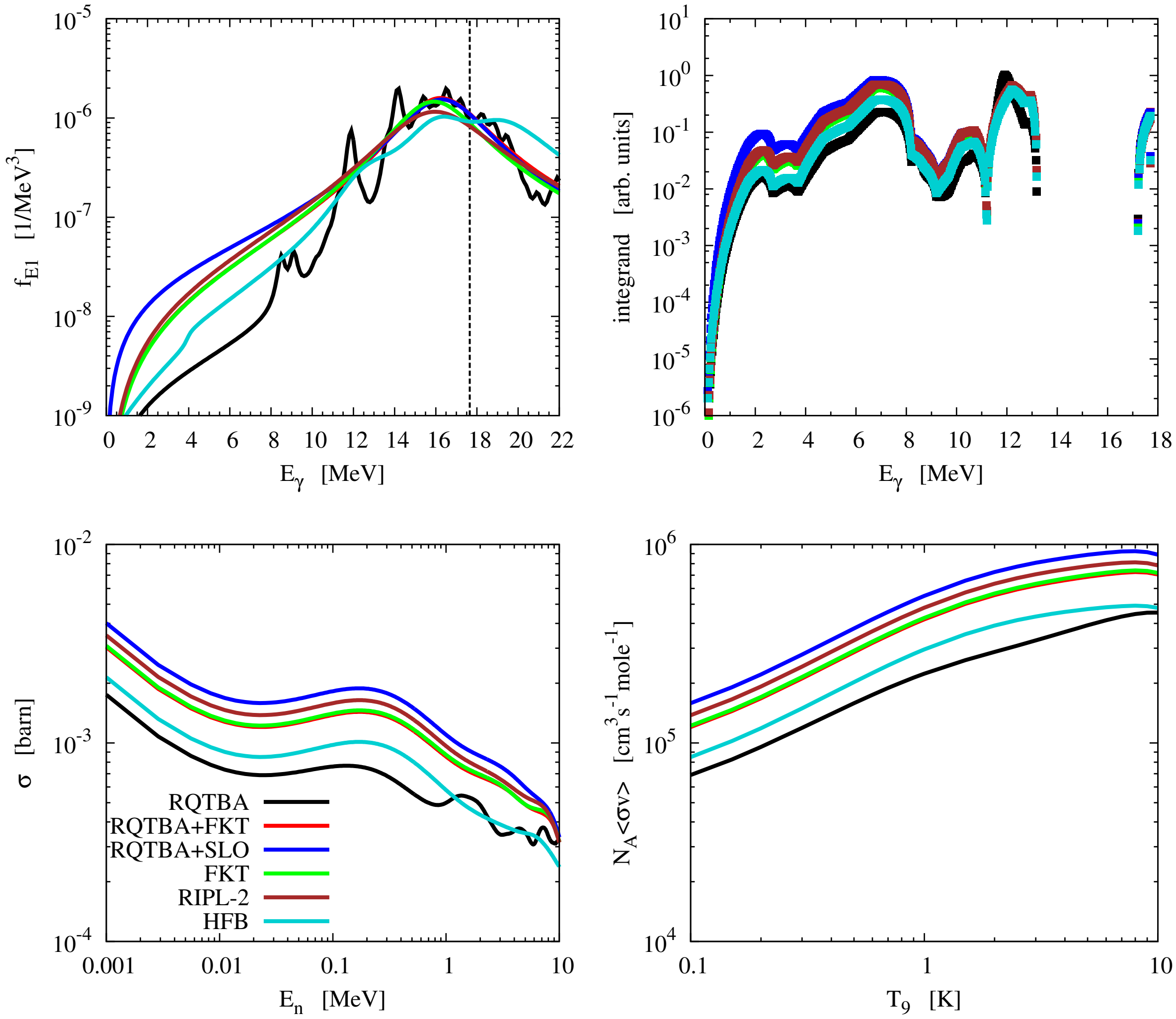

Figure 7.6: ^{99}Sn$(n,\gamma)^{100}$Sn - The same as fig. 7.4 but without the parity weighting in the compound. The level density is the same!

7.2.2.2 ^{106}Sn

The nucleus ^{106}Sn can also be considered proton-rich (or neutron-deficient) as the neutron separation energy is $S_n = 12.23$ MeV. The corresponding reaction ^{105}Sn$(n,\gamma)^{106}$Sn is consequently not part of the r-process path. Nevertheless, the strength function of this nucleus in fig. 7.7 is very different to the strength function of ^{100}Sn in fig. 7.4 and that is why it is worth to shortly address the differences.

The integrand in the upper right corner of fig. 7.7 indicates that the dominant γ-transitions are the ones with E_γ = 2-8 MeV and we see that the RQTBA-strength function is the smallest in this energy region. Therefore, the cross section and the reaction rate of the RQTBA model are considerably smaller compared to the other models. The isolated dots to the right of the integrand belong to transitions to experimentally known levels, the right most representing the ground state.

The resonance parameters in table 7.4 are very similar for the LD+SC and the RIPL-2 models and hence the corresponding strength functions are nearly equal. The same accounts for the cross section and the reaction rate. Interestingly, the centroid energy E_0 of the RQTBA+MLO in table 7.4 is slightly higher. Nevertheless, the RQTBA+MLO strength function is still similar to the LD+SC and RIPL-2 strength functions. This shows that small differences in the parameters do not lead to strong variations in the strength function for the relevant energies in this reaction.

model	E_0 [MeV]	Γ [MeV]
RQTBA+SLO/RQTBA+MLO	16.63	5.07
LD+SC	15.91	5.07
RIPL-2	16.02	5.20

Table 7.4: Theoretical Lorentzian parameters of the giant dipole resonance in ^{106}Sn.

The other microscopic strength function, i.e. the HFB-strength function, lies in between the RQTBA and the Lorentzian strength functions. Again the HFB strength function gives additional strength above ≈ 17 MeV which we would start to see for neutron energies $E_n \geq 4.8$ MeV. However, the maximum of the integrand would still lie far below these E_γ. The Lorentzian without the energy-dependent width, the RQTBA+SLO model, clearly gives the largest strength function in magnitude and consequently the largest cross section and reaction rate.

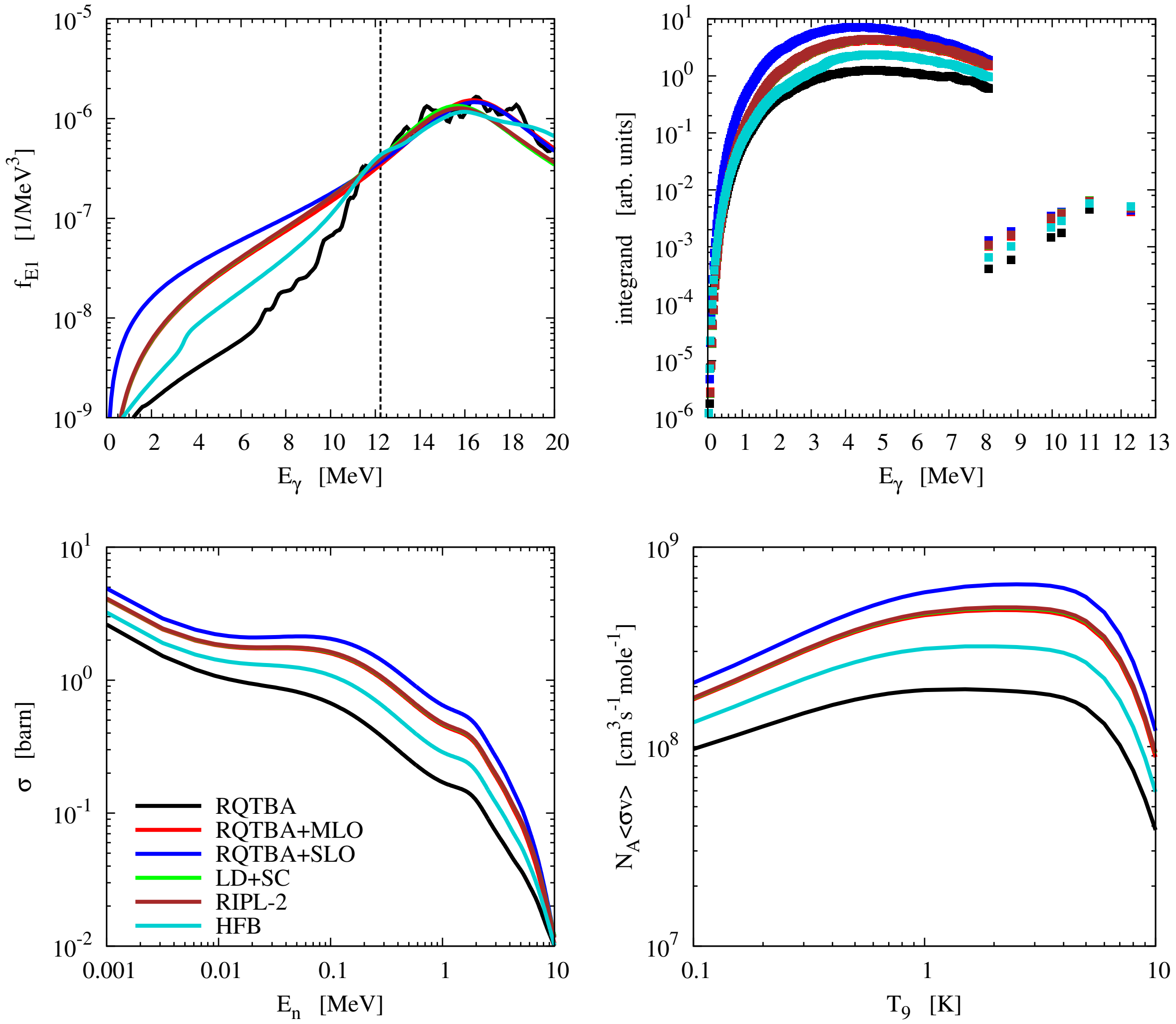

Figure 7.7: ^{105}Sn$(n,\gamma)^{106}$Sn - the upper left panel shows the different E1 strength functions and the vertical line marks the neutron separation energy. The upper right panel shows the γ-integrand as explained in section 7.1.2.1 evaluated for a kinetic neutron energy of $E_{\mathrm{kin}} = 45$keV. The lower-left panel shows the laboratory ^{105}Sn$(n,\gamma)^{106}$Sn cross section. The lower-right panel shows the stellar reaction rate. Note that the red, the green, and the brown lines are upon each other due to the similar resonance parameters (see table 7.4).

7.2.2.3 ^{110}Sn

The neutron separation energy of the nucleus ^{110}Sn is $S_n = 11.28$ MeV. The reaction properties plotted in fig. 7.8 for the reaction ^{109}Sn$(n,\gamma)^{110}$Sn are very similar to the ones plotted in fig. 7.7 for the reaction ^{105}Sn$(n,\gamma)^{106}$Sn.

model	E_0 [MeV]	Γ [MeV]
RQTBA+SLO/RQTBA+MLO	16.23	5.44
LD+SC	15.84	5.44
RIPL-2	15.92	5.14

Table 7.5: Theoretical Lorentzian parameters of the giant dipole resonance in ^{110}Sn.

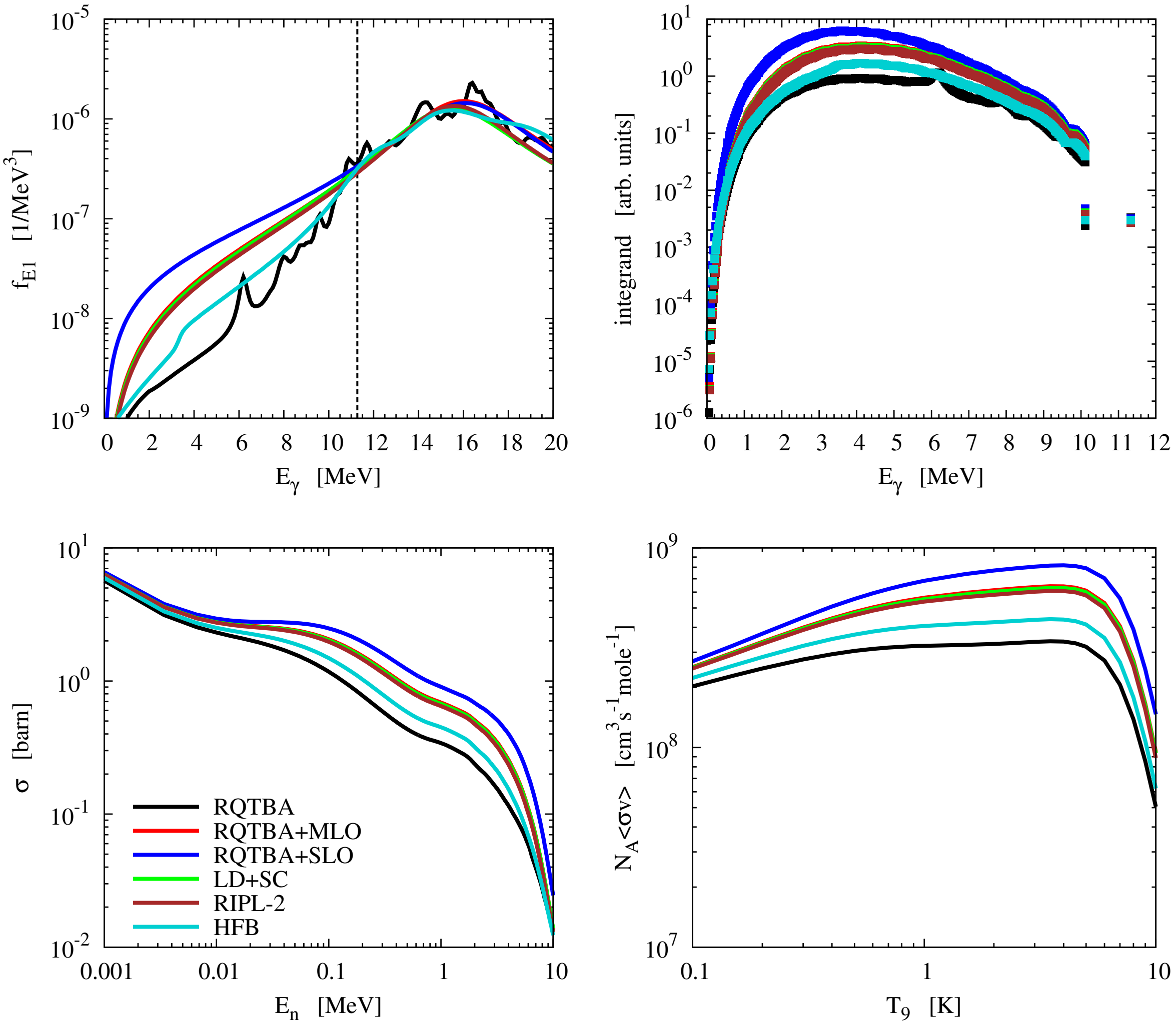

Figure 7.8: ^{109}Sn$(n,\gamma)^{110}$Sn - the upper left panel shows the different E1 strength functions and the vertical line marks the neutron separation energy. The upper right panel shows the γ-integrand as explained in section 7.1.2.1 evaluated for a kinetic neutron energy of $E_{\rm kin} = 48$keV. The lower-left panel shows the laboratory ^{109}Sn$(n,\gamma)^{110}$Sn cross section. The lower-right panel shows the stellar reaction rate. Note that the red, the green, and the brown lines are upon each other due to the similar resonance parameters (see table 7.5).

Basically, there is one fundamental difference between both calculations. The calculation of ${}^{105}\mathrm{Sn}(n,\gamma){}^{106}\mathrm{Sn}$ involved more experimental levels than the calculation of ${}^{109}\mathrm{Sn}(n,\gamma){}^{110}\mathrm{Sn}$ in the compound/daughter nucleus. The nuclear levels experimentally known in ${}^{106}\mathrm{Sn}$ and used in our calculation are (ordered in energy) of spin and parity 0^+ (the ground state), 2^+, 4^+, 6^+, 8^+, and 10^+; the recommendation is to use these six levels as the level scheme is assumed to be complete up to the last of these levels [IAEb]. Even though ${}^{110}\mathrm{Sn}$ is more stable than ${}^{106}\mathrm{Sn}$ ($T_{1/2}^{\beta^+}({}^{106}\mathrm{Sn}) \approx 115\mathrm{s}$ versus $T_{1/2}^{\beta^+}({}^{110}\mathrm{Sn}) \approx 4.11\mathrm{h}$), the level scheme is only considered complete up to the second level because a level has been identified around 2.121 MeV but its spin and parity properties have not been measured yet [IAEb]. This discrepancy in the recommended experimental level scheme shows a general problem of Hauser-Feshbach calculations concerning the experimental levels and their interplay with the level density.

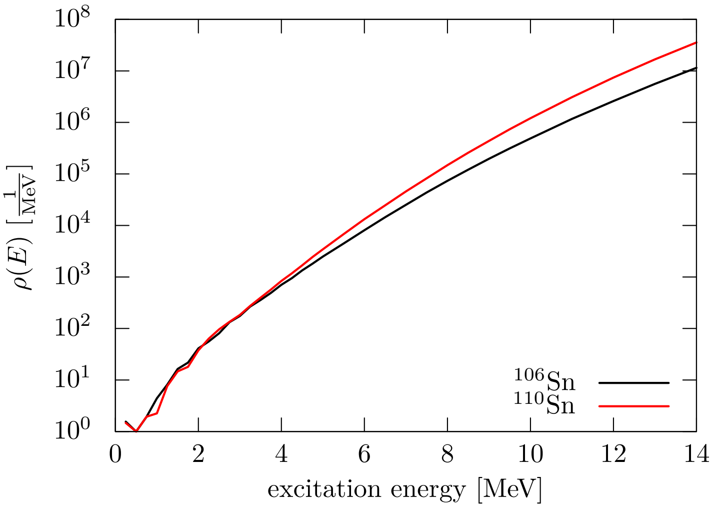

Figure 7.9: The total nuclear level densities of ${}^{106}\mathrm{Sn}$ and ${}^{110}\mathrm{Sn}$ from [GHK08].

Although the neutron separation energy in ${}^{106}\mathrm{Sn}$ is larger than in ${}^{110}\mathrm{Sn}$, we see in fig. 7.9 that the nuclear level density in ${}^{110}\mathrm{Sn}$ is bigger than in ${}^{106}\mathrm{Sn}$. However, the integrand in fig. 7.7 and fig. 7.8 have roughly the same maximum value. The only difference results from the number of nuclear levels used. In ${}^{109}\mathrm{Sn}(n,\gamma){}^{110}\mathrm{Sn}$ we use less experimental levels for the the γ-decay than in ${}^{105}\mathrm{Sn}(n,\gamma){}^{106}\mathrm{Sn}$ and therefore the cross section of the latter reaction is smaller than the cross section of the former reaction (compare upper right panels of figs. 7.7 and 7.8).

This result is rather easy to understand and could have been shown for one specific (n,γ)-reaction by using different levels. But in our case we have to notice an additional component: the questions of the experimental levels to be used does not only affect the reaction itself, it also affects its competitive properties towards other reactions on neighbouring nuclei.

7.2.2.4 ^{114}Sn

The nucleus ^{114}Sn that is formed in the reaction ^{113}Sn$(n,\gamma)^{114}$Sn is a stable isotope of tin, although considered as one of the rare tin isotopes due to its small natural abundance of 0.66%. It has a neutron separation energy of $S_n = 10.30$ MeV and it is not synthesised by the r-process because it is shielded by ^{114}Cd from the β^--decay. It is therefore synthesised by the p-process and the s-process, the contribution of the latter being comparatively small [BWK89, NKT$^+$94]. The results plotted in fig. 7.10 show some interesting features regarding the microscopic strength functions, i.e. the RQTBA and the HFB strength functions.

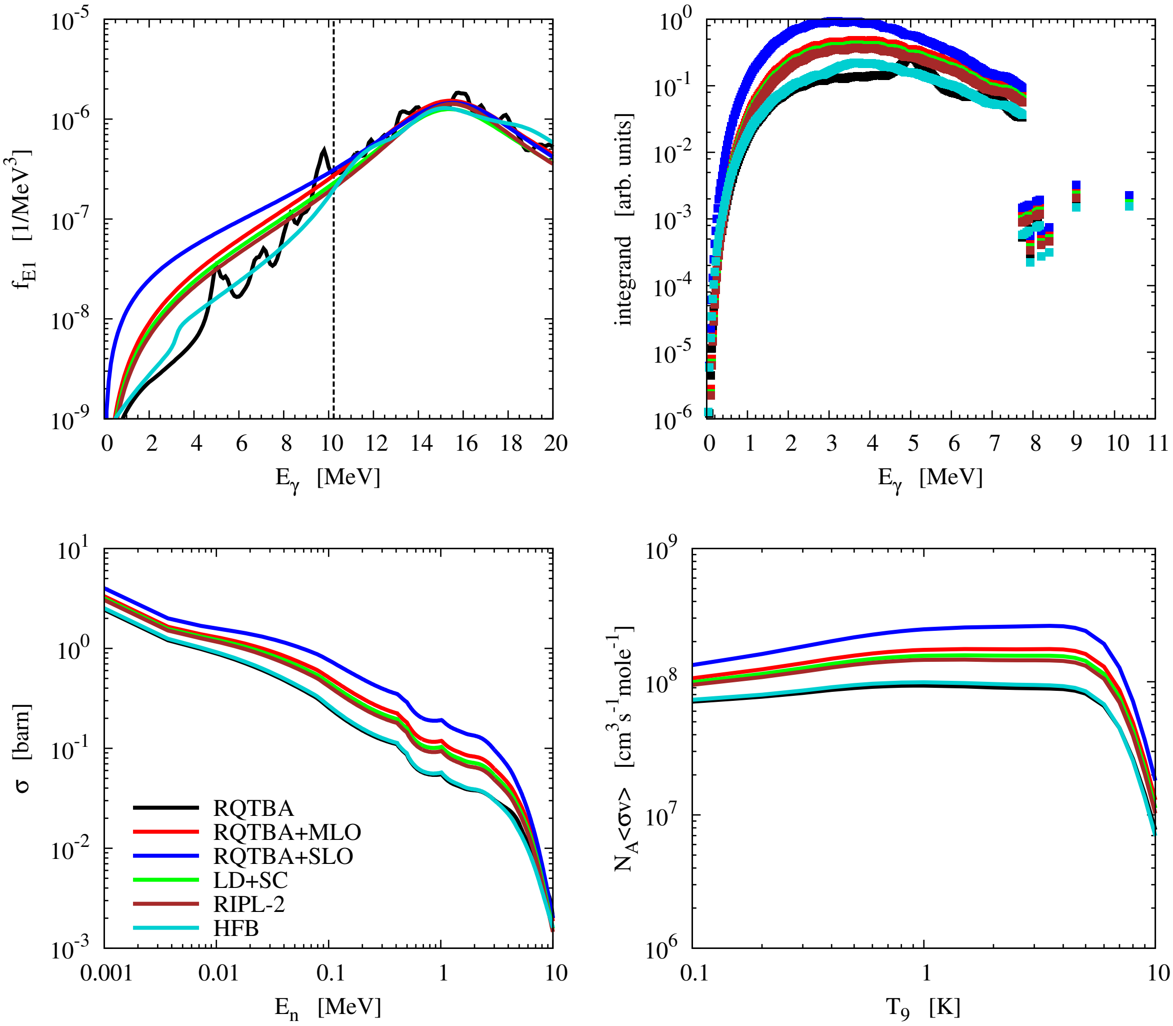

Figure 7.10: ^{113}Sn$(n,\gamma)^{114}$Sn - the upper left panel shows the different E1 strength functions and the vertical line marks the neutron separation energy. The upper right panel shows the γ-integrand as explained in section 7.1.2.1 evaluated for a kinetic neutron energy of $E_{\text{kin}} = 53$keV. The lower-left panel shows the laboratory ^{113}Sn$(n,\gamma)^{114}$Sn cross section. The lower-right panel shows the stellar reaction rate.

We can see in fig. 7.10, that the both strength functions are roughly the same in magnitude, i.e. the HFB strength function looks like an more smeared out version of the RQTBA strength function. As the neutron threshold lies just above the distinctive peak at 9.5-10 MeV in the RQTBA strength function, this peak would only affect the transitions to experimentally known states (which corresponds to the energy range from 7.7 MeV to 10.3 MeV). The similar magnitude in the strength function can also bee seen in the integrand plot, in which the peak around 5 MeV in the RQTBA strength function leads to an enhancement due to which the cross sections obtained with both models are very similar. The same applies to the reaction rate.

The two dips around 0.5 MeV and 1.0 MeV in the cross section result from excited levels in the target nucleus ^{113}Sn with $J^\pi = \frac{3}{2}^+$ at these energies. For kinetic neutron energies smaller than the first excited state in the target nucleus, the neutron exit-channel in the Hauser-Feshbach formula (see eq. (2.21)) is given only by the decay to the ground state in the target. If the neutron energy becomes larger than the first excited state in the target, the compound state may decay into the ground state or the first excited state by neutron emission. This additional probability increases the total transmission coefficient $T_{\text{tot.}}$ in eq. (2.21) which gives a reduction of the (n,γ) cross section. The magnitude of the reduction depends on the multipolarities, i.e. the spins and parities involved. The other experimental levels in between the states mentioned above are a $\frac{7}{2}^+$ at 0.8 MeV, a $\frac{5}{2}^+$ at 0.41 MeV, and a $\frac{11}{2}^-$ at 0.74 MeV. But as the ground state has $J^\pi = \frac{1}{2}^+$, the neutron decay to the $\frac{3}{2}^+$ states is favourable compared to the other states.

model	E_0 [MeV]	Γ [MeV]
RQTBA+SLO/RQTBA+MLO	15.81	5.71
LD+SC	15.76	5.71
RIPL-2	15.78	5.06

Table 7.6: Theoretical Lorentzian parameters of the giant dipole resonance in ^{114}Sn.

The Lorentzian parameters are given in table 7.6. For the corresponding strength functions, the same applies as in the previous calculations.

7.2.2.5 ^{116}Sn

The isotope ^{116}Sn is also a stable isotope and experimental Lorentzian parameters have been obtained by a fit of a Lorentzian to measured data. These are listed in table 7.7 as a reference to compare to the theoretically obtained parameters.

model	E_0 [MeV]	Γ [MeV]
RQTBA+SLO/RQTBA+MLO	15.47	5.65
LD+SC	15.72	5.65
RIPL-2	15.73	5.02
exp. [FBC$^+$69]	15.74	4.34
exp. [LBB$^+$74]	15.69	5.24

Table 7.7: Experimental and theoretical Lorentzian parameters of the giant dipole resonance in ^{116}Sn. The experimental values were determined between 13 and 18 MeV (see [DB88]).

The results obtained from the different strength function models are given in fig. 7.11; the neutron separation energy for ^{116}S is $S_n = 9.56$ MeV. In contrast to ^{114}Sn, the isotope ^{116}Sn is synthesised in the s-process [NKT$^+$94] as it is shielded from r-process contributions by ^{116}Cd.

Again, we notice in fig. 7.11 that the RQTBA and HFB strength functions are rather similar for E_γ below 3-4 MeV. However, above this energy we can identify additional strength on the RQTBA strength function leading to a slightly larger integrand and also a slightly larger cross section and reaction rate.

The dip around 0.5 MeV in the cross section results from the first excited $\frac{3}{2}^+$ level at that energy. The subsequent but smaller dips result from the levels shown in table 7.8. We see in fig. 7.11 that the "high-spin" levels with $\frac{7}{2}^+$ and $\frac{11}{2}^-$ give much smaller contributions to the integrand than the other levels. For an explanation for the physical reason of these dips see section 7.2.2.4.

energy [MeV]	J^π
0.000000	$\frac{1}{2}^+$
0.497334	$\frac{3}{2}^+$
0.612810	$\frac{7}{2}^+$
0.713640	$\frac{11}{2}^-$
0.986560	$\frac{5}{2}^+$
1.280280	$\frac{3}{2}^+$
1.416900	$\frac{5}{2}^+$

Table 7.8: Experimental levels in ^{115}Sn used for the ^{115}Sn(n,γ)^{116}Sn reaction calculation.

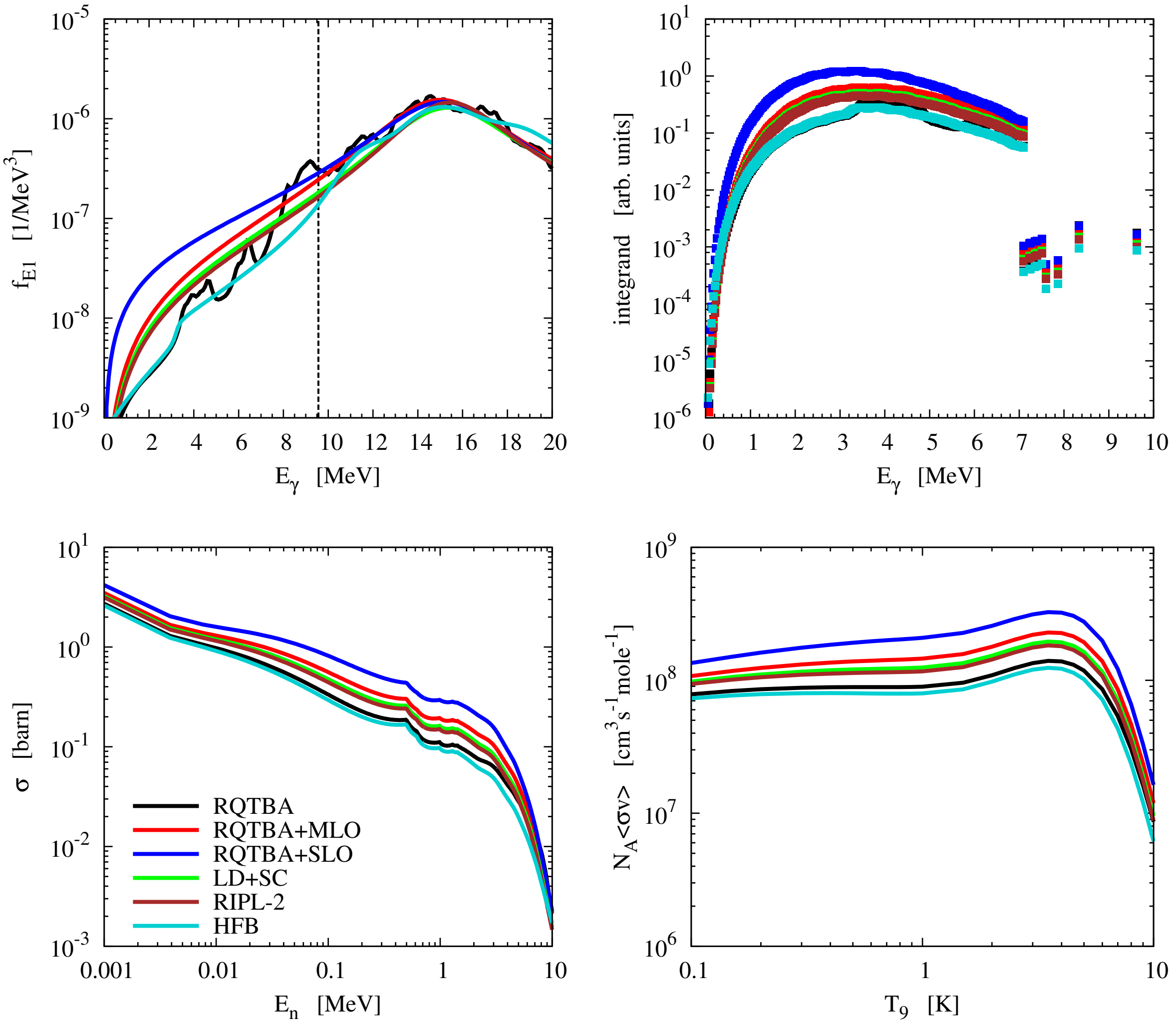

Figure 7.11: ^{115}Sn(n,γ)^{116}Sn - the upper left panel shows the different E1 strength functions and the vertical line marks the neutron separation energy. The upper right panel shows the γ-integrand as explained in section 7.1.2.1 evaluated for a kinetic neutron energy of E_{kin} = 55keV. The lower-left panel shows the laboratory ^{115}Sn(n,γ)^{116}Sn cross section. The lower-right panel shows the stellar reaction rate. The green and the brown lines lie upon each other.

7.2.2.6 ^{120}Sn

The isotope ^{120}Sn is the most abundant tin isotope (natural abundance of 32.58%), particularly formed in the s-process but also with contributions from the r-process. The corresponding neutron separation energy is $S_n = 9.11$ MeV. In this reaction, the RQTBA strength function shows a crucial interplay with the neutron separation energy for the first time in our discussion: the RQTBA strength function has a peculiar peak just located at the (experimental) neutron separation energy in the upper left panel of fig. 7.12.

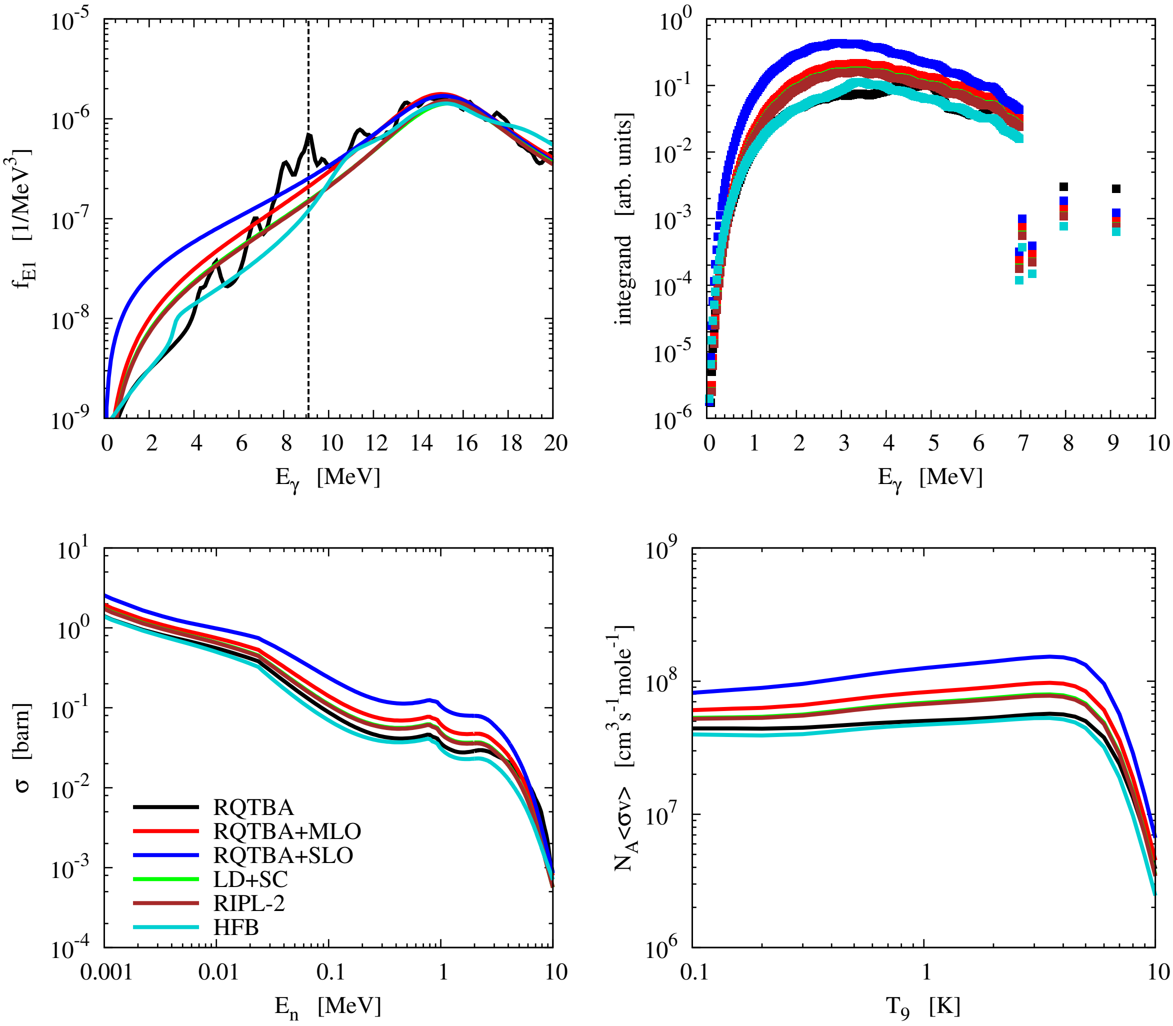

Figure 7.12: ^{119}Sn(n,γ)^{120}Sn - the upper left panel shows the different E1 strength functions and the vertical line marks the neutron separation energy. The upper right panel shows the γ-integrand as explained in section 7.1.2.1 evaluated for a kinetic neutron energy of $E_{\text{kin}} = 24$keV. The lower-left panel shows the laboratory ^{119}Sn(n,γ)^{120}Sn cross section. The lower-right panel shows the stellar reaction rate. The green and the brown lines lie upon each other.

We see the influence of this peak in the isolated dots of the integrand in this figure, i.e. the transitions to experimental levels. For these the RQTBA strength function gives the dominant strength. However, the maximum of the integrand is located around 2-5 MeV and therefore the additional (pygmy) strength in the RQTBA strength function does not visibly affect the cross section and the reaction rate. Hence, this reaction is a nice example for a nucleus having a very peculiar pygmy resonance that does not affect the (n,γ) cross section noticeably as the level density shifts the dominating transitions to other energy regions. We have to keep in mind that the level scheme in ^{120}Sn is considered to be complete up to the fifth excited level at 2.16 MeV.

The experimental levels used are also the reason why the RQTBA strength function and the HFB strength function - which are perspicuously distinct - give very similar cross sections and reaction rates. Both strength functions differ mostly in the energy regions of the transitions to the excited states. Therefore we only see a minor difference in the cross section and the reaction rate because this energy region contributes marginally.

model	E_0 [MeV]	Γ [MeV]
RQTBA+SLO/RQTBA+MLO	15.35	5.25
LD+SC	15.67	5.25
RIPL-2	15.60	4.94
exp. [FBC+69]	15.53	5.03
exp. [LBB+74]	15.50	5.26

Table 7.9: Experimental and theoretical Lorentzian parameters of the giant dipole resonance in ^{120}Sn. The experimental values were determined between 13 and 18 MeV (see [DB88]).

7.2.2.7 ^{124}Sn

^{124}Sn is the heaviest stable tin isotope that can be found in nature with an abundance of 5.79%. It is considered to be synthesised mainly from r-process as the lighter ^{123}Sn is β^--unstable and the s-process cannot reach ^{124}Sn. The neutron separation energy is $S_n = 8.49$ MeV. The situation for the ^{123}Sn$(n,\gamma)^{124}$Sn is similar to the ^{119}Sn$(n,\gamma)^{120}$Sn reaction. Figure 7.13 shows that the RQTBA model predicts again additional E1 strength at the neutron separation energy but inhibiting a much broader structure. However, this additional strength does not affect the cross section and the reaction rate. We can see that the additional strength does effect the transitions to the ground state and the first excited state in fig. 7.13, nonetheless. Finally, we note that the integrand in fig. 7.13 has a much broader structure than the one in fig. 7.12. This results from a particularly larger predicted level density in ^{124}Sn compared to ^{120}Sn, which can be seen in fig. 7.16.

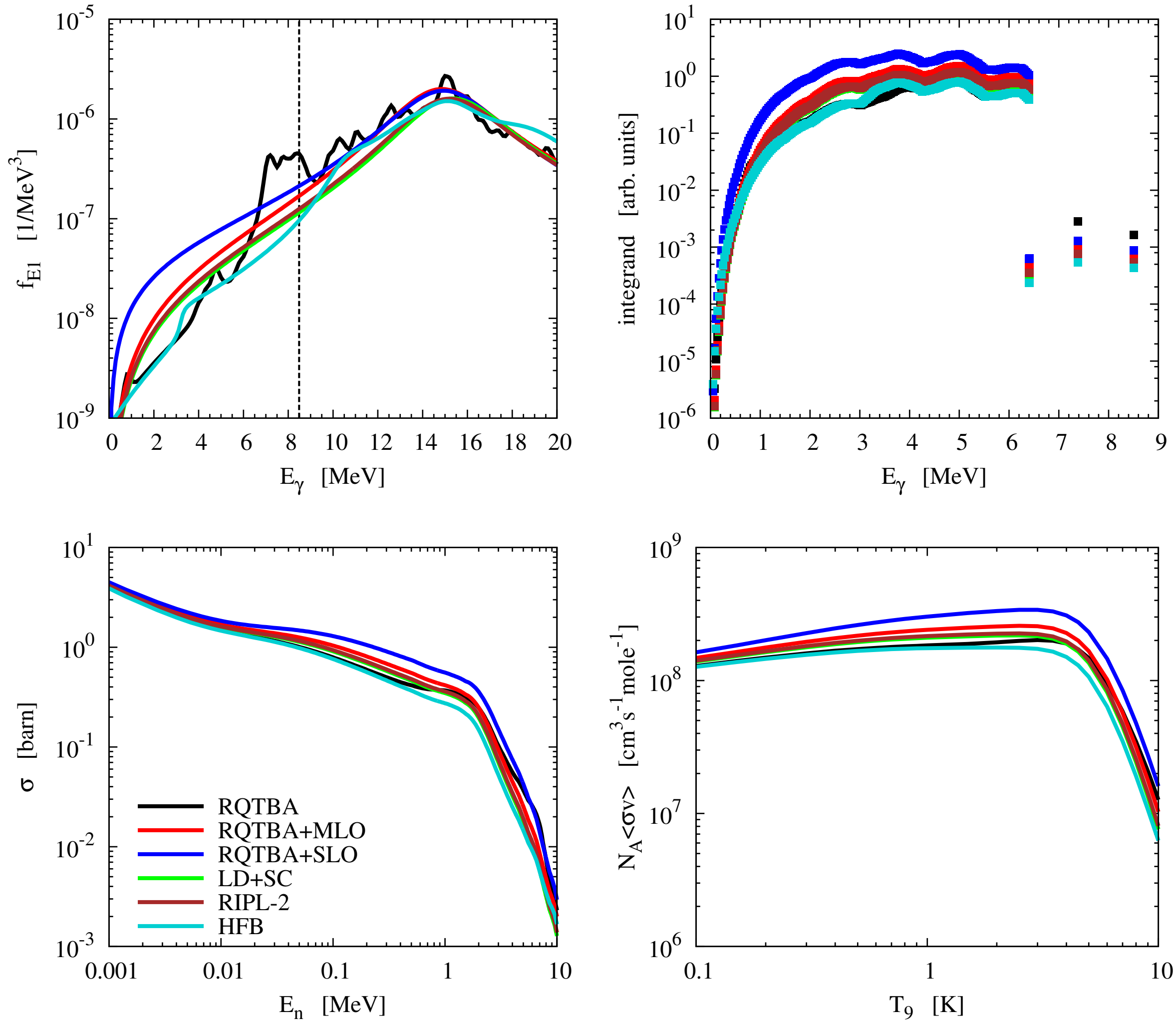

Figure 7.13: ^{123}Sn$(n,\gamma)^{124}$Sn - the upper left panel shows the different E1 strength functions and the vertical line marks the neutron separation energy. The upper right panel shows the γ-integrand as explained in section 7.1.2.1 evaluated for a kinetic neutron energy of $E_{\mathrm{kin}} = 24$keV. The lower-left panel shows the laboratory ^{123}Sn$(n,\gamma)^{124}$Sn cross section. The lower-right panel shows the stellar reaction rate. The green and the brown lines lie upon each other.

The existence of a pygmy dipole resonance in ^{124}Sn has been experimentally studied in [ÖEv$^+$07, ELS$^+$10].

model	E_0 [MeV]	Γ [MeV]
RQTBA+SLO/RQTBA+MLO	15.13	4.77
LD+SC	15.63	4.77
RIPL-2	15.48	4.87
exp. [FBC+69]	15.30	4.98
exp. [LBB+74]	15.39	4.90
exp. [IAEb]	15.40	5.00

Table 7.10: Experimental and theoretical Lorentzian parameters of the giant dipole resonance in ^{124}Sn. The experimental values were determined between 13 and 18 MeV (see [DB88]).

7.2.2.8 ^{130}Sn

With the isotope ^{130}Sn we are now on the neutron-rich side of the nuclear chart with a neutron separation energy of $S_n = 7.61$ MeV. We are going to discuss the first nucleus in which the predicted Lorentz parameters differentiate much stronger between the different approaches compared to the nuclei discussed before; see table 7.11.

The (n,γ) cross section and reaction rate of this reaction are particularly relevant during the freeze-out of the r-process, as a change in this cross section does not only change abundance of ^{130}Sn, but also leads to a shift in the abundance pattern in the rare earth region and the regions of the third peak [BBH$^+$09].

model	E_0 [MeV]	Γ [MeV]
RQTBA+SLO/RQTBA+MLO	14.63	4.18
LD+SC	15.59	4.18
RIPL-2	15.31	4.77
exp. [AKF$^+$05]	15.9(5)	4.80(1.7)

Table 7.11: Experimental and theoretical Lorentzian parameters of the giant dipole resonance in ^{130}Sn.

From table 7.11 we can see that the decrease in the centroid energy E_0 in the RQTBA+MLO and RQTBA+SLO models, which we have already seen between ^{120}Sn and ^{124}Sn, continues also in ^{130}Sn. The other Lorentzian approaches give a much smaller decrease.

The very striking dips in the integrand of fig. 7.14 are dips in the level density; we can correlate them to the dips shown in fig. 7.15. Moreover, the level density in ^{130}Sn is particularly smaller compared to ^{124}Sn and according to [IAEb], the level scheme cannot be considered complete. Thus, we have to employ the level density treatment to all excited states in ^{130}Sn. All these issues lead to the combined effect that the integrand's maximum in fig. 7.14 becomes very broad compared to the previous reactions. Similar to the previously discussed nuclei, the RQTBA strength function shows a particularly enhanced strength around the neutron separation energy. As the integrand shows the aforementioned broad structure, this additional strength can be identified in the integrand for the transitions between 6.5 to 7.61 MeV. This additional strength is compensated by the low strength for smaller E_γ.

The fact that the integrand shows this broad structure implies that the energy E_γ^3 energy dependence of the γ-transmission coefficient can compete with the level density due to the small level density and the absence of experimental excited states. Thus, the high energy transitions are of contrastable magnitude as the medium energy transitions. This can be seen in the cross section for the RQTBA strength function in fig. 7.14: with increasing neutron energy the cross section for the RQTBA strength function becomes larger than all the other cross sections. In particular it becomes larger than the RQTBA+SLO cross section due to the additional structure in the strength function.

The possibility of a pygmy dipole resonance in ^{130}Sn has been experimentally addressed in [AKF$^+$05, KPA$^+$07]. In these experiments additional E1 strength being assigned to a pygmy resonance was found, however at larger energies than predicted by the RQTBA. Unfortunately, the results are not conclusive enough to prove the existence of a pygmy resonance and the experiments are going to be repeated.

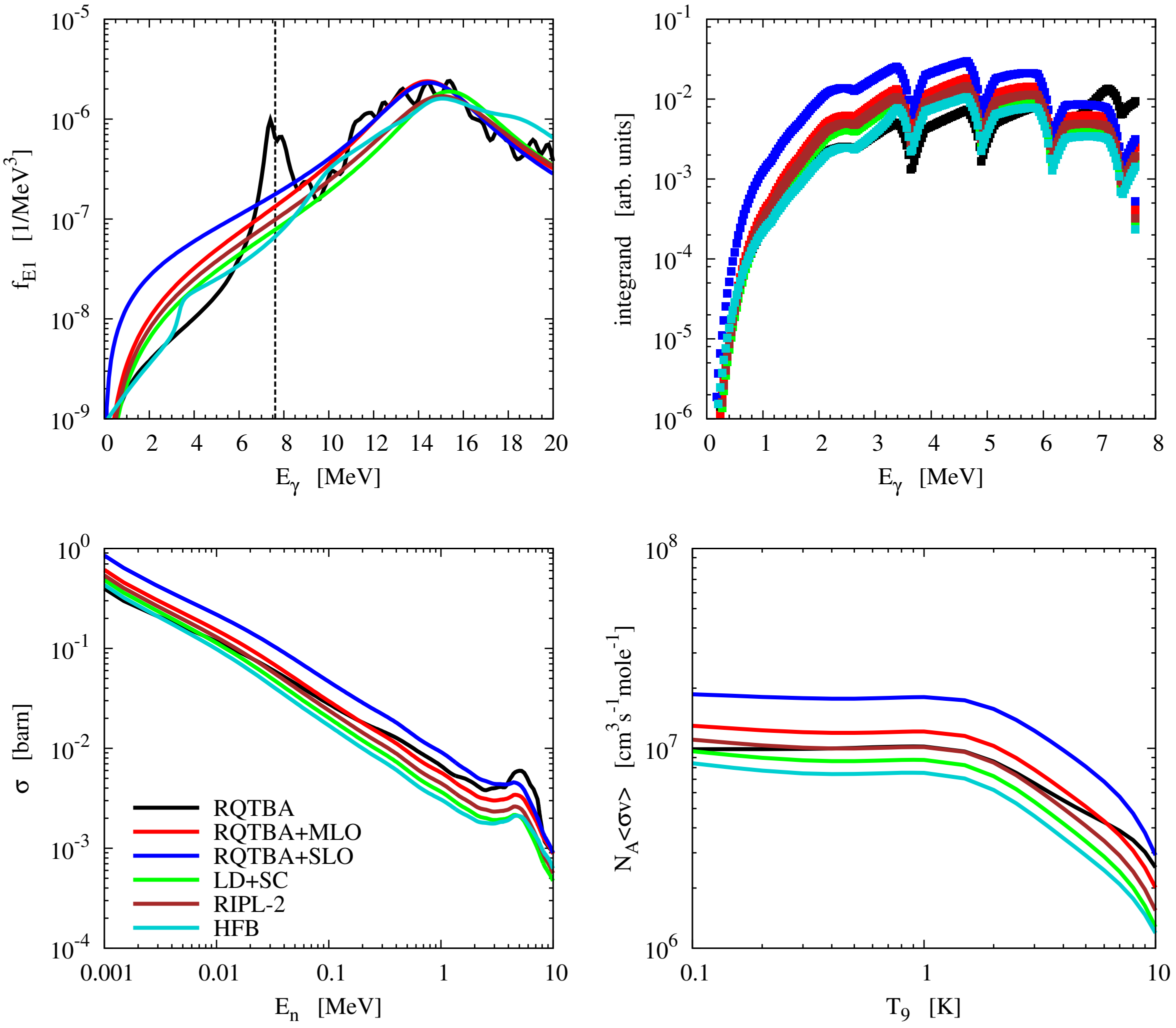

Figure 7.14: ^{129}Sn(n,γ)^{130}Sn - the upper left panel shows the different E1 strength functions and the vertical line marks the neutron separation energy. The upper right panel shows the γ-integrand as explained in section 7.1.2.1 evaluated for a kinetic neutron energy of $E_{\mathrm{kin}} = 27$keV. The lower-left panel shows the laboratory ^{129}Sn(n,γ)^{130}Sn cross section. The lower-right panel shows the stellar reaction rate.

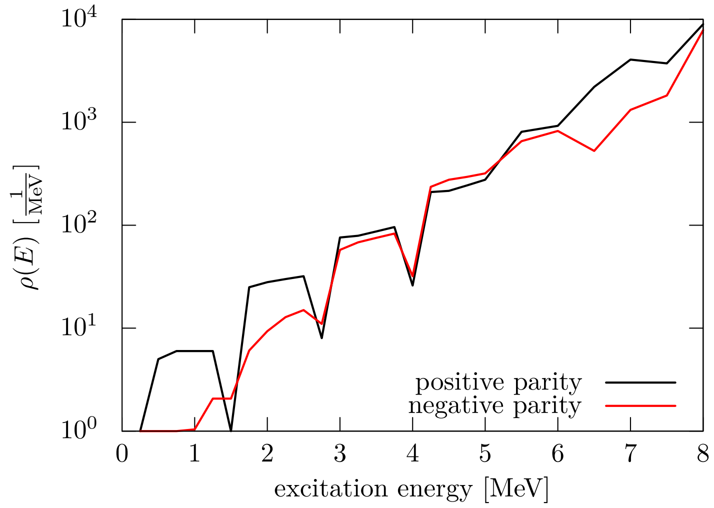

Figure 7.15: Parity projected nuclear level densities of ^{130}Sn from [GHK08].

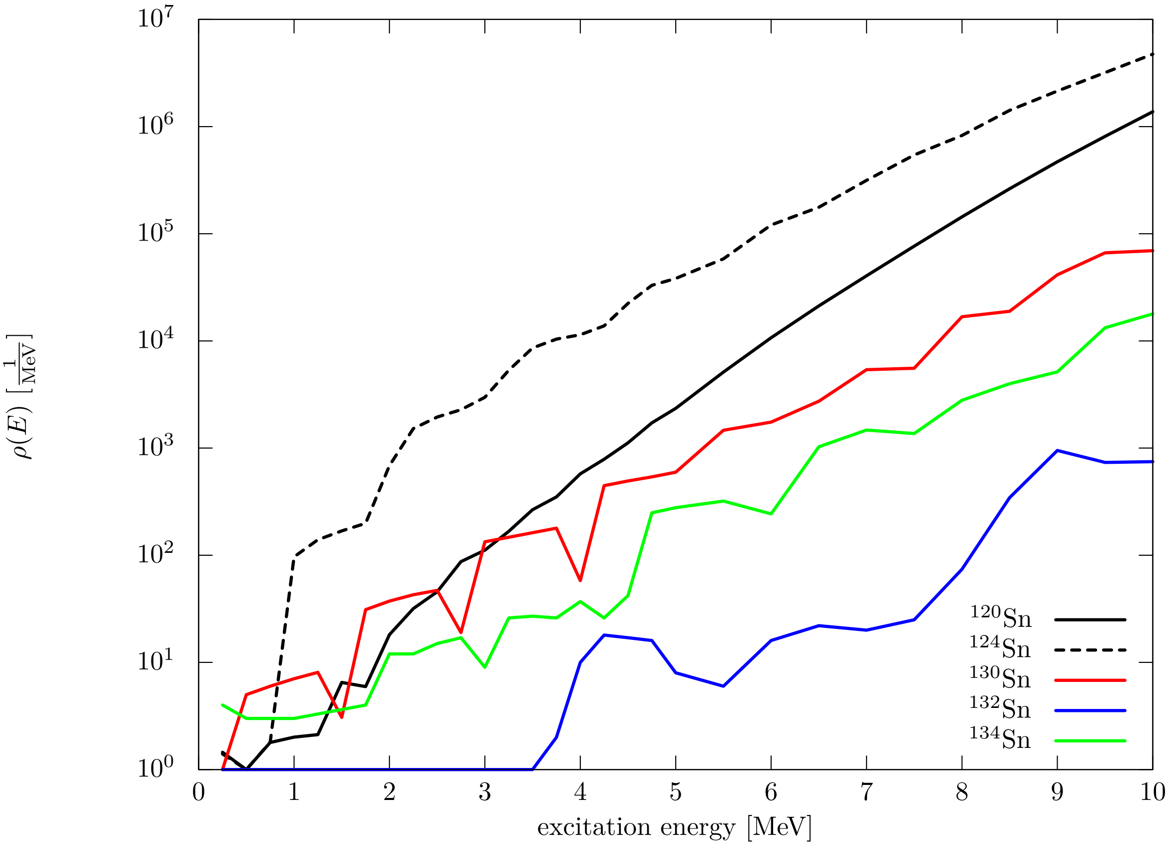

Figure 7.16: Nuclear level densities of ^{120}Sn, ^{124}Sn, ^{130}Sn, and ^{132}Sn from [GHK08]. The enhancement of the level density of ^{124}Sn compared to the one of ^{120}Sn probably results from the fact that in ^{120}Sn the 3s2d-shell is closed (N=70) in the single particle picture. The much smaller level density of ^{132}Sn results from the fact that this nucleus is doubly magic.

7.2.2.9 ^{132}Sn

The doubly magic nucleus ^{132}Sn [JAB^{+}10] is of particular interest for the r-process as it might act as a waiting point nucleus, although the neutron separation energy is relatively large with $S_n = 7.35$ MeV.

As ^{132}Sn is doubly magic, the level density in this nucleus is particularly low and a rather large shell gap exists; the first excited state is a 2^+ state located at 4.04 MeV [ENS]. We can see this large gap in the integrand of fig. 7.17. The exceedingly small level density suppresses transitions of low and intermediate energy. The large shell gap additionally obviates transitions between 3.5 and 7.3 MeV.

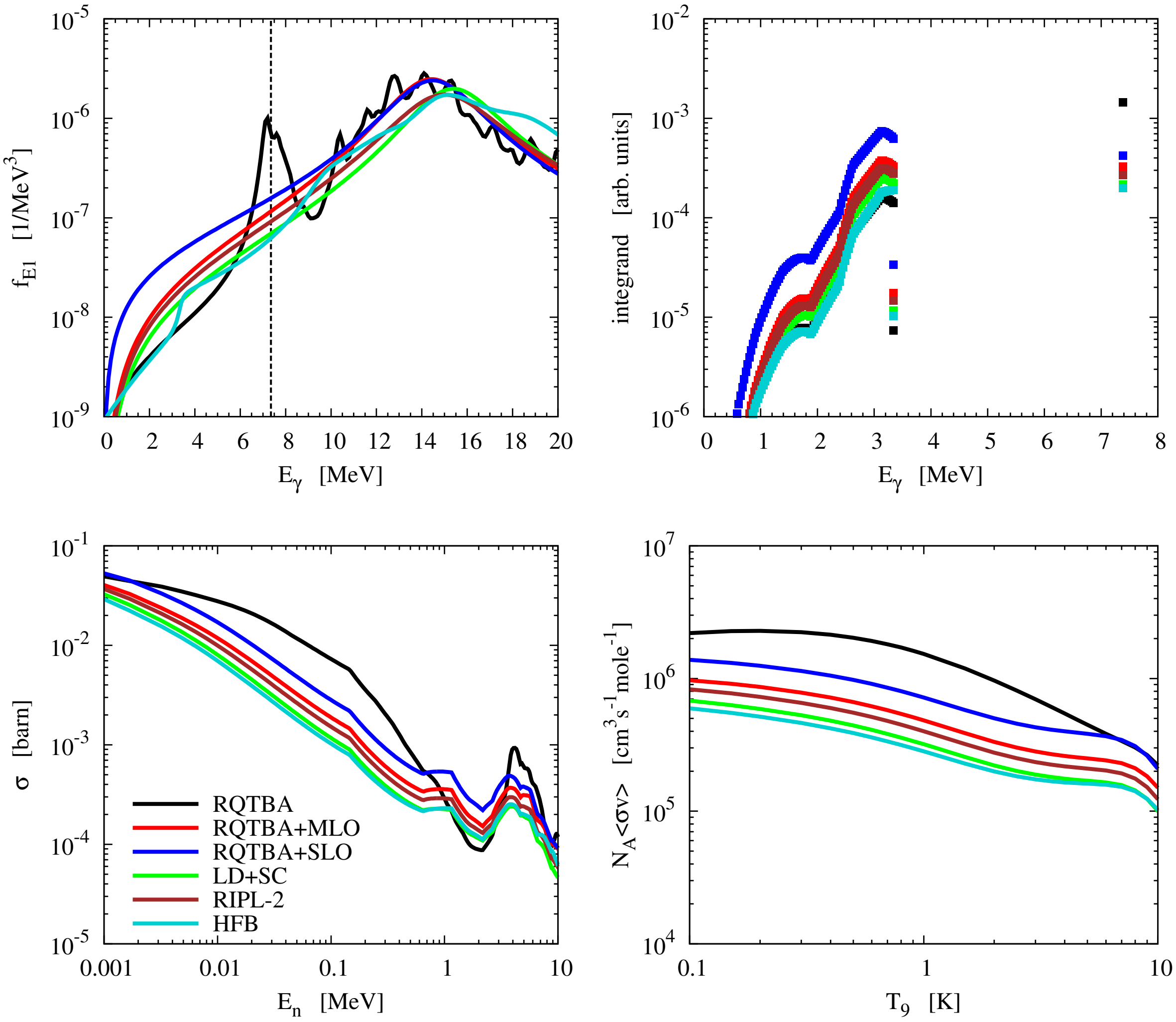

Figure 7.17: ^{131}Sn(n,γ)^{132}Sn - the upper left panel shows the different E1 strength functions and the vertical line marks the neutron separation energy. The upper right panel shows the γ-integrand as explained in section 7.1.2.1 evaluated for a kinetic neutron energy of E_{kin} = 28keV. The lower-left panel shows the laboratory ^{131}Sn(n,γ)^{132}Sn cross section. The lower-right panel shows the stellar reaction rate.

In fig. 7.17 we notice that we have again a strong enhancement of the RQTBA strength function around the neutron threshold like in the previously discussed nuclei. However, as the the transitions to the level density regime are suppressed, this additional strength notably enhances the transition to the ground state. This enhancement in the RQTBA strength function at the neutron separation energy induces the dominance of the ground state transition relative to the transitions to excited states for this particular strength function. The other models do not predict an additional strength, thus the integrand has its maximum around E_γ =3 MeV for these strength functions.

The cross section and the reaction rate show the enhancement of the additional E1 strength in the

model	E_0 [MeV]	Γ [MeV]
RQTBA+SLO/RQTBA+MLO	14.62	4.02
LD+SC	15.58	4.02
RIPL-2	15.26	4.74
exp. [AKF$^+$05]	16.1(5)	4.7(2.1)

Table 7.12: Experimental and theoretical Lorentzian parameters of the giant dipole resonance in ^{132}Sn.

RQTBA approach. The cross section shows the structure of the RQTBA strength function with increasing energy, i.e. the transition to the ground state notably contributed to the cross section for even higher neutron energies. The dip in the cross section of all used strength functions, results from the use of non uniformly distributed parities at the relevant compound energy [LLMP$^+$08, LLL$^+$09]. With regard to the RQTBA strength function, the minimum between 9 to 10 MeV interferes with the parity treatment, leading to a deeper dell in the cross section compared to the other strength functions.

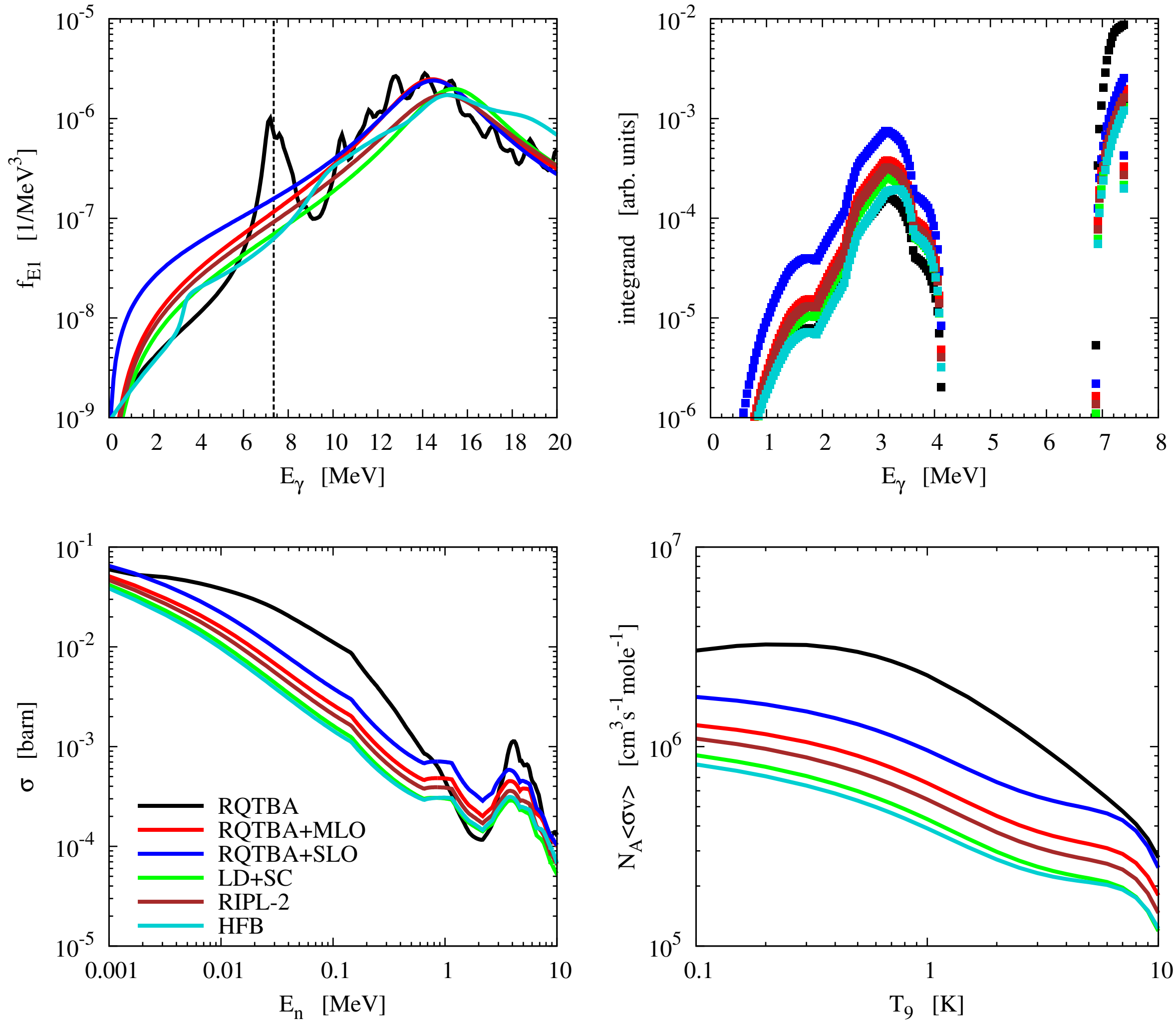

Figure 7.18: Same as fig. 7.17, but without the first excited 2^+ state. This plot also gives an example with respect to a general problem in the level density; see text for details.

In fig. 7.18 we have plotted the same quantities as in fig. 7.17, however we have artificially removed the first excited 2^+ state. By comparing the integrands in fig. 7.17 and fig. 7.18, we can see that the gap in the level density accounts for the high lying 2^+ state. Despite the fact that we can see transitions to states just above the ground state (which result from interpolation), the situation does not change much. However, this is an example of a problematic issue regarding the level densities of [GHK08]: apparently the ground state is included as the level density is non-vanishing at the lowest grid point of 0.25 MeV, which leads to the aforementioned interpolation issues. Nevertheless, in the case of fig. 7.18 the peak of the RQTBA strength function has a much larger influence on the cross section and the reaction rate. Hence, this is a nice example how important the knowledge of individual levels at low excitation energies can be; note that the reaction rate in fig. 7.18 is larger by a factor of 1.25 to 2 compared to fig. 7.17.

Finally, it is necessary to note, that the application of the Hauser-Feshbach model for the reaction $^{131}\mathrm{Sn}(n,\gamma)^{132}\mathrm{Sn}$ is questionable due to the low level density in $^{132}\mathrm{Sn}$. Nevertheless, our calculations show how important possible pygmy resonances might become.

7.2.2.10 ^{134}Sn

The reaction $^{133}\mathrm{Sn}(n,\gamma)^{134}\mathrm{Sn}$ has a much smaller cross section and reaction rate compared to the previously discussed reaction due to the considerably smaller phase space defined by the neutron separation energy $S_n = 3.54$ MeV.

The most striking detail of the integrand in fig. 7.19 is the fact that its maximum corresponds to the transitions of the highest available energies. This is due to a rather small level density (see fig. 7.16) in the relevant energy range up to the neutron threshold.

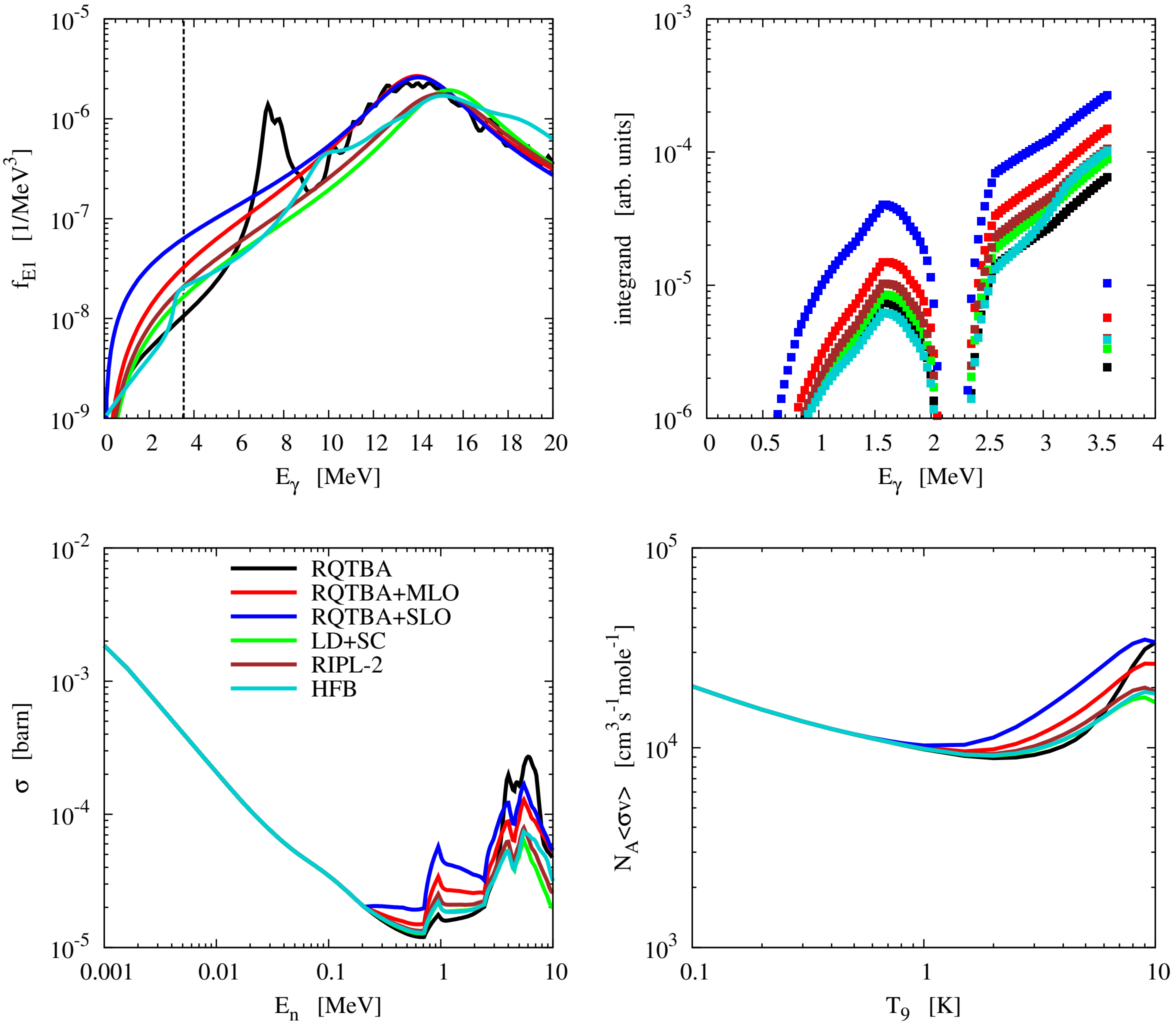

Figure 7.19: $^{133}\mathrm{Sn}(n,\gamma)^{134}\mathrm{Sn}$ - the upper left panel shows the different E1 strength functions and the vertical line marks the neutron separation energy. The upper right panel shows the γ-integrand as explained in section 7.1.2.1 evaluated for a kinetic neutron energy of $E_{\mathrm{kin}} = 25$keV. The lower-left panel shows the laboratory $^{133}\mathrm{Sn}(n,\gamma)^{134}\mathrm{Sn}$ cross section. The lower-right panel shows the stellar reaction rate.

In ^{134}Sn we have a peculiar situation regarding the distribution of parities and spins around and above the neutron threshold: up to 3.75 MeV no states with negative parity are predicted. From this energy on, 3^- levels are predicted; the other spins occur at slightly higher energies with negative parity - see fig. 7.20. We can explain the very peculiar behaviour of the cross section in fig. 7.19 with fig. 7.20.

The fact that no states with negative parity are predicted below 3.75 MeV completely suppresses parity-changing transitions, i.e. E1 transitions in our case. Therefore, we do not see any difference between the used strength functions up to neutron energies of around 0.2 MeV- the cross section is dominated by M1 transitions up to this energy. The sudden change around 0.2 MeV arises from the

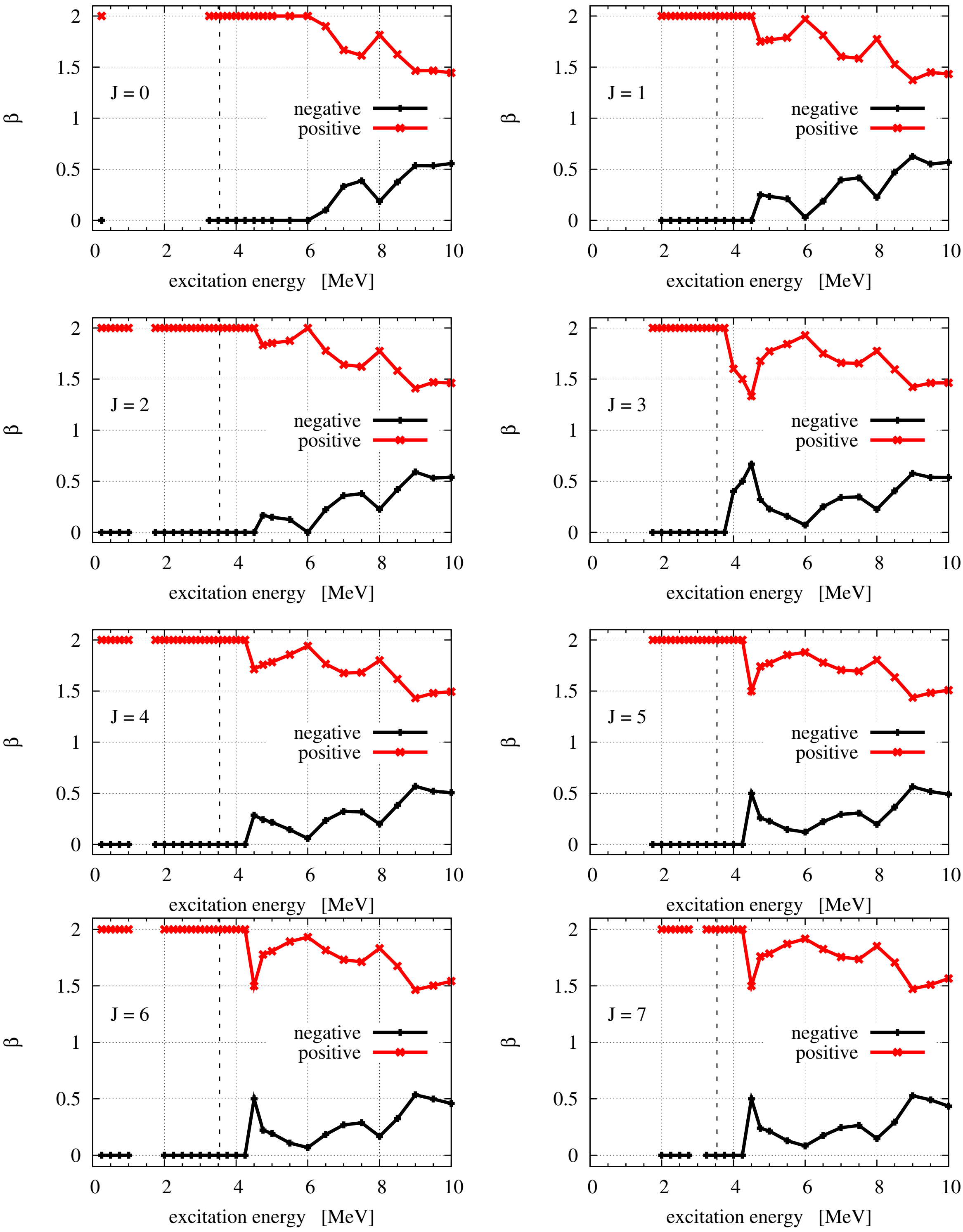

Figure 7.20: β-values for ^{134}Sn for J=0 to J=7. Missing points correspond to the fact that none of the two parities are predicted; this corresponds to $\beta = 1$. However, we do not have transitions into these regions, as there are no levels predicted.

availability of J=3$^-$ states. The effect turns out to be so strong, because the E1 transitions are larger than the M1 transitions and J=3 states are favoured in the compound nucleus, as the ground state of

^{133}Sn is a $\frac{7}{2}^-$ state thus favouring J=3,4 states in ^{134}Sn via s-wave neutron capture. The kink around 0.7 MeV corresponds to a compound energy of 4.25 MeV at which other J$^-$ states are predicted. The same accounts for the prominent peak around 1.0 MeV, as this peak can be related to the sudden increase in negative parity states for J=1 to J=7 at 4.5 MeV. The dip around 4 to 5 MeV corresponds to the dip in the β values at 8 MeV in fig. 7.20.

model	E_0 [MeV]	Γ [MeV]
RQTBA+SLO/RQTBA+MLO	14.17	4.17
LD+SC	15.57	4.17
RIPL-2	15.20	4.70

Table 7.13: Theoretical Lorentzian parameters of the giant dipole resonance in ^{134}Sn.

The RQTBA model also predicts additional E1 strength around 6 to 9 MeV. Again we have a rather small level density, so that we can see the structure of this peak (overlaid with the aforementioned level density features) for neutron energies from 4 to 7 MeV. The reaction rate is not strongly affected by the different E1 prescriptions for temperatures up to $T_9 \approx 1$ K. For higher energies, we start to see differences as these favour larger neutron energies. The reaction rate is strongly influenced by the M1 transitions, because the E1 transitions are damped in this reaction when allowing for non-uniformly distributed parities in the compound nucleus (and when using the level densities of [HG07, GHK08]). This is an example that for certain reactions, not only a good description for the E1 transitions is needed, but also for the M1 transitions. In conclusion, we have to note that we have excluded E2 transitions for our calculations. As E2 transitions - like the M1 transitions - do not change parity, they may be important in this particular reaction.

7.2.2.11 ^{136}Sn

The reaction ^{135}Sn(n,γ)^{136}Sn is of particular interest as the RQTBA predicts a rather broad structure of additional E1 strength around 7 MeV in ^{134}Sn compared to the previous cases. In fig. 7.21 we can see that the cross section becomes sensitive to this strength at neutron energies between 3 to 8 MeV. This results again from the small phase space ($S_n = 3.77$ MeV): the integrand also shows a well-defined maximum around 2 to 2.5 MeV, however the transitions to the low-lying excited states are of comparable magnitude. Therefore, the structure effects of the RQTBA strength function plainly influence the cross section.

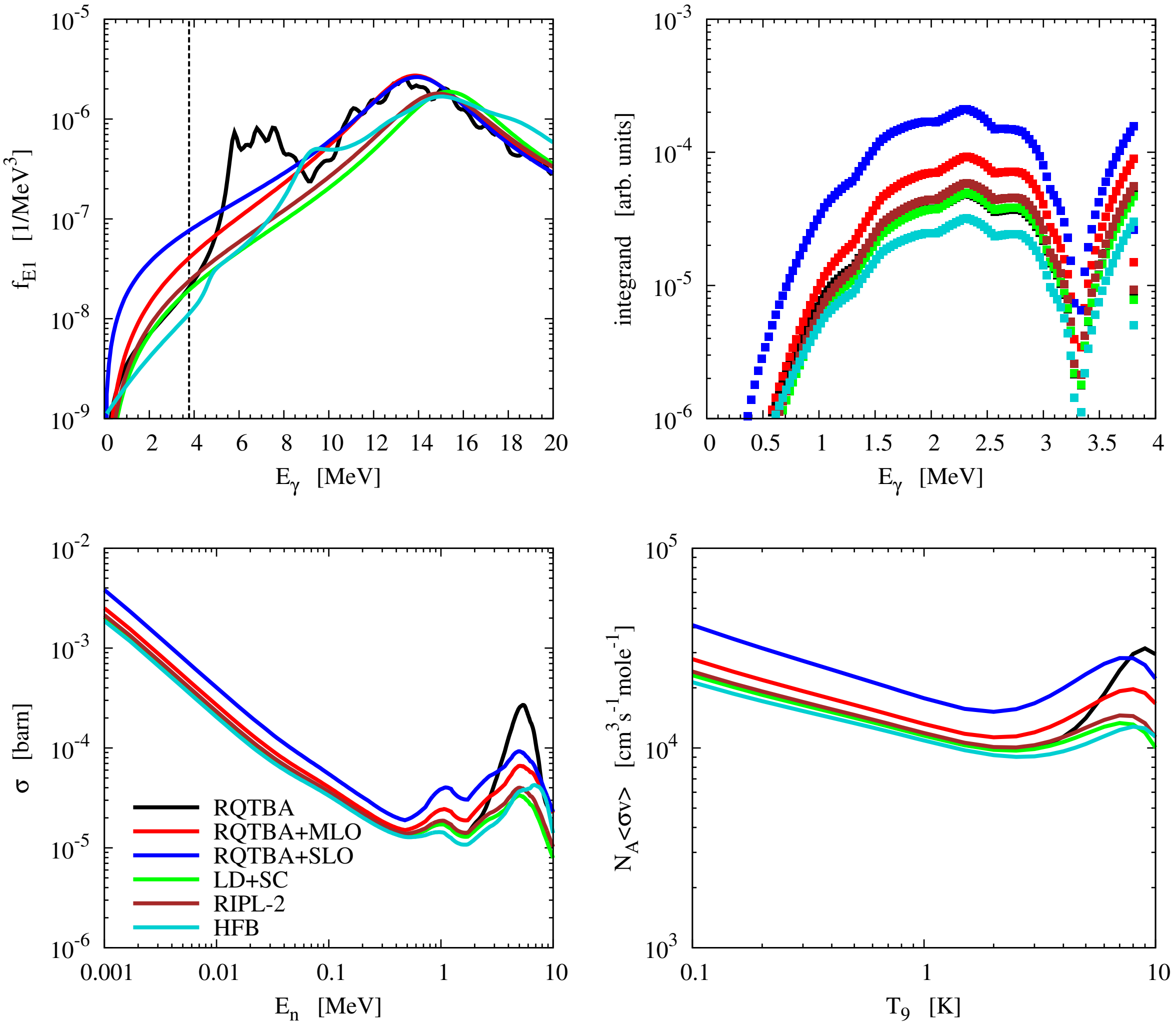

Figure 7.21: ^{135}Sn(n,γ)^{136}Sn - the upper left panel shows the different E1 strength functions and the vertical line marks the neutron separation energy. The upper right panel shows the γ-integrand as explained in section 7.1.2.1 evaluated for a kinetic neutron energy of $E_{\mathrm{kin}} = 29$keV. The lower-left panel shows the laboratory ^{135}Sn(n,γ)^{136}Sn cross section. The lower-right panel shows the stellar reaction rate.

The HFB strength function also shows additional strength for this nucleus, however at slightly higher energies of around 9 MeV. This additional strength is also visible in the cross section at neutron energies above 6 to 7 MeV.

As there are practically no states with negative parity predicted in ^{136}Sn below the neutron separation energy (see fig. 7.22), we mainly have M1 transitions. We do not see this in the integrand as the integrand does not account for the parity-dependence in the compound nucleus, i.e. it assumes that both parities are uniformly distributed for the initial compound states.

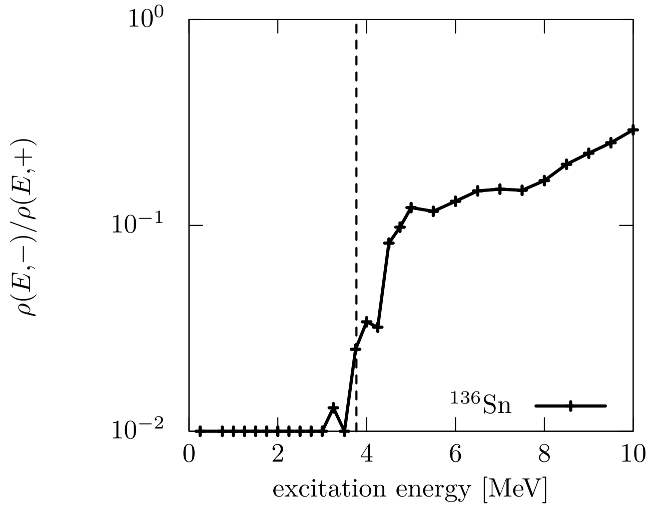

Figure 7.22: The ratio of the negative parity level density to the positive parity level density in ^{136}Sn from [GHK08]. The vertical dashed line marks the neutron separation energy. Note that the y-axis ends at unity, i.e. uniformly distributed parities.

model	E_0 [MeV]	Γ [MeV]
RQTBA+SLO/RQTBA+MLO	14.11	4.33
LD+SC	15.56	4.33
RIPL-2	15.15	4.67

Table 7.14: Theoretical Lorentzian parameters of the giant dipole resonance in ^{136}Sn.

7.2.2.12 ^{138}Sn

The reaction ^{137}Sn(n,γ)^{138}Sn - its details shown in fig. 7.23 - is very similar to the reaction ^{133}Sn(n,γ)^{134}Sn - which is shown in fig. 7.19 - in the sense, that we have one parity dominating up to energies above the neutron threshold, the latter being $S_n = 3.49$ MeV (theoretical values from HFB14 [GSP07]). Additionally, the RQTBA strength function shows a peculiar additional strength around 5 to 8 MeV. This strength can be identified in the cross section for higher neutron energies, like in the reaction ^{135}Sn(n,γ)^{136}Sn (see fig. 7.21). According to table 7.15, the predicted centroid energies differ quite strongly, which is the reason why all RQTBA-based strength functions predict larger cross sections (in the relevant energy range) and reaction rates compared to the other approaches. Nevertheless, the RQTBA strength function in fig. 7.23 shows a very broad resonance structure, i.e. the fitted width is about $\Gamma_{\mathrm{RQTBA}} \approx 5.3$ MeV; substantially larger than the widths in table 7.15. A re-fit with the fixed width given in table 7.15 would slightly shift the centroid energy for the **RQTBA+MLO/SLO** strength functions. This shift would not have a noteworthy impact on the presented outcomes.

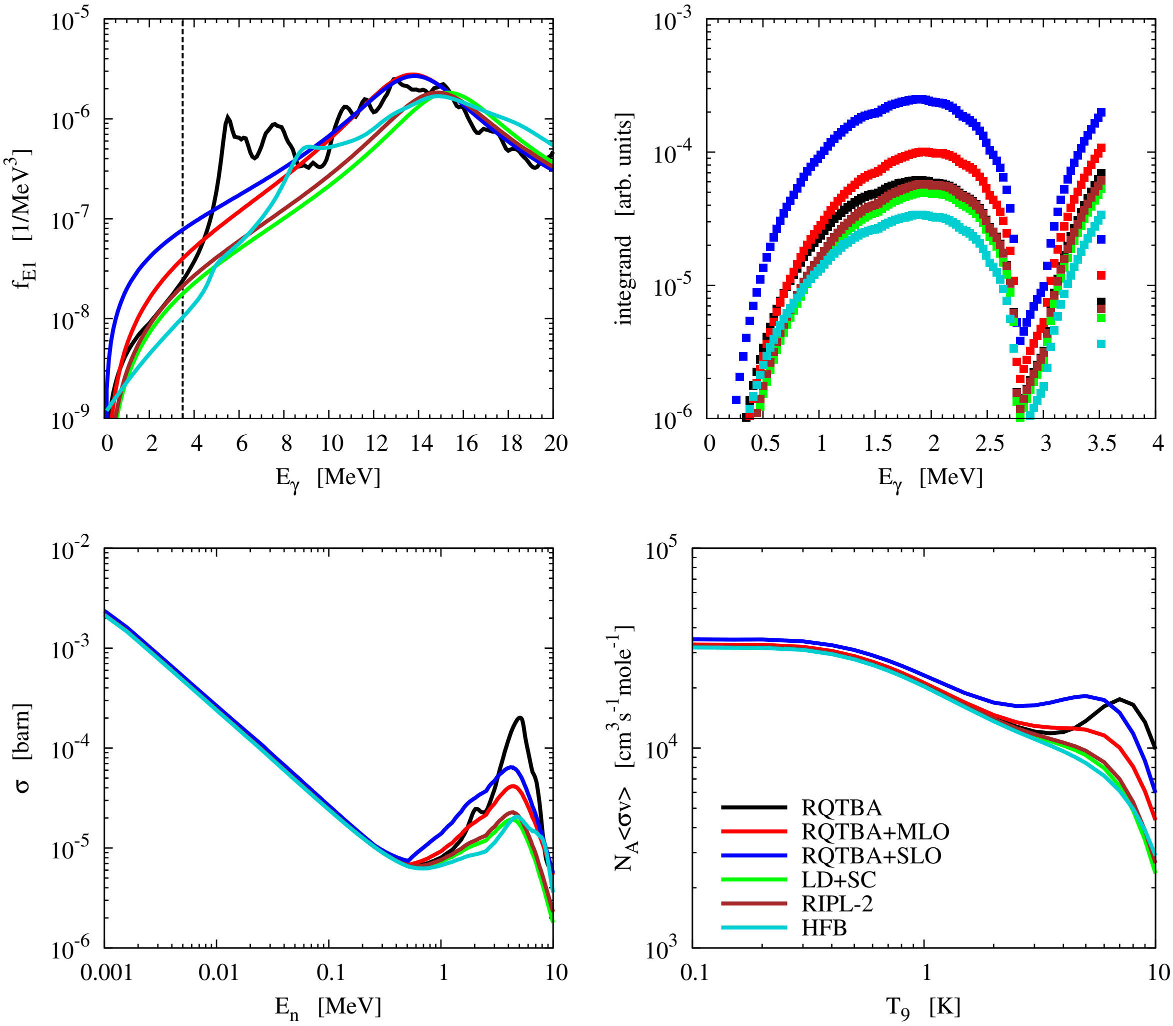

Figure 7.23: ^{137}Sn(n,γ)^{138}Sn - the upper left panel shows the different E1 strength functions and the vertical line marks the neutron separation energy. The upper right panel shows the γ-integrand as explained in section 7.1.2.1 evaluated for a kinetic neutron energy of $E_{\mathrm{kin}} = 26$keV. The lower-left panel shows the laboratory ^{137}Sn(n,γ)^{13}Sn cross section. The lower-right panel shows the stellar reaction rate.

model	E_0 [MeV]	Γ [MeV]
RQTBA+SLO/RQTBA+MLO	14.00	4.51
LD+SC	15.52	4.51
RIPL-2	15.01	4.61

Table 7.15: Theoretical Lorentzian parameters of the giant dipole resonance in ^{138}Sn.

7.2.2.13 ^{140}Sn

The RQTBA model predicts substantial low-lying E1 strength between 4 to 5 MeV. As the HFB14 mass model predicts the neutron separation in ^{140}Sn to be $S_n = 4.16$ MeV, we have once again the case (as in ^{132}Sn), that this additional E1 strength is located at the neutron threshold. Similar to the ^{131}Sn(n,γ)^{132}Sn reaction, the nucleus ^{140}Sn shows a rather small level density and the transitions to the ground state and the first excited states are rather large according to the integrand in fig. 7.24 (compared to the transitions into the level density regime). However, a nearly vanishing level density between 0.5 and 1.5 MeV strongly damps all transitions into this region. Moreover, we have a dominance of M1 transitions, as positive parity states prevail at these energies (see fig. 7.25). Nevertheless, we have an E1 contribution from transitions up to E_γ =1.0 MeV. As the integrand of the RQTBA+SLO strength function is much larger than the integrand for the other strength function in the range up to 1.0 MeV, the cross section obtained with the RQTBA+SLO is slightly larger compared to the other approaches, although M1 transitions dominate. With increasing neutron energy, i.e. from 1 to 8 MeV, the cross section becomes sensitive to the individual structure in the RQTBA strength function, in particular to the two peaks around 5 and 7.5 MeV. This feature is passed over to the reaction rate, which shows an eminent enhancement at higher temperatures due to the structure of the RQTBA strength function.

This reaction is an example for a reaction in which at first, M1 transitions dominate the cross section and reaction rate when using the picture of non-uniformly distributed parities in the compound nucleus. With increasing neutron energy, the contribution of E1 transitions grows due to the admixture of negative parity levels. Due to the large magnitude of E1 transitions relative to the M1 transitions, this enhancement in the contribution notably influences the cross section. The M1 transitions are still dominating regarding the number of transitions, though.

The discussed reaction is therefore an example for a nucleus in which we need to know all quantities as good as possible, i.e. the parity distribution within the level density, the M1 transitions, and the E1 transitions.

model	E_0 [MeV]	Γ [MeV]
RQTBA+SLO/RQTBA+MLO	13.92	4.66
LD+SC	15.55	4.66
RIPL-2	15.05	4.61

Table 7.16: Theoretical Lorentzian parameters of the giant dipole resonance in ^{140}Sn.

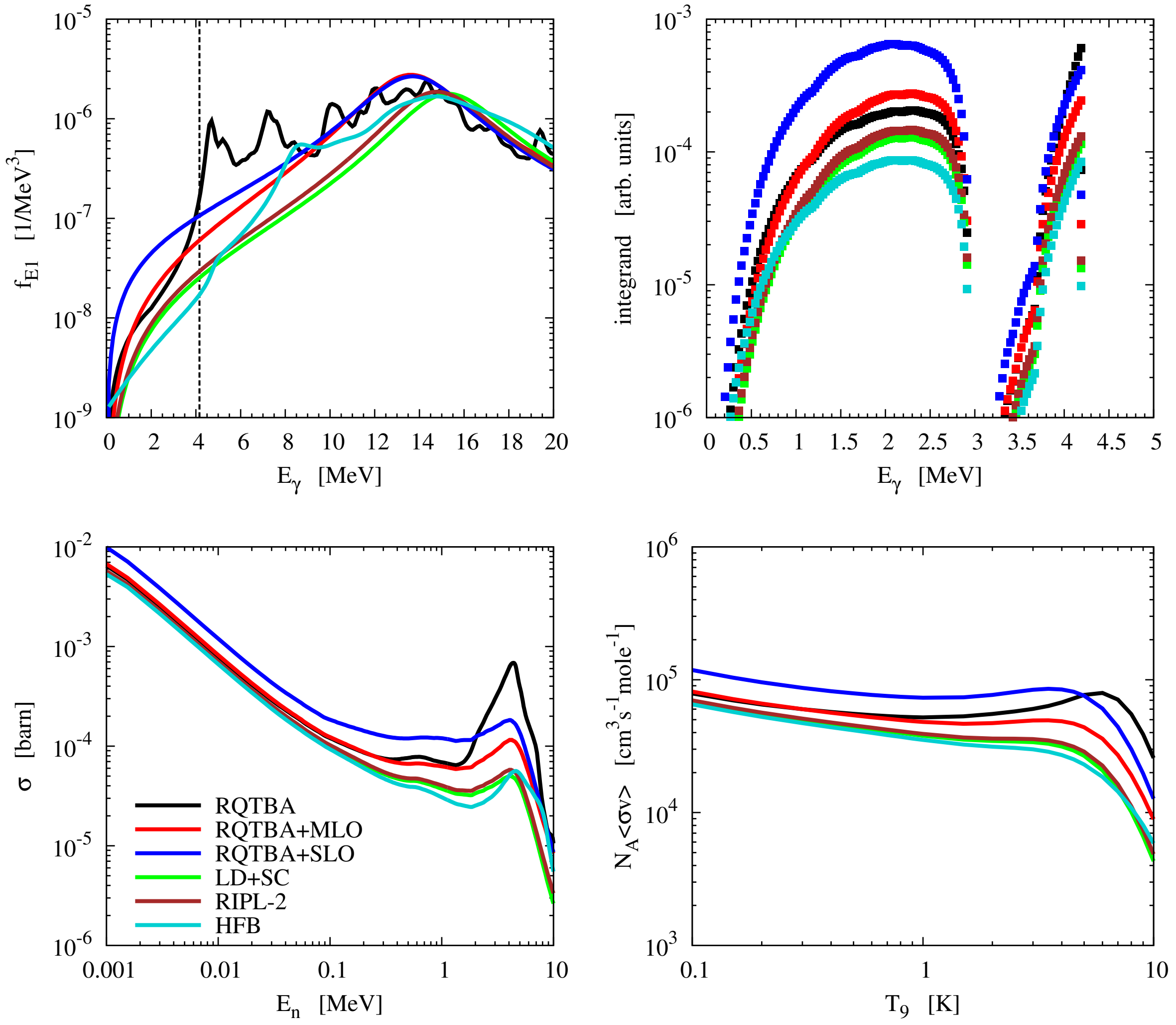

Figure 7.24: ^{139}Sn(n,γ)^{140}Sn - the upper left panel shows the different E1 strength functions and the vertical line marks the neutron separation energy. The upper right panel shows the γ-integrand as explained in section 7.1.2.1 evaluated for a kinetic neutron energy of $E_{\mathrm{kin}} = 23$keV. The lower-left panel shows the laboratory ^{139}Sn(n,γ)^{140}Sn cross section. The lower-right panel shows the stellar reaction rate.

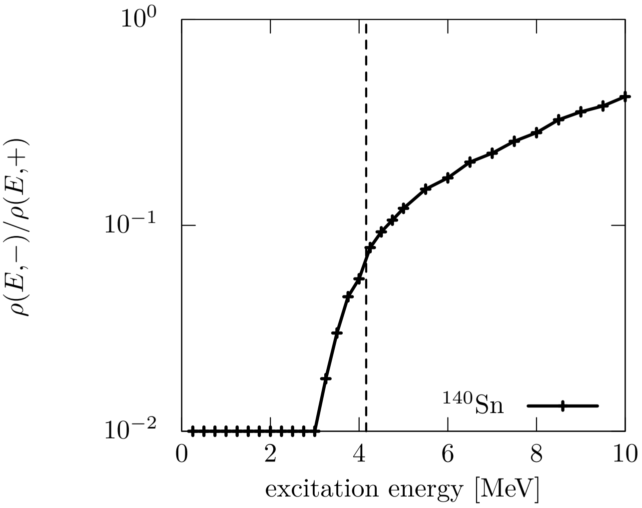

Figure 7.25: The ratio of the negative parity level density to the positive parity level density in ^{140}Sn from [GHK08]. The vertical dashed line marks the neutron separation energy. Note that the y-axis ends at unity, i.e. uniformly distributed parities.

7.2.3 Nickel Isotopes

We have repeated the investigations of section 7.2.2 with the even-even nickel isotopes $^{68-78}$Ni. With Z=28 protons, nickel belongs to the lighter elements created in the r-process. Most of its stable isotopes are mainly formed in the s-process with ^{58}Ni being the exception. This isotope cannot be formed by astrophysical neutron capture processes.

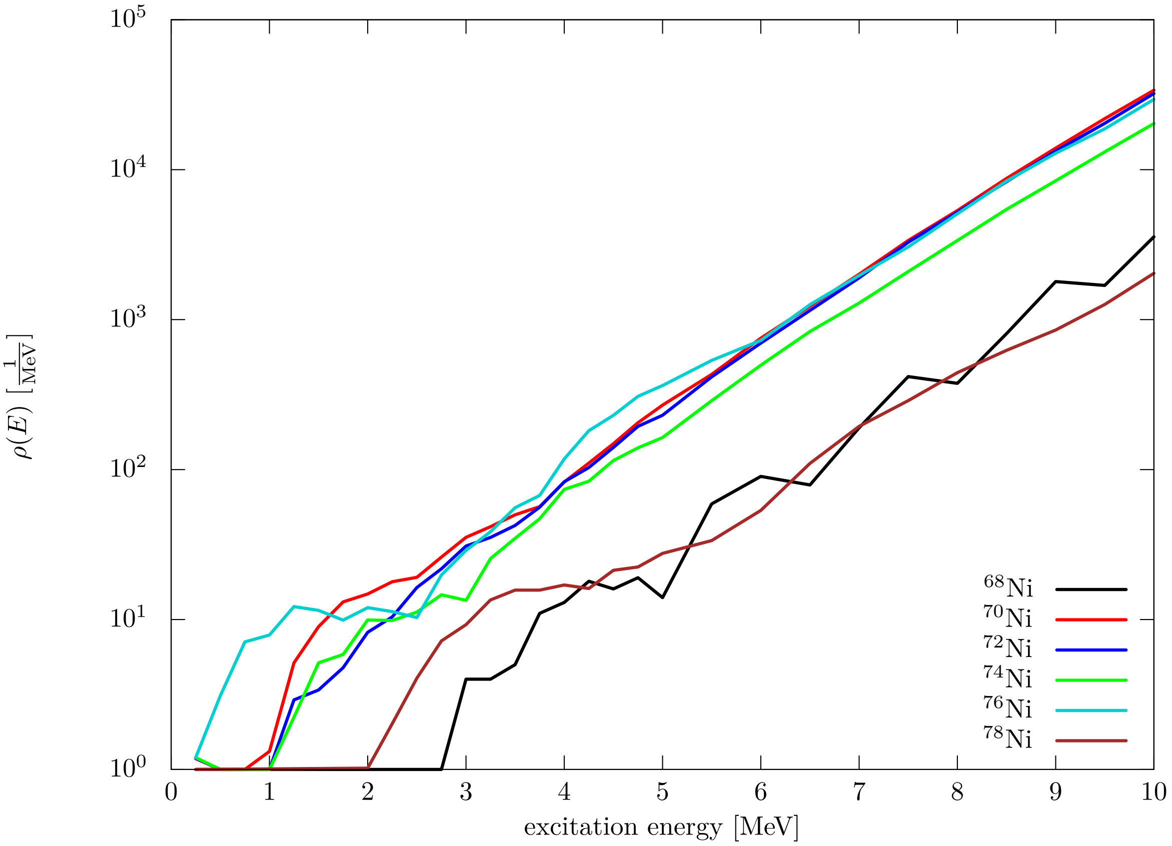

Figure 7.26: Nuclear level densities (summed over parity and spin) for the even-even nickel isotopes $^{68-78}$Ni of [GHK08]. **Important note:** the level density of ^{68}Ni appears to be of the same magnitude as the level density of ^{78}Ni up to 2 MeV, because we chose a logarithmic scale for the y-axis. The predicted HFB level density [GHK08] of ^{78}Ni vanishes between 0.25 MeV and 2 MeV, while the level density of ^{68}Ni is close to unity.

7.2.3.1 ^{68}Ni

The isotope ^{68}Ni, with its 28 protons and 40 neutrons, is of particular interest as the 40 neutrons just close the pf-shell in the single-particle picture. Thus, we expect that ^{68}Ni has a smaller level density than its neighbours (see fig. 7.26). Its neutron separation energy of $S_n = 7.8$ MeV indicates that it is located too close to the valley stability to be in the r-process path. Nevertheless, the RQTBA model predicts additional E1 strength just around the neutron thresholds, see fig. 7.27. This and the small level density enhance the transition to the ground state relative to the transitions to excited states as we can see in the integrand of fig. 7.27 and results in an enhancement of the cross section for low energies and the reaction rate for low temperatures. With increasing neutron energy, the transition to the ground state becomes smaller (due to the strength function) and less dominant. This explains the decrease of the cross section with increasing neutron energy relative to the other E1 strength functions. Furthermore, this argumentation can be assigned to the reaction rate in the same manner. At neutron energies between 1 to 10 MeV we start to see the structure effects of the RQTBA strength function[1]. This shows that the transition to the ground state (for a given neutron energy) is still important, although not dominating the cross section.

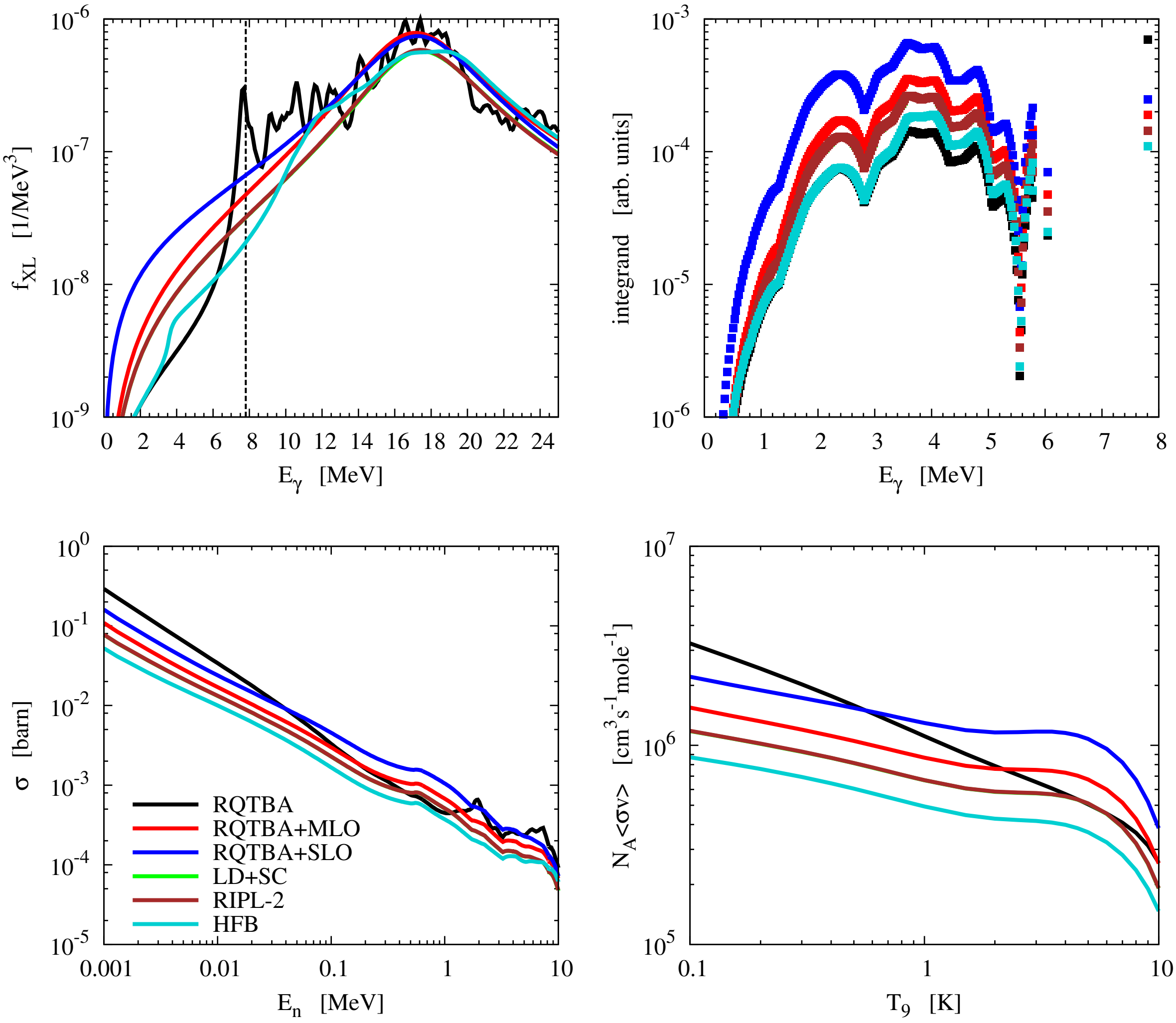

Figure 7.27: ^{67}Ni(n,γ)^{68}Ni - the upper left panel shows the different E1 strength functions and the vertical line marks the neutron separation energy. The upper right panel shows the γ-integrand as explained in section 7.1.2.1 evaluated for a kinetic neutron energy of $E_{\rm kin} = 21$keV. The lower-left panel shows the laboratory ^{67}Ni(n,γ)^{68}Ni cross section. The lower-right panel shows the stellar reaction rate.

The strong change in the temperature dependence of the reaction rate shows how important a possible pygmy resonance can become. The additional RQTBA strength is very narrow. With increasing neutron energy this strength is shifted into the energy region into which the level density prescription prevents transitions (the additional strength would lead to states in the shell-gap of the spectrum) and the cross section becomes insensitive to this strength. This results in a larger decline of the cross section and the reaction rate compared to the decrease when the other strength functions are utilised. This has a particularly large effect on the temperature dependence of the reaction rate. As we have already discussed in section 7.1.2.2, a change in the temperature dependence can establish a different r-process path, thus affecting the quality of the simulation. However, it is sufficient to mention that pygmy resonances in ^{68}Ni have been recently measured [WBC$^+$09] giving the pygmy resonance around 11 MeV.

We have to stress that the discussion above heavily depends on the predicted nuclear level density

---

[1] Note that the x-axis for the cross section is logarithmic, while the one of the strength function is linear.

of ^{68}Ni, which is particular small in the model we have used [GHK08]. The back-shifts obtained from nuclear masses according to section 3.2.1.2 are $\delta(^{68}\mathrm{Ni}) = 2.33$ MeV(from experiment; the theoretical value [MNMS95] would be 2.51 MeV) and $\delta(^{78}\mathrm{Ni}) = 2.34$ MeV (theoretical value from [MNMS95]). This already indicates that also in the back-shifted Fermi gas model, both level densities would be of similar magnitude.

model	E_0 [MeV]	Γ [MeV]
RQTBA+SLO/RQTBA+MLO	17.57	6.49
LD+SC	17.89	6.49
RIPL-2	17.84	6.39

Table 7.17: Theoretical Lorentzian parameters of the giant dipole resonance in ^{68}Ni.

As a final remark, it should be noted that due to the N=40 closure of the pf-shell ^{68}Ni is seen as a candidate for a neutron rich magic nucleus. This issue has been addressed in [LTN^{+}03].

7.2.3.2 ^{70}Ni

The RQTBA strength function in ^{70}Ni in fig. 7.28 is similar to the one of ^{68}Ni in fig. 7.27: it also shows additional E1 strength around and above the neutron separation energy of $S_n = 7.24$ MeV. However, the level density in ^{70}Ni is larger than in ^{68}Ni (see fig. 7.26) and the ground state transition cannot compete with the transitions to the level density regime. This highlights again the role of the level density in the competition between the γ-transitions to different energy regions.

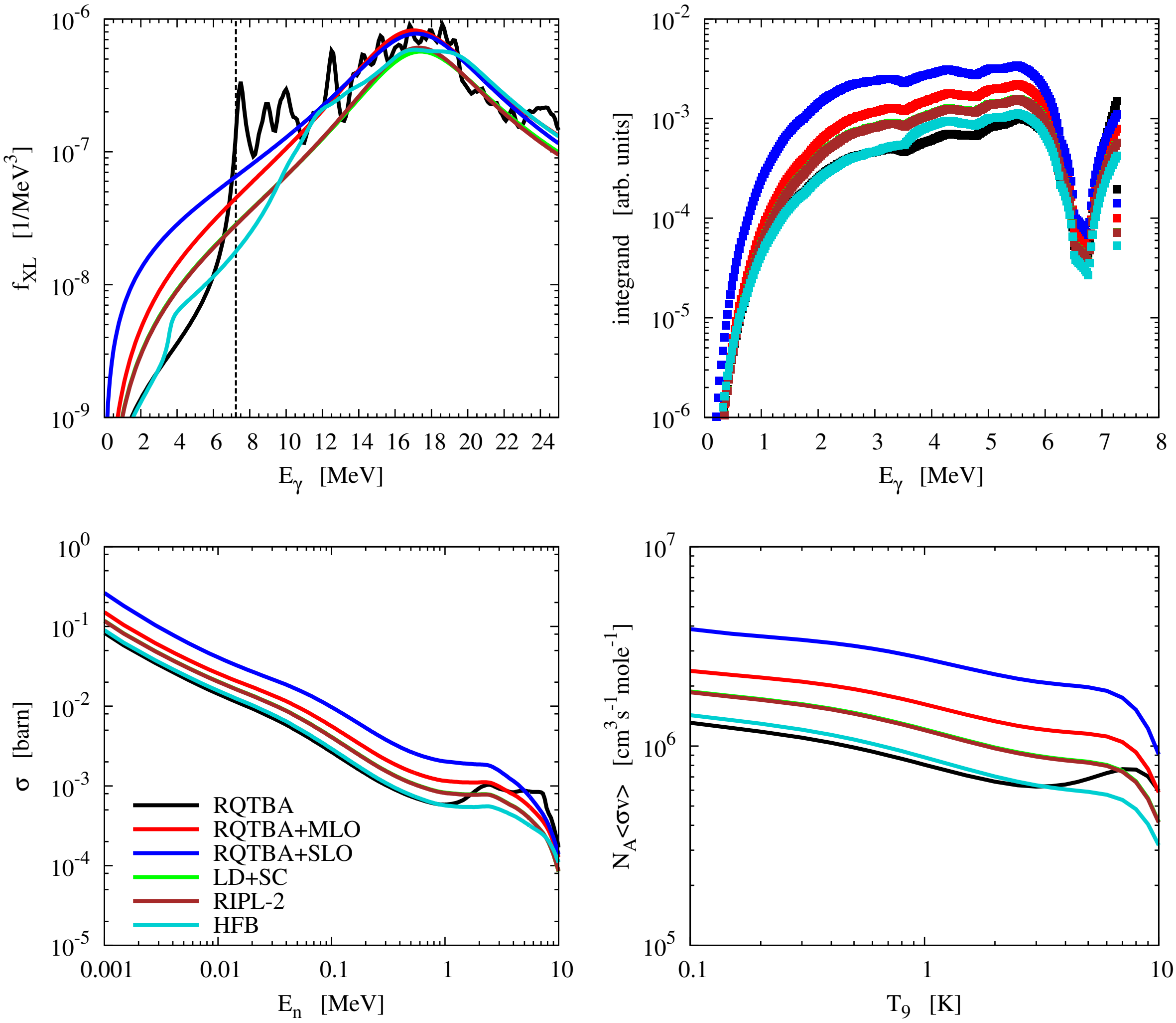

Figure 7.28: ^{69}Ni(n,γ)^{70}Ni - the upper left panel shows the different E1 strength functions and the vertical line marks the neutron separation energy. The upper right panel shows the γ-integrand as explained in section 7.1.2.1 evaluated for a kinetic neutron energy of $E_{\text{kin}} = 26$keV. The lower-left panel shows the laboratory ^{69}Ni(n,γ)^{70}Ni cross section. The lower-right panel shows the stellar reaction rate.

The dip in the integrand of fig. 7.28 around 6.5 MeV results from the dip in the level density for ^{70}Ni in fig. 7.26.

model	E_0 [MeV]	Γ [MeV]
RQTBA+SLO/RQTBA+MLO	17.49	6.68
LD+SC	17.86	6.49
RIPL-2	17.21	6.30

Table 7.18: Theoretical Lorentzian parameters of the giant dipole resonance in ^{70}Ni.

7.2.3.3 ^{72}Ni

The reaction ^{71}Ni(n,γ)^{72}Ni shows very similar features to the ^{69}Ni(n,γ)^{70}Ni reaction. The additional E1 strength in the RQTBA strength function leads to an enhancement of the ground state transition, but the smaller strength in the between E_γ = 2-5 MeV completely negates this enhancement. Only for higher neutron energies we become sensitive to the structure of the strength functions; this is indicated by the cross section of fig. 7.29.

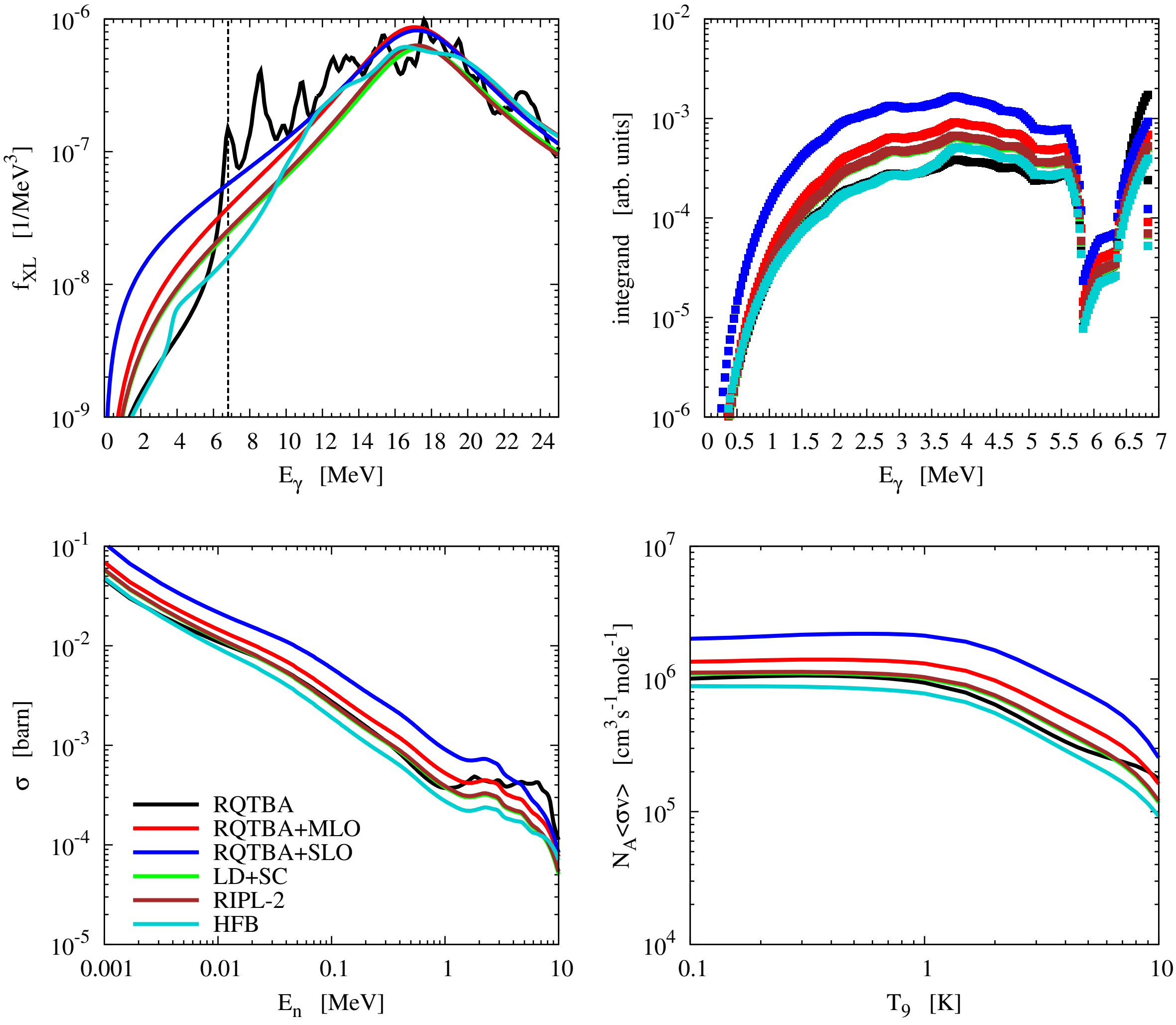

Figure 7.29: ^{71}Ni(n,γ)^{72}Ni - the upper left panel shows the different E1 strength functions and the vertical line marks the neutron separation energy. The upper right panel shows the γ-integrand as explained in section 7.1.2.1 evaluated for a kinetic neutron energy of E_{kin} = 24keV. The lower-left panel shows the laboratory ^{71}Ni(n,γ)^{72}Ni cross section. The lower-right panel shows the stellar reaction rate.

model	E_0 [MeV]	Γ [MeV]
RQTBA+SLO/RQTBA+MLO	17.50	6.40
LD+SC	17.82	6.40
RIPL-2	17.60	6.22

Table 7.19: Theoretical Lorentzian parameters of the giant dipole resonance in ^{72}Ni.

7.2.3.4 ^{74}Ni

In principle, the radiative neutron capture on ^{73}Ni appears to have rather similar properties as the reaction discussed before. The main difference is the parity distribution of the level density, though. The fact that most cross sections become very similar for low neutron energies indicates that M1 transitions are preferred. This is supported by fig. 7.31, which shows that in ^{74}Ni we damp E1 transitions much stronger (at small neutron energies) than in ^{72}Ni. Nevertheless, the RQTBA+SLO strength function's magnitude at low energies results in a clear dominance compared to the other E1 strength functions.

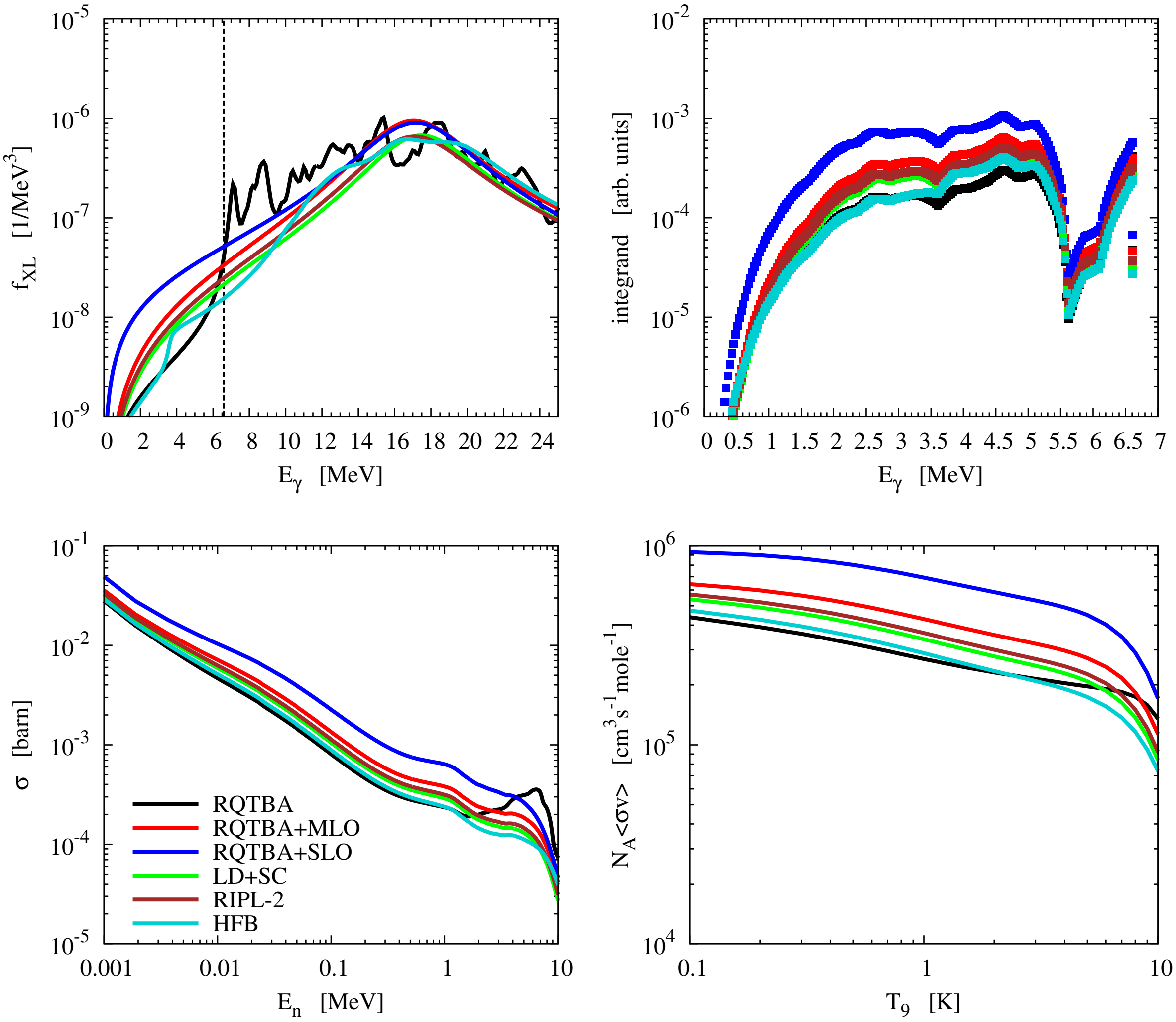

Figure 7.30: ^{73}Ni(n,γ)^{74}Ni - the upper left panel shows the different E1 strength functions and the vertical line marks the neutron separation energy. The upper right panel shows the γ-integrand as explained in section 7.1.2.1 evaluated for a kinetic neutron energy of $E_{\rm kin}$ = 27keV. The lower-left panel shows the laboratory ^{73}Ni(n,γ)^{74}Ni cross section. The lower-right panel shows the stellar reaction rate.

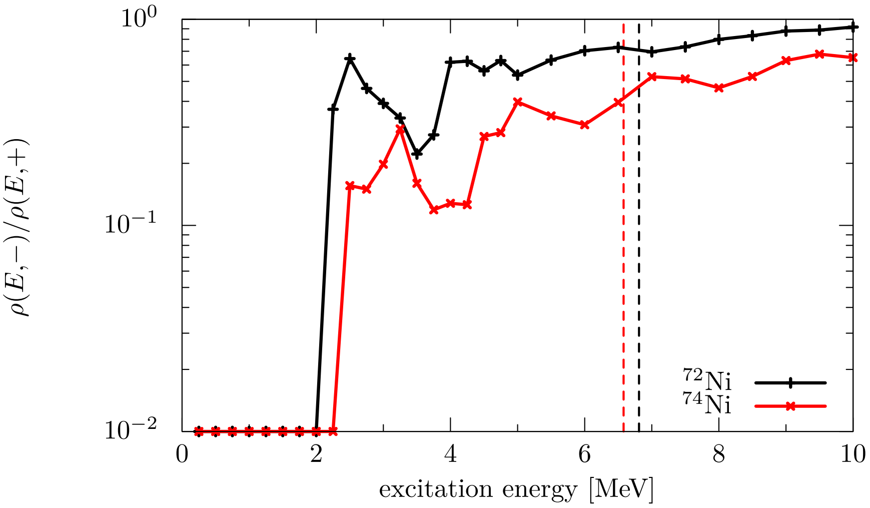

Figure 7.31: Ratio of the level densities for the two different parities of ^{72}Ni and ^{74}Ni. Any values below 10^{-2} have been capped and set to 10^{-2}.

model	E_0 [MeV]	Γ [MeV]
RQTBA+SLO/RQTBA+MLO	17.49	5.85
LD+SC	17.86	5.85
RIPL-2	17.71	6.14

Table 7.20: Theoretical Lorentzian parameters of the giant dipole resonance in ^{74}Ni.

7.2.3.5 ^{76}Ni

In ^{76}Ni, the RQTBA strength function does not predict additional E1 strength at the neutron threshold, but at higher energies. Nevertheless, for low neutron energies, M1 transitions dominate due to the parity distribution of the level density (see fig. 7.33). The cross section becomes sensitive to the structure of the RQTBA strength functions for neutron energies above 1 MeV. This enhancement also affects the reaction rate for temperatures around $T_9 = 6 - 10$K. We also see a starting deviation in the resonance parameters, in particular the centroid energy E_0. If this indicates a fundamental difference between the RQTBA model and the other approaches based on liquid drop models remains an open question.

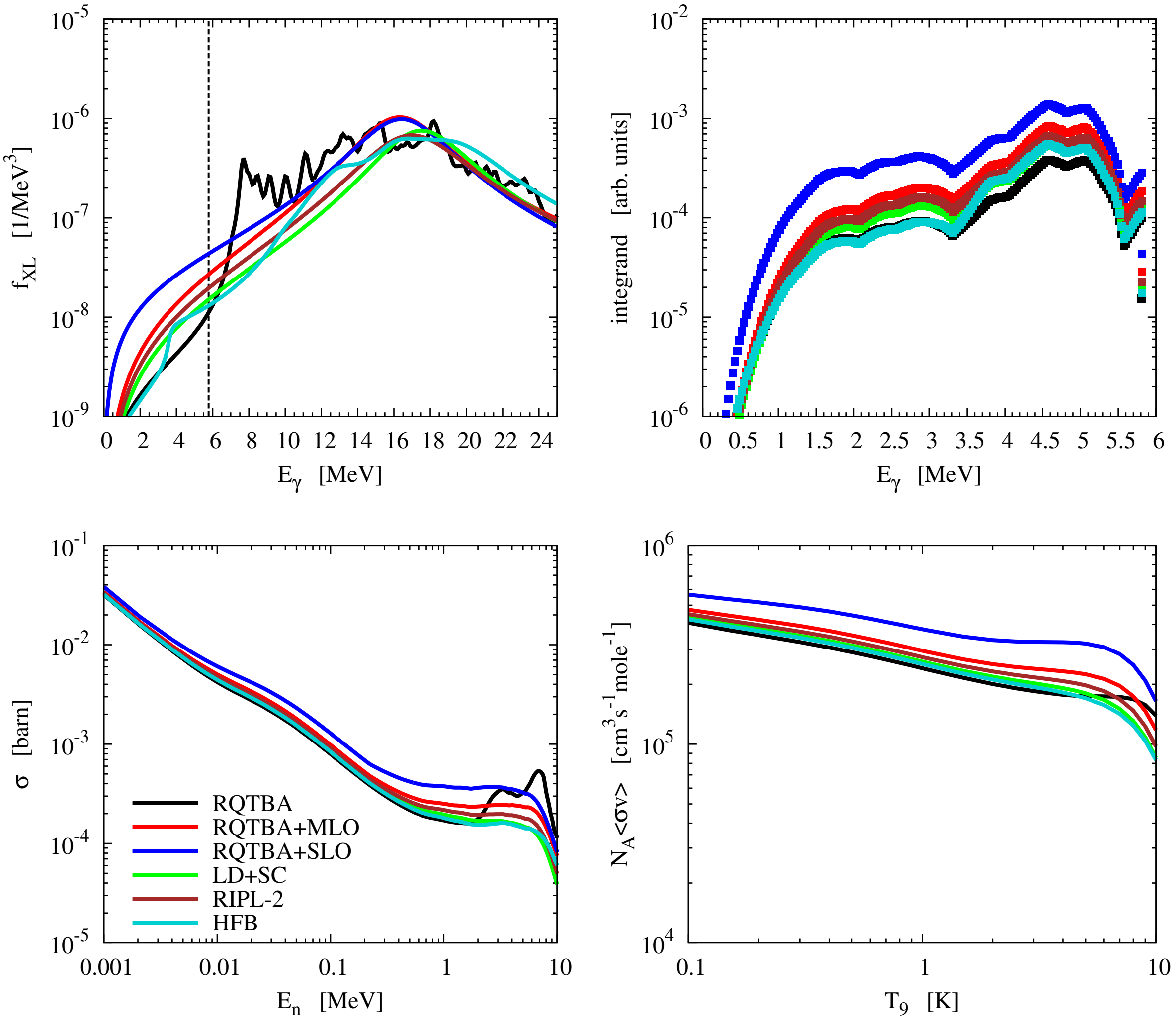

Figure 7.32: ^{75}Ni(n,γ)^{76}Ni - the upper left panel shows the different E1 strength functions and the vertical line marks the neutron separation energy. The upper right panel shows the γ-integrand as explained in section 7.1.2.1 evaluated for a kinetic neutron energy of $E_{\text{kin}} = 31$keV. The lower-left panel shows the laboratory ^{75}Ni(n,γ)^{76}Ni cross section. The lower-right panel shows the stellar reaction rate.

Additionally, we start to see a change in the centroid energy of the RQTBA model (see table 7.21), being substantially lower relative to the other approaches and compared to the previous reactions. Apparently this is connected to the magic shell closure at N=50, as we have seen a similar feature in ^{130}Sn (see table 7.11).

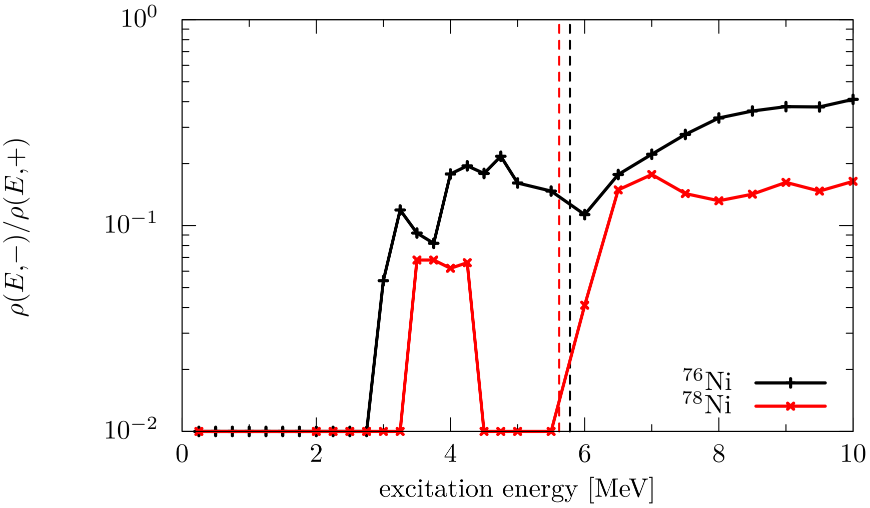

Figure 7.33: Ratio of level densities for the two different parities. The strong non-equipartition of parities in ^{78}Ni is expected because of the magic shell-closures. Additionally, the level density is particularly small and shows a prominent shell-gap (see upper right panel of fig. 7.26). Any values below 10^{-2} have been capped and set to 10^{-2}.

model	E_0 [MeV]	Γ [MeV]
RQTBA+SLO/RQTBA+MLO	16.62	5.27
LD+SC	17.80	5.27
RIPL-2	17.37	6.07

Table 7.21: Theoretical Lorentzian parameters of the giant dipole resonance in ^{76}Ni.

7.2.3.6 ^{78}Ni

This doubly magic nucleus is believed to be very crucial for r-process nucleosynthesis, as it would function as a waiting-point nucleus. Its mass is still rather unknown and we have used a neutron separation energy of $S_n = 5.62$ MeV deduced from systematics trends [AWT03, WAT03]. However, the ENSDF database gives a neutron separation energy of $S_n = 5.45$ MeV [ENS], possibly also resulting from systematic trends. Due to the small deviation, we stick to the value obtained from systematic trends by the AME2003 mass evaluation [AWT03, WAT03]. It is worthwhile to note that the HFB14 mass model [GSP07] predicts $S_n = 3.93$ MeV and the FRDM mass mode [MNMS95] $S_n = 5.98$ MeV.

Figure 7.33 shows that both parities are far from being uniformly distributed in ^{78}Ni. Moreover, the level density is especially small in ^{78}Ni because of the magic shell-closures; we can deduce this from the large shell-gap in the integrand of fig. 7.34. The small level density emphasises transitions to the ground state (and the states just above) relative to the transitions to the level density regime, i.e. excited states. From fig. 7.34 we see that the ground state transition of the integrand is of comparable magnitude as the transitions in the level density range between 2 to 3.5 MeV. A problem in this calculation might be that the nuclear level density of [GHK08] does not vanish for excitation energies up to 0.25 MeV (the ground state is included in the value at 0.25 MeV); as there are no experimental levels known in ^{78}Ni thus introducing some additional transitions into this regime. But since ^{78}Ni is a doubly magic nucleus, we can expect that the first excited state should be located notably above 0.25 MeV.

In contrast to the reaction ^{131}Sn$(n,\gamma)^{132}$Sn (see fig. 7.17), the RQTBA model does not predict additional E1 strength around or below the neutron separation energy in the compound nucleus ^{78}Ni. The predicted additional strength is located around 2 MeV above the neutron threshold, but we do not see the particular strength in the cross section for neutron energies below 4 MeV. The reason is, that for neutrons with 4-10 MeV, the additional strength in the RQTBA strength function connects transitions into the level density regime[1].

Nevertheless, E1 transitions are damped in our approach, due to the non-uniformly distributed parities (as indicated in fig. 7.33). The point in the cross section between 0.3 and 0.4 MeV at which the different E1 treatments predict different cross section results from the fact, that negative parities are predicted from 6 MeV upwards (see the discussion in section 7.2.2.10 for example).

model	E_0 [MeV]	Γ [MeV]
RQTBA+SLO/RQTBA+MLO	15.94	4.78
LD+SC	17.79	4.78
RIPL-2	17.27	6.00

Table 7.22: Theoretical Lorentzian parameters of the giant dipole resonance in ^{78}Ni.

Due to the magicity of this nucleus, the RQTBA strength function has a much smaller centroid energy E_0 compared to the other approaches (see table 7.22). The same behaviour have been already observed in ^{132}Sn (see table 7.12).

---

[1] The shell gap is about 2 MeV (see integrand of fig. 7.34) and the additional strength starts about 2 MeV above the neutron threshold. This roughly sums up to the 4 MeV.)

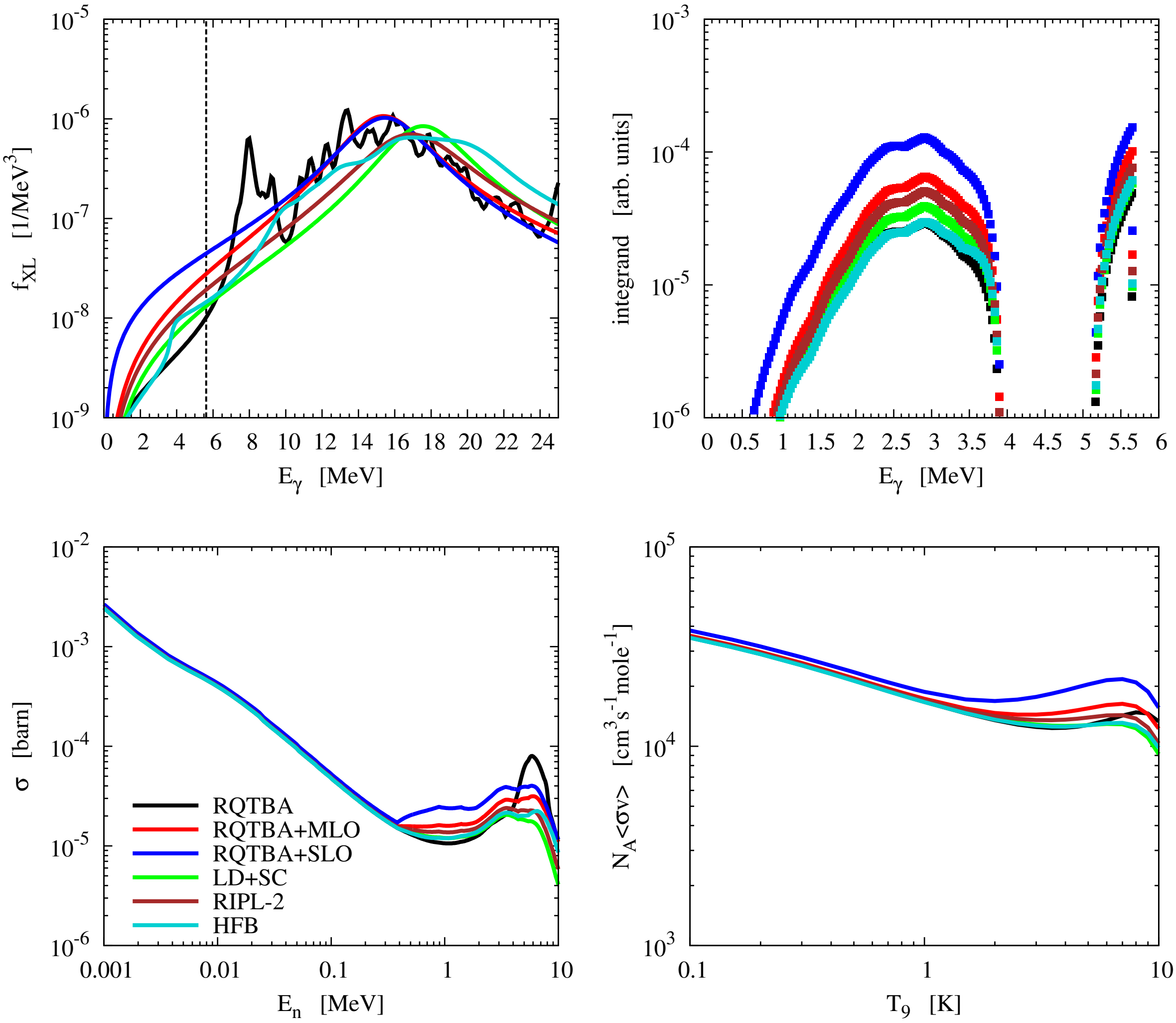

Figure 7.34: ^{77}Ni(n,γ)^{78}Ni - the upper left panel shows the different E1 strength functions and the vertical line marks the neutron separation energy. The upper right panel shows the γ-integrand as explained in section 7.1.2.1 evaluated for a kinetic neutron energy of $E_{\text{kin}} = 29$keV. The lower-left panel shows the laboratory ^{77}Ni(n,γ)^{78}Ni cross section. The lower-right panel shows the stellar reaction rate.

7.3 Microscopic M1 strength functions

In the preceding chapter we have discussed the influence of nuclear structure effects in E1 strength functions on (n,γ)-reactions. We can therefore extend this investigation towards M1 transitions, however we have to keep in mind, that M1 transitions usually exhibit much smaller transitions strengths compared to E1 transitions.

In astrophysical (n,γ) cross sections the E1 contribution is usually much larger than the M1 contribution. Therefore, one has put less emphasis on a detailed description of the M1 transitions despite the progress in nuclear modelling. However, recently it was shown that the inclusion of non-uniformly distributed parities in the level density in statistical model calculations of (n,γ) cross sections may enhance M1 transitions while damping E1 transitions (see [LLMP$^+$08] and section 7.2). These results showed that an improvement of the M1 strength functions used in the statistical model calculations for astrophysical reaction rates is needed.

Moreover, M1 transitions can also have a low-lying collective strength like the E1 transitions we discussed in the previous section. This scissors mode, however, only occurs in deformed nuclei [EvRR05, HvR10].

This is the reason why we cannot use the RQTBA model to obtain the low-lying scissors mode as this model assumes spherical nuclear shapes. However, the nuclear shell model [CMPN$^+$05] is capable of modelling this strength including the scissors mode (see for example [FHL$^+$03]), provided the calculations is performed in a model space which considers both spin-orbit partner orbitals. For example, complete ($0\hbar\omega$) shell model calculations can be performed nowadays for nuclei like iron isotopes including the full pf-shell. We will use this capability of the shell model to determine M1 strength functions for selected iron nuclei. Additionally, we can calculate the M1 transitions also for excited states in the nuclear shell model, thus having a tool to study Brink's hypothesis regarding the scissors mode. All results have been obtained with the ANTOINE code [Cau].

Besides the scissors mode, the M1 strength shows a pronounced spin-flip mode (see section 5.2.3). To correctly describe this collective excitation in full detail both spin-orbit partners have to be in our model space. This is the case for the iron nuclei up to ^{60,62,64}Fe. However for even heavier isotopes the neutron $g_{9/2}$ orbital becomes important. We then change from the pf-shell model space outside a ^{40}Ca core to a model space which assumes an occupied ^{48}Ca core, but explicitly allowing excitations to the neutron $g_{9/2}$ orbital. While this model space should be sufficient to describe the low-energy excitation spectrum, it misses the $f_{7/2} \rightarrow f_{5/2}$ and $g_{9/2} \rightarrow g_{7/2}$ neutron excitations and hence a part of the spin M1 excitations.

It is important to note that Brink's hypothesis has been originally shown to be valid for collective excitations, i.e. giant resonances. It has not been formulated to be applied to single-particle transitions. We may therefore expect that Brink's hypothesis does not hold for low-lying single-particle strength. Instead, we intend to discuss to what extent low-lying collective modes are affected.

For some nuclei we will also give stellar (n,γ) reaction rates. These were obtained by assuming Brink's hypothesis and using the FRDM mass model [MNMS95] and a BSFG level density [RTK97] using the statistical model formulation as given in [LLMP$^+$08].

7.3.1 Obtaining the Strength Function

The shell model provides us with the reduced transition probabilities B(M1) (see eq. (5.14)) to discrete final states. For the applications in the statistical model a continuous function is required, which we obtain by folding our B(M1) distribution with Gaussians, i.e.

$$\Phi_{\mathrm{M1}}(E_x) = \sum_i B_i(\mathrm{M1}) \cdot \frac{1}{\sqrt{2\pi\sigma^2}} e^{-(E_x - E_i)^2/2\sigma^2}. \tag{7.3}$$

Here E_x is the excitation energy relative to the parent state (this energy can be related to E_γ). The sum runs over all final states.

As stated above, we will use two different valence spaces to obtain our results. The first valence space is given by the complete pf-shell for neutrons and protons with a ^{40}Ca core. The second valence space consists of a ^{48}Ca core and the pf-shell for the protons and the $f_{5/2}$-, $p_{3/2}$-, $p_{1/2}$- and the $g_{9/2}$-shell for the neutrons. In the latter case, the $f_{7/2}$-shell is closed for neutrons, i.e. $f_{7/2} \rightarrow f_{5/2}$ neutron excitations cannot occur. For the valence space based on the ^{40}Ca core, we employ the KB3G interaction [GBD$^+$08] and for the valence space based on the ^{48}Ca core we employ the interaction discussed in [SLD$^+$02, DFG$^+$10].

Moreover, we will often divide the strength into a *spin* part and into an *orbital* part. The spin part we get by setting the g-factors for the orbital part g_l of the M1 operator to zero, the orbital part by doing the same for the g-factor g_s. We have to keep in mind that the orbital and spin B(M1) values do not add up, instead they can interfere either constructively or destructively.

We will also use quenched spin g-factors in our calculations instead of the bare values given in section 5.1.2. The quenching factor we choose is 0.75, i.e. we obtain the g-factors given in table 7.23.

7.3.2 Nuclei in the pf- and pf+$g_{9/2}$-Shell

In this section we discuss features of the M1 strength function that could be relevant for (n,γ) reaction rate determinations, although the discussed nuclei are not r-process nuclei. Importantly, the shell model strength functions will be compared to the the M1 strength functions commonly used to describe (n,γ) cross sections for r-process simulations.

	protons	neutrons
g_s	4.1895	-2.8695
g_l	1	0

Table 7.23: Table of values for the quenched g-factors (see section 5.1.2) used in this thesis.

7.3.2.1 The Different M1 Strength Functions

We will discuss three different approaches towards the M1 strength function. The first assumes a constant strength which is adjusted to data. We call this a modified single-particle approach and we abbreviated it by SP (see section 5.3.3 and [HWFZ76]). The second model we will use is based on a phenomenologic approach inspired by the successful description of the E1 giant dipole resonance strength (see section 5.3.3 and [BBC⁺06]). It assumes a Lorentzian form factor for the M1 strength with a fixed width $\Gamma = 4$ MeV and a centroid at $E_0 = 41 \cdot A^{-1/3}$. The total strength is parametrised as described in section 5.3.3. This approach gives an energy-dependent M1 strength function (compared to the energy independent single-particle approach) and tries to recover the spin-flip resonance. Low-lying collective orbital strength cannot be explicitly reproduced by this model, although the tail of the Lorentzian gives M1 strength at low energies. This approach will be abbreviated with LOR. The third approach is based on the nuclear shell model and it is the only approach that is able to reproduce nuclear structure effects appearing in the strength function. In particular we may specifically investigate the occurrence of low-lying collective orbital strength. In order to obtain a smooth function, we fold the B(M1) distribution with Gaussians (see section 7.3.1). This strength function will be abbreviated by SM.

We can calculate the radiative strength function for odd nuclei as well as excited states. As this enables us to calculate the radiative magnetic dipole strength function for $J \neq 0$ states, some peculiarities arise:

- States with $J \neq 0$ have a finite magnetic dipole moment, i.e. we will have a finite $B(M1; J \to J)$-value for $E_\gamma = 0$ MeV [BG77]. This B(M1) value must not be taken into account in the summation of eq. (7.3) because it accounts for elastic scattering which we must not include in the strength function if we want to determine (n,γ) cross sections.
- For $J \neq 0$ states M1 transitions lead to two or three final states.

7.3.2.2 ^{54}Fe and ^{55}Fe: Even-Even versus Even-Odd Nuclei

The first nucleus we will discuss is ^{54}Fe, which is semi-magic because of its N=28 neutron shell closure and therefore has a spherical shape. Hence, we do not see any considerable low-lying orbital M1 strength in fig. 7.36. We will use this nucleus as a reference when discussing the M1 strength distribution of ^{55}Fe.

In the nucleus ^{55}Fe, we have N=29 neutrons, i.e. we have one neutron above the magic shell-closure. Therefore, the ground state of ^{55}Fe is $3/2^-$ and we have three contributions to the M1 strength, as we have plotted in fig. 7.37. By comparing the results for ^{54}Fe in fig. 7.36 with the results for ^{55}Fe in fig. 7.37 we see some fundamental differences. While there is no significant M1 strength for $E_\gamma < 6$ MeV in ^{54}Fe, we find notable low energy strength in ^{55}Fe, including a prominent transition to the $1/2^-$ state at $E_x = 0.52$ MeV. This shows that there can be important differences between neighbouring even and odd nuclei regarding the M1 strength. In principle, this is expected because the unpaired neutron in ^{55}Fe can be easily excited, while in ^{54}Fe we have to break a pair to excite a nucleon. Our example portrays a general problem of radiative strength functions, though, as the extrapolation of the spin-flip resonance (or the GDR in case of E1) is not able to show this very low-lying structure in global parametrisations, mainly resulting from single-particle excitations. We can assume that in a more neutron-rich nucleus (with smaller neutron separation energy) similar effects can occur, thus affecting the γ-channel differently in even and odd nuclei.

In fig. 7.37 we show the M1 strength function ϕ_{M1} for the odd-even nucleus ^{55}Fe. The ground state of ^{55}Fe has $J^\pi = 3/2^-$. In contrast to an even nucleus with ground state $J^\pi = 0^+$, the ground state radiative strength function of an odd nucleus consists always of two or three components (for dipole

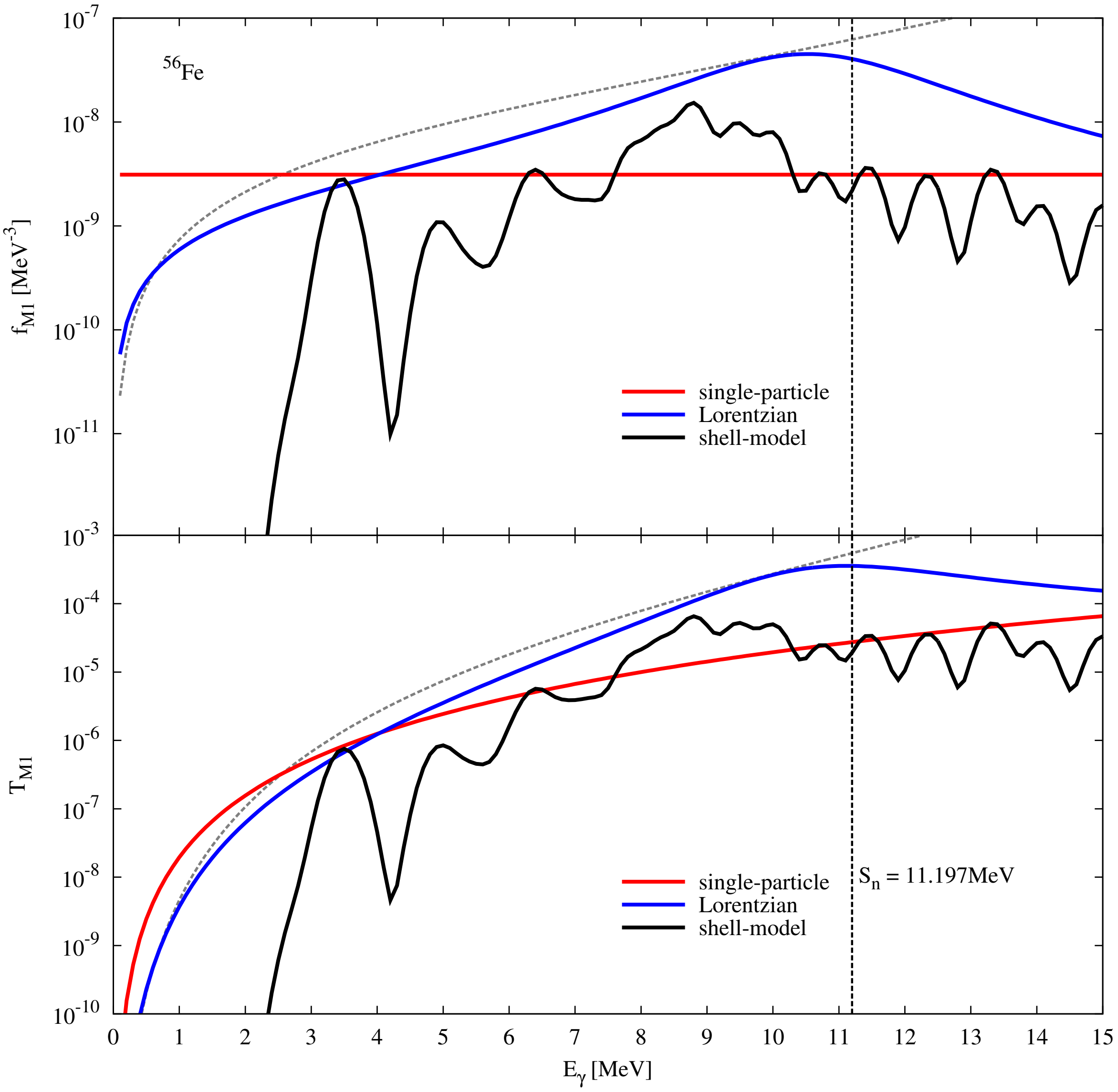

Figure 7.35: Upper panel: radiative M1 strength functions for ^{56}Fe; lower panel: transmission coefficients obtained with the strength functions in the upper panel. The vertical line marks the neutron separation energy S_n in ^{56}Fe, the grey dashed line corresponds to an exemplary Lorentzian E1 strength function in ^{56}Fe (refer to the model RIPL-2 in section 7.2). The very prominent strength located at around 3.5 MeV has been subject to different studies [FHL$^+$03] and results from the orbital part of the M1 operator (see fig. 7.39).

radiation) to different spins. Moreover, there is a non-vanishing B(M1) value for elastic scattering, i.e. for $E_\gamma = 0$.

We have calculated the B(M1) distribution for the ground state and this low-lying state in fig. 7.38. For the $3/2^-$ ground state, we do not see any particular low-lying orbital strength. This is different for the $1/2^-$ state: we obtain some noticeable orbital strength at 1.3 MeV and 1.45 MeV. The first is a transition to a $1/2^-$ state, the second a transition to a $3/2^-$ state. We also see these transitions in the distribution on the ground state shifted upwards by the excitation energy of the $5/2^-$ state, i.e. 0.52 MeV. This is an example for a nucleus in which the ground state does not show peculiar orbital strength but an excited state does. This is an indication, that the occurrence and magnitude of a Scissors

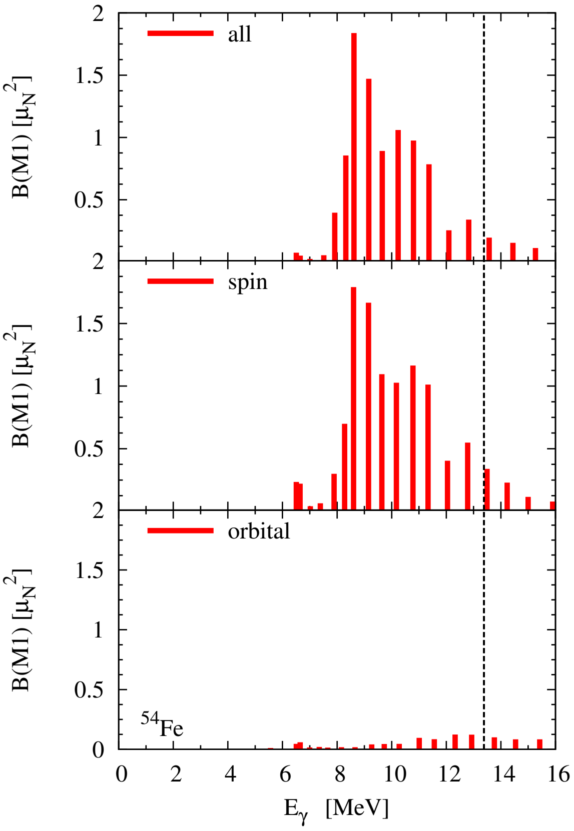

Figure 7.36: B(M1) distribution on the 0^+ ground state in ^{54}Fe. The uppermost panel shows the complete strength, the panel in the middle shows the spin contribution, and the lower panel shows the orbital contribution.

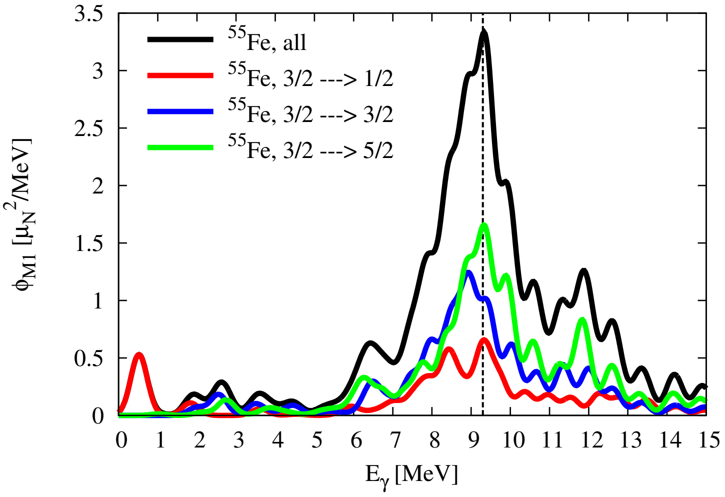

Figure 7.37: M1 strength function ϕ_{M1} on the ground state $(3/2^+)$ of ^{55}Fe. The small bump at 0.52 MeV corresponds to a transition to the first excited state at that energy with $J^\pi = 1/2^-$; the experimental energy of that state is 0.411 MeV [ENS].

.

mode depend on the initial state. Therefore, Brink's hypothesis seems to be not valid in this particular case.

Another feature we can see is that the total strength for the $1/2^-$ state is larger. We obtain $\sum_i B_i(\mathrm{M1}) = 11.31\ \mu_N^2$ for the ground state and $\sum_i B_i(\mathrm{M1}) = 12.33\ \mu_N^2$ for the excited $1/2^-$ state.

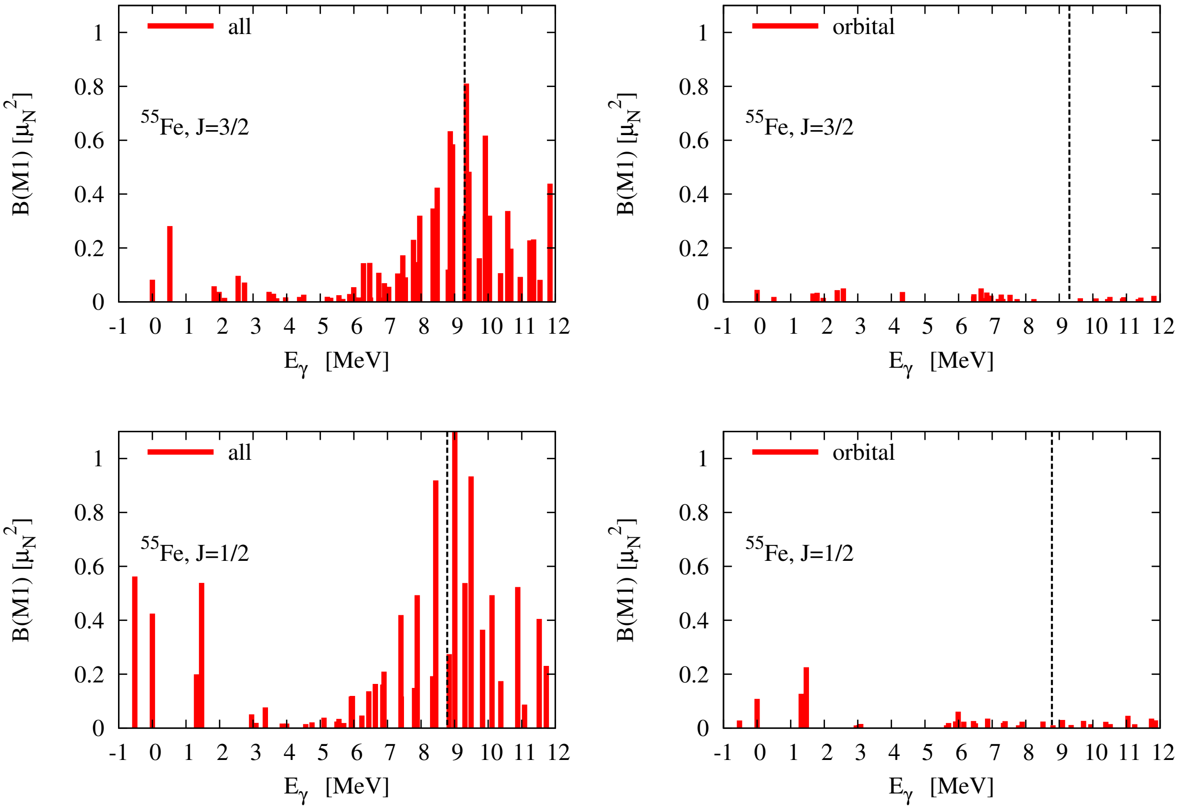

Figure 7.38: The upper panels show the B(M1) distribution in ^{55}Fe on top of the $3/2^-$ ground state. The lower panels show the same on the first excited $1/2^-$ state at an excitation energy of 0.52 MeV. The left panels show the complete strength, while the right panels only show the orbital part. The vertical black line gives the experimental neutron separation energy relative to the chosen state.

7.3.2.3 ^{56}Fe: Brink's Hypothesis for Orbital Strength

According to fig. 7.39, the nucleus ^{56}Fe shows a very distinct scissors mode around 3.5 MeV (see the caption of fig. 7.35) which has been verified experimentally in [FHL$^+$03]. This orbital strength enhances M1 transitions in that energy range if we assume the validity of Brink's hypothesis. The fact that this orbital strength is also very isolated, i.e. the other transition probabilities around 3.5 MeV are much smaller, makes this nucleus a very nice example to study the evolution of this orbital strength with excitation. In the following we will discuss two aspects: the evolution of the low-lying orbital strength with excitation energy but for fixed J^π values, i.e. for excited 0^+ states and the general evolution of the strength on excited states with different spin than the ground state spin. The latter we do for excited states that are not connected to the ground state via M1 transitions and states that can be connected via M1 transitions, i.e. the 1^+ states.

In fig. 7.40 we have plotted the M1 strength function ϕ_{M1} for different states calculated from the shell model. The energies of the states are listed in the caption. Our results show that Brink's hypothesis works very well for the spin-flip resonance, i.e. the centroid energy of the resonance does not change between the states. We will come back to that issue in section 7.3.2.4 where we will discuss the evolution of the orbital strength with excitation energy in an odd nucleus.

The situation is different regarding the orbital strength at 3.5 MeV for the 0^+ ground state (upper

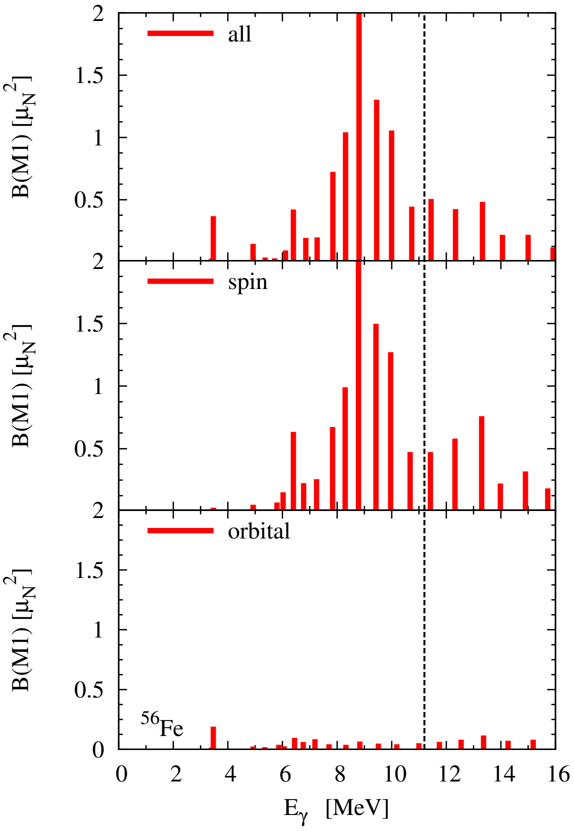

Figure 7.39: B(M1) strength distribution on the ground state of ^{56}Fe. The vertical line marks the experimental neutron separation energy.

left panel). We note that the orbital reduced transition probability for that transition is $B(\mathrm{M1;orb.}) \approx 0.19\ \mu_N^2$. By comparing with the other 0^+ states (upper right panel and lower right panel) we see that the location of that orbital strength changes. For the first excited 0^+ state we see a distinct orbital strength at 2.2 MeV and an additional transition at 0.7 MeV. Interestingly, the transition at 0.7 MeV stems from the spin part and not from the orbital part and its energy tells us that this transitions leads to the same 1^+ state as the ground state's 3.5 MeV transition. Apparently, the structure of the first excited 0^+ state is different to the structure of the 0^+ ground state in such a way that the distinct orbital strength to the 1^+ on the ground state becomes a nearly completely spin part dominated transition for the first excited 0^+. The orbital strength at 2.2 MeV can be identified with the small bump around 5 MeV (2.727 MeV + 2.2 MeV) in the ground states strength function. Here the opposite occurs, i.e. for the ground state the transition at 5 MeV shows only a small orbital strength but on the first excited 0^+ the corresponding transition has a particular orbital strength. The strength at 6.5 MeV in the ground state's strength function cannot be identified in the strength function of the first excited 0^+ but it shows up again in the strength function of the second excited 0^+ at around 3 MeV. The ground state's strength at 3.5 MeV is not plotted for the second excited 0^+ because it lies below that state. The ground state's 5 MeV strength we see at 1.4 MeV in the strength function of the second excited 0^+, though. In principle, the low-energy strength of the second excited 0^+ is the low-energy strength of the ground state shifted by the excitation energy of the second 0^+, i.e. 3.58 MeV; note that the spin-flip resonance is not shifted. These considerations clearly show that for ^{56}Fe Brink's hypothesis is very questionable for the 0^+ states.

The situation changes considering the strength functions on the 2^+ and 4^+ states. The results in fig. 7.40 for the first excited 2^+ state show some additional low-lying M1 strength around 1.5-2.5 MeV. This strength does not have a very strong orbital contribution. The broad structure results from two transitions in that region having an orbital contribution of $B(\mathrm{M1;orb.}) \approx 0.1\ \mu_N^2$ and these add up in our continuous strength function. The spin and the orbital strength are of comparable magnitude in that region. For the first excited 4^+ state the situation is different: we see that around 0.8 MeV a transition with a large orbital strength of about $B(\mathrm{M1;orb.}) \approx 0.2\ \mu_N^2$ is predicted. To sum it up, we see for 2^+ and 4^+ additional low-lying orbital strength that cannot be given in the ground state's strength function. This additional strength is also not located at the ground states scissor mode at 3.5 MeV (relative to the state we calculate upon). This is another indication that Brink's hypothesis is not valid for M1 transitions at low energies.

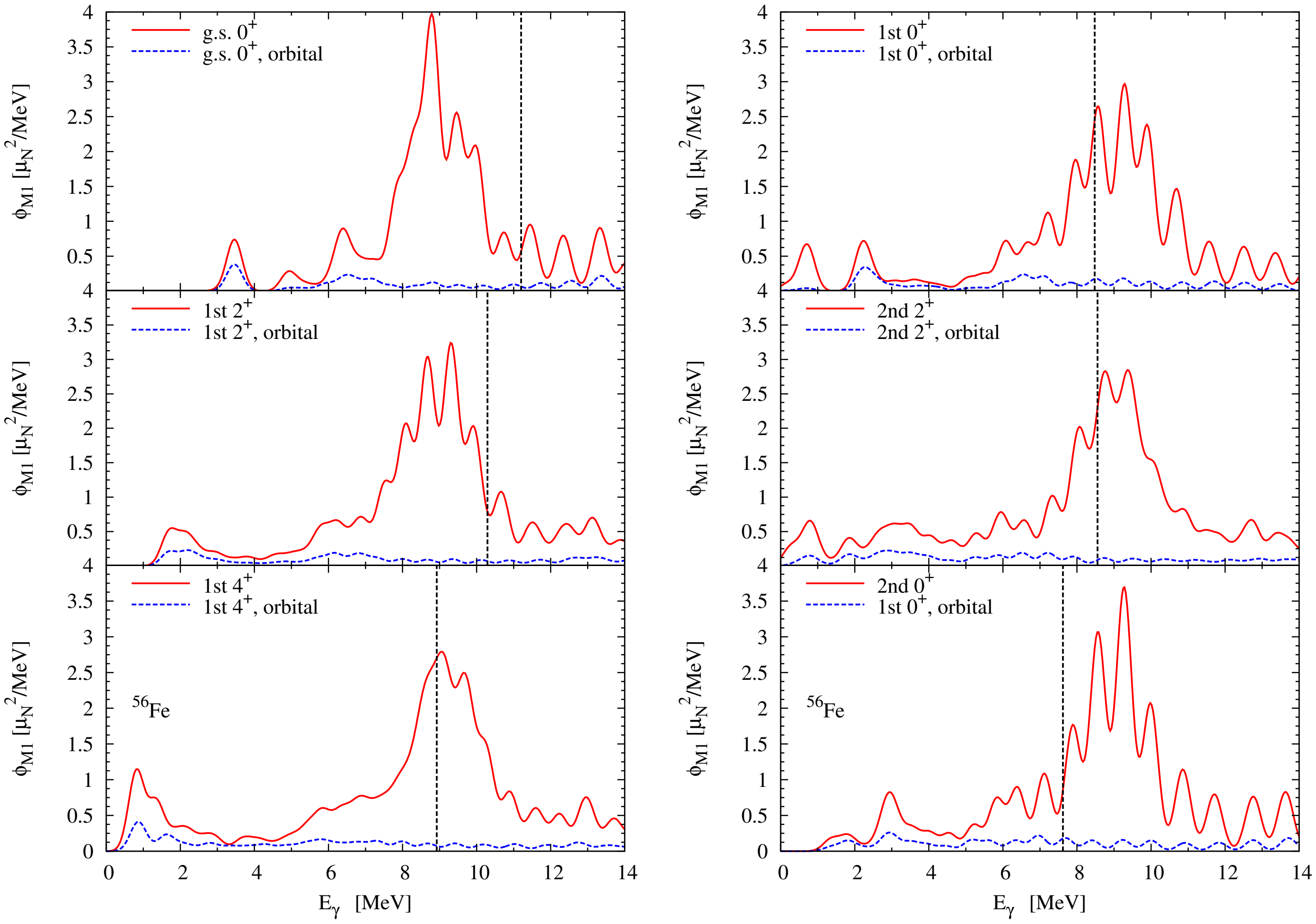

Figure 7.40: M1 strength function ϕ_{M1} of ^{56}Fe for various states: the 0^+ ground state (top left), the first excited 2^+ at 0.906 MeV (experimental value: 0.846 MeV; middle left), the first excited 4^+ at 2.276 MeV (experimental value: 2.085 MeV; bottom left), the first excited 0^+ at 2.727 MeV (experimental value: 2.941 MeV; top right), the second excited 2^+ at 2.646 MeV (experimental value: 2.657; middle right), and the third excited 0^+ at 3.58 MeV (experimental value: 3.61 MeV; bottom right). The blue curves are the ϕ_{M1} obtained from taking the orbital strength only. The black vertical lines mark the experimental neutron separation energy relative to the corresponding state. The experimental energies were taken from [ENS]. We plot here the strength function ϕ_{M1} instead of the B(M1) in order to be able to compare the total strength, too.

So far we have compared to states with even spin only. Another option is to examine the change of the orbital strength based on the first 1^+ at 2.907 MeV state which is connected to the 0^+ ground state and all other 1^+ states. However, we do not plot the downwards transition here. The results are given in fig. 7.41. The prominent 1^+ state in the strength function of the ground state at 3.5 MeV, which is a scissors mode, can be identified with the 1^+ state at 0.6 MeV in the strength function on the first excited 1^+ state. In the latter case, the transition does not have a distinct orbital strength. In the contrary, we see transitions with notable orbital strength between 2.8 MeV and 3.1 MeV (note the width of the bump, indicating that there are several states involved) in the strength function of the first excited 1^+ state. There are two $1^+ \rightarrow 2^+$ transitions at 2.8 MeV and 3.05 MeV with $B(\mathrm{M1;orb.}) \approx 0.075\ \mu_N^2$ and $B(\mathrm{M1;orb.}) \approx 0.06\ \mu_N^2$, respectively. Additionally, there is a $1^+ \rightarrow 1^+$ transitions at 2.92 MeV with $B(\mathrm{M1;orb.}) \approx 0.045\ \mu_N^2$.

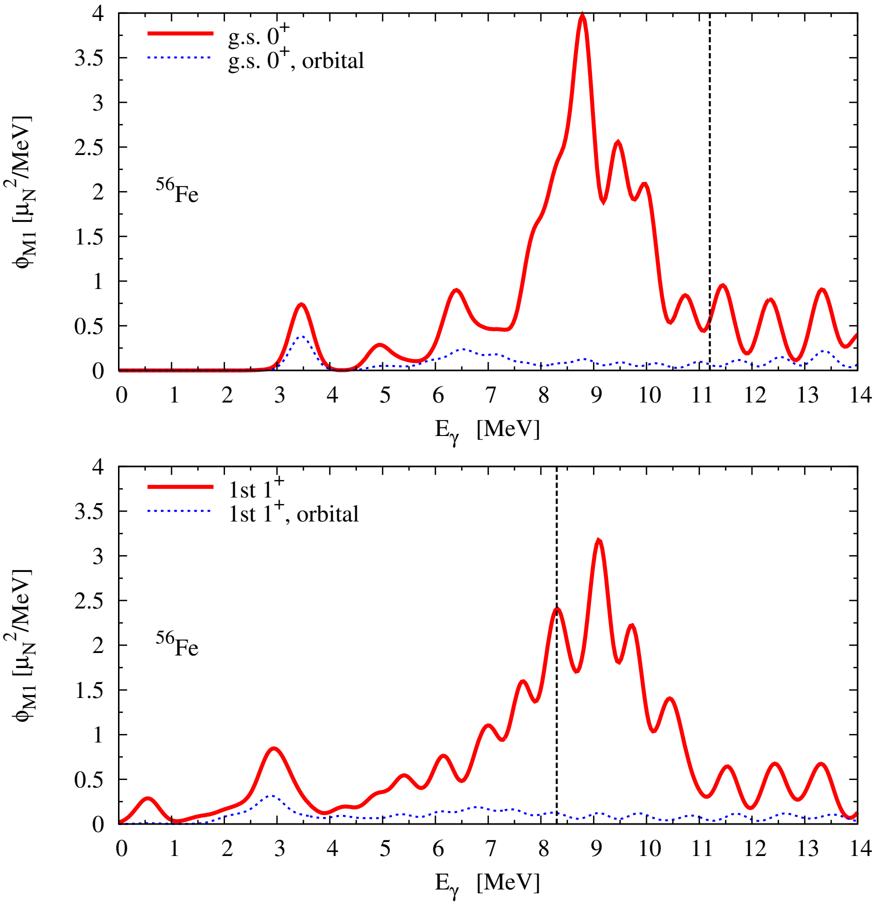

Figure 7.41: M1 strength function ϕ_{M1} of ^{56}Fe for the 0^+ ground state (upper panel) and the first excited 1^+ state at 2.907 MeV. The blue curves are the ϕ_{M1} obtained from taking the orbital strength only. The black vertical lines mark the neutron separation energy relative to the corresponding state.

As we have discussed before, ^{56}Fe exhibits a scissors mode around 3.5 MeV. The strength functions are plotted in fig. 7.35. The reaction rate we obtain from these strength functions is shown in fig. 7.42. The large separation energy of 11.2 MeV in ^{56}Fe opens up a large phase space. As we can see from fig. 7.35, E1 transitions dominate in this reaction and different M1 treatment only give a change of several percent in the full (E1 and M1) rate. We see that the LOR strength function gives an enhancement of the reaction rate due to the spin-flip resonance. For the rates obtained with the M1 transitions only, we see that the different treatments can change the rate by a factor of 2-3.

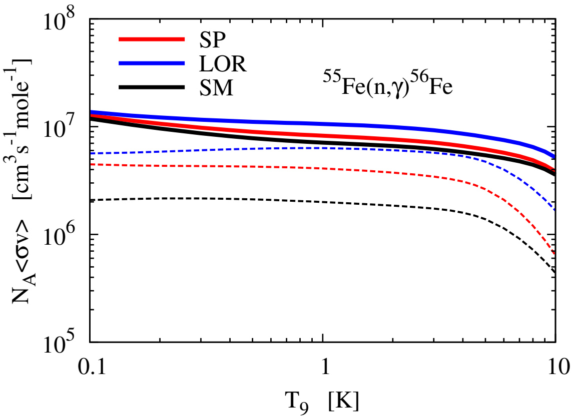

Figure 7.42: Reaction rate for the reaction ^{55}Fe$(n,\gamma)^{56}$Fe and for three different M1 treatments. The full lines include E1 transitions and the dashed lines are M1 transitions only.

7.3.2.4 ^{57}Fe: Scissors Mode on Excited States in an Odd Nucleus

In fig. 7.43 we show the B(M1) strength distribution of ^{57}Fe. The $1/2^-$ ground state shows particular orbital strength at 1.6 MeV and 2.5 MeV (upper right panel), which also corresponds to additional strength for these energies in the complete strength (upper left panel). Interestingly, this strength is particularly smaller for the strength distribution on the first excited $3/2^-$ state (middle panels), while for the first excited $5/2^-$ state, we again see additional orbital strength, but less strong than for the $1/2^-$.

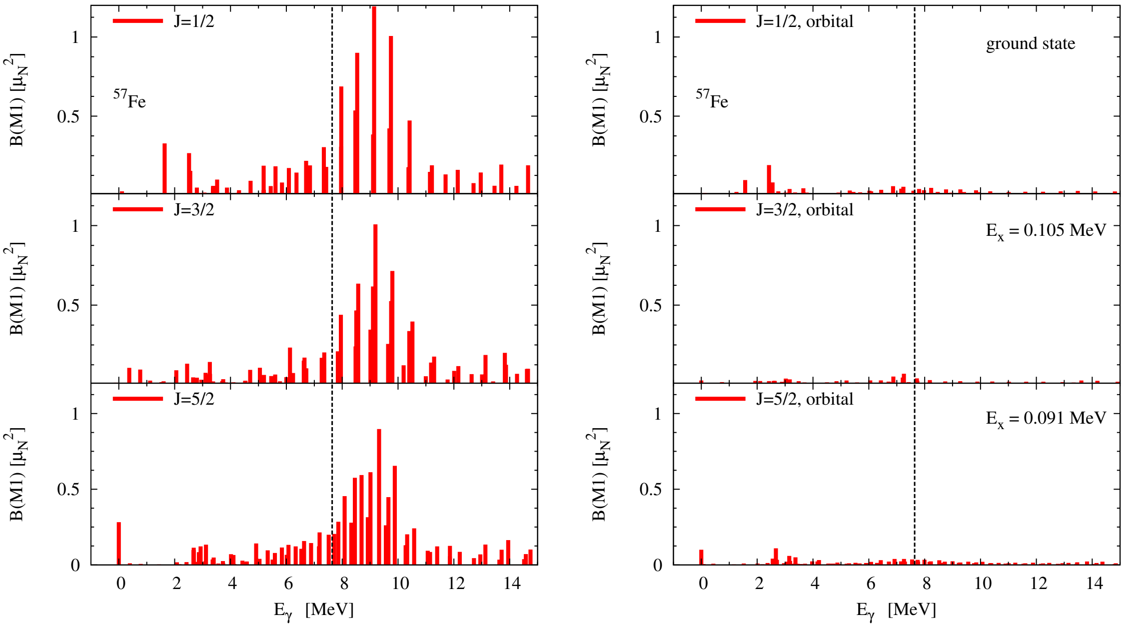

Figure 7.43: The B(M1) strength on the $1/2^-$ ground state, the first excited $3/2^-$ state, and the first excited $5/2^-$ state in ^{57}Fe. The left panels shows the full strength, while the right panel shows the orbital part only. The excitation energies within the shell model are given in the right panels. The vertical line marks the neutron separation energy relative to the ground state (we would have to shift the line downwards by the excitation energy relative to the ground state for the excited states; we do not do this here, because of the small excitation energies).

This is again an indication that Brink's hypothesis is questionable for the low-energy region, in particular for a possible scissors mode, as we have already discussed above for ^{55}Fe and ^{56}Fe. At the same time, we can see that Brink's hypothesis is - as expected - a very robust approximation regarding the spin-flip resonance for the states we calculated, because the location is very similar for all three strength distributions. If we switch over to the strength function ϕ_{M1} plotted in fig. 7.44, we see that the strength of the spin-flip resonance is not affected.

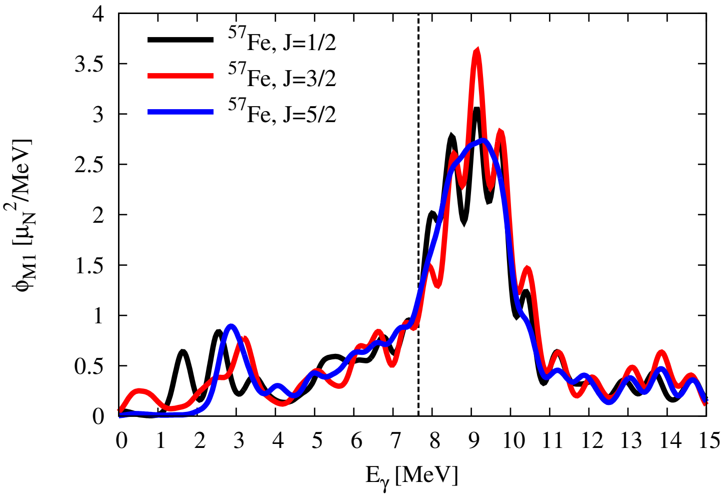

Figure 7.44: The strength function ϕ_{M1} of ^{57}Fe obtained from the B(M1) distribution of fig. 7.43.

Additionally, we see from fig. 7.43 (left panels) that the $5/2^-$ state exhibits a strong magnetic dipole moment (the strength at $E_\gamma = 0$ MeV), while the other two states show a much smaller magnetic dipole moment. This is in agreement with experiment, as the $5/2^-$ state's magnetic moment is nearly one order of magnitude larger compared to the magnetic dipole moment of the other two states (see fig. 7.43). Finally, it is important to mention that experiment shows a different level ordering with the $3/2^-$-state at 0.014 MeV and the $5/2^-$ state at 0.135 MeV.

J^π	$\mu^{\mathrm{sm}}_{\mathrm{M1}}$ $[\mu_N]$	$\mu^{\mathrm{exp}}_{\mathrm{M1}}$ $[\mu_N]$ [Rag89, ENS]
$1/2^-$	0.102	+0.090
$3/2^-$	0.141	-0.155
$5/2^-$	0.919	+0.935

Table 7.24: Shell model and experimental magnetic dipole moments of the first three states in ^{57}Fe.

7.3.2.5 ^{60,62,64}Fe: the ^{40}Ca Core versus the ^{48}Ca Core

In fig. 7.45 we sketch the influence of the different valence spaces we use in this thesis. Apparently, the removal of the $f_{7/2} \leftrightarrow f_{5/2}$ correlations for neutrons affect the spin-flip part in case of the calculations based on the ^{48}Ca core. Therefore, the spin-flip resonance in case of the ^{48}Ca results originates mainly from the proton $f_{7/2} \leftrightarrow f_{5/2}$ correlations. Nevertheless, in case of (n,γ) cross section this only plays a minor role as the calculations are mainly sensitive to the energy range $E_\gamma = 2 - 5$ MeV in the strength function, i.e. to the tail of the spin-flip resonance which resides around $9 - 10$ MeV. However, for Gamow-Teller transitions for neutrino-nucleus reactions this could become an important aspect, as the spin part of the M1 operator is proportional to the Gamow-Teller operator [MPLD00].

However, regarding the low-energy region we see that all calculations give similar results if we compare the same nucleus. The individual differences for the low-lying strength are additionally smeared out if we calculate the strength function ϕ_{M1}. Therefore, we may use the model space with the ^{48}Ca core for the investigation of the low-lying orbital strength.

All three nuclei in fig. 7.45 show a distinct low-lying scissors mode. The strength of this mode is similar to the scissors mode in ^{56}Fe. Interestingly, we see a general decline of that strength when going from ^{60}Fe to ^{64}Fe.

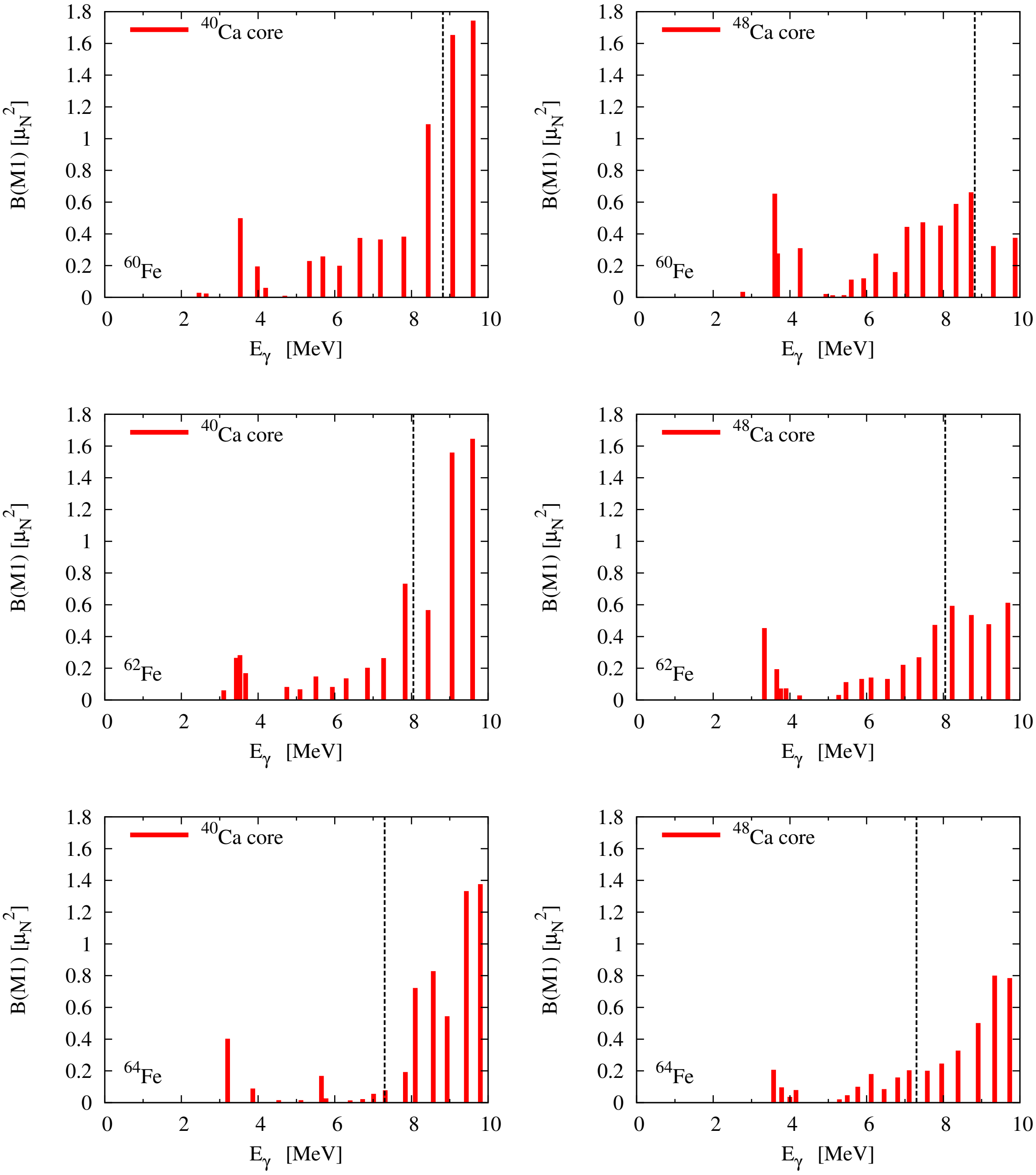

Figure 7.45: B(M1) distributions for ^{60,62,64}Fe. The left column are the results obtained from the ^{40}Ca core calculations, the right column the results obtained with the ^{48}Ca core.

It is worthwhile to have a focus on ^{60}Fe as the reaction ^{60}Fe(n,γ)^{61}Fe has been recently measured [URS^{+}09] because ^{60}Fe has been observed in a manganese crust in the deep sea [KKF^{+}04]. Its half-life is about 2.62 million years [RFK^{+}09] and it is speculated that the measured ^{60}Fe has been injected into the solar system by a nearby supernova about 2.8 Myr ago [URS^{+}09]. The formation of ^{60}Fe is subject to the relevant (n,γ) rates and their backwards rates as well as the half-life of ^{60}Fe. As the M1 strength function affects the (n,γ) rates, we would like to discuss this nucleus in a little more detail.

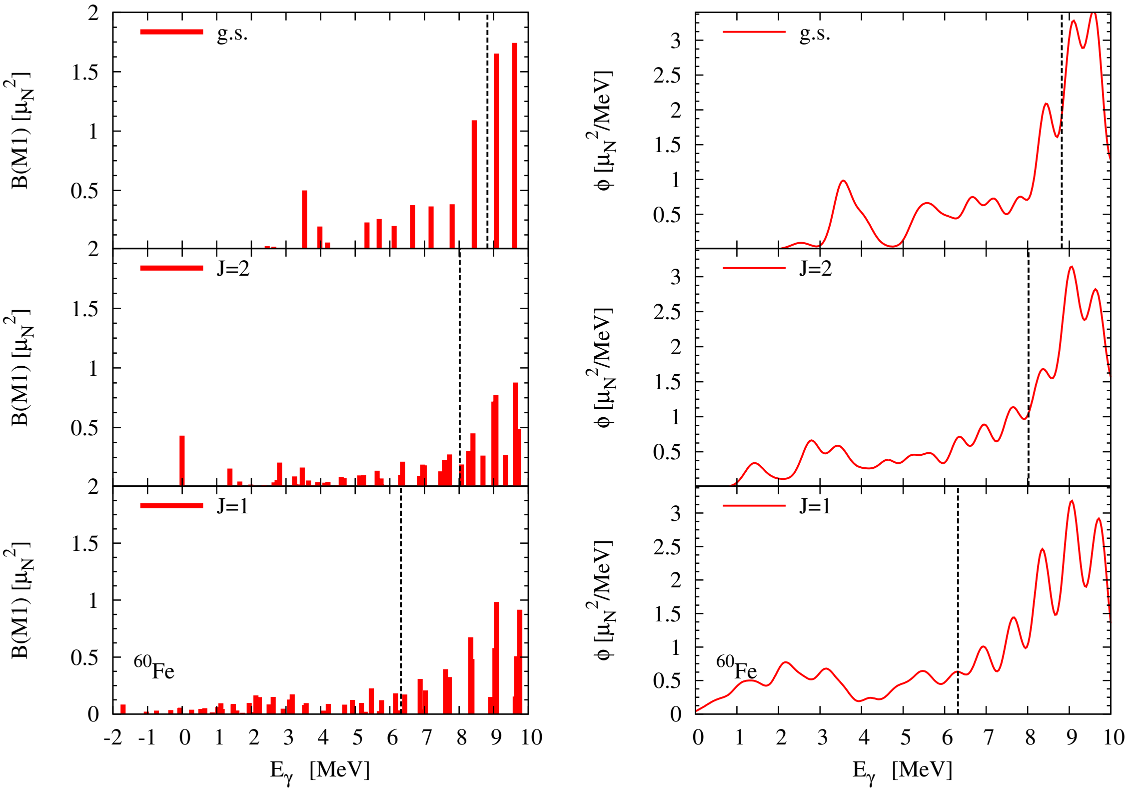

Figure 7.46: B(M1) strength distributions (left panels) and ϕ_{M1} (right panels) on the 0^+ ground state of ^{60}Fe (upper panels), the first excited 2^+ state at 0.8 MeV [experimental value: 0.823 MeV [ENS]] (middle panels), and the first excited 1^+ state at 2.5 MeV (lower panels). The vertical lines mark the relative experimental neutron separation energy.

In fig. 7.46 we have plotted the B(M1) distribution and the ϕ_{M1} strength functions for M1 capture on the 0^+ ground state, on the first excited 2^+ state, and the first excited 1^+ state.[1] The ground state and the 1^+ can be connected via M1 transitions, as well as the 2^+ and the 1^+. while the ground state shows an emphasised orbital transitions at 3.5 MeV, the other states do not exhibit such a transition. The orbital B(M1) strength on the 1^+ strength never exceeds 0.075 μ_N^2 for a single state and on the 2^+ states it never exceeds 0.09 μ_N^2.[2] The spin strength is of similar magnitude for these states at low energies (i.e. below 5 MeV). The whole B(M1) spectra of the two excited states consists of spin and orbital contributions of similar magnitude. For the ground state, we have a large gap of 2.5 MeV (= energy of the first excited 1^+), while for the other two states we see a lot more strength at low energies. Interestingly, if we compare the strength function ϕ_{M1} of the ground state with the strength function of one of the excited states at the relative neutron separation energy of this excited state, we see that the ground state strength function would be a very appropriate approximation to the other strength function around the neutron separation energy of that state. This is a strong indication that for these states Brink's hypothesis would work well. The picture changes drastically if we go to states with lower relative neutron separation energy, though.

The large amount of small low-lying strength in the strength functions of the excited states - which is missing in the ground state strength function - shows that already from the spin combinations (the excited states can connect to many more spins) it can be dangerous to use the ground state strength function for all states.

---

[1] The first excited 1^+ state in ^{60}Fe is still experimentally unknown.

[2] With one exception: the orbital B(M1) value for the magnetic dipole moment of the 2^+ state is about 0.31 μ_N^2

We have plotted the ^{59}Fe(n,γ)^{60}Fe reaction rate in fig. 7.47. We can see that the low-energy region of the SM strength function does not change remarkably when we use a different valence space. However, the spin-flip resonance is particularly smaller when using the ^{48}Ca core (see fig. 7.45) due to the closure of the $f_{7/2}$ shell. The importance of the reaction rate in fig. 7.47 is given by the fact that the γ-channel is described completely with microscopic strength functions. This has the consequence that we have a reduction of the E1 transitions relative to the default approach (there is no pygmy mode and microscopic E1 transitions are generally smaller at low energies than the Lorentzian E1 strength functions) and we have a reduction of the M1 strength relative to the default approach with the single-particle strength. yet, the impact of the M1 strength functions is rather small, but we see that the SM strength function for the ^{48}Ca core gives a slightly larger reaction rate, because the total M1 strength up to the separation energy is larger in that case.

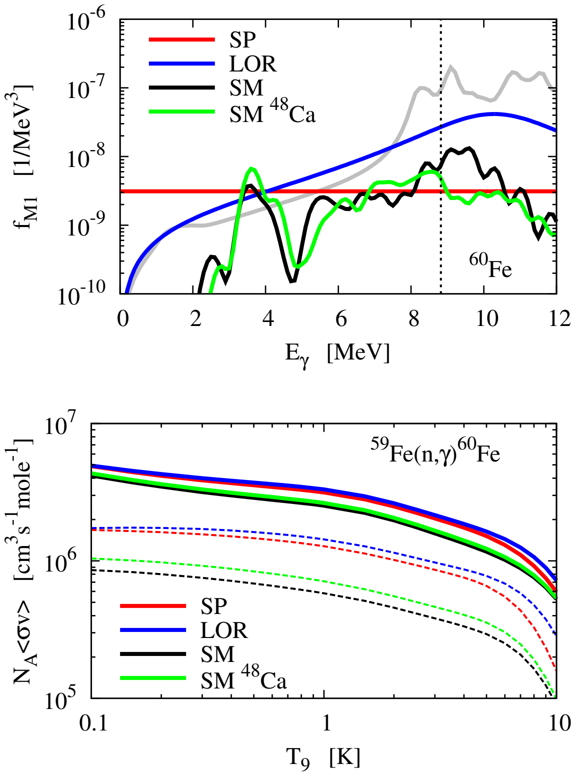

Figure 7.47: Upper panel: M1 strength functions f_{M1} for the different M1 prescriptions and the E1 strength function from the RQTBA model; lower panel: the corresponding reaction rates for the reaction ^{59}Fe(n,γ)^{60}Fe with E1 and M1 transitions (full lines) and M1 transitions only (dashed lines). The SM strength function was obtained by using a ^{40}Ca core, the other SM strength function using a ^{48}Ca core. The small bump in the E1 strength function stems from a spurious state in the RQTBA model.

7.3.2.6 ^{69}Fe: States of Different Parity

So far we have discussed states of the same parity. However, we also would like to investigate how the M1 strength evolves on states with different parity. To do so, we chose ^{69}Fe which has N=43 neutrons. The ground state in the shell model is a $9/2^+$ state. Additionally, we calculate the B(M1) distribution on the first $1/2^-$, $3/2^-$, and $5/2^-$ states. For the neutrons we use the pf-shell without the $f_{7/2}$-shell (i.e. a ^{48}Ca core) but with the $g_{9/2}$-shell. For the protons we used the complete pf-shell. As the $g_{9/2} \rightarrow g_{7/2}$ neuron transitions are outside our model space we will miss part of the spin-flip resonance. We will mainly get the proton contribution to the spin-flip resonance. However, due to the low neutron separation energy in ^{69}Fe of $S_n = 3.34$ MeV, only the tail of the resonance would become relevant.

In fig. 7.48 we have plotted the B(M1) distributions for the $9/2^+$ ground state and the first excited

$1/2^-$, $3/2^-$, and $5/2^-$ states. Despite the general feature that the M1 strength has a minimum around 3-5 MeV, the low-energy region looks very different for the different states. First of all, we see a large magnetic moment for the $9/2^+$ ground state. The orbital strength is rather small for that state but still gives noticeable strength up to 3 MeV. These transitions between 0 MeV and 3 MeV are transitions to $7/2^+$, $9/2^+$, and $11/2^+$ states. The strength function on the $1/2^-$ state shows quite different features, though. First, it has a prominent spin transitions at 0.7 MeV as well as a distinct orbital strength around 2.5 MeV. From the location of the neutron separation energy we see that in an astrophysical (n,γ) reaction, all transitions to that state would be subject to these particular strength, which consists of a spin and an orbital part. For the $3/2^-$ and the $5/2^-$ states, the strength distribution shows also enhanced spin transitions. Surprisingly, the $3/2^-$ strength still has a notable orbital strength while the $5/2^-$ strength does not show any features of a possible scissors mode.

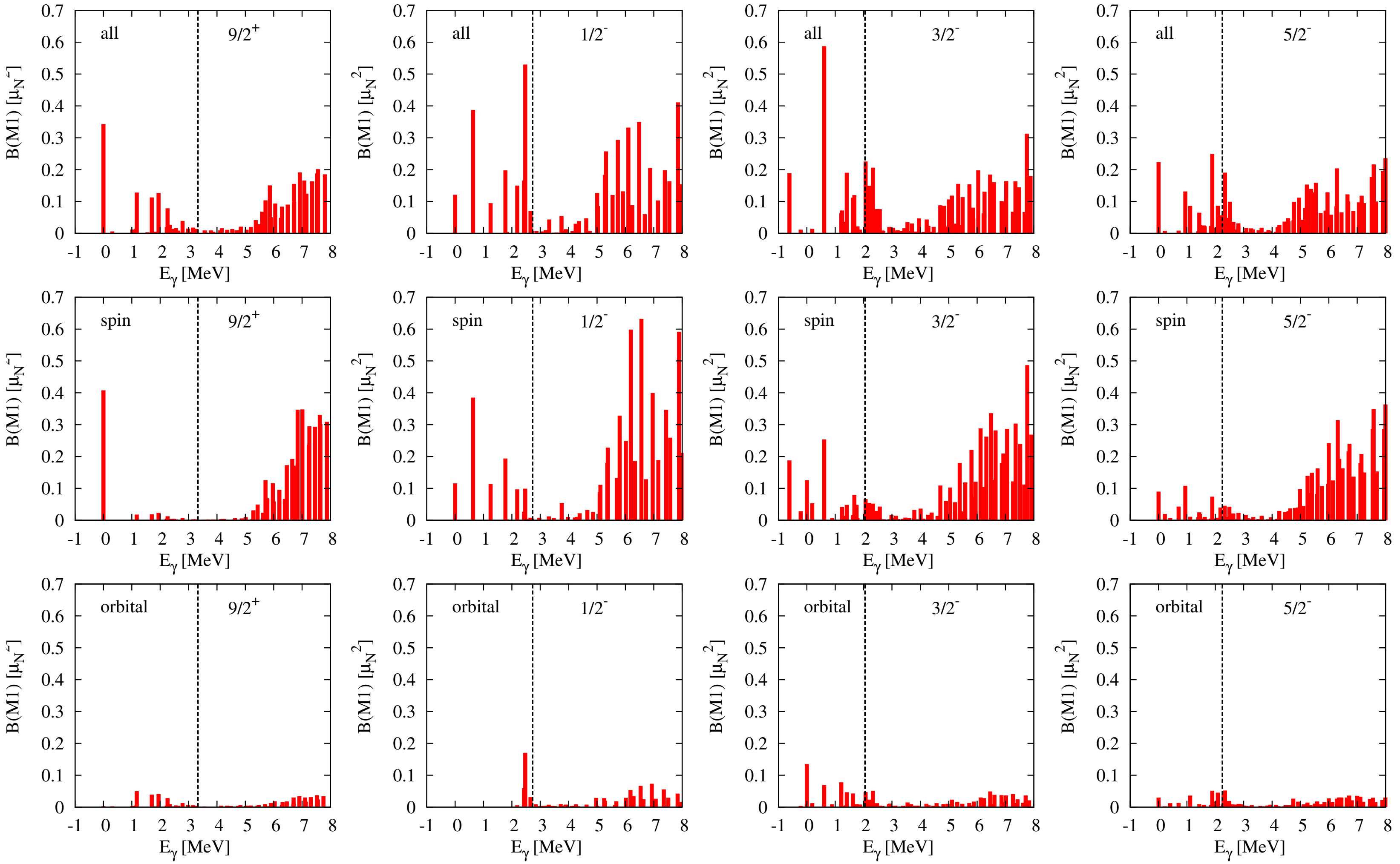

Figure 7.48: B(M1) distribution of ^{69}Fe. The first column is the distribution for the (shell model) ground state with $9/2^+$, the second column for the first excited $1/2^-$ at $E_x = 0.6$ MeV, the third column for the first excited $3/2^-$ at $E_x = 1.28$ MeV, and the fourth column for the first excited $5/2^-$ at $E_x = 1.08$ MeV. The first row gives the complete strength, the second row gives the strength from the spin part, and the third row gives the strength from the orbital part. The vertical lines mark the (experimental) neutron separation energy S_n relative to that state and the E_γ are defined relative to the corresponding state. Negative E_γ values are transitions going downwards, e.g. the two transitions with negative E_γ in $3/2^-$ are the transitions to the $1/2^-$ and the $5/2^-$ state.

In fig. 7.49 we plot the ^{68}Fe(n,γ)^{69}Fe reaction rate and notice a small change in the reaction rate. This is again due to the fact that the E1 transitions dominate, although the neutron separation energy is rather small for this nucleus. We give the SM strength function for the first $1/2^-$ and the first $9/2^+$ states to investigate the influence of different strength functions on the cross sections. Indeed we find differences of nearly a factor of 2 in the reaction rates which implies that such calculations are quite sensitive to the detailed structure of the strength function. We note that this nucleus has a neutron threshold similar to the values found in the r-process path.

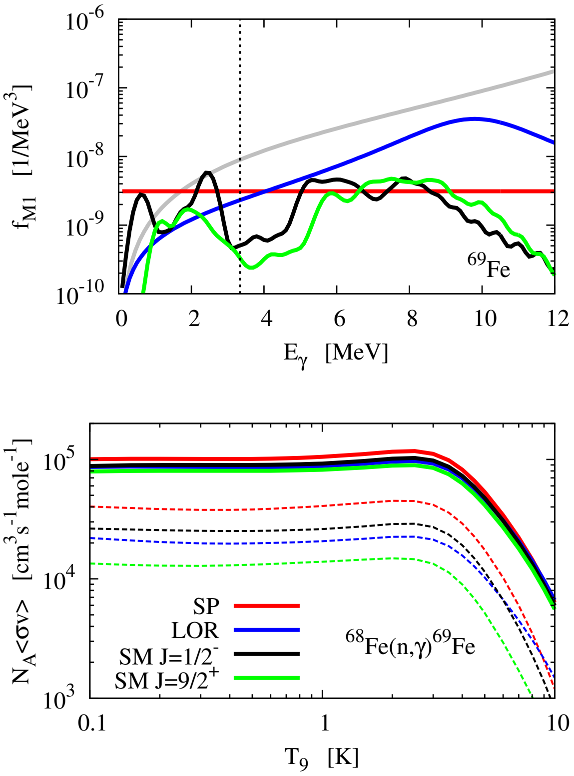

Figure 7.49: Upper panel: M1 strength functions f_{M1} for the different M1 prescriptions and the E1 strength function from the RIPL-2 model; lower panel: the corresponding reaction rates for the reaction ^{68}Fe(n,γ)^{69}Fe. The two SM strength functions are given for the first $1/2^-$ state and the first $9/2^+$ states. Systematics predict the $1/2^-$ to be the ground state while the shell model predicts the $9/2^+$ to be the ground state.

8

Microscopic Mass Properties and Fission Barriers of Heavy and Super-Heavy Elements

The r-process can reach the region in the nuclear chart in which fission may occur. Fission can move considerable amounts of matter to lower mass regions and thus prevent the build up of heavier elements. However, this depends delicately on the astrophysical conditions, the nuclear masses, and the fission barriers. In this chapter we will discuss the fission barriers, in particular in the region of the so-called super-heavy nuclei.

During the r-process flow, neutron-induced fission is a competing reaction to the (n,γ) reactions taking place. After the freeze-out, the synthesised heavy neutron-rich isotopes β-decay towards "stability" until α-decay sets in (or we reach a stable isotope). During the β-decay phase, β-delayed fission can occur thus shifting matter to lower mass regions. In case of super-heavy nuclei, spontaneous fission might compete with α-decay, thus being able to remove even more matter from the actinides or super-heavy regions.

In this chapter we employ the Skyrme-Hartree-Fock-BCS model to obtain ground state and fission properties of heavy and super-heavy nuclei. Additionally, we employ collective rotational and vibrational corrections following [Klü08, EKR11].

8.1 Introduction

Before starting to discuss the outcomes of our calculations, we need to define some nomenclature and explain some basic assumptions we have made. As we will compare the results of different Skyrme functionals in this chapter, we will also try to focus on the differences between these forces. A general overview on the Skyrme interaction and its applications, in particular fission barriers, can be found in [SR07]. An overview on the properties of super-heavy nuclei can be found in [ĆHN05]. In general, super-heavy elements are usually defined as those nuclei for which a liquid-drop barrier vanishes and which are stabilised against immediate fission by shell effects only [ĆDH$^+$96]. Therefore, super-heavy elements are very sensitive to the shell-structure [BRR$^+$99].

The effective mass is a property that takes a specific value in every Skyrme functional as it depends on the Skyrme parameters (see section 4.2.5). It has been shown that the effective mass is proportional to the mean level density of single-particle states around the Fermi energy [JM86, DNW95]. A small effective mass leads thus to a small level density and to an enhancement of shell effects [BRR$^+$99]. Skyrme functionals with different effective masses will therefore predict different shell effects. In the case of fission barriers in super-heavy nuclei this results in rather small barriers predicted by functionals with a large effective mass, i.e. predicting small shell effects, and rather large barriers predicted by functionals with a small effective mass.

We will only present results for even-even nuclei, as for these the BCS method is known to be a good approximation. For odd nuclei, one usually employs the so-called *blocking* approximation [RS00]. In this approximation the single-particle state of the unpaired nucleon is explicitly removed from the BCS treatment. The quality of this approximation is questionable for the calculation of fission barriers, because the single-particle level scheme changes with deformation. Additionally, for odd nuclei time-reversal symmetry is broken and time-odd contributions arise in the Skyrme functional [Ben97, BHR03, PERN10]. Although we disregard the odd nuclei, we can still examine global aspects like the evolution of the barrier with neutron number. This assumption is justified by the fact that empirical fission barriers usually do not show large odd-even effects [IAEa].

All nuclei we discuss here can be approximately considered to be bound. Since we only consider even-even nuclei we cannot use the neutron- or proton-separation energy to define the neutron or proton drip line. Instead, we consider the Fermi energy ϵ_F as determined form the BCS treatment of pairing. If the Fermi energy becomes positive for any deformation along our fission path, we consider this nucleus as not bound. This is not an unambiguous approximation, as the nucleus may have a negative separation energy although the Fermi energy is still negative.

Another approximation we have to make is that we generally assume axial symmetric nuclear shapes. Triaxial shapes are numerically much more difficult to handle and it is not yet feasible to perform a large scale examination on fission barriers allowing for triaxial deformations. Nevertheless, triaxial configurations can be important for fission barriers as they usually lower the first barrier in super-heavy elements [BBMR04]. Therefore, we can regard our obtained barriers as upper boundaries. Moreover, we find certain nuclei to exhibit extremely deformed ground states. An example for three such nuclei is shown in fig. 8.1. In this figure we have plotted the *fission path* through the *potential energy surface*. The energy surface is the evolution of the binding energy (including collective corrections) with the different deformation parameters and it is restricted by our assumption of axial-symmetric shapes. The fission path is the path of lowest energy through this energy surface.

The uppermost panel in fig. 8.1 shows a nucleus with a very distinct global minimum at $\beta_2 \approx -0.45$. Since it is very likely that the (real) fission path leads through the triaxial region (which we cannot handle), we could have a triaxial minimum and the maximum barrier at $\beta_2 \approx 0.0$ would be circumvented. The panel in the middle of fig. 8.1 shows a nucleus for which we would probably need triaxial configurations, too. The global minimum is at $\beta_2 \approx -0.45$, while we have another distinct local minimum at $\beta_2 \approx 0.38$. These two minima can be connected by a valley leading through the triaxial region. We will mark nuclei with exhibit one of this two features in their fission path as nuclei for which triaxial configurations are needed. Such nuclei will be shown in grey colours in the following figures.

The lowermost panel shows a similar case to the panel in the middle, but the prolate minimum is the global minimum. Thus, we can at least assume that from the prolate minimum on we might need triaxiality only for the fission barrier, not necessarily for the ground state. As we have to face the issue of triaxiality affecting our barriers in all our results, we will consider such a nucleus in our discussion.

The relevance of triaxial configurations in nuclei is discussed in [ĆHN05, RRGS09] for microscopic approaches; Möller *et al.* [MBC$^+$08] discuss the issue of reflection asymmetric and triaxial nuclear shapes in the microscopic-macroscopic finite-range droplet model.

As we have already discussed above, our model provides us with the potential energy surface. An example is shown in fig. 8.2. In the following we will call the global minimum in such a curve the *ground state* of this nucleus if it is not too strongly deformed (i.e. $|\beta_2| \lesssim 0.5$). From this "ground state" we obtain the binding energy and the ground state properties. The fission barriers are derived relative to this ground state. In general Skyrme forces lead to large deviations in the binding energy of several MeV compared to experimental data [SR07]. However, separation energies like two-neutron separation energies and Q_α-values are usually reproduced with smaller deviations [Erl11].

The *scission* point is the point beyond which fission is inevitable. In a liquid drop model one defines this scission point as the point at which the two drops separate, i.e. at which the barrier is traversed and fission occurs. As we are not able to find this point automatically, we make use of a simpler and approximate definition. We regard the scission point to be crossed if the following conditions are fulfilled:

1. The potential energy surface (with collective corrections) is energetically below our ground state

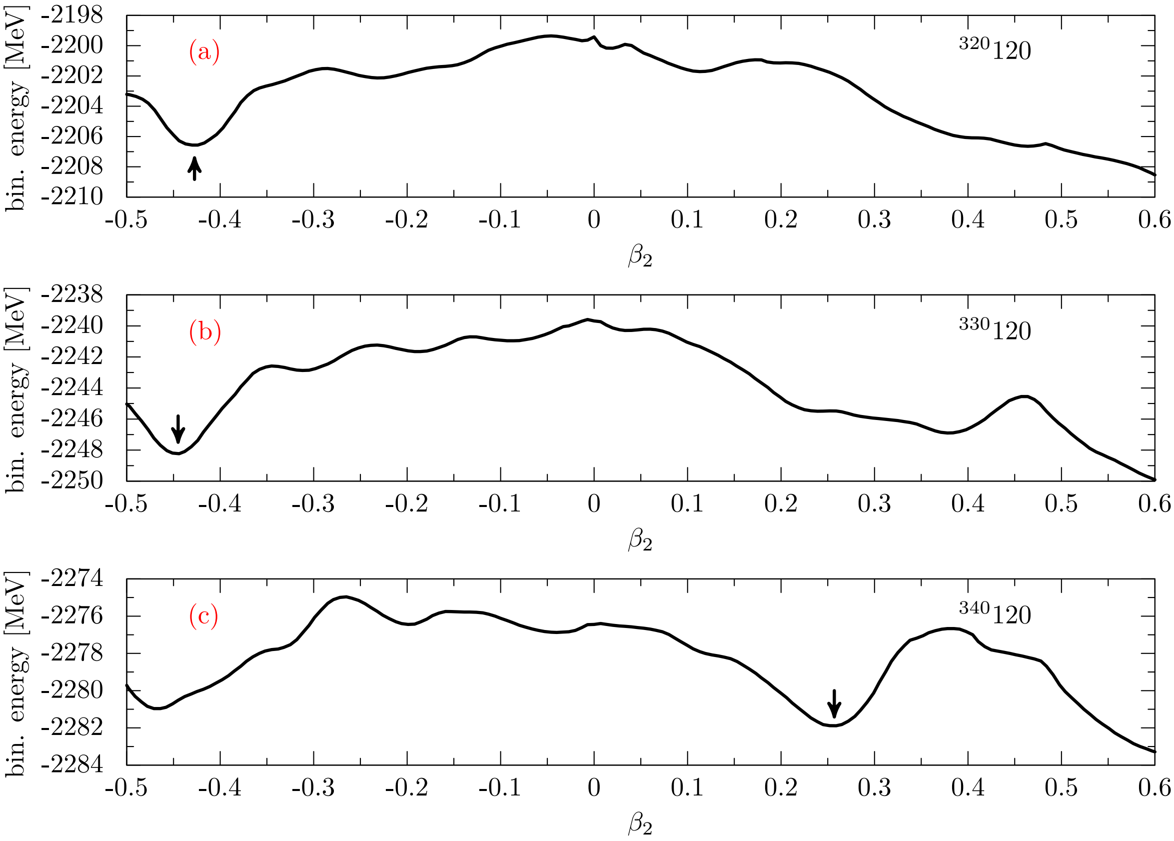

Figure 8.1: Potential energy surfaces for $^{320,330,340}120$. Case (a) is a nucleus with a very distinct minimum in the oblate region and has no corresponding minimum in the prolate region. Case (b) has a prominent global oblate minimum and also a prolate minimum; it is very likely that these two minima are connected through the triaxial region. Case (c) we do not consider as triaxial, since the prolate minimum is the global one. The arrows mark the global minima which we consider as ground states.

minimum.

2. The quadrupole deformation has to be above a certain value. We take this value to be $\beta_2 = 1.3$ in super-heavy elements. For lighter elements we take $\beta_2 = 1.8 - 2.0$ as minimum deformation, but a clear limit cannot be easily found.

3. The first derivative in energy has to be zero, i.e. the potential energy surface has to be abating. This ensures us that we do not miss a barrier at larger deformation.

A different issue is that the scission point might not be unambiguously known. Figure 8.2 shows two different fission paths depending on whether one restricts the calculation on reflection symmetry or not. This suggests a structure of two valleys where symmetric fission competes with asymmetric fission [BRR+98].

As we have already mentioned in section 4.2, there exists a huge variety of different Skyrme parametrisations; for an overview see [BHR03, SR07].

In this thesis we will exclusively use Skyrme forces with density-dependent pairing [Ben97, BHR03]. This is important because the functionals SLy6 and SkI3 were obtained assuming density independent pairing [CBH+98, RF95]. In principle all these functionals were obtained from fits to ground state properties of mostly magic nuclei; mostly binding energy, radii, et cetera. However, there some important differences between the functionals we employ in this thesis:

SLy6: The SLy functional family [CBH+98] has been additionally fitted to nuclear matter properties. The goal was to obtain a Skyrme functional that would perform more reliable for neutron-rich

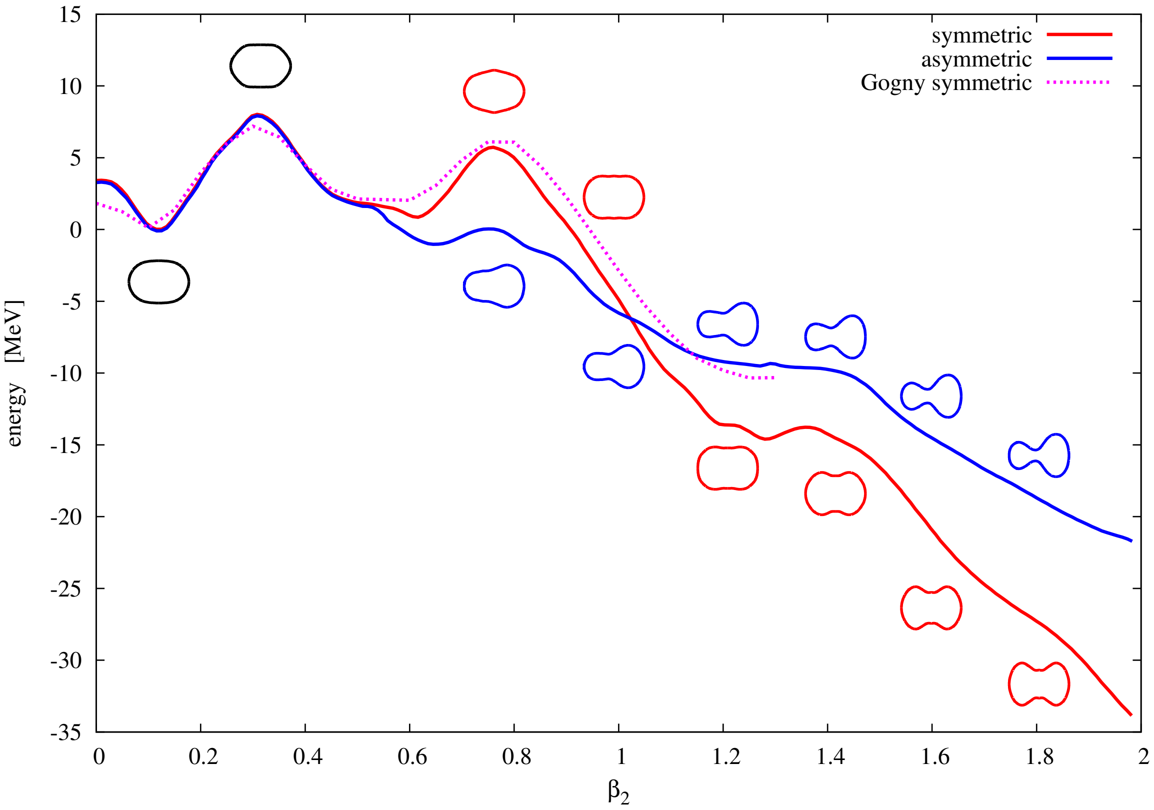

Figure 8.2: Potential energy surfaces for $^{288}_{112}$Cn$_{176}$ for two different calculations: (red) forcing reflection and axial symmetry and (blue) forcing only axial symmetry and allowing for reflection asymmetric shapes. The plotted nuclear shapes schematically represent the contour lines of the neutron density at $\rho = 0.07\text{fm}^{-3}$.

nuclei. SLy6 is the starting point of the SLy functional family. The other functionals SLy4 and SLy7 differ from SLy6 by the centre-of-mass correction and the treatment of the $\boldsymbol{J}^2$-term in the functional (see [Ben97] for more information). The SLy6 functional predicts a small effective mass $m^*/m = 0.69$.

SkI3: The SkI functional family [RF95] was fitted using properties of exotic nuclei. The different functionals of that family differ by the treatment of the LS-coupling. The effective mass of the SkI3 functional is $m^*/m = 0.577$ and thus particularly small.

SV-min: The SV functionals [KRBM09] have been developed very recently and can be considered as modern Skyrme functionals because they try to obtain an effective mass of $m^*/m \approx 0.9$. SV-min has been deduced by an unconstrained fit to properties of finite nuclei only. The effective mass of the SV-min functional is $m^*/m = 0.95$.

BSk14: This functional has been obtained by a fit to experimental masses and experimental fission barriers [GSP07]. Although it is a Skyrme functional, the pairing part is described with more parameters than in a “traditional” Skyrme functional. Therefore, we chose not to use this functional but rather use the published results for fission properties [Brua]. However, the method(s) applied to obtain the published results for this functional are different to the methods we have used here. Hence, a direct comparison between our results and these results is not possible. Consequently, we will depict the results obtained from that functional with the term “HFB14” from now on to emphasise the differences in the functional and the method. Nevertheless, it is possible to compare the functionals on a large scale, i.e. comparing the trends they predict regarding certain properties.

The effective mass of this functional is $m^*/m = 0.8$.

An alternative functional would be the Gogny functional [DG80], for which a database of ground state properties has been compiled [HG08]. Alternatively, relativistic mean-field approaches and their functionals can be applied, see [BBMR04] for a comparison of non-relativistic Skyrme and relativistic mean-field approaches towards fission properties of super-heavy elements.

8.2 Ground State Properties

In this section we will focus on the ground state properties while the fission properties will be discussed in the subsequent section, i.e. section 8.3.

8.2.1 Ground State Deformation

In fig. 8.3 we have plotted the quadrupole deformation of the ground state. The grey marked nuclei are the nuclei for which we assume that triaxial configurations are needed. At first glance we identify a regular oscillation of the quadrupole deformation with neutron number: starting from the N=126 nuclei on the left bottom of fig. 8.3 (which show spherical shapes due to the neutron shell closure) the nuclei become more and more deformed with increasing neutron number. Suddenly at neutron numbers N=170 to N=180, oblate ground state deformations arise. Then a transition to spherical shapes around the N=184 shell closure follows. This process repeats now for nuclei beyond N=184 until a region around N=260 is reached which again shows tendencies towards spherical shapes. This is a hint that another shell closure is given around N=260.

Some of the peculiarities mentioned above, we will discuss in more detail:

- For nuclei with neutron numbers between N=170 and N=180 we obtain oblate ground state deformations, however the exact details are sensitive to the used functional. The exact definition of the ground state can be ambiguous especially in the transition region around N=168/170 as these nuclei all have two local minima; one is oblate, the other prolate. It is possible that these nuclei tend to have triaxial ground states, because triaxial ground states are predicted for nuclei just before the N=126 closure by the Gogny and the SLy4 functional [RRGS09].
- Beyond the N=184 shell closure one can observe a jump in β_2 with increasing proton number. These nuclei are predicted to have very strongly deformed prolate shapes. The blue marked nuclei for the asymmetric SLy6 results could also be accounted to the region of nuclei where triaxial shapes might occur. We cannot exclude that the very strongly prolate deformed shapes (marked by orange and red squares) are fission isomers, because many of these nuclei have a local minima at smaller prolate deformations.
- We also see a difference between the quadrupole deformation between the reflection symmetric and asymmetric SLy6 results around Z=100 - 106 and N= 192 - 196. These are related to octupole deformations in the ground state which lead to different minima in certain cases. For more details see section 8.2.1.1 and in particular fig. 8.5.

We find the spherical nuclei around the neutron shells N=126 and N=184 in fig. 8.3. However, we do not find a similar behaviour with regard to certain proton numbers. This indicates that the Skyrme functionals presented here do not predict a magic proton shell closure at Z=114[1].

---

[1] Many liquid-drop models predict a proton shell closure at Z=114.

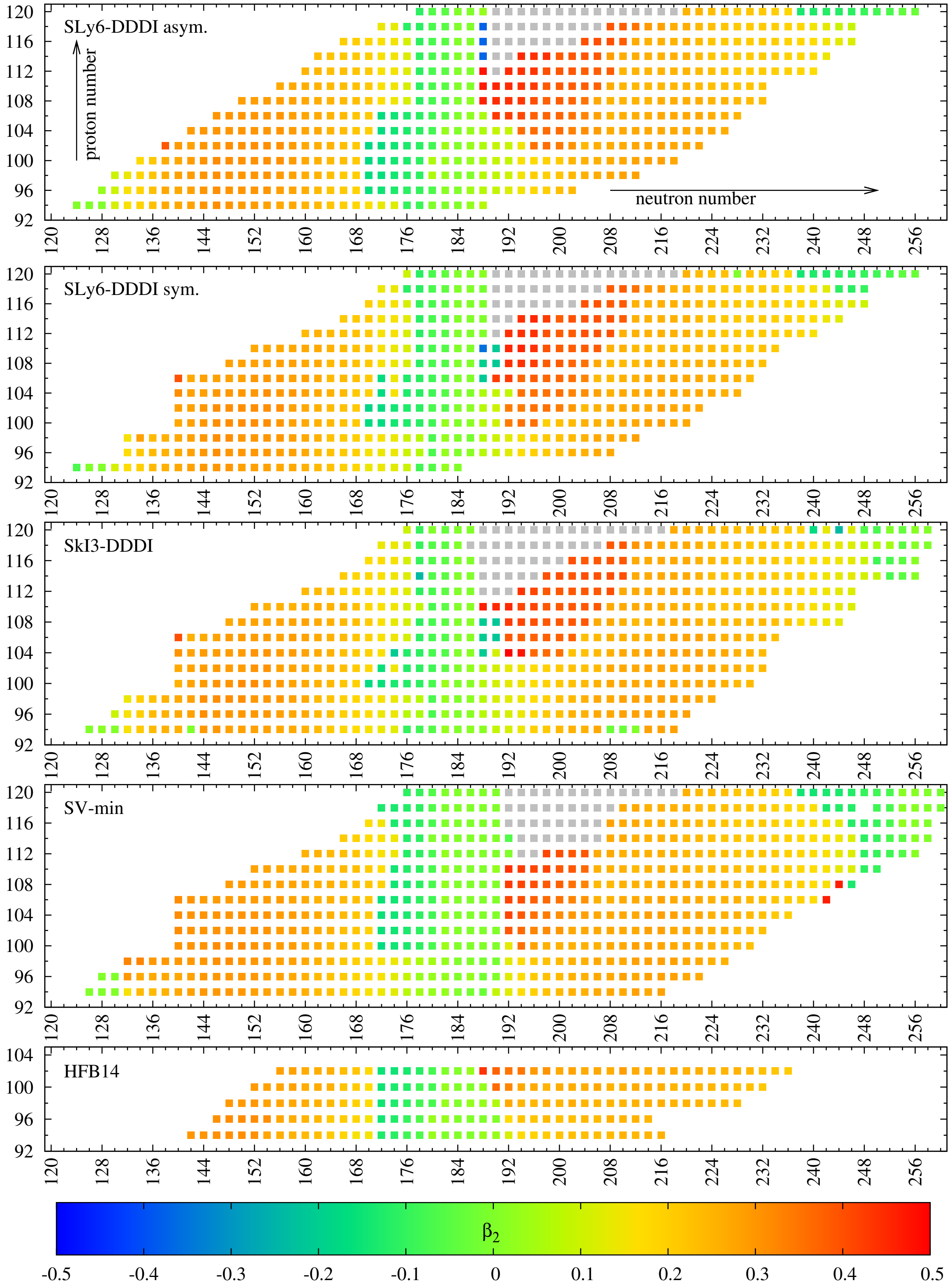

Figure 8.3: Quadrupole deformation of the ground state for different Skyrme functionals. The symmetric results for SLy6, SkI3, and SV-min were calculated by J. Erler [Erl11]. The HFB14 results are taken from [GSP07, Brua].

8.2.1.1 Reflection Asymmetric Ground States

Besides the quadrupole and hexadecupole deformation of the ground state, we might have to consider octupole deformations. As discussed above, octupole shapes are correlated to reflection asymmetric nuclear shapes. An example for a nucleus with a reflection asymmetric ground state shape is given in fig. 8.4.

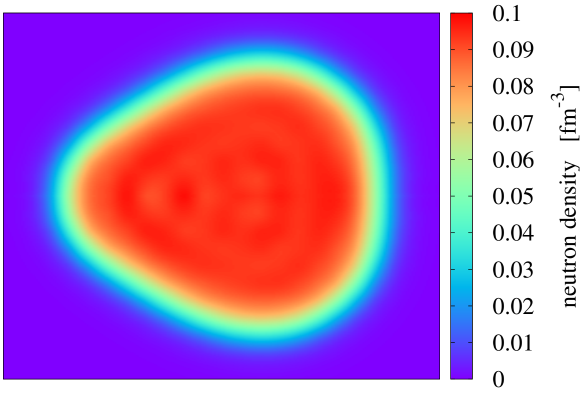

Figure 8.4: Neutron density distribution of $^{294}_{102}\mathrm{No}_{192}$ at ground state deformation predicted by the SLy6 functional.

In fig. 8.5 we mark those nuclei for which the inclusion of reflection asymmetric shapes results in a gain in binding energy. The numbers indicate the energy gain, more details are given in the figure caption. We see from this figure that the differences between the forces are large, not only regarding which nuclei are affected, but also concerning the gain in binding due to the reflection asymmetric shapes. This is important for the prediction of fission barriers as this changes the height of the barrier. Moreover, the nuclei shown in fig. 8.5 emphasise the importance of reflection asymmetric shapes not only for the fission path but also for the ground state.

The nuclei with underlined numbers are very peculiar cases in which the reflection asymmetric ground state has a different quadrupole deformation β_2 than the reflection symmetric ground state. For nuclei with bold and underlined numbers, this difference in the quadrupole deformation is very large. It is worthwhile to note that always the minimum with the smaller quadrupole deformation is lowered by reflection asymmetry, i.e. it appears as if reflection asymmetry favours smaller quadrupole deformations.

The tendency of a certain Skyrme force to predict reflection asymmetric shapes (and the difference in energy from octupole deformations) is governed by several aspects. The pairing correlations are known to affect octupole shapes in a way that stronger pairing correlations have the tendency to make the nucleus less octupole deformed [BN96]. The octupole deformation itself is produced by the long-range octupole-octupole interaction between nucleons; this depends on the matrix elements between single particle states with $\Delta J = \Delta L = 3$ and their relative spacing [AB93, BN96]. According to the mentioned articles, the nuclei with the most evident tendency to have reflection asymmetric ground states are nuclei with neutron numbers just beyond a magic shell-closure[1]; for an explanation based on a liquid-drop approach we refer the reader to [LSM⁺82]. The disappearance of the octupole ground state shapes with increasing proton number is related to the shift of the ground state quadrupole deformation to larger deformations, i.e. into regions where reflection asymmetric shapes are again favourable. The gain in energy from octupole deformation does not vanish for these nuclei though, but it affects the potential energy surface in the region “left” of the ground state.

The appearance of these effects just above magic shell-closure is in complete conformance with our outcomes in fig. 8.5 and fig. 8.6 in which we see that the effect of octupole deformations occur after the N=184 and the N=126 shell closure, respectively. In our case, the coupling between the $k_{17/2}$ and $2h_{11/2}$ shells induces the octupole deformations beyond the N=184 shell.

In fig. 8.7 we have plotted the neutron single-particle levels for the nuclei ^{290}Fm and ^{306}Fm. The

---

[1] In the cited papers the authors discuss this issue for the N=126 shell closure.

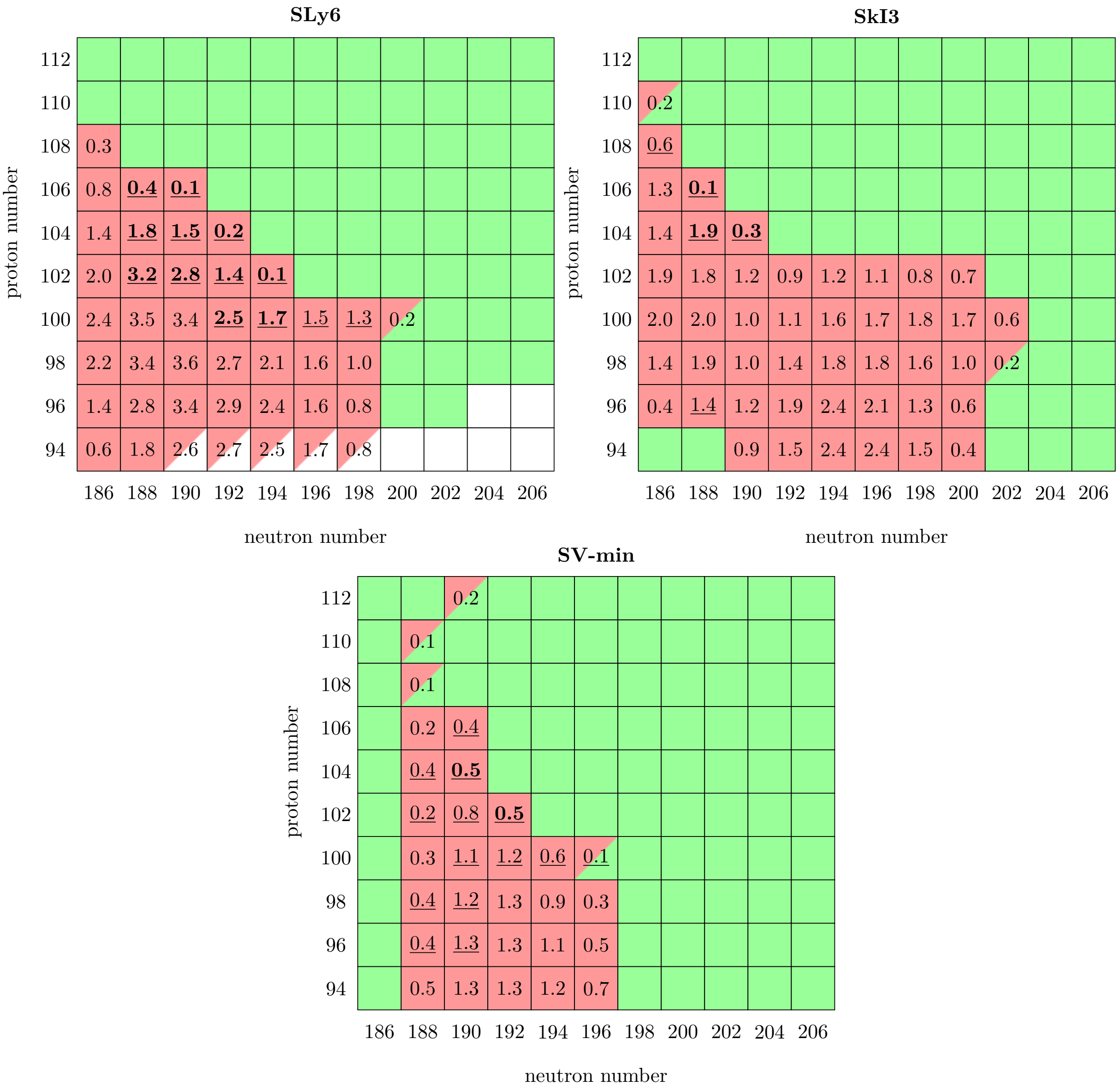

SLy6

proton number	186	188	190	192	194	196	198	200	202	204	206
112	🟩	🟩	🟩	🟩	🟩	🟩	🟩	🟩	🟩	🟩	🟩
110	🟩	🟩	🟩	🟩	🟩	🟩	🟩	🟩	🟩	🟩	🟩
108	0.3	🟩	🟩	🟩	🟩	🟩	🟩	🟩	🟩	🟩	🟩
106	0.8	**0.4**	**0.1**	🟩	🟩	🟩	🟩	🟩	🟩	🟩	🟩
104	1.4	**1.8**	**1.5**	**0.2**	🟩	🟩	🟩	🟩	🟩	🟩	🟩
102	2.0	**3.2**	**2.8**	**1.4**	**0.1**	🟩	🟩	🟩	🟩	🟩	🟩
100	2.4	3.5	3.4	**2.5**	**1.7**	1.5	1.3	0.2	🟩	🟩	🟩
98	2.2	3.4	3.6	2.7	2.1	1.6	1.0	🟩	🟩	🟩	🟩
96	1.4	2.8	3.4	2.9	2.4	1.6	0.8	🟩	🟩		
94	0.6	1.8	2.6	2.7	2.5	1.7	0.8				

neutron number

SkI3

proton number	186	188	190	192	194	196	198	200	202	204	206
112	🟩	🟩	🟩	🟩	🟩	🟩	🟩	🟩	🟩	🟩	🟩
110	0.2	🟩	🟩	🟩	🟩	🟩	🟩	🟩	🟩	🟩	🟩
108	0.6	🟩	🟩	🟩	🟩	🟩	🟩	🟩	🟩	🟩	🟩
106	1.3	**0.1**	🟩	🟩	🟩	🟩	🟩	🟩	🟩	🟩	🟩
104	1.4	**1.9**	**0.3**	🟩	🟩	🟩	🟩	🟩	🟩	🟩	🟩
102	1.9	1.8	1.2	0.9	1.2	1.1	0.8	0.7	🟩	🟩	🟩
100	2.0	2.0	1.0	1.1	1.6	1.7	1.8	1.7	0.6	🟩	🟩
98	1.4	1.9	1.0	1.4	1.8	1.8	1.6	1.0	0.2	🟩	🟩
96	0.4	1.4	1.2	1.9	2.4	2.1	1.3	0.6	🟩	🟩	🟩
94	🟩	🟩	0.9	1.5	2.4	2.4	1.5	0.4	🟩	🟩	🟩

neutron number

SV-min

proton number	186	188	190	192	194	196	198	200	202	204	206
112	🟩	🟩	0.2	🟩	🟩	🟩	🟩	🟩	🟩	🟩	🟩
110	🟩	0.1	🟩	🟩	🟩	🟩	🟩	🟩	🟩	🟩	🟩
108	🟩	0.1	🟩	🟩	🟩	🟩	🟩	🟩	🟩	🟩	🟩
106	🟩	0.2	0.4	🟩	🟩	🟩	🟩	🟩	🟩	🟩	🟩
104	🟩	0.4	**0.5**	🟩	🟩	🟩	🟩	🟩	🟩	🟩	🟩
102	🟩	0.2	0.8	**0.5**	🟩	🟩	🟩	🟩	🟩	🟩	🟩
100	🟩	0.3	1.1	1.2	0.6	0.1	🟩	🟩	🟩	🟩	🟩
98	🟩	0.4	1.2	1.3	0.9	0.3	🟩	🟩	🟩	🟩	🟩
96	🟩	0.4	1.3	1.3	1.1	0.5	🟩	🟩	🟩	🟩	🟩
94	🟩	0.5	1.3	1.3	1.2	0.7	🟩	🟩	🟩	🟩	🟩

neutron number

Figure 8.5: Overview on the relevance of reflection asymmetric nuclear shapes for the determination of the ground state. The red squares mark nuclei for which we obtain reflection asymmetric ground states, the green ones have reflection symmetric ground states. The white squares mark nuclei beyond the drip line. Squares that are partly filled red mark nuclei which may be unstable against neutron emission when using the stated force, but asymmetry would still affect the ground state. The red and green filled squares mark nuclei for which the shift in the ground state binding energy due to reflection asymmetric shapes is small and could be neglected. If a number is given, it is approximately the gain in binding energy from allowing the reflection asymmetric shapes. If the number is underlined, then the asymmetric calculations predicts a slightly different quadrupole deformation. If the number is underlined and bold, then the quadrupole deformation is strongly shifted.

results in the right panels allow for reflection asymmetry while the left ones force reflection symmetry. The figure clearly shows how octupole correlations mix the single-particle scheme. The SLy6 functional predicts a non-vanishing octupole deformation for quadrupole deformation $\beta_2 = 0$ and thus re-arranges the single-particle levels. The relevant levels for the ground state we find by looking for minima or level crossings (lying slightly below the Fermi energy) at the marked ground state deformation (the vertical green lines). The upper right panel shows a very distinct local minimum at ground state deformation (just below -3 MeV). The ground state for the reflection symmetric calculation (upper left panel) is defined by a level crossing (also just below -3 MeV). Figure 8.7 therefore outlines, how the octupole

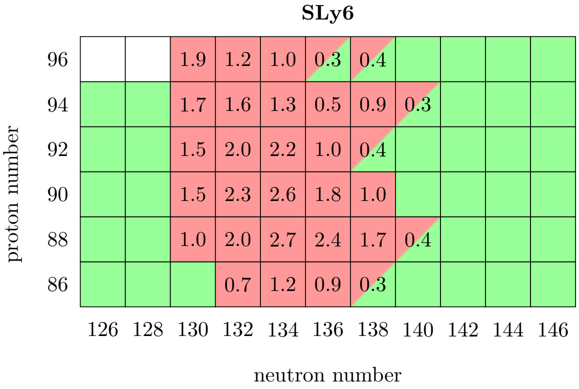

SLy6

proton number	126	128	130	132	134	136	138	140	142	144	146
96			1.9	1.2	1.0	0.3	0.4	🟩	🟩	🟩	🟩
94	🟩	🟩	1.7	1.6	1.3	0.5	0.9	0.3	🟩	🟩	🟩
92	🟩	🟩	1.5	2.0	2.2	1.0	0.4	🟩	🟩	🟩	🟩
90	🟩	🟩	1.5	2.3	2.6	1.8	1.0	🟩	🟩	🟩	🟩
88	🟩	🟩	1.0	2.0	2.7	2.4	1.7	0.4	🟩	🟩	🟩
86	🟩	🟩	🟩	0.7	1.2	0.9	0.3	🟩	🟩	🟩	🟩

neutron number

Figure 8.6: Same as fig. 8.5 but for the region around N=126.

shapes rearrange the single-particle level schemes to form different minima or crossings, respectively.

The tendency towards octupole deformations depends on the predicted effective mass of the used Skyrme functional. A larger effective mass leads to a larger level density around the Fermi energy. This leads to stronger pairing correlations and thus weakens octupole deformation. This is supported by our results, as from fig. 8.5 we see that the SkI3 force gives the most nuclei with reflection asymmetric ground states. The SkI3 functional has the smallest effective mass. However, SkI3 does not give the strongest gain in energy from the reflection asymmetric shapes, we find the largest difference between the asymmetric and symmetric shapes for the SLy6 force. This force has a slightly larger effective mass, this indicates that the gain in binding energy might not be related to the effective mass only.

The sudden disappearance of octupole ground state deformations in the SkI3 results from Z=102 to Z=104 with increasing neutron numbers stems from shape coexistences in these nuclei. A shape coexistence occurs when there are two competing minima in the potential energy surface. For Z=102 the nuclei with N=188 - 200 have a second prolate isomeric (reflection symmetric) minimum around $\beta_2 \approx 0.35$. In Z=104 and starting from N= 194 on, this second minimum becomes energetically favourable, resulting in a shift regarding the ground state deformation.

The SV-min force, with its particularly large effective mass, shows the least disposition for octupole shapes (see fig. 8.5). The aforementioned shape transitions occurs for SV-min at smaller neutron numbers.

The previous discussions showed that octupole deformations can lead to a gain in binding energy for nuclei just beyond a nuclear shell closure. We will see later that this affects our fission barriers, because the dominant fission barrier is reflection symmetric for most of these nuclei. Thus our barrier is enhanced by the octupole deformation of the ground state. Additionally, this affects the neutron separation energy (and the two-neutron separation energy) for the nuclei at the transition points between reflection symmetric and asymmetric ground states (see fig. 8.9). The impact on the r-process depends on the relative increase of the neutron separation energy and of the fission barrier, though. It is possible that the increase in separation energy is compensated by the increase in the fission barrier regarding neutron induced fission. As we are not able to obtain the neutron separation energy on an qualitatively acceptable level, we point out that future studies are needed.

At the same time, Q_β values can be affected likewise, in particular as the discussed effect vanishes with increasing proton number. However, it is important to note here that the relevant nuclei are always beyond a neutron shell closure and it is an open question if the r-process would cross the corresponding shell closure and synthesise a significant amount of these nuclei.

There is another possibility in which reflection asymmetric ground states can affect the r-process: these nuclei usually show low-lying 1^- states (in even-even nuclei; the negative parity results from the parity breaking nuclear shape) which could be excited via a E1 transitions (for more details see [AB93, BN96]). From section 7.2 we know how low-lying E1 strength can affect the (n,γ) cross section; these 1^- states should appear in a microscopic calculation (that would have to deal with the deformation!) and would enhance the E1 strength function at low energies.

The ground state deformation in microscopic-macroscopic nuclear models is discussed in [MNMS95, MBC$^+$08], with the latter one specifically concentrating on reflection asymmetric and triaxial shapes.

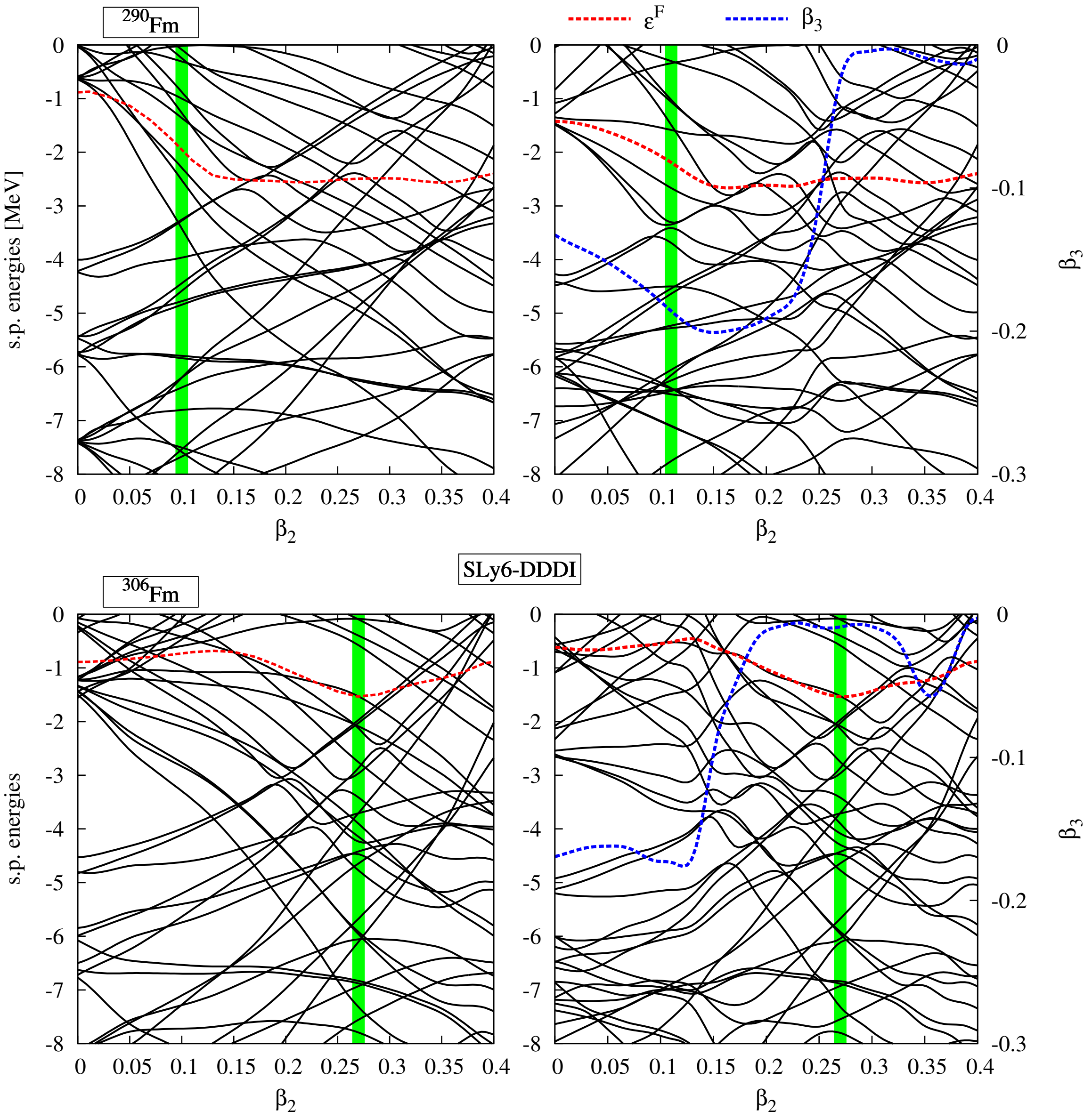

Figure 8.7: Neutron single-particle level scheme for reflection symmetric (left panels) and reflection asymmetric (right panels) calculations of the two nuclei ^{290}Fm (upper panels) and ^{306}Fm (lower panels). The red line shows the Fermi energy ε_F for neutrons. The blue curve shows the evolution of the octupole deformation β_3 with the quadrupole deformation β_2; the right axes correspond to the blue curves in the right panels. Note that an additional β_4 deformation is inhered in all four results which is not necessarily the some for all four cases! The vertical green line marks the ground state quadrupole deformation and its width estimates the related uncertainty. Note that there is a small difference in the predicted ground state deformation for ^{290}Fm.

Also the FRDM mass model [MNMS95] predicts octupole deformations for nuclei just beyond a shell closure, although less in number than SLy6 or SkI3.

8.2.2 Separation Energies

8.2.2.1 Two-Neutron Separation Energies

We show the two-neutron separation energy for the SLy6 functional in fig. 8.8 and for all functionals in fig. 8.10. In the former figure, the shell-closures at N=184 and N=126 can be easily identified, but we note an additional effect around N=162: a sudden drop in S_{2n} appears, becoming larger with increasing proton number. This drop cannot result from a change in the ground state deformation as fig. 8.3 clearly indicates that the relevant nuclei have a very similar deformation that is independent of the proton number. Furthermore, we can exclude shape coexistence or other effects in this region that would cause this drop in S_{2n}. Hence, our results indicate that there might be a deformed shell-closure around N=162. We also note that a similar feature can be seen in fig. 8.10 with regard to the SkI3 functional, while it is not present for the other functionals. This indicates that this effect is very likely related to the effective mass, which is known to affect shell-structures [BHR03]. We have checked if the SLy6 predicts a shell gap for these nuclei. In principle, we found that there is a gap, however this gap was not much larger than in the SV-min calculations. It is therefore not possible to judge if this is a deformed shell-closure. The experimental data for these nuclei is still very scarce, thus we can not judge the quality of our predictions regarding this change in S_{2n}.

In fig. 8.9 we have plotted the two-neutron separation energies for nuclei around the N=184 shell closure and for all three Skyrme functionals used in this thesis. We note a decrease in S_{2n} for N=186-194 particularly for the SLy6 and the SkI3 functional if we allow for reflection asymmetric shapes. The SV-min functional predicts substantially smoother curves. This comes from the small tendency towards octupole shapes and the general tendency of this functional to produce smoother potential energy surfaces; again this stems from the larger effective mass of the SV-min force. The overall effect of the shell closure in S_{2n} appears to be damped in SV-min compared to the other two functionals, as the jump in S_{2n} is smaller in SV-min.

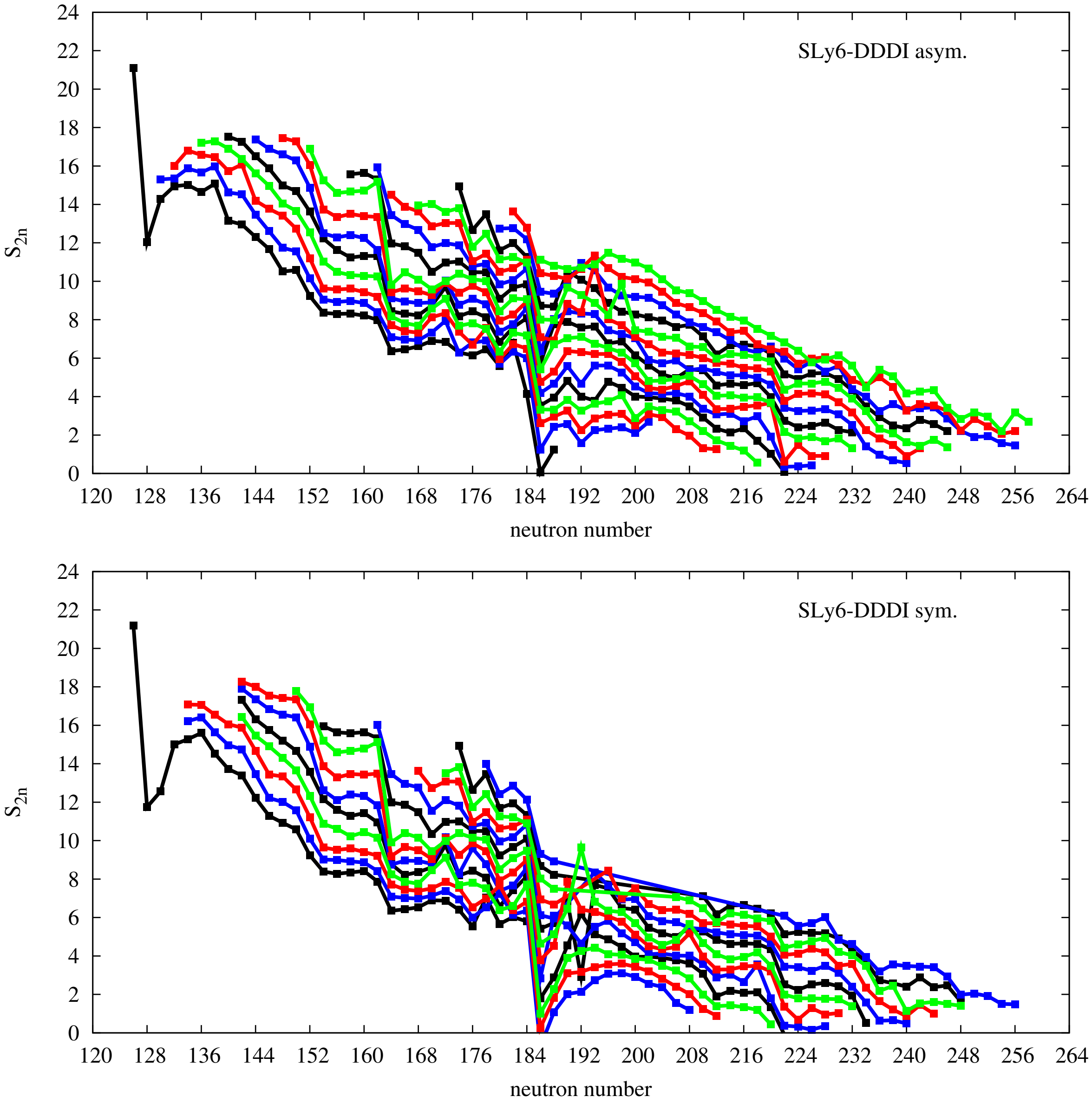

Figure 8.8: Two-neutron separation energy S_{2n} for the SLy6 functional for Z=94,102,110,118 and Z=96,104,112,120 and Z=98,106,114,122 and Z=100,108,116,124 - in the lower panel the results for Z=122 and Z=124 are not given. The results given in the upper panel include reflection asymmetric shapes, the results of the lower panel only allow reflection symmetric shapes. The results of the lower panel were calculated by J. Erler [Erl11].

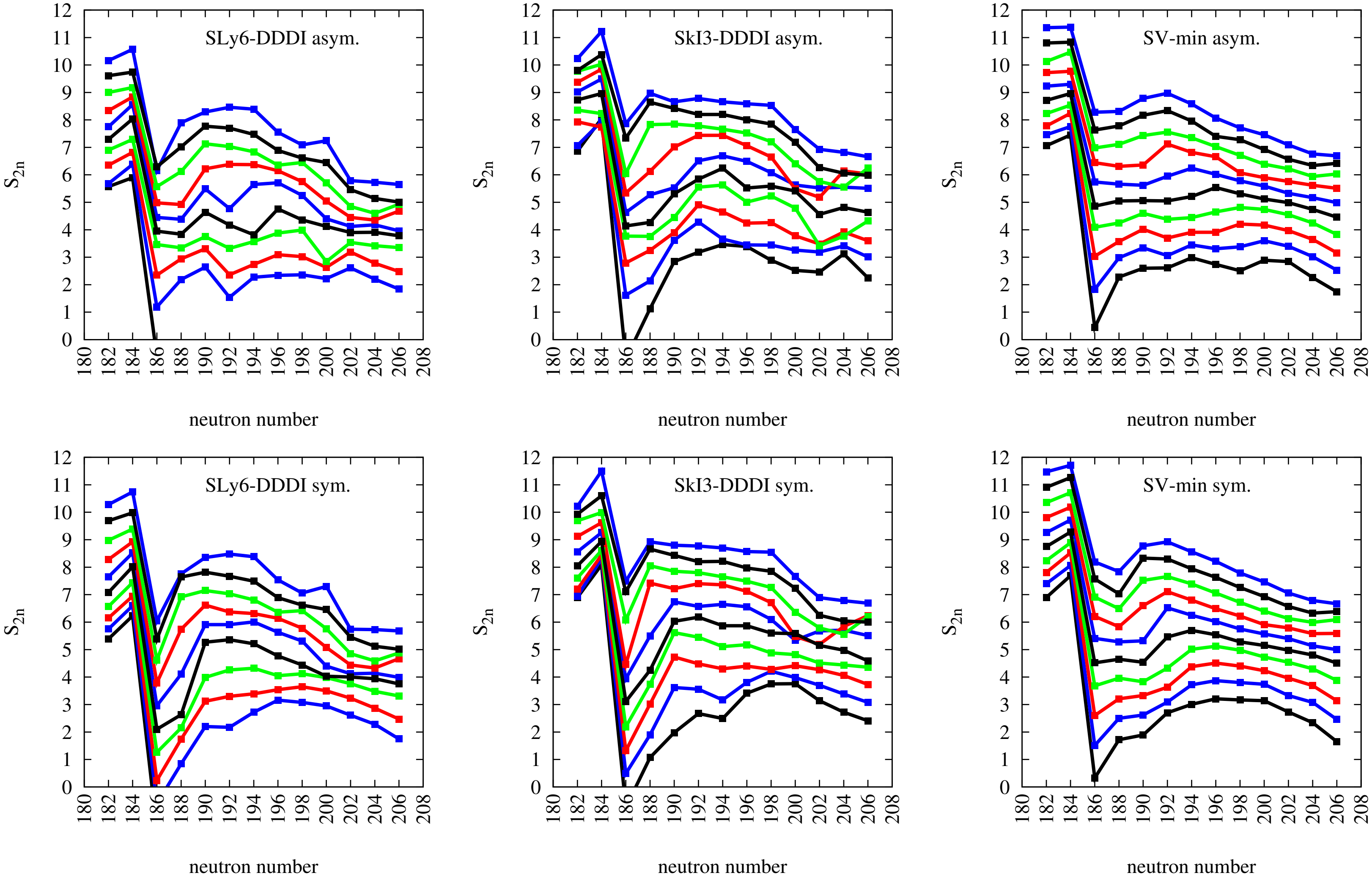

Figure 8.9: Two-neutron separation energy S_{2n} for nuclei around the N=184 shell closure and different Skyrme functionals. The upper panels show reflection asymmetric calculations, the lower ones reflection symmetric calculations. The colour coding is Z=94,102,110 and Z=96,104,112 and Z=98,106 and Z=100,108. The lowest curve corresponds to Z=94, the highest to Z=112.

In fig. 8.10 we have plotted the two-neutron separation energy S_{2n} for different Skyrme functionals. As we can see, the global behaviour of the two-neutron separation energy is not very sensitive to the used functional. Thus it is difficult to judge the quality of a functional regarding the two-neutron separation energy.

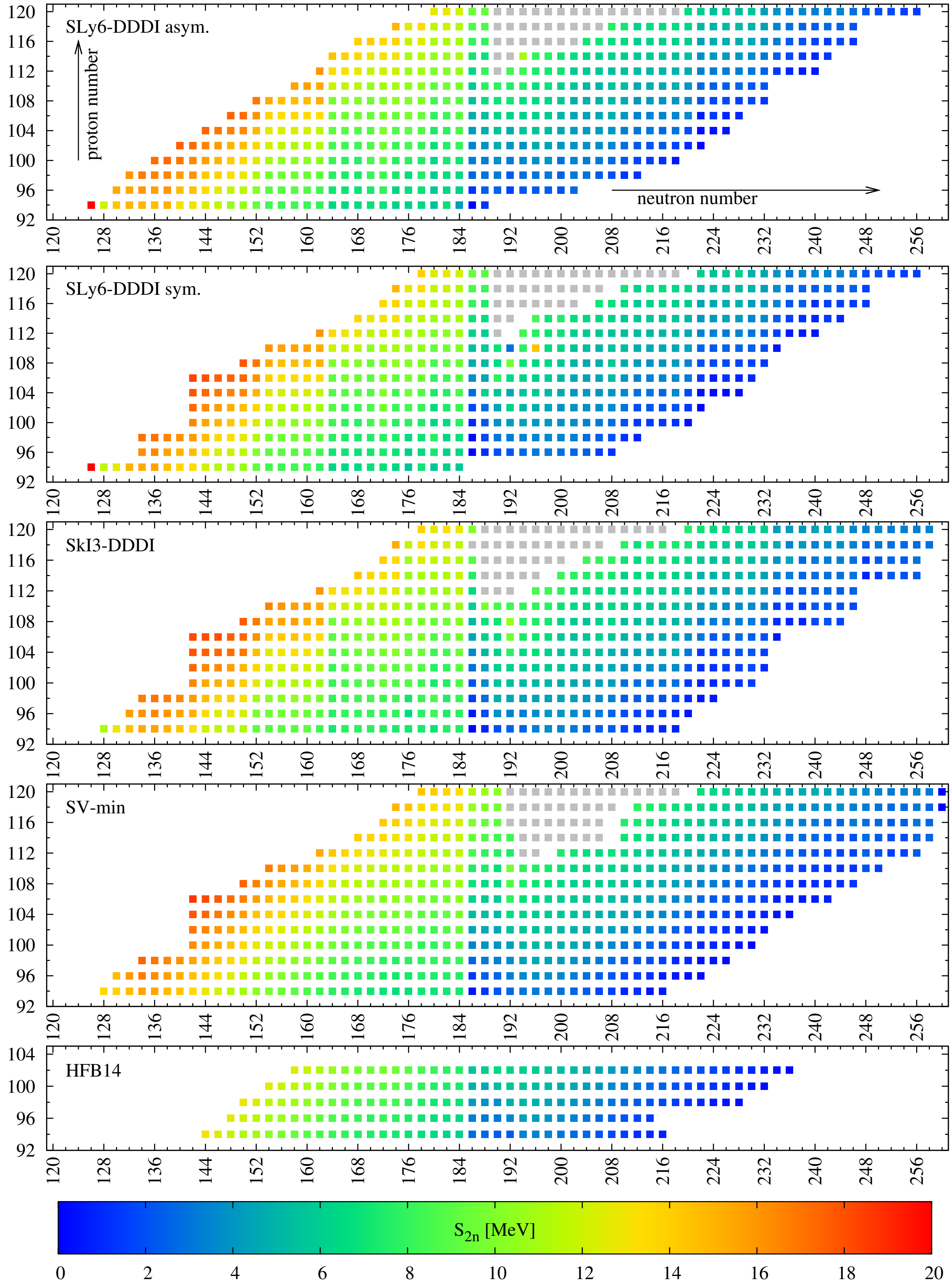

Figure 8.10: Two-neutron separation energy S_{2n} for different Skyrme functionals. The symmetric results for SLy6, SkI3, and SV-min were calculated by J. Erler [Erl11]. The HFB14 were calculated from [GSP07, Brub].

8.2.2.2 Q-values for α-Decay

Similarly to section 8.2.2.1, we may also calculate the Q-values for the α-decay. The Q_α-values is defined according to eq. (A.7) with $Q_\alpha = -S_\alpha$. According to fig. 8.11, the Q_α values do not change drastically between the different Skyrme functionals, although we see a small impact resulting from the possible deformed neutron shell closures in SkI3 and SLy6 (see preceding section). Additionally, we notice that reflection asymmetric shapes do not have an influence on the Q_α values, with the exception of the region just beyond the neutron shell closure discussed in the preceding section. A general investigation on Q values for α-decay and for other Skyrme functionals has been done in [TB03].

In fig. 8.12 we have plotted the Q_α values for all three functionals discussed. The upper panels show the results obtained by allowing reflection asymmetric shapes, the lower panels show the results from forcing reflection symmetry. Our results illustrate how the influence of octupole deformation in the ground state vanishes with increasing proton numbers, because the Q_α values for the heaviest isotopes are very similar between the reflection asymmetric results and the symmetric results. However, we also see how the reflection asymmetry reduces the Q_α value for the "lighter" isotopes plotted in fig. 8.12. Interestingly, the general evolution of the Q_α beyond the shell closure at N=184 looks very similar if we compare the reflection asymmetric SkI3 and SLy6 results with the SV-min results. The octupole deformation broadens the peak at N=186 (upper left panel) giving a shape that becomes similar to the peak predicted by SV-min.

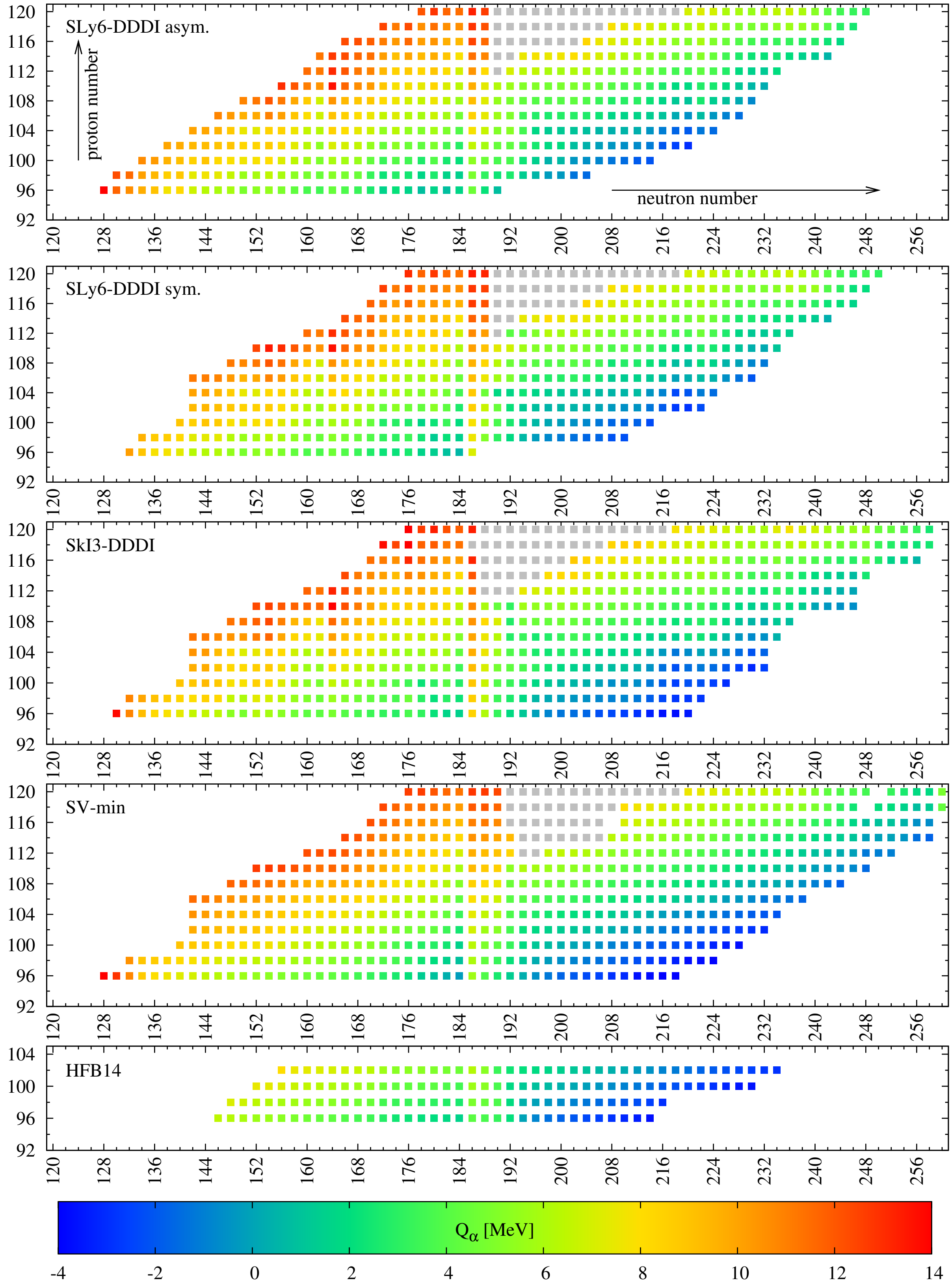

Figure 8.11: Q-values for α-decay Q_α for different Skyrme functionals. The symmetric results for SLy6, SkI3, and SV-min were calculated by J. Erler [Erl11]. The HFB14 results were calculated from [GSP07, Brub].

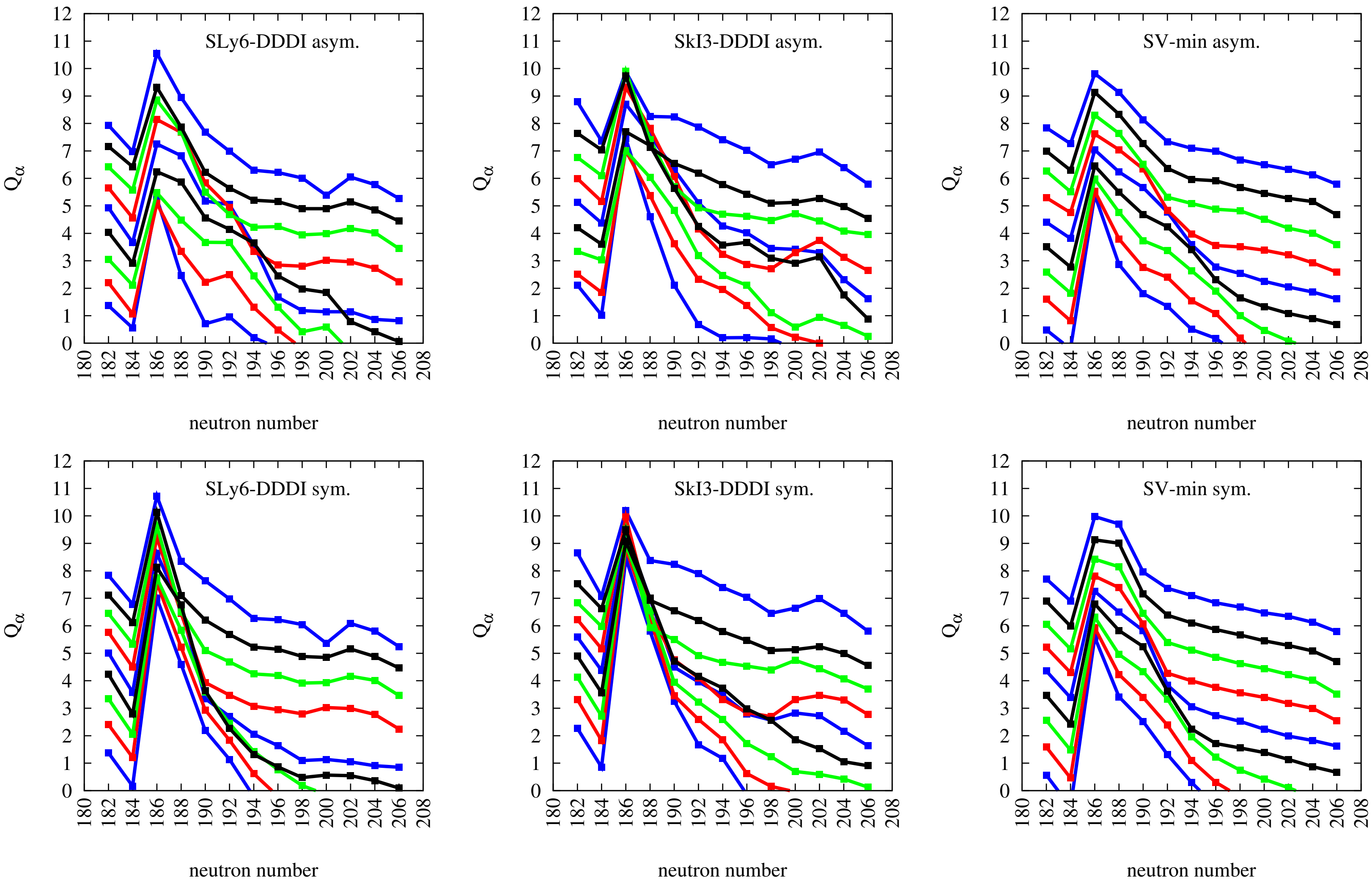

Figure 8.12: Q-value for α-decay Q_α for nuclei around the N=184 shell closure and different Skyrme functionals. The upper panels show reflection asymmetric calculations, the lower ones reflection symmetric calculations. The colour coding is Z=102,110 and Z=96,104,112 and Z=98,106 and Z=100,108. The lowest curve corresponds to Z=96, the highest to Z=112.

8.3 Fission Properties

We have calculated fission barriers for nuclei with $Z \geq 86$. However, for nuclei between $Z = 86 - 92$ the fission barriers become so broad that it is numerically very difficult to reach the scission point. Therefore we focus our discussion on nuclei with $Z \geq 94$ as for these we can be sure to have reached the scission point (at least according to our definitions given in section 8.1). The remaining nuclei are discussed in an independent section, i.e. section 8.3.5.

We have plotted the maximum fission barrier for the three different functionals in fig. 8.13; the calculations for reflection symmetric calculations with the SLy6, SV-min, and SkI3 functionals were performed by Jochen Erler [Erl11]. In the following we will discuss certain aspects by the means of fig. 8.13 regarding the different functionals and features. All approaches - despite the ETFSI approach - can be considered fully microscopic and all are based upon Skyrme functionals. The ETFSI (extended Thomas-Fermi-Strutinksy integral) method can be considered as an approximation to mean-field calculations (see [MPRT98] and references therein).

8.3.1 Global Characteristics

As we have already stated above, we restricted ourselves to even-even nuclei because the global characteristics of the fission barriers should not be too sensitive on odd-even effects.

For all approaches an island of comparatively large fission barriers is predicted around N=150 - 160, followed by a valley with smaller fission barriers. This island is particularly distinct for the SLy6 and SkI3 functionals. The SV-min functional and the BSk-type functional used in HFB14 give much smaller fission barriers. This is very likely related to the difference in the effective mass, being rather large for the two latter approaches. In general, functionals with larger effective masses tend to predict more flattened potential energy surfaces [Erl11]. Nuclei in this island will mostly decay by α-decay. However, the small barriers of the SV-min functional enhance spontaneous fission so that it competes with α-decay in certain cases [Erl11].

A second island of large fission barriers is seen for N=208 and beyond for the SLy6 functional; the same island is also seen for the SkI3 functional but smaller in extent. The SV-min approach also predicts this island but with smaller barriers compared to the other functionals. The same accounts for the HFB14 and the ETFSI approach.

Regarding the different functionals, we note that the SLy6 functional predicts less neutron rich nuclei in comparison to the other Skyrme functionals. The drip line emerges at smaller neutron numbers, because the SLy6 functional predicts much smaller nuclear binding energies than the other functionals for neutron-rich nuclei.

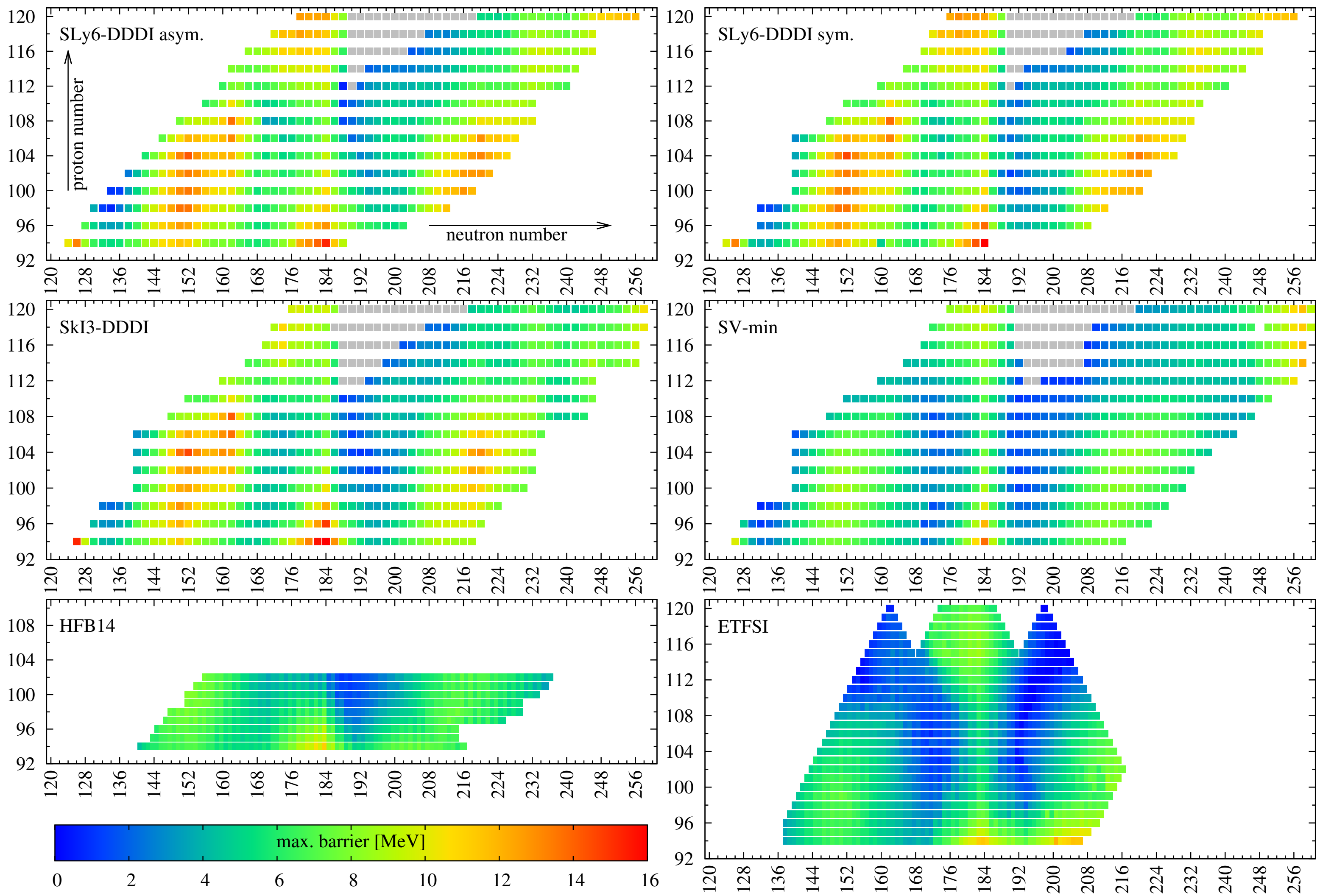

Figure 8.13: Maximum fission barrier for different functionals. The top-left panel shows fission barriers obtained from calculations allowing reflection asymmetric shapes with the SLy6 functional. The other panels show the barriers for symmetric calculations only. The two lower panels show the HFB14 and ETFSI fission barriers (again the maximum barrier only) for which reflection asymmetric shapes were allowed. For the grey marked areas we expect triaxial ground states, viz. triaxiality is very likely needed to determine the fission barrier. See text for more details.

8.3.1.1 Relevance for the r-Process

The general role of fission in the r-process has been addressed in chapter 1. Here we will discuss what the general results for the maximum fission barrier, shown in fig. 8.13, might have on the r-process. Other aspects, such as the role of reflection asymmetry, double-humped barriers, or bimodal fission will be discussed in the subsequent sections.

The island of relatively large fission barriers around N=152 becomes important after the freeze-out as the neutron separation energies in this area are around 5 to 6 MeV for Z=94, becoming larger with Z. Typically, these nuclei are too close to stability for the r-process, which is usually running in regions with neutron separation energies of 2 to 4 MeV. Moreover, all so far experimentally synthesised elements belong to this island (see fig. 8.14). Therefore, these nuclei will probably be synthesised by β-decay after the freeze-out. The competition of α-decay versus spontaneous fission can be derived from experiment for most of these nuclei.

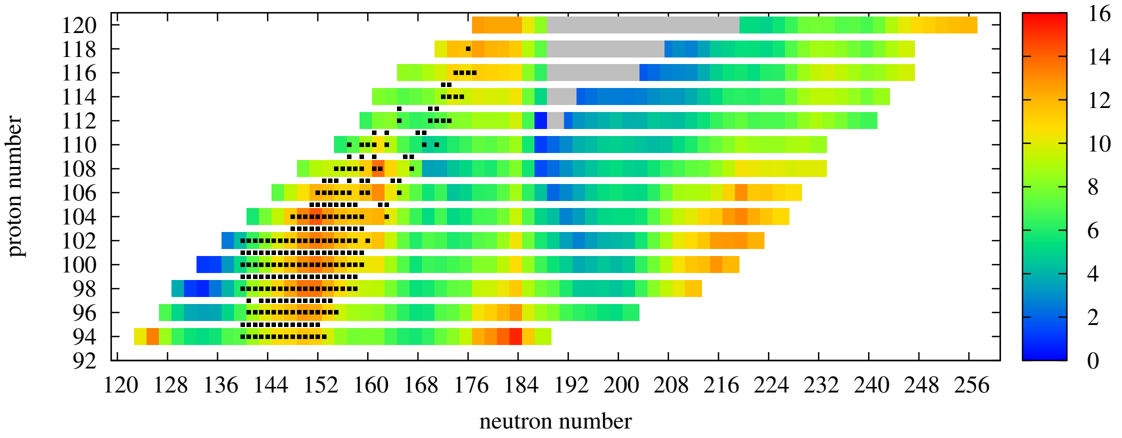

Figure 8.14: Maximum fission barrier for SLy6 with reflection asymmetric shapes allowed. The black dots mark nuclei for which experimental data exist.

Another very important feature is the valley between the aforementioned island and the N=184 ridge. The r-process is likely to run into this valley, thus these small barriers could favour neutron-induced fission, particularly for the SV-min functional that predicts very small barriers in this valley. The second important aspect of this valley is its reach downwards to lighter elements. For the SV-min functional, this valley continues to Z=88 [Erl11]. The ETFSI predicts the valley to end around Z=93/94. The SLy6 and SkI3 functionals predict this valley to reach down to Z=86; both functionals also predict that this valley becomes broad and flat with decreasing proton number (see fig. 8.23 and [Erl11]). The extent of this valley is crucial, as it can be seen as a possible bottleneck for the matter flow to the ridge of larger barriers around N=184 in the r-process.

The ridge of large barriers around the magic shell-closure N=184 is very important for the synthesis of super-heavy elements. Depending on the astrophysical conditions, the r-process might be able to cross the valley of small fission barriers below N=180 and run into the relatively stable (regarding fission) N=184 region. Here it is possible that the r-process climbs upwards, by subsequent (n,γ)-reactions and fast β-decays, along this ridge (not being sufficiently affected by fission to be terminated) and reaches the region of super-heavy elements. This has been shown in a r-process simulation in which the ETFSI fission barriers were employed [PMPA$^+$10]. If the r-process overcomes the lowest barriers in the ridge between Z=106-112 (for SLy6 and SkI3) or Z=102-112 (for SV-min), it can reach the island of especially large fission barriers at Z=114-120 and N=170-184.

The valley of (again) smaller fission barriers beyond the N=184 ridge could become important for very drastic astrophysical conditions: high neutron densities could lead the r-process (partly) beyond the N=184 shell closure, however it is not clear for which elements. The bottom of that valley is around N=192-194. Again, the barriers for SLy6 and SkI3 are larger than the ones for SV-min. Moreover, reflection asymmetric ground states start to play a role, thus possibly enhancing the effective barrier because the maximum barrier is not lowered by reflection asymmetric shapes in many nuclei if we assume axial symmetric shapes only. Hence, if the r-process manages to pass this valley and to reach the region of larger barriers (corresponding to N=200 and more), any material synthesised beyond this valley will very likely fission during the decay back to stability (either by β-delayed fission or spontaneous fission).

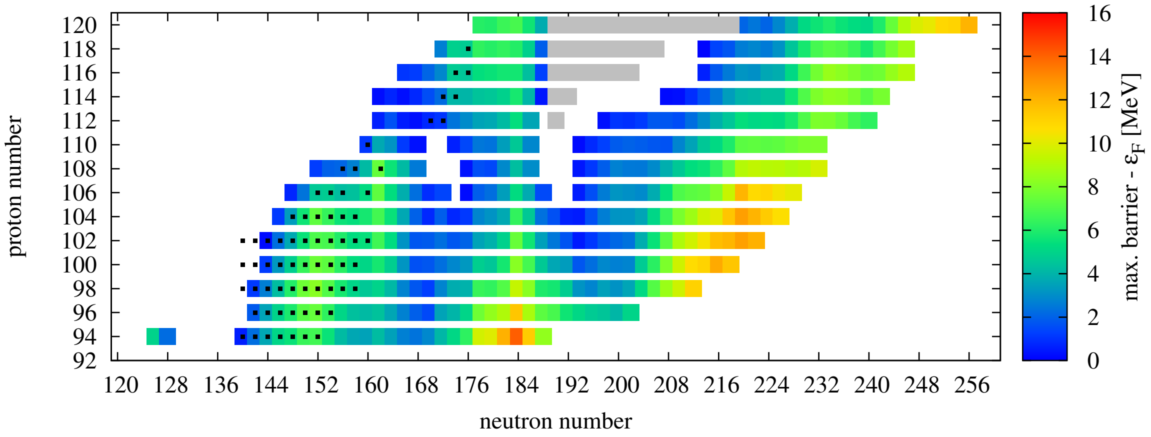

Figure 8.15: Difference of the maximum fission barrier and the Fermi energy ϵ_F for neutrons. The black dots indicate observed even-even nuclei. Nuclei for which the difference is negative have not been plotted.

In order to get an impression of the relevance of neutron-induced fission, we may look at the difference between the maximum fission barrier and the neutron separation energy. If a neutron is captured on the isotope with N-1 neutrons, the effective barrier for fission is roughly the energy difference between the maximum barrier and the minimum compound excitation energy ($\approx S_n$).[1] If this quantity becomes negative, i.e. the neutron separation energy is larger than the maximum barrier, neutron-induced fission will probably dominate the neutron capture cross section. The drawback in our case is that for neutron separation energies, we would have to calculate odd-N nuclei. As we do not include time-odd terms in the mean-field and do not use a blocking approximation, we will refrain from trying to give nuclear binding energies for odd-N nuclei. Instead, we approximate the neutron separation energy by the neutron Fermi energy ϵ_F for neutrons.

We have plotted the difference of the maximum barrier and the neutron Fermi energy in fig. 8.15. The results show that the large barriers of SLy6 lead to a broad ridge around N=184 that leads towards super-heavy elements. Jochen Erler extended this study towards the SV-min functional and calculated the neutron separation energy including the time-odd fields and a blocking approximation. A comparison shows, that our approximation with the neutron Fermi energy works rather well and the small barriers predicted by the SV-min functional may prevent the r-process from synthesising super-heavy elements with $Z \geq 106/108$ [Erl11]. A general overview on the important evolution of the difference between the maximum barrier and the neutron separation energy of theoretical predictions of fission barriers can be found in [PKR$^+$10].

8.3.2 Barrier Deformation

In this section we will focus on the deformation of the barriers. Depending on the size of the quadrupole deformation we get an estimate which of the possibly several barriers of a nucleus is the dominating one. Additionally, we investigate if there are barriers affected by reflection asymmetry by looking at the octupole deformation of the barrier.

---

[1] In the r-process we deal with typical neutron energies up to 100keV, which we can usually neglect in comparison to the separation energies of the MeV scale.

8.3.2.1 Quadrupole Deformation of the Barrier

The quadrupole deformation at the maximum barrier - described by the parameter β_2 - gives us a handle to determine which barrier, if multiple barriers exist in a nucleus, is dominating. In the actinide region, the isotopes have mostly double-humped barriers [BBMR04] of which the first barrier is often considered to be subject to possible triaxial configurations (which we can not handle here) and the second barrier is often lowered (or even removed) by reflection asymmetric shapes. The latter phenomenon leads to the dominance of asymmetric fission in the actinide region.

Figure 8.16 shows the quadrupole deformation of the maximum barrier. It becomes obvious that the location of the maximum barrier in the quadrupole deformation space is not very sensitive to the used functional if we consider the functionals SLy6, SV-min, and SkI3. This is in complete conformance to the barrier heights shown in fig. 8.13. Moreover, we see that the maximum barrier is usually around $\beta_2 = 0.3$-0.7. This indicates that in nearly all cases shown here, the first barrier is the dominating one. This is supported by the fact that with increasing neutron number, the maximum barrier is pushed to larger deformations until we reach the region of shape coexistencies (N=170-180) before the magic neutron shell closure N=184.

Another important issue is the fact that the barrier deformation is apparently not affected by the reflection asymmetry. That supports our result that the first barrier is the dominant barrier in super-heavy nuclei in case of multiple barriers. Moreover, the possible second barrier is usually not the dominating barrier in case of the symmetric results. This shows that reflection asymmetric shapes remove a second barrier, but the dominating barrier is always the first barrier. It is important to note that this deduction is only valid for the super-heavy nuclei. The reflection symmetric calculations were made to only moderate quadrupole deformations for certain nuclei with Z=94-98. Hence, a possible second barrier occurring at larger deformation is not seen in this case.

The obvious differences to the BsK14 functional used in the HFB14 approach result from the fact that the affected nuclei exhibit a single-humped but very broad barrier with several local minima and maxima in between. The maximum that defines the dominant barrier in the HFB14 approach, is removed by the reflection asymmetry for the SLy6 functional, because the reflection asymmetry allows a path circumventing the maximum. The discrepancy between the HFB14 results and the other reflection symmetric calculations ensues from the competition between the local maxima. This competition is subject to the functional used and to the collective corrections applied, the latter usually damp maxima with large quadrupole deformation more strongly than maxima with smaller quadrupole deformation.

The differences for Z=94 and Z=96 nuclei on the proton-rich side around N=126-134 are due to the fact that the symmetric calculations in the region were not performed to deformations beyond $\beta_2 = 0.8$. The results from the reflection asymmetric calculations already indicate that for lighter elements the dominant barriers move out to larger deformations (independently of the reflection asymmetry).

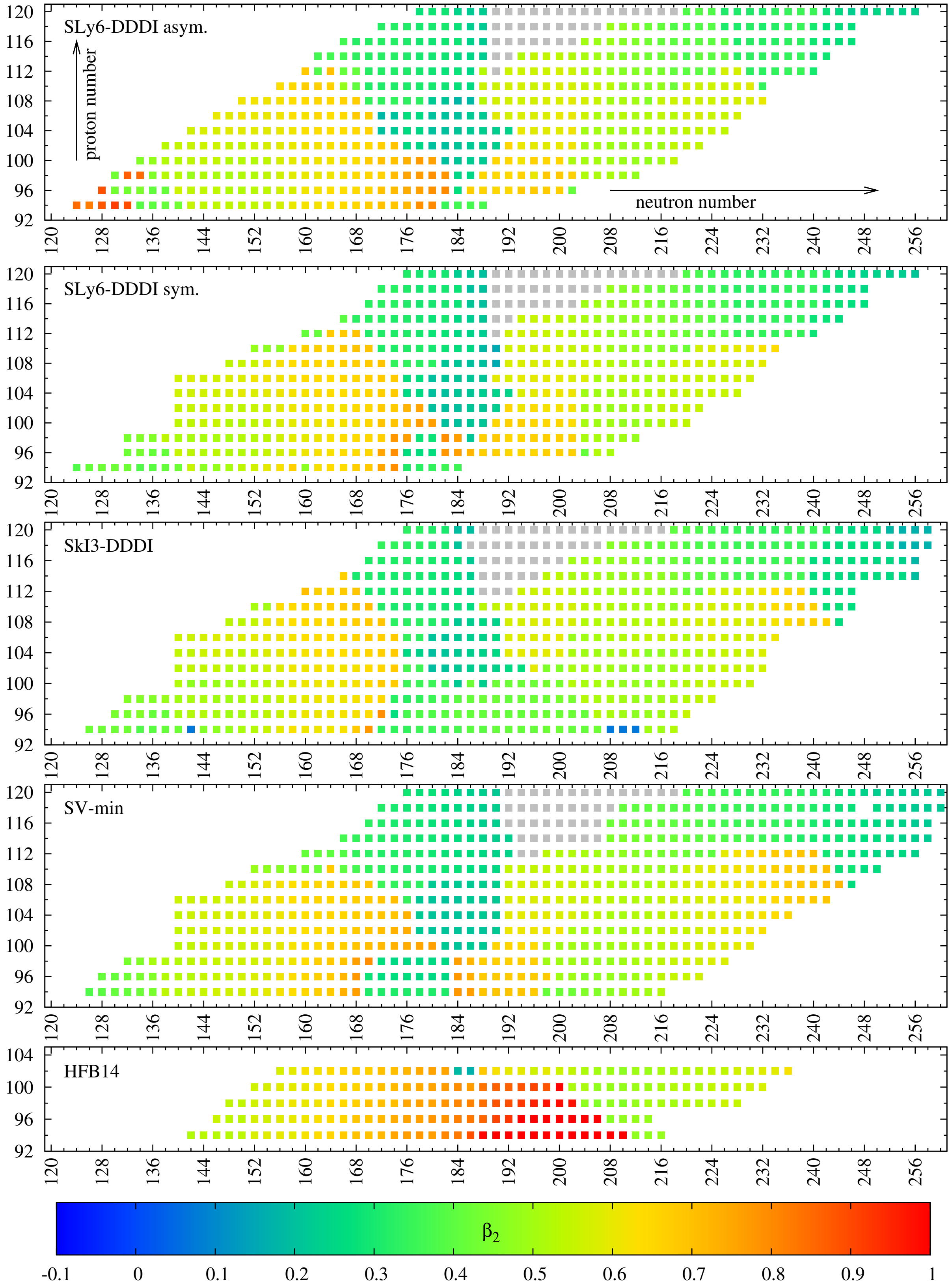

Figure 8.16: Quadrupole deformation β_2 of the maximum barrier. The results for the symmetric SLy6, SkI3, and SV-min functionals were calculated by Jochen Erler [Erl11]. The HFB14 results are taken from [GSP07, Brua].

8.3.2.2 Reflection Asymmetric Barriers

In fig. 8.13 we have plotted the maximum barrier for different Skyrme functionals. Regarding the SLy6 functional we have performed calculations allowing for reflection asymmetric shapes and reflection symmetric shapes. By comparing the upper-two panels of fig. 8.13 it is obvious that the dominant barrier is only weakly affected by octupole deformations since we do not see substantial differences between the barriers. This is supported by fig. 8.17.

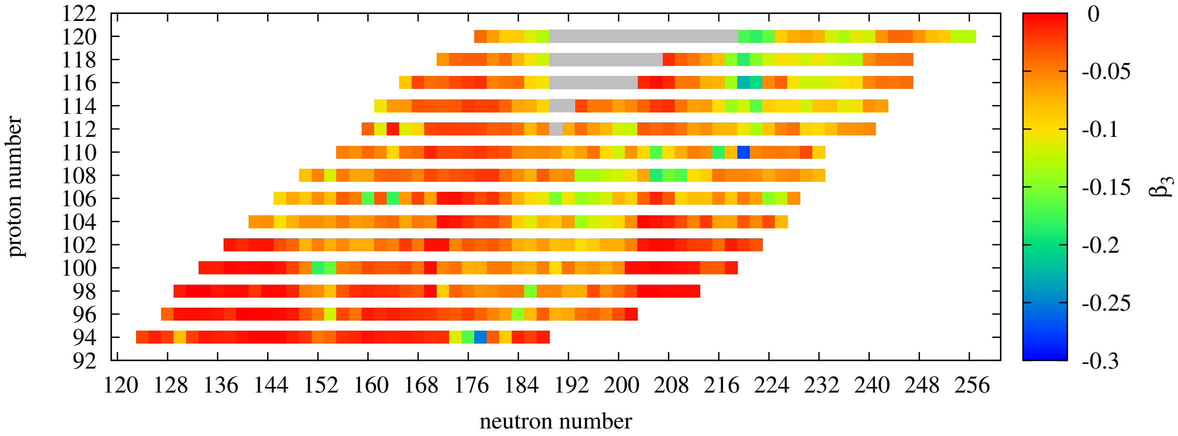

Figure 8.17: Octupole deformation of the maximum barrier for the SLy6 functional.

However, a possible second barrier is often strongly reduced by reflection asymmetric configurations (see [W$^+$91, BBMR04, SR07] and references therein) which become important at large quadrupole deformations. Nevertheless we have learned in section 8.3.2.1, that the first barrier is generally the dominating one.

We still find some nuclei which show a non-vanishing octupole deformation at the maximum barrier and most of these nuclei have only one barrier, even under the restriction to reflection symmetric shapes. It turns out, that a small reflection asymmetric deformation skirts the barrier, thus slightly cutting off the peak of the barrier. An example is plotted in fig. 8.18 for the very neutron-rich nucleus ^{296}Cm. First, both fission paths, one assuming reflection symmetry (red) and one allowing for reflection asymmetry (blue), have the same ground state at $\beta_2 = 0.22$. From $\beta_2 \approx 0.7$ on an alternative path exhibiting octupole deformations becomes favourable. The reflection asymmetric path circles the barrier until it meets the reflection symmetric path again.

8.3.3 Barrier Widths

So far we have discussed the dominant barrier as the primary quantity affecting the fission probability and neglected the effect of the width of the barrier. Nuclei with a small but broad barrier can have a comparative fission probability to nuclei with larger but narrower barriers. The width of the barrier is approximately giving the limits of the integral in eq. (6.13). As the barrier is by definition a positive function, the integral becomes larger if the interval of the integral limits becomes larger.

Figure 8.19 shows the width of the barrier for the SLy6 functional and allowing for reflection asymmetry. The general evolution of the barrier width shows some important peculiarities:

- The magic neutron shell closure appears to affect the barrier width for nuclei with Z$\leq$102 by giving larger widths. This is probably related to the fact that these nuclei fission symmetrically, so that octupole configurations are not able to narrow the barrier. For nuclei with larger proton numbers, a ridge of comparatively broad barriers (compared to the neighbouring nuclei) exists. Together with the particularly large barriers in this region, this can support the r-process to go through this ridge to larger proton numbers.

- The nuclei in the valley of small barriers between N=160-178 also partly exhibit narrow barriers. This can have an additional effect on a possible r-process in this region, besides the already small

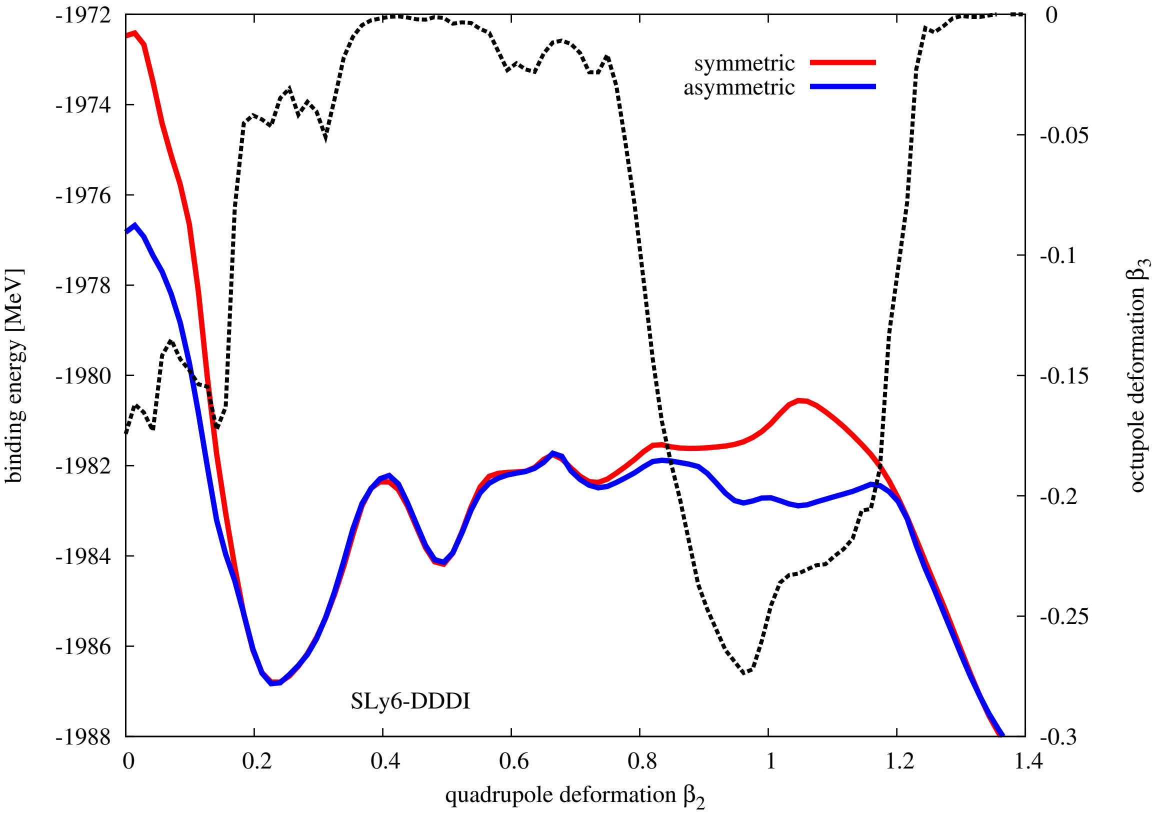

Figure 8.18: Fission path for ^{296}Cm using the SLy6 functional. The left y-axis corresponds to the reflection symmetric and reflection asymmetric paths. The right y-axis is the octupole deformation of the reflection asymmetric path.

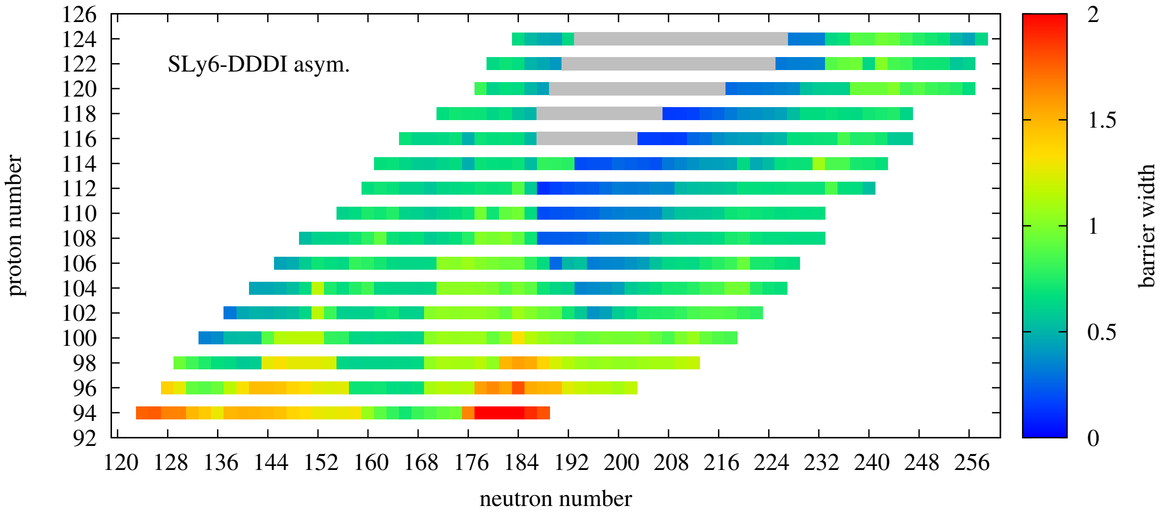

Figure 8.19: Width of the dominating fission barrier for the SLy6 functional allowing for reflection asymmetric configurations.

barriers.

- Beyond the N=184 shell closure - where the barriers are also small - the barriers do not become narrow for Z≤100. However, with increasing Z, the barriers in the N=190-210 region become very narrow. The comparison with the ground state deformation in fig. 8.3 shows that most of these nuclei have strongly prolate deformed ground states. The low and narrow barriers would make it very difficult for the r-process to cross or trespass this region.

Despite the features mentioned above, it becomes obvious that the barriers become narrower for super-heavy elements. This is in accordance to previous results [BBMR04].

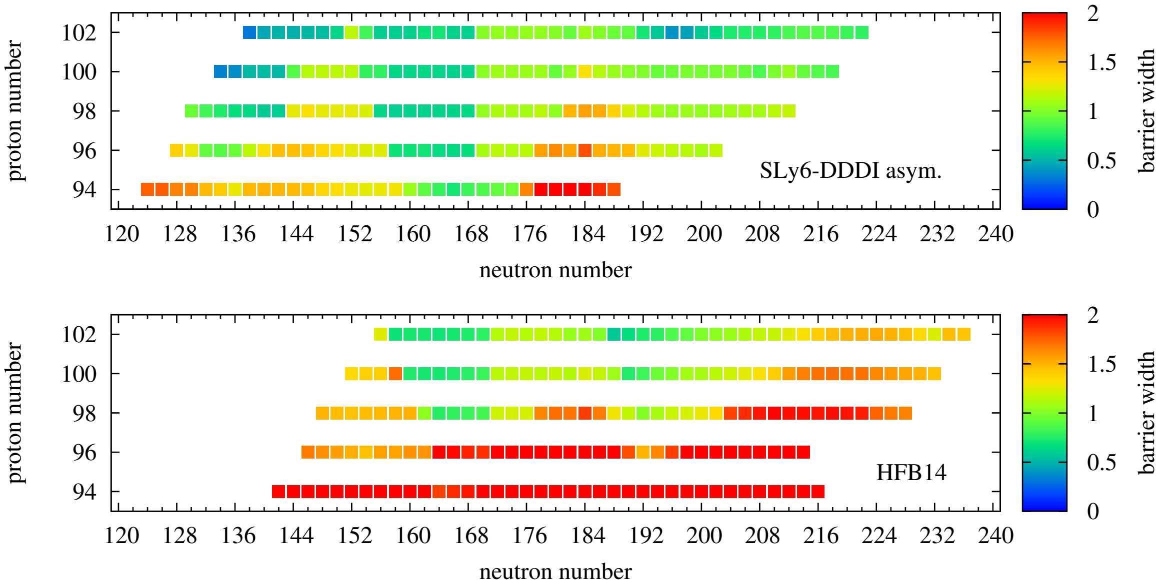

Figure 8.20: Width of the dominating barrier for the SLy6 functional and the HFB14 results. All results are obtained by allowing for reflection asymmetric shapes.

The barrier width is also sensitive to the used functional. In fig. 8.20 we have plotted the barrier width for the SLy6 functional and the HFB14 calculations. Both approaches allow reflection asymmetric nuclear shapes. The difference in the tendency towards reflection asymmetric shapes of both functionals might explain the large differences in the barrier width for nuclei with Z=94-98. For these nuclei the HFB14 approach gives much broader barriers, although the ground state deformation is very similar (see fig. 8.3). The fact that both functionals produce very similar predictions regarding symmetric or asymmetric fission in this region (see section 8.3.4) seems to contradict our results in fig. 8.20. However, the HFB14 calculations predict much larger quadrupole deformations for the dominating barrier (see fig. 8.16) in these nuclei and this leads to the discrepancies in the barrier widths shown in fig. 8.20.

8.3.4 Symmetric and Asymmetric Fission

As we have already discussed in chapter 6, asymmetric fission is related to octupole deformations along the fission path towards the scission point and beyond. As it is known that most actinides fission asymmetrically [W$^+$91, SR07], we see from our results that according to fig. 8.21, asymmetric fission becomes important for super-heavy nuclei with $Z \gtrsim 108$ according to the SLy6 functional. This result would probably also apply to other functionals, as for large quadrupole deformations the tendencies towards octupole shapes between different functionals become similar. The crux of the matter would be the transitional region of bimodal fission; this region could be slightly different for other Skyrme functionals; an example is discussed below.

By comparing fig. 8.21 with fig. 8.14 we notice that our model predicts asymmetric fission for most nuclei that have been synthesised experimentally. In fig. 8.22 we compare the prediction of asymmetric or symmetric fission of the SLy6 functional with the HFB14 approach. As the BSk functional of the HFB14 model has a larger effective mass, it tends to predict more symmetrically fissioning nuclei. Nevertheless, the global systematics look very similar. This might indicate that the octupole deformations at large quadrupole deformations, that lead to asymmetric fission, might be subject to the mean-field approach.

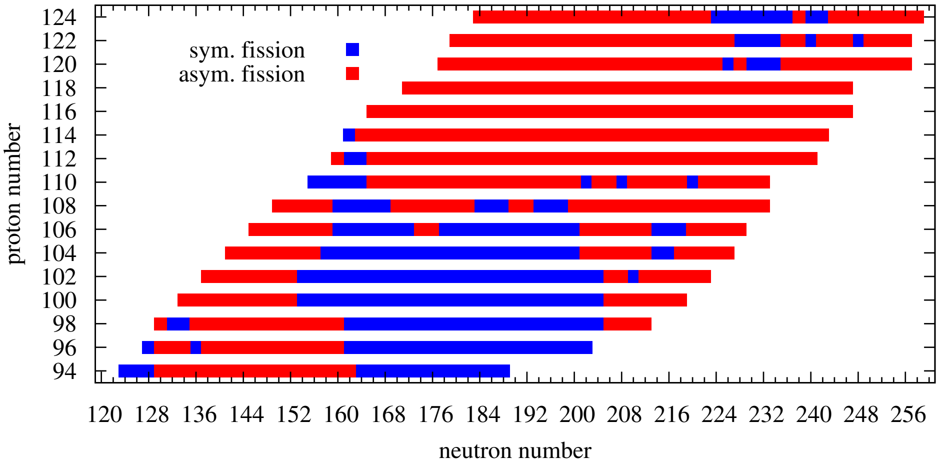

Figure 8.21: Overview on nuclei that fission either symmetrically or asymmetrically according to the SLy6 functional. We neglected bimodal fission here.

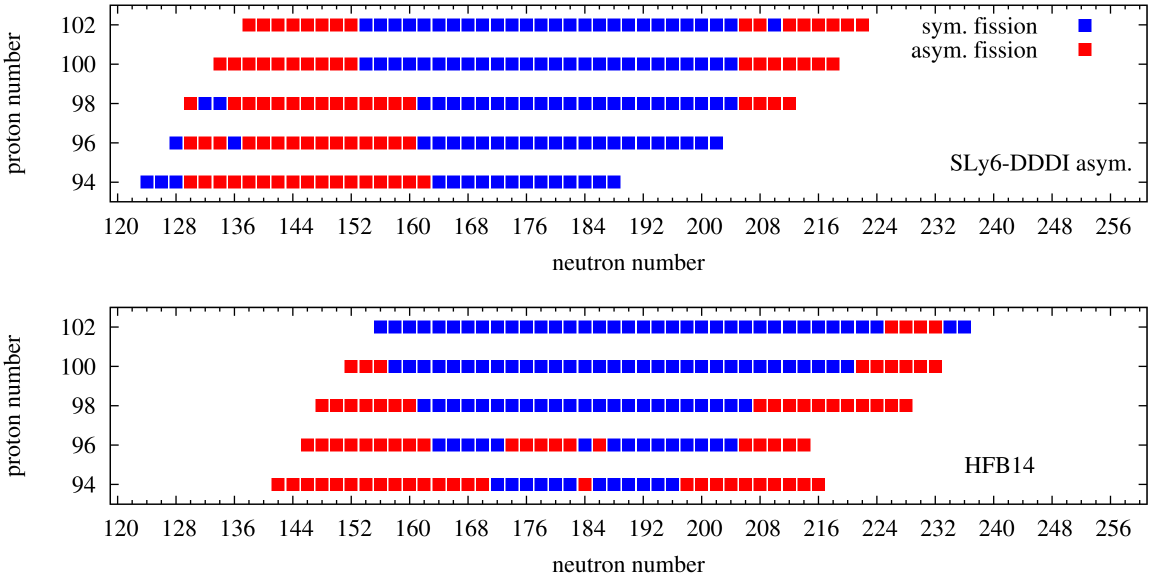

Figure 8.22: Overview on nuclei that fission either symmetrically or asymmetrically for the SLy6 and the BSk functional. Note that we restricted the latter results to even-even nuclei only. Moreover, the HFB14 barriers do not reach to the proton-rich side.

The relevance of symmetric fission versus asymmetric fission for r-process can be currently characterised as secondary. There exist up to now no r-process simulations which specifically track the fission products (and the released neutrons). Nevertheless, the question if a nucleus fissions symmetrically or asymmetrically is important as the fission would feed different mass regions. A problem in that picture are the nuclei which show bimodal fission behaviour: depending on the excitation energy these nuclei might fission symmetrically or asymmetrically.

Of particular importance is the A=280 [MPMZ$^+$07] region which corresponds to the region around the N=184 shell closure in figs. 8.21 and 8.22. These nuclei are predicted to fission symmetrically in the approaches shown here, thus creating nuclei with $A \approx 138$ in the tin region.

8.3.5 The Actinides Between Z=86 and Z=92

So far we have presented and discussed our results for nuclei with Z≥94. With decreasing proton number, the barriers become much broader so that we have to constrain our Hartree-Fock-BCS method to very large quadrupole deformations, sometimes beyond $\beta_2 = 3.0$. With these large deformations, numerical problems and instabilities arise, so that for many nuclei in the Z=86 to Z=92 regime, we cannot calculate the complete fission path, i.e. the potential energy surface from the ground state to the point we define as the scission point. Thence, we will discuss the nuclei in the Z=86-92 range qualitatively and note here that these results are to be seen less reliable compared to the results presented in the previous sections.

According to the lower panel of fig. 8.23, the valley of small barriers around N=168 show in fig. 8.13 is shifted towards N=162-164 for Z≤92 (uranium). Even in Z=86 (radon) we see a dip in the maximum barrier, i.e. the end of this valley is not necessarily reached, yet. The neutron separation energy for ^{86}250164Rn is 3.3 MeV in the FRDM mass model and 2.8 in the HFB14 mass model, i.e. this nucleus might lie in the r-process region. However, the barrier is about 7-8 MeV high, i.e. fission would only play a minor role. This discussion is valid for the SLy6 functional. For the SV-min functional, the valley ends at Z=90 (thorium), giving barriers of more than 10 MeV for Z=88 (radium) and more than 12 MeV for Z=86 [Erl11]. The SkI3 functional however, shows a stronger tendency to small barriers in this region by giving barrier heights of 4-5 MeV [Erl11]. This indicates once more how different the predictions of the various Skyrme functionals can become. In the case of SkI3, the r-process might have problems to overcome this region of small barriers in Z=86, while in the SV-min the large barriers would damp any fission processes.

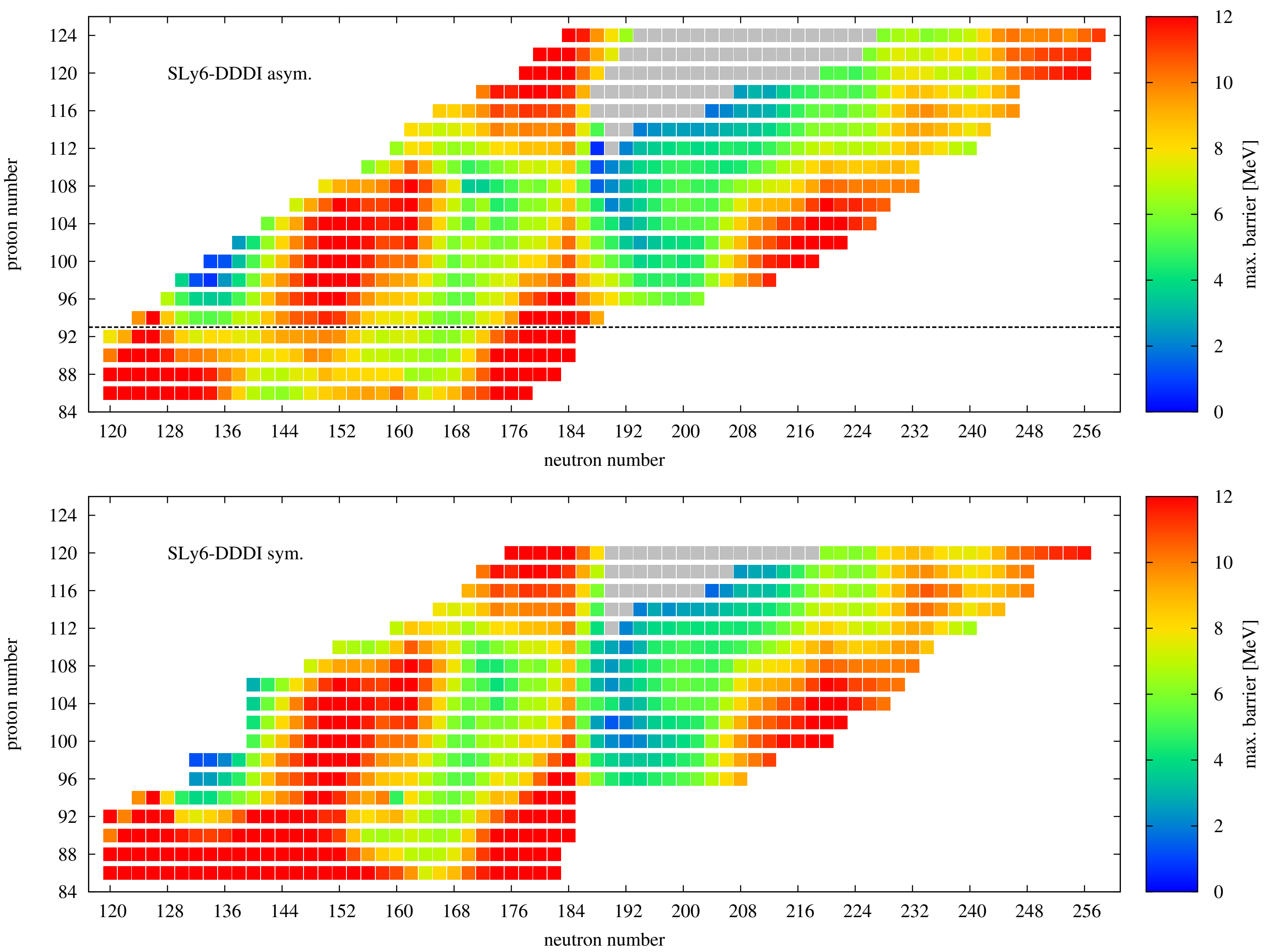

Figure 8.23: Maximum barrier predicted by the SLy6 functional. For all nuclei below the black dashed line we assume an error of ±2 MeV; see text for more details.

The situation becomes more complicated if we allow for reflection asymmetric shapes (upper panel of fig. 8.23). We see a strong reduction of the maximum barrier around N=142/144. Although this region would be located at the very left border of the r-process path[1], it appears as if there is a small valley or basin in the map of fig. 8.23 that extends to even lighter elements. The reduction due to asymmetric shapes is experimentally known, e.g. the maximum fission barrier of ${}^{232}_{90}\mathrm{Th}_{142}$ is about 6 MeV and it fissions asymmetrically (see [IAEa] and references therein). This is a strong proof that for these nuclei, reflection asymmetric shapes are mandatory to obtain a good approximation to the fission barrier, because the reflection symmetric barrier is too large. In the preceding sections we have often discussed that the occurrence and the impact of reflection asymmetric configurations is very sensitive to the effective mass of the functional, i.e. to the functional itself. Interestingly, this seems to be different for what we are discussing at this point. As an example, we have calculated the fission path for ${}^{228}_{86}\mathrm{Th}_{142}$ and ${}^{232}_{90}\mathrm{Th}_{142}$ with the SV-min functional that showed the weakest tendencies towards octupole deformation in the preceding sections. We have plotted these results in fig. 8.24.

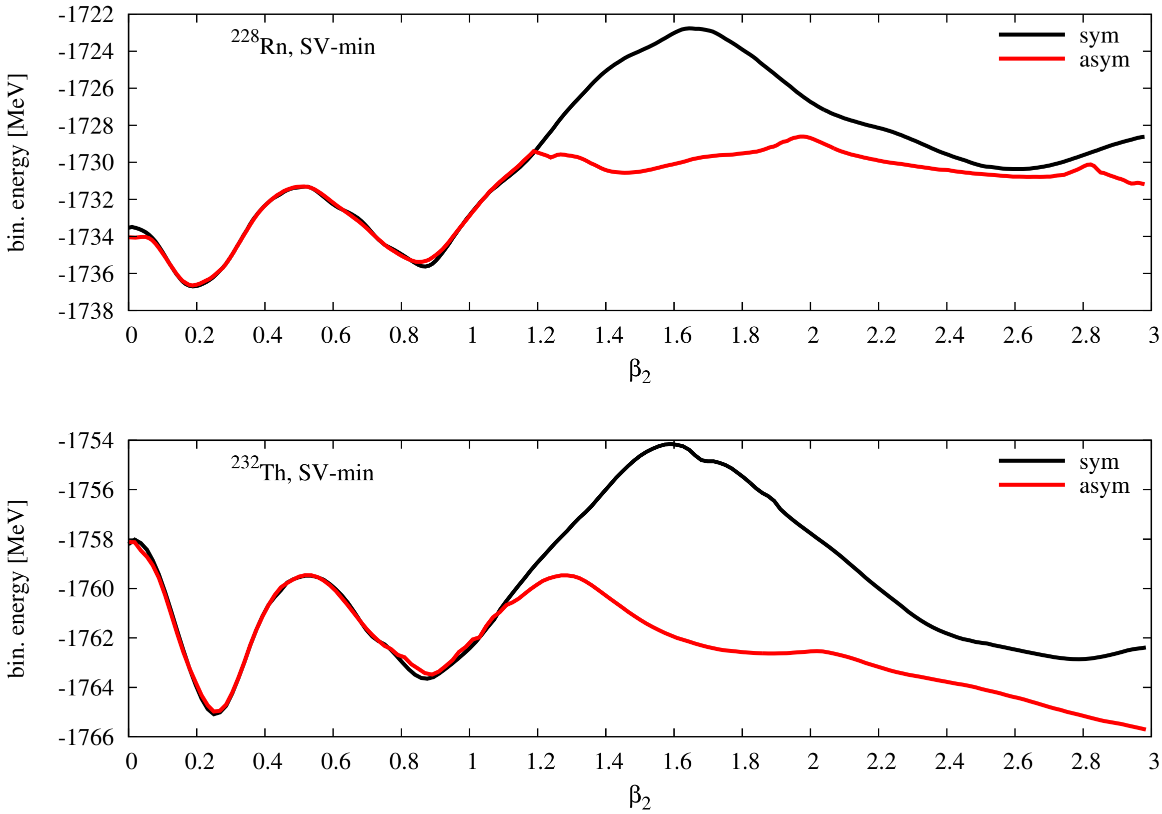

Figure 8.24: Potential energy surface of ${}^{228}\mathrm{Rn}$ and ${}^{232}\mathrm{Th}$ for reflection symmetric calculations (black) and reflection asymmetric calculations (red). In the calculation of ${}^{228}\mathrm{Rn}$ we did not reach the scission point. The ground states of both nuclei are well defined at $\beta_2 = 0.19$ in ${}^{228}\mathrm{Rn}$ and $\beta_2 = 0.23$ in ${}^{232}\mathrm{Th}$. Note that the maximum barrier for the asymmetric results is about 6 MeV in ${}^{232}\mathrm{Th}$ which corresponds with the experimental value (see text).

Figure 8.24 shows that we obtain a large reduction of the maximum barrier even for the SV-min functional. Again, this might indicate that for nuclei in the actinide region, reflection asymmetric fission paths can become very important. Depending on the employed functional, this region seems to continue to lower proton numbers and thus it could easily affect the r-process path in this region. Despite the strong reduction of the barrier, we have to keep in mind that these nuclei show very broad barriers compared to the barriers of the super-heavy nuclei. However, the width of the barrier mainly affects

---

[1] The experimental neutron separation energy of ${}^{228}_{86}\mathrm{Rn}_{142}$ is $S_n = 5.67$ MeV; for ${}^{227}_{86}\mathrm{Rn}_{141}$ it is $S_n = 3.86$ MeV.

the spontaneous fission, because for induced fission processes and β-delayed fission the effective width is reduced due to the excitation of the fissioning nucleus.

9

Summary and Outlook

The r-process is considered to form about half of the elements with nucleon numbers A>70. In order to perform r-process simulations, many different nuclear ingredients are needed. Most of these have to be provided by nuclear theory, because the nuclei within the r-process path exhibit a large neutron excess and the experimental data on these isotopes is very scarce.

In this thesis we have studied possible improvements of the nuclear input to r-process simulations obtained from recent advances in nuclear theory. We have focused on radiative strength functions for E1 and M1 transitions needed for the determination of (n,γ) reaction rates as well as on fission properties for heavy and super-heavy nuclei.

The radiative neutron capture cross sections have been calculated with the Hauser-Feshbach model. In this model, the radiative strength function is needed not only for the ground state but also for excited states. Here we employed Brink's hypothesis in which one makes the assumption that the strength function for all excited states is the same as for the ground state. This hypothesis was originally formulated for giant collective resonances and it is an open question if it is valid for low-energy collective modes, e.g. the pygmy mode.

In section 7.2 we have utilised different E1 strength functions in order to draw a comparison between the standard approaches based upon a Lorentzian description of the giant dipole resonance and two microscopic approaches. Only the latter two models are able to predict additional low-lying E1 strength. The influence of this strength on the cross section depends on the interplay of the nuclear level density, the relevant Q-value, and the energetical position of the additional strength. For nuclei with neutron separation energies $S_n \approx$ 7-8 MeV, the dominating γ-energies are roughly between 2-5 MeV for kinetic neutron energies emerging in the r-process.

For r-process nuclei, this region can shift up to the neutron separation energy. In nuclei with a particularly small level density, the transitions with $E_\gamma \approx S_n$ can become dominant. Therefore, a small level density leads to an additional shift of the dominant energy region towards the neutron threshold. The radiative neutron capture on ^{131}Sn is an example for such a case: the small level density of ^{132}Sn damps the E1 transitions to excited states relative to the transitions to the ground state. The RQTBA model predicts additional low-lying E1 strength in ^{132}Sn around the neutron separation energy, thus enhancing γ-transitions to the ground state relative to the transitions to excited states. The other discussed models either cannot predict this strength (the Lorentzian based models) or do not predict low-lying strength at that energy (the HFB model). Therefore, the RQTBA strength function strongly enhances the (n,γ) cross section for the radiative neutron capture on ^{131}Sn relative to the results obtained with the other approaches. However, we note here that we have used the Brink hypothesis in this context for the RQTBA strength function, i.e. we assumed that also excited states exhibit this additional low-lying strength at the same energy as the ground state.

By assuming the validity of Brink's hypothesis for low-lying E1 strength, we can deduce that such strength can only affect the (n,γ) cross sections if it occurs at E_γ that are in the dominant energy region. The upper limit of the dominant energy region can never notably exceed the neutron threshold due to the small kinetic neutron energies of 10-100 keV in the r-process. Hence, low-lying additional strength only affects the (n,γ) cross section if situated below or around the neutron threshold, if we assume Brink's hypothesis to be valid.

As the r-process operates at a typical temperature of $T_9 = 1$ K, we can approximately deduce the impact on a r-process simulation, from different E1 strength functions, by looking at the reaction rate at that temperature. The reaction $^{129}\mathrm{Sn}(n,\gamma)^{130}\mathrm{Sn}$ shows effects of additional E1 strength on the reaction rate, thus enhancing the rate. In the peculiar case of $^{131}\mathrm{Sn}(n,\gamma)^{132}\mathrm{Sn}$ we have seen how additional E1 strength at the neutron threshold (combined with a particularly small level density) strongly enhances the reaction rate: the RQTBA strength function gives the largest reaction rate at 10^9 K for radiative neutron capture on ^{131}Sn. The neutron separation energy drops beyond the doubly magic nucleus ^{132}Sn and the level density prescription we employ predicts the dominance of of states with positive parity at low energies. This damps the parity changing E1 transitions relative to the parity-conserving M1 transitions, making the cross sections sensitive to the M1 transitions as these are enhanced in turn. For the (n,γ) reactions on ^{133,135,137,139}Sn, the M1 transitions are enhanced while the E1 transitions are damped. Consequently the reaction rates are very similar for most approaches. An exception is the RQTBA+SLO strength function, which gives the largest E1 strengths. In case of ^{136,140}Sn, these are so large that the aforementioned damping of E1 transitions (in these two nuclei) can not completely remove any visible E1 sensitivity of the cross section to the E1 strength function.

Our results for the nickel isotopes show how important a realistic description of the E1 strength can become, especially regarding the Lorentzian approaches. In nickel, the giant dipole resonance is located at higher energies compared to tin, thus our calculations are even more sensitive to the tail of the Lorentz function. In general, we obtain the result that the microscopic strength functions predict much smaller E1 strength functions at low-energies (neglecting additional strength at low energies) which leads to a general reduction of the reaction rate. In the case of the reaction $^{67}\mathrm{Ni}(n,\gamma)^{68}\mathrm{Ni}$ we see that differences in the parameters of the Lorentz form factor can have a large impact on the reaction rate. Additionally, ^{68}Ni is another example nucleus with a rather small level density at whose neutron threshold the RQTBA model predicts an enhancement of the strength function. However, the corresponding peak is so narrow, that the reaction rate drops faster with temperature than for the other approaches.

A remark regarding the RQTBA strength function is appropriate: the RQTBA strength function predicts fragmentation and additional low-lying strength in neutron-rich nuclei mostly above the neutron threshold. If further correlations beyond the RQTBA approach will lead to a larger fragmentation and push certain "peaks" to smaller energies, is an open question. Therefore, improved "versions" of the RQTBA model might give different results.

We have also calculated the (n,γ) reaction rate on stable and on proton rich tin nuclei. These nuclei are not relevant for r-process nucleosynthesis, however the results show that there are large differences in the predictions of (n,γ) rates between these models. Generally, we see that a pure Lorentzian parametrisation gives a very large E1 strength for energies below the giant resonance. This leads to an overestimation of the (n,γ) cross section. Therefore, various modifications of the Lorentzian form factor were developed to account for this problem [MSC81, KU90, PKB$^+$06, PKK$^+$08, BBC$^+$06]. In this thesis we employed one such modification by introducing an energy-dependent width of the Lorentzian (see eq. (7.2)). Nevertheless, we still see the general trend that the Lorentzian strength functions give larger E1 strength at low energies compared to the microscopic models.

We employed the Hauser-Feshbach model for all reactions in this chapter, although its use might be questionable for certain reactions [RTK97]. Additionally to the compound mechanism, one would have to regard direct reaction mechanisms. These mechanisms could become especially important for tin isotopes with A$\geq$ 132 - for an overview see [OHRB96, CKH$^+$08]. Nevertheless, the Hauser-Feshbach mechanism is still the default approach to obtain astrophysical reaction rates. The incorporation of direct or pre-equilibrium mechanisms is still in its beginnings and needs to be elaborated and examined in the coming years [CKH$^+$08]; for a first study on global scales see [OBMP$^+$10].

Motivated by the question if Brink's hypothesis is applicable to low-lying strength, we started to investigate this issue regarding M1 transitions in section 7.3. Here we have employed the nuclear shell model to obtain the M1 strength functions, because this model enables us to calculate the strength function or the reduced transitions probabilities, respectively, also for excited states. We choose the M1 strength functions because they are the second important input to the γ-channel in (n,γ) cross section calculations for the r-process and they also exhibit a low-lying collective mode, i.e. the scissors mode [Ric95, HvR10]. Moreover, our model space in the shell model allows a very good description of the M1 transitions below the spin-flip resonance. We calculated the M1 strength function for different iron nuclei and determined the reaction rates for selected cases. Our results clearly show that Brink's hypothesis is not valid for low-lying orbital strength, while it is appropriate for the collective spin-flip resonance. This is an expected result, because this hypothesis was initially formulated for highly collective modes [Bri55]. It was the lack of a realistic description of the low-energy regime that forced people to apply this hypothesis for all transitions. It is an open question if we can infer from the results for the M1 transitions that Brink's hypothesis also fails for the pygmy mode. Therefore, there is future work needed to finally examine the evolution of the pygmy resonance with excitation energy.

We have employed three different M1 strength function models for the nuclei ^{56,60,69}Fe and calculated the neutron cross sections that form these nuclei. The first strength function is based upon a single-particle model and gives a constant M1 strength. The second approach tries to parametrise the spin-flip resonance with a Lorentzian form factor, motivated by the successful description of the electric giant dipole resonance with such a distribution. The third strength function is obtained from the shell model. Our results show that the different treatments of M1 transitions in Hauser-Feshbach calculations are subject to large uncertainties. This is generally not a problem because E1 transitions usually dominate for nuclei (or reactions) in which we may safely apply the Hauser-Feshbach model. However, there exist nuclei in which the M1 transitions may dominate and for these nuclei, the (n,γ) cross section would be particularly sensitive to changes in the M1 strength function [LLMP$^+$08, Loe07]. Additionally, we have illustrated a general problem of M1 strength functions used in Hauser-Feshbach calculations: all three strength functions show large variations regarding their total strength. The Lorentzian strength functions are generally about a factor 2-4 larger than the shell model strength functions. On the other hand, the uncertainty range of the parametrisation that is used in the Lorentzian strength function (see [BBC$^+$06] and references therein) is a factor three. The lack of a model independent sum rules for M1 transitions (like the Thomas-Reiche-Kuhn sum rule for E1 transitions) prevents us to obtain a general measure on the total M1 strength in a nucleus.

The r-process may also reach the region of the nuclear chart, where fission becomes important. Therefore, we have studied the ground state and fission properties of a large number of even-even nuclei from Z=86 to Z=122. We employed the Skyrme-Hartree-Fock-BCS model and assumed axial-symmetric nuclear shapes. All results were obtained in close cooperation with the nuclear structure theory group of the university of Erlangen-Nürnberg [Erl11].

We put a particular emphasis on the influence of the used Skyrme functional and deduced that the differences regarding the ground state properties are less strongly affected by different Skyrme functionals than the fission properties. We focused on the role of the effective mass and chose two functionals with a small effective mass (SLy6, SkI3) and a very recently developed Skyrme functional with a large effective mass (SV-min). Skyrme functionals with a small effective mass show an enhancement of shell effects. For super-heavy nuclei, shell effects strongly influence the fission barrier, i.e. super-heavy are only stable against immediate fission because of shell-effects, therefore we see large differences in the predicted fission barrier heights between the utilised functionals. Additionally, we see discrepancies in the role of octupole deformations and possible deformed shell closures.

Albeit the differences in the predicted fission barrier heights, our results show that the evolution of the maximum fission barrier with proton and neutron number is very generic and is only weakly affected by the Skyrme functional in case of super-heavy nuclei. In a second study we have shown that this also partly true for nuclei in the actinide region. Moreover, a comparison to other standard theoretical models for fission barriers has been drawn, in particular to HFB14 and ETFSI.

The influence on r-process nucleosynthesis was discussed qualitatively depending on the height and widths of fission barriers as well as the general trend the barriers show. We conclude that there is currently no "best" Skyrme functional to describe fission for the r-process. The only possibility would be to constrain a model on experimental data, but the data are scarce (for the actinides) or not available (for the super-heavy elements) in the region where the r-process would take place. Therefore, we can summarise that the distinctively larger barriers of the SLy6 and SkI3 functionals could allow the formation of super-heavy elements in the r-process. The much smaller barriers predicted by the SV-min functional will probably not allow the synthesis of super-heavy elements, though. Nevertheless, this also depends on the astrophysical conditions, i.e. very high neutron fluxes could still move considerable amounts of matter beyond the valleys of small fission barriers predicted by the SV-min functional.

Another emphasis was put on the relevance of octupole deformation in nuclei. We showed that this is very sensitive to the effective mass, as this is also sensitive to shell-effects. Reflection asymmetric ground state shapes occur beyond magic shell closures and increase the nuclear binding. However, this effect vanishes with increasing proton number.

The additional gain in binding increases the barrier while the neutron separation energy is not affected. This stabilisation against fission due to the octupole deformation might allow the r-process to cross these regions. Reflection asymmetry can strongly reduce a possible second barrier for super-heavy nuclei. In general, our findings agree with other results [BRR$^+$99, BBMR04]. In the actinide region, the second barrier is also reduced due to reflection asymmetry but generally not removed.

In the current status the barriers obtained here cannot be used for a global determination of neutron-induced fission rates because the odd nuclei are missing. A reliable method to calculate the fission path in odd nuclei is needed sooner or later. An advantage of the applied model is that it calculates the complete fission path and the collective mass at the same time [EKR11, Erl11]. This fact calls for a change in the treatment of fission in reaction rate determinations, since these are still based upon the approximation that the fission barriers can be described by inverted parabolas [BL80, VH73, W$^+$91]. This approximation strongly simplifies the semi-classical description of the tunnelling process. As our results provide us with the complete fission path, we could also use the full information of the fission barrier in these methods and thus obtain the fission probability on a more reliable and consistent level [GHK$^+$09, SEK$^+$09, Erl11].

Regarding the nuclear shapes, we will need to go beyond axial-symmetric calculations as triaxial configurations may lower the first barrier [Ben97, BBMR04]. In our results we identified some nuclei of which we believe that triaxial configurations are also needed to describe the ground state. However, large-scale predictions of fission barriers exhibiting possible triaxial configurations are not feasible yet.

Part III

Appendices

A

Observables

This appendix gives a short overview as well as the basic corresponding definitions of the most commonly used nuclear observables in this thesis. In nuclear physics one usually gives masses in units of energy (related to c^2). We will therefore set $c^2 = 1$ due to convenience.

A.1 Nuclear Mass

The nuclear mass has been and still is one of the the most important observables regarding the nucleus. Its definition involving the proton number Z and the neutron number N is straightforward:

$$M(Z,N) = (Z \cdot m_p + N \cdot m_n) - B(Z,N)/c^2 = (Z \cdot m_p + N \cdot m_n) + E(Z,N)/c^2. \tag{A.1}$$

The nuclear mass is the sum of the masses of the constituents that build up the nucleus minus the binding energy. Nuclear masses are often given in atomic mass units u. This u is defined as the 1/12 of the atomic mass of ^{12}C,

$$u = 931.394 \text{ MeV}/c^2. \tag{A.2}$$

In mass tables the so called mass excess $X(Z,N)$ is usually given. It is the mass difference of the measured (or calculated) nuclear mass to the mass of an imaginary nucleus in which every nucleon is bound as in ^{12}C:

$$X(Z,N) = M(Z,N) - A \cdot u = E(Z,N) + Z \cdot X_H + N \cdot X_n \tag{A.3}$$

with the mass excesses X_H for hydrogen and X_n for a neutron.

A.2 Binding Energies

The binding energy B is the energy gain of the nucleus compared to completely independent nucleons:

$$B(Z,N) = (Z \cdot m_p + N \cdot m_n) - M(Z,N). \tag{A.4}$$

The nucleus is bound if the binding energy $B(Z,N)$ is positive. If it is negative, it is not possible to form a nucleus with the corresponding proton number Z and neutron number N. However, in the literature the binding energy is often defined as a negative number:

$$E(Z,N) = -B(Z,N). \tag{A.5}$$

The binding energy of a nucleus can be roughly estimated as being 1% of the total mass of the nucleus.

A.3 Separation Energies

The separation energy $S_q(Z,N)$ gives the energy that is needed to remove one nucleon q from the nucleus with proton number Z and neutron number N. Usually one refers to the so called one nucleus separation energy which we can write as,

$$S_q(Z,N) = \begin{cases} E(Z,N-1) - E(Z,N) & \text{if q} \mathrel{\hat{=}} \text{n} \\ E(Z-1,N) - E(Z,N) & \text{if q} \mathrel{\hat{=}} \text{p.} \end{cases} \tag{A.6}$$

The determination of this observable is extremely sensitive to pairing correlations since one substracts the masses of even A and odd A nuclei.

A.3.1 Drip Lines

The so called neutron and proton drip lines are the boundaries for nuclei concerning the spontaneous emission of either a proton (proton drip line) or a neutron (neutron drip line). For a given element Z, the nucleus with the most neutrons whose neutron separation energy S_n is just above zero, i.e. the nucleus with an additional neutron has a negative neutron-separation energy, lies on the neutron drip line. All nuclei with more neutrons (for a fixed Z) are therefore unstable against neutron emission.

The definition of the proton drip line is equivalent, e.g. the proton separation energy has to become negative. However, this is not unambiguous: protons are charged nucleons and therefore “feel” a coulomb barrier. It is therefore possible that a nucleus has a negative proton separation energy but the coulomb barrier hinders the spontaneous emission - although it cannot avoid the emission. The proton would have to tunnel through the barrier. This becomes even more important with regard to the α-separation energy

$$S_\alpha = E(Z-2,N-2) - E(Z,N) - 28.295 \text{ MeV}. \tag{A.7}$$

S_α can become negative but the α-particle is not necessarily “immediately” emitted since the coulomb barrier drastically lowers the emission probability - nevertheless the phenomena of α-decay exists and it is due to a negative S_α. Light and medium mass nuclei with a negative S_α are usually unstable against β^+ decay and therefore rather decay via the β^+-channel.

In principle the drip lines define which nuclei are energetically stable against the corresponding nucleon emission.

A.3.2 Two Nucleon Separation Energies

One can also define the separation energy S_{2q} needed to remove two nucleons of the same sort:

$$S_{2q}(Z,N) = \begin{cases} E(Z,N-2) - E(Z,N) & \text{if q} \mathrel{\hat{=}} \text{n} \\ E(Z-2,N) - E(Z,N) & \text{if q} \mathrel{\hat{=}} \text{p.} \end{cases} \tag{A.8}$$

This observable is very convenient for microscopic mean-field calculations since it is insensitive to pairing effects in the nuclear masses, i.e. we may study the predictive power of different nuclear mass models without having to care about the pairing correlations that are often treated differently between the models.

B

Skyrme Functionals

In this thesis we use three different Skyrme functionals, i.e. SLy6, SkI3, and SV-min. The parameters of these functionals are given in table B.1. However, we use a different notation in this thesis [Rei92, SR07]. the relations between the original Skyrme parameters and the parameters we use in this thesis is tabulated in table B.2. There also exists a more general relation to the parameters of an energy density functional [SR07].

name	t_0	t_1	t_2	t_3	t_4	$V_{\mathrm{Pair,p}}$	$V_{\mathrm{Pair,n}}$	ρ_{Pair}
ref.	x_0	x_1	x_2	x_3	b_4'	α	μ_p	μ_n
SLy6-DDDI	-1762.88	561.608	-227.09	8106.2	188.508	1213.70	968.364	0.16
[CBH$^+$98]	0.3083	-1.1722	-1.0907	12926	0	0.25	20.752	20.752
SkI3-DDDI	-2479.50	462.180	-448.61	13673.0	122.0	1053.12	864.174	0.16
[RF95]	0.825	-0.465	-1.0	1.355	61.0	0.1666667	20.735	20.735
SV-min	-2112.248	295.781	142.268	13988.567	111.291	601.160	567.191	0.21159
[KRBM09]	0.243886	-1.434926	-2.625899	0.258070	45.93615	0.255368	20.749	20.721

Table B.1: Table of Skyrme functionals used in this thesis. $V_{\mathrm{Pair,q}}$ is the pairing parameter for protons (q=p) or neutrons (q=n). μ_q is the inverse nucleon mass, i.e. $\mu_q = \hbar/2m_q$ that is used within the functional for the kinetic energy. Note that SV-min is a "DDDI" functional by default. For an overview on the other parameters see [SR07] and references therein.

$$b_0 = t_0\left(1+\frac{1}{2}x_0\right) \qquad b'_0 = t_0\left(\frac{1}{2}+x_0\right)$$

$$b_1 = \frac{1}{4}\left[t_1\left(1+\frac{1}{2}x_1\right)+t_2\left(1+\frac{1}{2}x_2\right)\right] \qquad b'_1 = \frac{1}{4}\left[t_1\left(\frac{1}{2}+x_1\right)-t_2\left(\frac{1}{2}+x_2\right)\right]$$

$$b_2 = \frac{1}{8}\left[3t_1\left(1+\frac{1}{2}x_1\right)-t_2\left(1+\frac{1}{2}x_2\right)\right] \qquad b'_2 = \frac{1}{8}\left[3t_1\left(\frac{1}{2}+x_1\right)+t_2\left(\frac{1}{2}+x_2\right)\right]$$

$$b_3 = \frac{1}{4}t_3\left(1+\frac{1}{2}x_3\right) \qquad b'_3 = \frac{1}{4}t_3\left(\frac{1}{2}+x_3\right)$$

$$b_4 = \frac{1}{2}t_4$$

Table B.2: Transformation relations between the original set of Skyrme parameters (t_i,x_i) [Sky59, VB70, VB72] and the notation in this thesis [Rei92].

C

Local Densities for Skyrme-Hartree-Fock

Here we will shortly summarise the needed densities of section 4.2. The subscript q stands for both nucleon types, u_α and v_α are the BCS amplitudes. The index α is always related to the index q, i.e. it regards either protons or neutrons and the sum index is always restricted to the set of single particles levels belonging to q. The $\phi_\alpha(\boldsymbol{r})$ are the wave-functions of the state labelled with α; the $\hat{\boldsymbol{\sigma}}$ are the well known Pauli spin matrices. For readability reasons we omit the argument of the ϕ_α and all the densities, i.e. they all depend on $\boldsymbol{r}$ which in turn represents all dependencies on the spatial coordinates and spin in our case; see [SR07, Ben97, Erl11] for more details. The f_α in the pairing density is a cut-off, see section 4.2.3.

particle/mass density:

$$\rho_q(\boldsymbol{r}) = \sum_\alpha |v_\alpha|^2 \, |\phi_\alpha|^2 \tag{C.1}$$

kinetic density:

$$\tau_q(\boldsymbol{r}) = \sum_\alpha |v_\alpha|^2 \, |\boldsymbol{\nabla}\phi_\alpha|^2 \tag{C.2}$$

spin-orbit density:

$$\boldsymbol{J}_q = -i \sum_\alpha |v_\alpha|^2 \, \phi_\alpha^+ \boldsymbol{\nabla} \times \hat{\boldsymbol{\sigma}} \phi_\alpha \tag{C.3}$$

pair density:

$$\chi_q = \sum_\alpha f_\alpha u_\alpha v_\alpha \, |\phi_\alpha|^2 \tag{C.4}$$

spin density:

$$\boldsymbol{s}_q(\boldsymbol{r}) = \sum_\alpha |v_\alpha|^2 \, \phi_\alpha^+ \hat{\boldsymbol{\sigma}} \phi_\alpha \tag{C.5}$$

current:

$$\boldsymbol{j}_q = \frac{1}{2i} \sum_{\alpha} |v_\alpha|^2 \left\{ \phi_\alpha^+ \boldsymbol{\nabla} \phi_\alpha - (\boldsymbol{\nabla} \phi_\alpha)^+ \phi_\alpha \right\} \tag{C.6}$$

spin-orbit tensor density:

$$J_{\mu\nu} = \frac{1}{2i} \sum_{\alpha} |v_\alpha|^2 \left\{ \phi_\alpha^+ \nabla_\mu \hat{\sigma}_\nu \phi_\alpha - (\nabla_\mu \phi_\alpha)^+ \hat{\sigma}_\nu \phi_\alpha \right\} \tag{C.7}$$

kinetic spin density:

$$\boldsymbol{\tau}_q = \sum_{\alpha} v_\alpha^2 (\boldsymbol{\nabla} \phi_\alpha)^+ \hat{\boldsymbol{\sigma}} \boldsymbol{\nabla} \phi_\alpha \tag{C.8}$$

Bibliography

[AB93] I. Ahmad and P. A. Butler, *Annu. Rev. Nucl. Part. S.*, **43** (1), 71, 1993.

[ABLN00] Y. Alhassid, G. F. Bertsch, S. Liu, and H. Nakada, *Phys. Rev. Lett.*, **84** (19), 4313, 2000.

[AGT07] M. Arnould, S. Goriely, and K. Takahashi, *Phys. Rep.*, **450**, 97, 2007.

[AK09] A. Avdeenkov and S. Kamerdzhiev, *Phys. At. Nuclei.*, **72**, 1332, 2009.

[AKF$^+$05] P. Adrich, A. Klimkiewicz, M. Fallot, K. Boretzky, T. Aumann, D. Cortina-Gil, U. D. Pramanik, T. W. Elze, H. Emling, H. Geissel, M. Hellström, K. L. Jones, J. V. Kratz, R. Kulessa, Y. Leifels, C. Nociforo, R. Palit, H. Simon, G. Surówka, K. Sümmerer, and W. Waluś, *Phys. Rev. Lett.*, **95** (13), 132501, 2005.

[ALN07] Y. Alhassid, S. Liu, and H. Nakada, *Phys. Rev. Lett.*, **99** (16), 162504, 2007.

[APDT95] Y. Aboussir, J. M. Pearson, A. K. Dutta, and F. Tondeur, *At. Data Nucl. Data Tables*, **61** (1), 127, 1995.

[Are79] H. Arenhövel, in H. Arenhövel and D. Drechsel (editors), *Nuclear Physics with Electromagnetic Interactions*, volume 108 of *Lecture Notes in Physics*, 159–169, Springer Berlin / Heidelberg, 1979.

[AT99] M. Arnould and K. Takahashi, *Rep. Prog. Phys.*, **62** (3), 395, 1999.

[AWT03] G. Audi, A. Wapstra, and C. Thibault, *Nucl. Phys. A*, **729**, 337, 2003.

[Axe62] P. Axel, *Phys. Rev.*, **126** (2), 671, 1962.

[BBB98] P. F. Bortignon, A. Bracco, and R. A. Broglia, *Giant Resonances: nuclear physics at finite temperature*, volume 10 of *Contemporary concepts in physics*, Harwood Academic Publishers, 1998.

[BBC$^+$06] T. Belgya, O. Bersillon, R. Capote, T. Fukahori, G. Zhigang, S. Goriely, M. Herman, A. V. Ignatyuk, S. Kailas, A. Koning, P. Oblozinsky, V. A. Plujko, and P. Young, *Handbook for calculations of nuclear reaction data, RIPL-2*, IAEA-TECDOC-1506, IAEA, Vienna, 2006,
Available online at `http://www-nds.iaea.org/RIPL-2/`.

[BBFH57] E. M. Burbidge, G. R. Burbidge, W. A. Fowler, and F. Hoyle, *Rev. Mod. Phys.*, **29** (4), 547, 1957.

[BBH$^+$09] J. Beun, J. C. Blackmon, W. R. Hix, G. C. McLaughlin, M. S. Smith, and R. Surman, *J. Phys. G: Nucl. Partic.*, **36** (2), 025201, 2009.

[BBMR04] T. Bürvenich, M. Bender, J. A. Maruhn, and P.-G. Reinhard, *Phys. Rev. C*, **69** (1), 014307, 2004.

[BCS57] J. Bardeen, L. N. Cooper, and J. R. Schrieffer, *Phys. Rev. Lett.*, **108**, 1175, 1957.

[BEF$^+$73] G. A. Bartholomew, E. D. Earle, A. J. Ferguson, J. W. Knowles, and M. A. Lone, *Adv. Nucl. Phys.*, **7**, 229, 1973.

[Bel58] S. T. Belyaev, *K. Dan. Vidensk. Selsk. Mat. Fys. Medd.*, **31** (11), 1958.

[Ben97] M. Bender, *Exotische Atomkerne im Skyrme-Hartree-Fock-Modell*, Ph.D. thesis, Johann Wolfgang von Goethe Universität Frankfurt am Main, 1997,
Available online at `http://theory.gsi.de/~bender/diss/dissertation.html`.

[Ber07] C. A. Bertulani, *Nuclear Physics in an Nutshell*, Princeton University Press, 1 edition, 2007.

[Bet36] H. A. Bethe, *Phys. Rev.*, **50**, 331, 1936.

[Bet39] H. A. Bethe, *Phys. Rev.*, **55** (5), 434, 1939.

[BG77] P. Brussaard and P. Glaudemans, *Shell-model applications in nuclear spetroscopy*, North-Holland Plublishing Company, 1977.

[BGG89] J. F. Berger, M. Girod, and D. Gogny, *Nucl. Phys. A*, **502**, 85, 1989.

[BHR03] M. Bender, P.-H. Heenen, and P.-G. Reinhard, *Rev. Mod. Phys.*, **75** (1), 121, 2003.

[BL80] S. Bjørnholm and J. Lynn, *Rev. Mod. Phys.*, **52** (4), 1980.

[BM69] Å. Bohr and B. R. Mottelson, *Nuclear Structure Volume 1*, W. A. Benjmain, Inc., 1969.

[BM75] Å. Bohr and B. R. Mottelson, *Nuclear Structure Volume 2*, W. A. Benjmain, Inc., 1975.

[BMP58] Å. Bohr, B. R. Mottelson, and D. Pines, *Phys. Rev.*, **110**, 936, 1958.

[BN96] P. A. Butler and W. Nazarewicz, *Rev. Mod. Phys.*, **68** (2), 349, 1996.

[Boh36] N. Bohr, *Nature*, **137**, 334, 1936.

[Boy08] R. N. Boyd, *An Introduction to Nuclear Astrophysics*, Univeristy of Chicago Press, 2008.

[Bri55] D. M. Brink, Ph.D. thesis, Oxford University, 1955.

[Bro01] B. A. Brown, *Prog. Part. Nucl. Phys.*, **47** (2), 517, 2001.

[BRR$^+$98] M. Bender, K. Rutz, P.-G. Reinhard, J. A. Maruhn, and W. Greiner, *Phys. Rev. C*, **58** (4), 2126, 1998.

[BRR$^+$99] M. Bender, K. Rutz, P.-G. Reinhard, J. A. Maruhn, and W. Greiner, *Phys. Rev. C*, **60** (3), 034304, 1999.

[BRRM00] M. Bender, K. Rutz, P.-G. Reinhard, and J. Maruhn, *Eur. Phys. J. A*, **8**, 59, 2000.

[Brua] Bruslib, HFB14 Fission Properties,
`http://www.astro.ulb.ac.be/pmwiki/Brusslib/FissionHfb`.

[Brub] Bruslib, HFB14 Mass Properties,
`http://www.astro.ulb.ac.be/pmwiki/Brusslib/Hfb14`.

[BW39] N. Bohr and J. A. Wheeler, *Phys. Rev.*, **56** (5), 426, 1939.

[BW52] J. Blatt and V. F. Weisskopf, *Theoretical Nuclear Physics*, Springer-Verlag, 1952.

[BWK89] H. Beer, G. Walter, and F. Kappler, *Astron. Astrophys.*, **211**, 245, 1989.

[Cau] E. Caurier, Antoine website, `http://sbgat194.in2p3.fr/~theory/antoine/menu.html`.

[CBH$^+$98] E. Chabanat, P. Bonche, P. Haensel, J. Meyer, and R. Schaeffer, *Nucl. Phys. A*, **635** (1-2), 231, 1998.

[ĆDH$^+$96] S. Ćwiok, J. Dobaczewski, P. Heenen, P. Magierski, and W. Nazarewicz, *Nucl. Phys. A*, **611**, 211, 1996.

[CFN$^+$07] M. Chernykh, H. Feldmeier, T. Neff, P. von Neumann-Cosel, and A. Richter, *Phys. Rev. Lett.*, **98** (3), 032501, 2007.

[CFN$^+$10] M. Chernykh, H. Feldmeier, T. Neff, P. von Neumann-Cosel, and A. Richter, *Phys. Rev. Lett.*, **105** (2), 022501, 2010.

[ĆHN05] S. Ćwiok, P. Heenen, and W. Nazarewicz, *Nat.*, **433** (7027), 705, 2005.

[CKH$^+$08] S. Chiba, H. Koura, T. Hayakawa, T. Maruyama, T. Kawano, and T. Kajino, *Phys. Rev. C*, **77** (1), 015809, 2008.

[CMPN+05] E. Caurier, G. Martínez-Pinedo, F. Nowacki, A. Poves, and A. P. Zuker, *Rev. Mod. Phys.*, **77** (2), 427, 2005.

[CTDL99a] C. Cohen-Tannoudji, B. Diu, and F. Laloë, *Quantenmechanik*, Walter der Gruyter, 2nd edition, 1999.

[CTDL99b] C. Cohen-Tannoudji, B. Diu, and F. Laloë, *Quantenmechanik 2*, Walter der Gruyter, 2nd edition, 1999.

[CTT91] J. J. Cowan, F.-K. Thielemann, and J. W. Truran, *Phys. Rep.*, **208** (4/5), 1991.

[DAB+08] M. Dworschak, G. Audi, K. Blaum, P. Delahaye, S. George, U. Hager, F. Herfurth, A. Herlert, A. Kellerbauer, H.-J. Kluge, D. Lunney, L. Schweikhard, and C. Yazidjian, *Phys. Rev. Lett.*, **100** (7), 072501, 2008.

[DB88] S. S. Dietrich and B. L. Berman, *At. Data Nucl. Data Tables*, **38**, 199, 1988.

[DFG+10] J. M. Daugas, T. Faul, H. Grawe, M. Pfützner, R. Grzywacz, M. Lewitowicz, N. L. Achouri, J. C. Angélique, D. Baiborodin, R. Bentida, R. Béraud, C. Borcea, C. R. Bingham, W. N. Catford, A. Emsallem, G. de France, K. L. Grzywacz, R. C. Lemmon, M. J. Lopez Jimenez, F. de Oliveira Santos, P. H. Regan, K. Rykaczewski, J. E. Sauvestre, M. Sawicka, M. Stanoiu, K. Sieja, and F. Nowacki, *Phys. Rev. C*, **81** (3), 034304, 2010.

[DFT84] J. Dobaczewski, H. Flocard, and J. Treiner, *Nucl. Phys. A*, **422** (1), 103, 1984.

[DG80] J. Dechargé and D. Gogny, *Phys. Rev. C*, **21** (4), 1568, 1980.

[DG01] P. Demetriou and S. Goriely, *Nucl. Phys. A*, **695**, 95, 2001.

[DNW95] J. Dobaczewski, W. Nazarewicz, and T. R. Werner, *Phys. Scripta*, **1995** (T56), 15, 1995.

[Eck30] C. Eckart, *Rev. Mod. Phys.*, **2** (3), 305, 1930.

[EKR08] J. Erler, P. Klüpfel, and P.-G. Reinhard, *Eur. Phys. J. A*, **37**, 81, 2008.

[EKR11] J. Erler, P. Klüpfel, and P.-G. Reinhard, *J. Phys. G: Nucl. Partic.*, **38** (3), 033101, 2011.

[EKvP07] J. Enders, O. Karg, P. von Neumann-Cosel, and V. Ponomarev, *Eur. Phys. J. A*, **31**, 15, 2007.

[ELS+10] J. Endres, E. Litvinova, D. Savran, P. A. Butler, M. N. Harakeh, S. Harissopulos, R.-D. Herzberg, R. Krücken, A. Lagoyannis, N. Pietralla, V. Y. Ponomarev, L. Popescu, P. Ring, M. Scheck, K. Sonnabend, V. I. Stoica, H. J. Wörtche, and A. Zilges, *Phys. Rev. Lett.*, **105** (21), 212503, 2010.

[ENS] ENSDF, Evaluated nuclear structure data file (ensdf), `http://www.nndc.bnl.gov/ensdf/`.

[Eri59] T. Ericson, *Nucl. Phys.*, **11**, 481, 1959.

[Eri60] T. Ericson, *Adv. Phys.*, **9** (36), 425, 1960.

[Erl11] J. Erler, *Exploration of (Super-)Heavy Elements using the Skyrme-Hartree-Fock model*, Ph.D. thesis, Friedrich-Alexander Universität Erlangen-Nürnberg, 2011.

[EvE+03] J. Enders, P. von Brentano, J. Eberth, A. Fitzler, C. Fransen, R. D. Herzberg, H. Kaiser, L. Käubler, P. von Neumann-Cosel, N. Pietralla, V. Y. Ponomarev, A. Richter, R. Schwengner, and I. Wiedenhöver, *Nucl. Phys. A*, **724** (3-4), 243, 2003.

[EvRR05] J. Enders, P. von Neumann-Cosel, C. Rangacharyulu, and A. Richter, *Phys. Rev. C*, **71**, 014306, 2005.

[FBC+69] S. C. Fultz, B. L. Berman, J. T. Caldwell, R. L. Bramblett, and M. A. Kelly, *Phys. Rev.*, **186** (4), 1255, 1969.

[FCZ67] W. A. Fowler, G. R. Caughlan, and B. A. Zimmerman, *Annu. Rev. Astron. Astrophys.*, **5**, 525, 1967.

[FCZ75] W. A. Fowler, G. R. Caughlan, and B. A. Zimmerman, *Annu. Rev. Astron. Astrophys.*, **13**, 69, 1975.

[Fes92] H. Feshbach, *Theoretical Nuclear Physics: Nuclear Reactions*, John Wiley & Sons, 1992.

[FHL$^+$03] R. W. Fearick, G. Hartung, K. Langanke, G. Martínez-Pinedo, P. von Neumann-Cosel, and A. Richter, *Nucl. Phys. A*, **727** (1-2), 41, 2003.

[FL96] P. Fröbrich and R. Lipperheide, *Theory of Nuclear Reactions*, Oxford Science Publications, 1996.

[FPW54] H. Feshbach, C. E. Porter, and V. F. Weisskopf, *Phys. Rev.*, **96** (2), 448, 1954.

[FWR$^+$90] D. Frekers, H. J. Wörtche, A. Richter, R. Abegg, R. E. Azuma, A. Celler, C. Chan, T. E. Drake, R. Helmer, K. P. Jackson, J. D. King, C. A. Miller, R. Schubank, M. C. Vetterli, and S. Yen, *Phys. Lett. B*, **244** (2), 178, 1990.

[GBD$^+$08] E.-W. Grewe, C. Bäumer, H. Dohmann, D. Frekers, M. N. Harakeh, S. Hollstein, H. Johansson, K. Langanke, G. Martínez-Pinedo, F. Nowacki, I. Petermann, L. Popescu, S. Rakers, D. Savran, K. Sieja, H. Simon, J. H. Thies, A. M. van den Berg, H. J. Wörtche, and A. Zilges, *Phys. Rev. C*, **77** (6), 064303, 2008.

[GC65] A. Gilbert and A. G. W. Cameron, *Can. J. Phys.*, **43**, 1446, 1965.

[GCP09] S. Goriely, N. Chamel, and J. M. Pearson, *Phys. Rev. Lett.*, **102** (15), 152503, 2009.

[GF85] M. K. Grossjean and H. Feldmeier, *Nucl. Phys. A*, **444** (1), 113, 1985.

[GHK08] S. Goriely, S. Hilaire, and A. J. Koning, *Phys. Rev. C*, **78** (6), 064307, 2008.

[GHK$^+$09] S. Goriely, S. Hilaire, A. J. Koning, M. Sin, and R. Capote, *Phys. Rev. C*, **79** (2), 024612, 2009.

[Gho50] S. N. Ghoshal, *Phys. Rev.*, **80** (6), 939, 1950.

[GKS04] S. Goriely, E. Khan, and M. Samyn, *Nucl. Phys. A*, **739**, 331, 2004.

[GM96] W. Greiner and J. Maruhn, *Nuclear Models*, Springer-Verlag, 1996.

[Goo79] A. L. Goodman, *Adv. Nucl. Phys.*, **11**, 263, 1979.

[Gor98] S. Goriely, *Phys. Lett. B*, **436**, 10, 1998.

[Gra04] H. Grawe, *Lect. Notes Phys.*, **651**, 33, 2004.

[GSBP03] S. Goriely, M. Samyn, M. Bender, and J. M. Pearson, *Phys. Rev. C*, **68** (5), 054325, 2003.

[GSP07] S. Goriely, M. Samyn, and J. M. Pearson, *Phys. Rev. C*, **75** (6), 064312, 2007.

[GT48] M. Goldhaber and E. Teller, *Phys. Rev.*, **74** (9), 1046, 1948.

[Hey94] K. Heyde, *The nucleaer shell model*, Springer-Verlag, 2nd edition, 1994.

[HG06] S. Hilaire and S. Goriely, *Nucl. Phys. A*, **779**, 63, 2006.

[HG07] S. Hilaire and S. Goriely, in M. Arnould, M. Lewitowicz, H. Emling, H. Akimune, M. Ohta, H. Utsunomiya, T. Wada, and T. Yamagata (editors), *Tours Symposium on Nuclear Physics VI*, volume 891, 348–354, AIP, Tours (France), 2007.

[HG08] S. Hilaire and M. Girod, *Int. Conf. on Nucl. Data for Sc. and Tech.*, 2008, `http://www-phynu.cea.fr/HFB-Gogny.htm`.

[HJS49] O. Haxel, J. H. D. Jensen, and H. E. Suess, *Phys. Rev.*, **75** (11), 1766, 1949.

[HK64] P. Hohenberg and W. Kohn, *Phys. Rev.*, **136** (3B), B864, 1964.

[HKZ03] M. Horoi, J. Kaiser, and V. Zelevinsky, *Phys. Rev. C*, **67** (5), 054309, 2003.

[HM72] J. R. Huizenga and L. G. Moretto, *Annu. Rev. Nucl. Par. Sci.*, 427–464, 1972.

[HvR10] K. Heyde, P. von Neumann-Cosel, and A. Richter, *Rev. Mod. Phys.*, **82** (3), 2365, 2010.

[HW53] D. L. Hill and J. A. Wheeler, *Phys. Rev.*, **89** (5), 1102, 1953.

[HWFZ76] J. A. Holmes, S. E. Woosley, W. A. Fowler, and B. A. Zimmerman, *At. Data Nucl. Data Tables*, **18**, 305, 1976.

[IAEa] IAEA, Reference input parameter library 2, `http://www-nds.iaea.org/RIPL-2/`.

[IAEb] IAEA, Reference input parameter library 3, `http://nds121.iaea.org/RIPL-3/`.

[INY09] T. Inakura, T. Nakatsukasa, and K. Yabana, *Phys. Rev. C*, **80** (4), 044301, 2009.

[IST75] A. V. Ignatyuk, G. N. Smirenkin, and A. S. Tishin, *Yad. Fiz.*, **21** (485), 1975.

[JAB$^+$10] K. L. Jones, A. S. Adekola, D. W. Bardayan, J. C. Blackmon, K. Y. Chae, K. A. Chipps, J. A. Cizewski, L. Erikson, C. Harlin, R. Hatarik, R. Kapler, R. L. Kozub, J. F. Liang, R. Livesay, Z. Ma, B. H. Moazen, C. D. Nesaraja, F. M. Nunes, S. D. Pain, N. P. Patterson, D. Shapira, J. F. Shriner, M. S. Smith, T. P. Swan, and J. S. Thomas, *Nature*, **465** (7297), 454, 2010.

[Jac98] J. D. Jackson, *Classical Electrodynamics, 3rd Edition*, 1998.

[JM86] A. S. Jensen and A. Miranda, *Nucl. Phys. A*, **449** (2), 331, 1986.

[JM89] M. Jaminon and C. Mahaux, *Phys. Rev. C*, **40** (1), 354, 1989.

[KAB$^+$07] A. Klimkiewicz, P. Adrich, K. Boretzky, M. Fallot, T. Aumann, D. Cortina-Gil, U. D. Pramanik, T. Elze, H. Emling, H. Geissel, M. Hellstroem, K. Jones, J. Kratz, R. Kulessa, Y. Leifels, C. Nociforo, R. Palit, H. Simon, G. Surowka, K. Sümmerer, S. Typel, and W. Walus, *Nucl. Phys. A*, **788** (1-4), 145, 2007.

[KB08] M. Krtička and F. Bečvář, *J. Phys. G: Nucl. Partic.*, **35** (1), 014025, 2008.

[KHG08] A. Koning, S. Hilaire, and S. Goriely, *Nucl. Phys. A*, **810**, 13, 2008.

[KKF$^+$04] K. Knie, G. Korschinek, T. Faestermann, E. A. Dorfi, G. Rugel, and A. Wallner, *Phys. Rev. Lett.*, **93** (17), 171103, 2004.

[KLF04] E. Kolbe, K. Langanke, and G. M. Fuller, *Phys. Rev. Lett.*, **92** (11), 111101, 2004.

[KLM$^+$07] Y. Kalmykov, K. Langanke, D. Mocelj, P. von Neumann-Cosel, I. Poltoraska, G. Martínez-Pinedo, A. Richter, A. Shevchenko, and J. Wambach, *Nucl. Phys. A*, **788**, 136, 2007.

[Klü08] P. Klüpfel, *Skyrme's Interaction Beyond Mean-Field: The DGCM+GOA Hamiltonian of Nuclear Quadrupole Motion*, Ph.D. thesis, Friedrich-Alexander Universität Erlangen-Nürnberg, 2008,
Available online at `http://www.theorie2.physik.uni-erlangen.de/publications/phd/pk-doctor.pdf`.

[KÖL$^+$07] Y. Kalmykov, C. Özen, K. Langanke, G. Martínez-Pinedo, P. von Neumann-Cosel, and A. Richter, *Phys. Rev. Lett.*, **99** (20), 202502, 2007.

[KPA$^+$05] K.-L. Kratz, B. Pfeiffer, O. Arndt, S. Hennrich, A. Wöhr, and the ISOLDE/IS333, IS378, IS393 Collaborations, *Eur. Phys. J. A*, **25**, 633, 2005.

[KPA$^+$07] A. Klimkiewicz, N. Paar, P. Adrich, M. Fallot, K. Boretzky, T. Aumann, D. Cortina-Gil, U. D. Pramanik, T. W. Elze, H. Emling, H. Geissel, M. Hellström, K. L. Jones, J. V. Kratz, R. Kulessa, C. Nociforo, R. Palit, H. Simon, G. Surówka, K. Sümmerer, D. Vretenar, and W. W. L. Collaboration, *Phys. Rev. C*, **76** (5), 051603, 2007.

[KPZ06] U. Kneissl, N. Pietralla, and A. Zilges, *J. Phys. G: Nucl. Partic.*, **32** (8), R217, 2006.

[KRBM09] P. Klüpfel, P. Reinhard, T. Bürvenich, and J. A. Maruhn, *Phys. Rev. C*, **79** (3), 034310, 2009.

[KS09] S. Krewald and J. Speth, *Int. J. Mod. Phys. E*, **18** (7), 1425, 2009.

[KTW98] F. Käppeler, F.-K. Thielemann, and M. Wiescher, *Annu. Rev. Nucl. Part. S.*, **48** (1), 175, 1998.

[KU90] J. Kopecky and M. Uhl, *Phys. Rev. C*, **41** (5), 1941, 1990.

[KU95] J. Kopecky and M. Uhl, Present status of experimental gamma-ray strength functions, Technical Report 1, NES/NCS/DOC, 1995.

[Lan98] K. Langanke, *Phys. Lett. B*, **438**, 235, 1998.

[LBB$^+$74] A. Leprêtre, H. Beil, R. Bergère, P. Carlos, A. D. Miniac, A. Veyssière, and K. Kernbach, *Nucl. Phys. A*, **219** (1), 39, 1974.

[LC81] H. Lee and W. Cheng, in T. Kuo and S. Wong (editors), *Topics in Nuclear Physics I*, volume 144 of *Lecture Notes in Physics*, 353–457, Springer Berlin / Heidelberg, 1981.

[LLL$^+$09] E. Litvinova, H. P. Loens, K. Langanke, G. Martínez-Pinedo, T. Rauscher, P. Ring, F.-K. Thielemann, and V. Tselyaev, *Nucl. Phys. A*, **823**, 26, 2009.

[LLMP$^+$08] H. P. Loens, K. Langanke, G. Martínez-Pinedo, T. Rauscher, and F.-K. Thielemann, *Phys. Lett. B*, **666** (4), 395, 2008.

[LMP03] K. Langanke and G. Martínez-Pinedo, *Rev. Mod. Phys.*, **75** (3), 819, 2003.

[Loe07] H. P. Loens, *Influence of parity-dependent nuclear level densities on astrophysical reactions*, Master's thesis, Technische Universität Darmstadt, 2007.

[LRT08] E. Litvinova, P. Ring, and V. Tselyaev, *Phys. Rev. C*, **78**, 014312, 2008.

[LRT10] E. Litvinova, P. Ring, and V. Tselyaev, *Phys. Rev. Lett.*, **105** (2), 022502, 2010.

[LRTL09] E. Litvinova, P. Ring, V. Tselyaev, and K. Langanke, *Phys. Rev. C*, **79** (5), 054312, 2009.

[LS89] E. Lipparini and S. Stringari, *Phys. Rep.*, **175**, 103, 1989.

[LSM$^+$82] G. A. Leander, R. K. Sheline, P. Möller, P. Olanders, I. Ragnarsson, and A. Sierk, *Nucl. Phys. A*, **388** (3), 452, 1982.

[LTN$^+$03] K. Langanke, J. Terasaki, F. Nowacki, D. J. Dean, and W. Nazarewicz, *Phys. Rev. C*, **67** (4), 044314, 2003.

[LVH70] K. E. G. Löbner, M. Vetter, and V. Hönig, *Nucl. Data Tables A*, **7**, 495, 1970.

[Man75] H. Mang, *Phys. Rep.*, **18** (6), 325, 1975.

[May49] M. G. Mayer, *Phys. Rev.*, **75** (12), 1969, 1949.

[MBC$^+$08] P. Möller, R. Bengtsson, B. Carlsson, P. Olivius, T. Ichikawa, H. Sagawa, and A. Iwamoto, *At. Data Nucl. Data Tables*, **94** (5), 758, 2008.

[MNMS95] P. Möller, J. R. Nix, W. D. Myers, and W. J. Swiatecki, *At. Data Nucl. Data Tables*, **59** (2), 185, 1995.

[Möl10] P. Möller, *Int. J. Mod. Phys. E*, **19** (4), 575, 2010.

[MPLD00] G. Martínez-Pinedo, K. Langanke, and D. J. Dean, *Astrophys. J. Supp.*, **126** (2), 493, 2000.

[MPMZ$^+$07] G. Martínez-Pinedo, D. Mocelj, N. T. Zinner, A. Kelic, K. Langanke, I. Panov, B. Pfeiffer, T. Rauscher, K.-H. Schmidt, and F.-K. Thielemann, *Prog. Part. Nucl. Phys.*, **59** (1), 199, 2007.

[MPRT98] A. Mamdouh, J. M. Pearson, M. Rayet, and F. Tondeur, *Nucl. Phys. A*, **644** (4), 389, 1998.

[MRMP$^+$07] D. Mocelj, T. Rauscher, G. Martínez-Pinedo, K. Langanke, L. Pacearescu, A. Faessler, F.-K. Thielemann, and Y. Alhassid, *Phys. Rev. C*, **75** (4), 045805, 2007.

[MRMPA03] D. Mocelj, T. Rauscher, G. Martínez-Pinedo, and Y. Alhassid, *Nucl. Phys. A*, **718**, 650, 2003.

[MRW10] G. E. Mitchell, A. Richter, and H. A. Weidenmüller, *Rev. Mod. Phys.*, **82** (4), 2845, 2010.

[MSC81] C. M. McCullagh, M. L. Stelts, and R. E. Chrien, *Phys. Rev. C*, **23**, 1394, 1981.

[MSK$^+$77] W. D. Myers, W. J. Swiatecki, T. Kodama, L. J. El-Jaick, and E. R. Hilf, *Phys. Rev. C*, **15** (6), 2032, 1977.

[MW79] C. Mahaux and H. A. Weidenmüller, *Annu. Rev. Nucl. Par. Sci.*, **29**, 1, 1979.

[NA97] H. Nakada and Y. Alhassid, *Phys. Rev. Lett.*, **79** (16), 2939, 1997.

[NA98a] H. Nakada and Y. Alhassid, *Phys. Lett. B*, **436**, 231, 1998.

[NA98b] H. Nakada and Y. Alhassid, in H. Horiuchi, M. Kamimura, H. Toki, Y. Fujiwara, M. Matsuo, and Y. Sakuragi (editors), *Innovative Computational Methods in Nuclear Many-Body Problems, Towards a New Generation of Physics in Finite Quantum Systems (INNOCOM97)*, 155–+, 1998.

[NKT$^+$94] Z. Nemeth, F. Kaeppeler, C. Theis, T. Belgya, and S. W. Yates, *Astrophys. J.*, **426**, 357, 1994.

[OBMP$^+$10] K. Otsuki, A. Burrows, G. Martínez-Pinedo, S. Typel, K. Langanke, and M. Matos, *AIP Conference Proceedings*, **1238** (1), 240, 2010.

[ÖEL$^+$09] B. Özel, J. Enders, H. Lenske, P. von Neumann-Cosel, I. Poltoratska, V. Y. Ponomarev, A. Richter, D. Savran, and N. Tsoneva, *ArXiv e-prints*, 2009, submitted to PLB.

[ÖEv$^+$07] B. Özel, J. Enders, P. von Neumann-Cosel, I. Poltoratska, A. Richter, D. Savran, S. Volz, and A. Zilges, *Nucl. Phys. A*, **788** (1-4), 385, 2007.

[OHRB96] H. Oberhummer, H. Herndl, T. Rauscher, and H. Beer, *Surv. Geophys.*, **17**, 665, 1996.

[ÖLMPD07] C. Özen, K. Langanke, G. Martínez-Pinedo, and D. J. Dean, *Phys. Rev. C*, **75** (6), 064307, 2007.

[Ots09] T. Otsuka, in J. Al-Khalili and E. Roeckl (editors), *The Euroschool Lectures on Physics with Exotic Beams, Vol. III*, volume 764 of *Lecture Notes in Physics*, 1–25, Springer Berlin / Heidelberg, 2009.

[PERN10] K. Pototzky, J. Erler, P.-G. Reinhard, and V. Nesterenko, *Eur. Phys. J. A*, **46**, 299, 2010.

[PKB$^+$06] V. A. Plujko, I. M. Kadenko, O. A. Bezshyyko, L. O. Golinka-Bezshyyko, and O. I. Davidovskaya, **15** (2), 387, 2006.

[PKK$^+$08] V. A. Plujko, I. M. Kadenko, E. V. Kulich, S. Goriely, O. I. Davidovskaya, and O. M. Gorbachenko, *0802.2183*, 2008.

[PKP$^+$05] I. V. Panov, E. Kolbe, B. Pfeiffer, T. Rauscher, K. Kratz, and F. Thielemann, *Nucl. Phys. A*, **747**, 633, 2005.

[PKR$^+$10] I. V. Panov, I. Y. Korneev, T. Rauscher, G. Martínez-Pinedo, A. Kelić-Heil, N. T. Zinner, and F.-K. Thielemann, *Astron. Astrophys.*, **513**, 14, 2010.

[PMPA$^+$10] I. Petermann, G. Martínez-Pinedo, A. Arcones, W. R. Hix, A. Kelić, K. Langanke, I. Panov, T. Rauscher, K.-H. Schmidt, F.-K. Thielemann, and N. T. Zinner, *J. Phys.: Conf. Ser.*, **202** (1), 012008, 2010.

[PN01] A. Poves and F. Nowacki, in J. Arias and M. Lozano (editors), *An Advanced Course in Modern Nuclear Physics*, volume 581 of *Lecture Notes in Physics*, 70–101, Springer Berlin / Heidelberg, 2001.

[PNVR05] N. Paar, T. Niksic, D. Vretenar, and P. Ring, *Phys. Lett. B*, **606** (3-4), 288, 2005.

[PT03] I. V. Panov and F.-K. Thielemann, *Nucl. Phys. A*, **718**, 647, 2003.

[PVKC07] N. Paar, D. Vretenar, E. Khan, and G. Colò, *Rep. Prog. Phys.*, **70** (5), 691, 2007.

[Qia02] Y.-Z. Qian, *Astrophys. J. Lett.*, **569** (2), L103, 2002.

[QW07] Y.-Z. Qian and G. J. Wasserburg, *Phys. Rep.*, **442** (1-6), 237, 2007, the Hans Bethe Centennial Volume 1906-2006.

[Rag89] P. Raghavan, *Atomic Data and Nuclear Data Tables*, **42** (2), 189, 1989.

[Rau08] T. Rauscher, *Phys. Rev. C*, **78** (3), 032801, 2008.

[Rei92] P. Reinhard, *Ann. Phys.*, **504** (8), 632, 1992.

[RF95] P.-G. Reinhard and H. Flocard, *Nucl. Phys. A*, **584** (3), 467, 1995.

[RFK$^+$09] G. Rugel, T. Faestermann, K. Knie, G. Korschinek, M. Poutivtsev, D. Schumann, N. Kivel, I. Günther-Leopold, R. Weinreich, and M. Wohlmuther, *Phys. Rev. Lett.*, **103** (7), 072502, 2009.

[RHK+02] N. Ryezayeva, T. Hartmann, Y. Kalmykov, H. Lenske, P. von Neumann-Cosel, V. Y. Ponomarev, A. Richter, A. Shevchenko, S. Volz, and J. Wambach, *Phys. Rev. Lett.*, **89** (27), 272502, 2002.

[Ric95] A. Richter, *Prog. Part. Nucl. Phys.*, **34**, 261, 1995.

[Ric04] A. Richter, *Nucl. Phys. A*, **731**, 59, 2004.

[RMRG95] K. Rutz, J. A. Maruhn, P.-G. Reinhard, and W. Greiner, *Nucl. Phys. A*, **590** (3-4), 680, 1995.

[RRGS09] L. M. Robledo, R. Rodríguez-Guzmán, and P. Sarriguren, *J. Phys. G: Nucl. Partic.*, **36** (11), 115104, 2009.

[RS00] P. Ring and P. Schuck, *The nuclear many-body problem*, Springer, 2000.

[RT00] T. Rauscher and F.-K. Thielemann, *At. Data Nucl. Data Tables*, **75**, 1, 2000.

[RT01] T. Rauscher and F.-K. Thielemann, *At. Data Nucl. Data Tables*, **79**, 47, 2001.

[RTGW00] T. Rauscher, F.-K. Thielemann, J. Görres, and M. Wiescher, *Nucl. Phys. A*, **675**, 695, 2000.

[RTK97] T. Rauscher, F.-K. Thielemann, and K.-L. Kratz, *Phys. Rev. C*, **56** (3), 1613, 1997.

[Rut11] E. Rutherford, *Philos. Mag.*, **21**, 669, 1911.

[RW10] D. J. Rowe and J. L. Wood, *Fundamentals of nuclear models*, World Scientific, 2010.

[SCG08] C. Sneden, J. J. Cowan, and R. Gallino, *Annu. Rev. Astron. Astrophys.*, **46** (1), 241, 2008.

[SEK+09] N. Schindzilorz, J. Erler, P. Klüpfel, P.-G. Reinhard, and G. Hager, *Int. J. Mod. Phys. E*, **18** (4), 773, 2009.

[SJ50] H. Steinwedel and J. H. D. Jensen, *Z. Nat. A.*, **5**, 413, 1950.

[SJJ50] H. Steinwedel, J. H. D. Jensen, and P. Jensen, *Phys. Rev.*, **79** (6), 1019, 1950.

[Sky59] T. Skyrme, *Nucl. Phys.*, **9** (4), 615, 1959.

[SLD+02] O. Sorlin, S. Leenhardt, C. Donzaud, J. Duprat, F. Azaiez, F. Nowacki, H. Grawe, Z. Dombrádi, F. Amorini, A. Astier, D. Baiborodin, M. Belleguic, C. Borcea, C. Bourgeois, D. M. Cullen, Z. Dlouhy, E. Dragulescu, M. Górska, S. Grévy, D. Guillemaud-Mueller, G. Hagemann, B. Herskind, J. Kiener, R. Lemmon, M. Lewitowicz, S. M. Lukyanov, P. Mayet, F. de Oliveira Santos, D. Pantalica, Y.-E. Penionzhkevich, F. Pougheon, A. Poves, N. Redon, M. G. Saint-Laurent, J. A. Scarpaci, G. Sletten, M. Stanoiu, O. Tarasov, and C. Theisen, *Phys. Rev. Lett.*, **88** (9), 092501, 2002.

[SMB+10] R. Schwengner, R. Massarczyk, B. A. Brown, R. Beyer, F. Dönau, M. Erhard, E. Grosse, A. R. Junghans, K. Kosev, C. Nair, G. Rusev, K. D. Schilling, and A. Wagner, *Phys. Rev. C*, **81** (5), 054315, 2010.

[SR07] J. Stone and P.-G. Reinhard, *Prog. Part. Nucl. Phys.*, **58** (2), 587, 2007.

[ST07] A. Schiller and M. Thoennessen, *At. Data Nucl. Data Tables*, **93**, 549, 2007.

[Suh07] J. Suhonen, *From nucleons to nucleus*, Springer, 2007.

[Sv81] J. Speth and A. van der Woude, *Rep. Prog. Phys.*, **44** (7), 719, 1981.

[SW91] J. Speth and J. Wambach, *Electric and Magnetic Giant Resonances in Nuclei*, volume 7 of *International Review of Nuclear Physics*, 1–97, World Scientific, 1991.

[Świ09] W. J. Światecki, *Int. J. Mod. Phys. E*, **18** (4), 747, 2009.

[TA83] F.-K. Thielemann and M. Arnould, in K. Böckhoff (editor), *Proc. Inter. Conf. on Nuclear Data for Science and Technology*, 762, 1983.

[TB03] S. Typel and B. A. Brown, *Phys. Rev. C*, **67** (3), 034313, 2003.

[THW74] J. W. Tepel, H. M. Hoffmann, and H. A. Weidenmüller, *Phys. Lett.*, **49B**, 1, 1974.

[TL08] N. Tsoneva and H. Lenske, *Phys. Rev. C*, **77** (2), 024321, 2008.

[TLA+10] H. K. Toft, A. C. Larsen, U. Agvaanluvsan, A. Bürger, M. Guttormsen, G. E. Mitchell, H. T. Nyhus, A. Schiller, S. Siem, N. U. H. Syed, and A. Voinov, *Phys. Rev. C*, **81** (6), 064311, 2010.

[Tri10] Trimble, V., *Eur. Phys. J. H*, **35** (1), 89, 2010.

[TWJ94] K. Takahashi, J. Witti, and H.-T. Janka, *Astron. Astrophys.*, **286**, 857, 1994.

[Typ05] S. Typel, *Phys. Rev. C*, **71** (6), 064301, 2005.

[URS+09] E. Uberseder, R. Reifarth, D. Schumann, I. Dillmann, C. D. Pardo, J. Görres, M. Heil, F. Käppeler, J. Marganiec, J. Neuhausen, M. Pignatari, F. Voss, S. Walter, and M. Wiescher, *Phys. Rev. Lett.*, **102** (15), 151101, 2009.

[Van87] A. Van Der Woude, *Prog. Part. Nucl. Phys.*, **18**, 217, 1987.

[VB70] D. Vautherin and D. M. Brink, *Phys. Lett. B*, **32** (3), 149, 1970.

[VB72] D. Vautherin and D. M. Brink, *Phys. Rev. C*, **5** (3), 626, 1972.

[VH73] R. Vandenbosch and R. Huizenga, *Nuclear Fission*, Academic Press, 1973.

[vHT76] H. von Groote, E. R. Hilf, and K. Takahashi, *At. Data Nucl. Data Tables*, **17**, 418, 1976.

[VPRL01] D. Vretenar, N. Paar, P. Ring, and G. A. Lalazissis, *Phys. Rev. C*, **63** (4), 047301, 2001.

[W+91] C. Wagemans *et al.*, *The Nuclear Fission Process*, CRC Press, 1991.

[WAT03] A. H. Wapstra, G. Audi, and C. Thibault, *Nucl. Phys. A*, **729**, 2003.

[WBC+09] O. Wieland, A. Bracco, F. Camera, G. Benzoni, N. Blasi, S. Brambilla, F. C. L. Crespi, S. Leoni, B. Million, R. Nicolini, A. Maj, P. Bednarczyk, J. Grebosz, M. Kmiecik, W. Meczynski, J. Styczen, T. Aumann, A. Banu, T. Beck, F. Becker, L. Caceres, P. Doornenbal, H. Emling, J. Gerl, H. Geissel, M. Gorska, O. Kavatsyuk, M. Kavatsyuk, I. Kojouharov, N. Kurz, R. Lozeva, N. Saito, T. Saito, H. Schaffner, H. J. Wollersheim, J. Jolie, P. Reiter, N. Warr, G. deAngelis deAngelis, A. Gadea, D. Napoli, S. Lenzi, S. Lunardi, D. Balabanski, G. LoBianco, C. Petrache, A. Saltarelli, M. Castoldi, A. Zucchiatti, J. Walker, and A. Bürger, *Phys. Rev. Lett.*, **102** (9), 092502, 2009.

[WFL83] D. Wintgen, H. Friedrich, and K. Langanke, *Nucl. Phys. A*, **408**, 239, 1983.

[Wig31] E. Wigner, *Gruppentheorie*, Vieweg Braunschweig, 1931.

[WIP+97] G. Wallerstein, I. Iben, P. Parker, A. M. Boesgaard, G. M. Hale, A. E. Champagne, C. A. Barnes, F. Käppeler, V. V. Smith, R. D. Hoffman, F. X. Timmes, C. Sneden, R. N. Boyd, B. S. Meyer, and D. L. Lambert, *Rev. Mod. Phys.*, **69** (4), 995, 1997.

[WVT+96] K. Wisshak, F. Voss, C. Theis, F. Käppeler, K. Guber, L. Kazakov, N. Kornilov, and G. Reffo, *Phys. Rev. C*, **54** (3), 1451, 1996.

[WWK80] R. Whitehead, A. Watt, and D. Kelvin, *Phys. Lett. B*, **89** (3-4), 313, 1980.

[WWM+94] S. E. Woosley, J. R. Wilson, G. J. Mathews, R. D. Hoffman, and B. S. Meyer, *Astrophys. J.*, **433**, 229, 1994.

[Zuk01] A. P. Zuker, *Phys. Rev. C*, **64** (2), 021303, 2001.

Lebenslauf

Name: Hans Peter Loens
Geburtstdatum: 30.1.1982
Geburtsort: Darmstadt
Staatsangehoerigkeit: deutsch

7/1988 - 7/1989	ehem. Brüder-Grimm Grundschule in Darmstadt-Ahrheilgen
8/1989 - 7/1992	Albert-Schweitzer Grundschule in Langen (Hessen)
8/1992 - 6/2001	Dreieichschule Langen (Gymnasium)
6/2001	Abitur
8/2001 - 6/2002	Zivildienst in der Erich-Kästner-Schule Langen (Schule für Körperbehinderte)
10/2002 - 9/2004	Studium der Physik an der Technischen Universität Darmstadt
9/2004	Vordiplom in Physik
10/2004 - 7/2007	Hauptstudium der Physik an der Technischen Universität Darmstadt
7/2006 - 7/2007	Diplomarbeit an der Gesellschaft für Schwerionenforschung in Darmstadt
8/2007	Diplom in Physik
10/2007 - 2/2011	Promotion an der Gesellschaft für Schwerionenforschung in Darmstadt und Promotionsstudium an der Technischen Universität Darmstadt

Erklärung

Hiermit erkläre ich an Eides statt, dass ich die vorliegende Dissertation selbständig verfasst, keine anderen als die angegebenen Hilfsmittel verwendet und nur unter Verwendung der in der Arbeit angegebenen Literatur angefertigt habe.
Die Arbeit wurde bisher in gleicher oder ähnlicher Form keiner anderen Prüfungsbehörde vorgelegt und auch nicht veröffentlicht.

Darmstadt den 2. Februar 2011,
Hans Peter Loens